Tectonothermal evolution of the Sarandí del Yí Shear Zone and adjacent

blocks (Uruguay): Implications for the assembly of Western Gondwana

Dissertation

zur Erlangung des mathemathisch-naturwissenschaftlichen Doktorgrades

„Doctor rerum naturalium"

der Georg-August-Universität Göttingen

im Promotionsprogramm Geowissenschaften

der Georg-August University School of Science (GAUSS)

vorgelegt von

Sebastián Oriolo

aus Buenos Aires

Göttingen 2016

Betreuungsausschuss

Prof. Dr. Siegfried Siegesmund

Abteilung Strukturgeologie und Geodynamik

Geowissenschaftliches Zentrum der Georg-August-Universität Göttingen

Prof. Dr. Pedro Oyhantçabal

Departamento de Geología

Facultad de Ciencias, Universidad de la República

Mitglieder der Prüfungskommission

Referent

Prof. Dr. Siegfried Siegesmund

Abteilung Strukturgeologie und Geodynamik

Geowissenschaftliches Zentrum der Georg-August-Universität Göttingen

Korreferent

Prof. Dr. Pedro Oyhantçabal

Departamento de Geología

Facultad de Ciencias, Universidad de la República

Weitere Mitglieder der Prüfungskommission

Prof. Dr. Jonas Kley

Abteilung Strukturgeologie und Geodynamik

Geowissenschaftliches Zentrum der Georg-August-Universität Göttingen

Prof. Dr. Bernd Lammerer

Fakultät für Geowissenschaften

Ludwig-Maximilians-Universität München

Dr. Klaus Wemmer

Abteilung Isotopengeologie

Geowissenschaftliches Zentrum der Georg-August-Universität Göttingen

Dr. Florian Heidelbach

Bayerisches Geoinstitut

Universität Bayreuth

Tag der mündlichen Prüfung: 14.07.2016

Map it, my boy, and it will all come out

Charles Lapworth

Rocks do not suffer deformation; they enjoy it

Robert Knipe

-Acknowledgements-

-PREFACE-

New data presented in this work are divided into different contributions, which are outlined below. These results as a whole comprise an integral approach to constrain the evolution of the study area. Chapter 1 and 2 are introductory, whereas results obtained in this thesis are included in Chapters 3 to 7. Chapter 8, in turn, presents a critical discussion of all new and available data, and Chapter 9 outlines the main conclusions of the work.

Chapter 1 presents the aim of the work as well as an overview of Gondwana evolution and regional geology of the study area. Chapter 2 reviews methodologies applied in this work, including all methods and analytical procedures.

Chapter 3 (Oriolo et al., 2016, Precambrian Research) presents new U-Pb and Hf zircon data from the basement of the study area, which comprise the Nico Pérez and Piedra Alta terranes. These results are integrated with available data from these blocks as well as from adjacent units in order to establish regional correlations and the allochthony/autochthony of the Nico Pérez Terrane regarding the Río de la Plata Craton.

Chapter 4 (Oyhantçabal et al., submitted to Precambrian Research) includes U-Pb and Hf detrital zircon data from the metasedimentary cover of the Dom Feliciano Belt, which overlains the basement units studied in Chapter 3. Age, provenance and tectonic setting of these units are thus discussed. In the corresponding manuscript, these results are integrated with geochemical and Sm-Nd whole-rock data from the same units, which were mostly analysed by the first author.

Chapter 5 (Oriolo et al., 2015, International Journal of Earth Sciences) presents kinematic, structural and microstructural data from the Sarandí del Yí Shear Zone and adjacent blocks. Quartz CPO data and strain analysis of the mylonites of the shear zone are integrated with these data in order to constrain the structural evolution of the Sarandí del Yí Shear Zone.

Chapter 6 (Oriolo et al., 2016, Tectonics) complements data from Chapter 5, as it incorporates geochronological data from the Sarandí del Yí Shear Zone. Hence, integration of structural, microstructural and geochronological data allows assessing the timing of deformation of the shear zone. Additionally, implications for dating the age of deformation in mylonitic rocks are discussed as well.

Chapter 7 (Oriolo et al., submitted to Journal of Structural Geology) presents structural, microstructural and geochronological data from the Dom Feliciano Belt. The timing of deformation and metamorphism and structural evolution of the belt are thus constrained.

Chapter 8 integrates all available data and results obtained in this work into an evolutionary model for the study area. As a corollary, the history of Western Gondwana assembly is reassessed, evaluating the role of major crustal blocks and Neoproterozoic orogenic belts (Oriolo et al., submitted to Geoscience Frontiers). Chapter 9 summarizes the main results of the work.

The following manuscripts are part of this doctoral thesis:

Oriolo, S., Oyhantçabal, P., Heidelbach, F., Wemmer, K., Siegesmund, S. 2015. Structural evolution of the Sarandí del Yí Shear Zone: kinematics, deformation conditions and tectonic significance. International journal of Earth Sciences 104, 1759-1777.

Oriolo, S., Oyhantçabal, P., Wemmer, K., Basei, M.A.S., Benowitz, J., Pfänder, J., Hannich, F., Siegesmund, S. 2016. Timing of deformation in the Sarandí del Yí Shear Zone, Uruguay: implications for the amalgamation of Western Gondwana during the Neoproterozoic Brasiliano–Pan-African Orogeny. Tectonics 35, 754-771.

Oriolo, S., Oyhantçabal, P., Basei, M.A.S., Wemmer, K., Siegesmund, S. 2016. The Nico Pérez Terrane (Uruguay): from Archean crustal growth and connections with the Congo Craton to late Neoproterozoic accretion to the Río de la Plata Craton. Precambrian Research 280, 147-160.

Oyhantçabal, P., **Oriolo, S.**, Basei, M.A.S., Frei, D., Marahrens, J., Wemmer, K., Siegesmund, S. Provenance and tectonic affinity of metasedimentary rocks of the western Dom Feliciano Belt in Uruguay: Insights from U-Pb detrital zircon geochronology, Hf isotopes, Sm-Nd whole-rock model ages and geochemical data. Submitted to Precambrian Research.

Oriolo, S., Oyhantçabal, P., Wemmer, K., Heidelbach, F., Pfänder, J., Basei, M.A.S., Hueck, M., Hannich, F., Siegesmund, S. Shear zone evolution and timing of deformation in the Neoproterozoic transpressional Dom Feliciano Belt, Uruguay. Submitted to Journal of Structural Geology.

Oriolo, S., Oyhantçabal, P., Wemmer, K., Siegesmund, S. The diachronous assembly of Western Gondwana: implications for the supercontinent cycle. Submitted to Geoscience Frontiers.

-ABSTRACT-

The Sarandí del Yí Shear Zone (Uruguay) is a crustal-scale structure that separates the Río de la Plata Craton from the Nico Pérez Terrane and Dom Feliciano Belt. Nevertheless, its evolution is poorly constrained, even though it represents a key structural feature of Western Gondwana. A multidisciplinary study was thus carried out, in order to assess the tectonic evolution of the Sarandí del Yí Shear Zone and adjacent blocks and the crustal affinity of the latter. Likewise, new and available data were integrated to provide a unified tectonic model for the history of amalgamation of Gondwana and the evolution of major mobile belts during the Neoproterozoic.

Geological, geochronological and isotopic data indicate that the Nico Pérez Terrane originated mostly from Archean episodic crustal growth and underwent dominantly crustal reworking during several Proterozoic events, whereas the Piedra Alta Terrane is made up of juvenile Paleoproterozoic continental crust. Hence, the Nico Pérez Terrane was allochthonous to the Río de la Plata Craton. In contrast, it shows an African crustal affinity and probably derived from the southwestern margin of the Congo Craton. Similarities of Archean and Proterozoic events recorded in the Nico Pérez Terrane basement and the overlying metasedimentary cover of the southwestern Dom Feliciano Belt further support an African derivation.

The onset of the deformation along the Sarandí del Yí Shear Zone is recorded at 630-625 Ma, giving rise to dextral shearing, and is coeval with the onset of deformation, metamorphism and exhumation of the Dom Feliciano Belt. This is related to the collision of the Río de la Plata and Congo Craton and the consequent juxtaposition of the Nico Pérez Terrane to the Río de la Plata Craton margin. Subsequent post-collisional exhumation, deformation and magmatism are ubiquitously recorded in the Dom Feliciano Belt up to 600 Ma. Sinistral shearing at ca. 600-580 Ma took place along the Sarandí del Yí Shear Zone as well as along NNE-striking shear zones of the Dom Feliciano Belt, and resulted from the onset of the Kalahari convergence with the already

amalgamated Río de la Plata and Congo cratons. The input of Kalahari-derived sediments is restricted to the late Ediacaran southeastern post-collisional sequences of the Dom Feliciano Belt, which further indicates that the Congo-Río de la Plata amalgamation predates the accretion of the Kalahari Craton.

As in the case of the Sarandí del Yí Shear Zone, collisional events up to 600 Ma along crustal-scale shear zones can be further traced to the north along the Transbrasiliano-Kandi Lineament, which gave rise to the birth of Western Gondwana. The late stages of Rodinia break-up associated with the opening of the Iapetus Ocean between Laurentia, Baltica and Amazonas occurred contemporaneously and were succeeded by collisional events at 580-550 Ma of the East African/Antartic Orogen. The latter gave rise to the amalgamation of Eastern and Western Gondwana and predated the incorporation of the Kalahari Craton into Gondwana during the late Ediacaran-early Cambrian.

Hence, the assembly of Gondwana comprised a protracted history of amalgamation of crustal blocks between ca. 630 and 530 Ma. Likewise, the existence of the Pannotia supercontinent can be ruled out, as the final configuration of Gondwana was attained during the early Cambrian and took place after rifting between Laurentia and Amazonas.

-ZUSAMMENFASSUNG-

Die zu untersuchende Sarandí del Yí Scherzone trennt den Río de la Plata Kraton von dem Nico Pérez Terran und dem Dom Feliciano Gürtel. Obwohl diese Scherzone entscheidende Kenntnisse hinsichtlich der genauen Verschmelzung Gondwanas bringen könnte, ist die Entwicklung dieser Struktur unbekannt. Diese multidisziplinäre Studie beschäftigt sich nicht nur mit der tektonischen Entwicklung der Sarandí del Yí Scherzone, sondern auch der benachbarten Terrane und ihren Krustensignaturen. Dabei wurden neue und vorhandene Daten verwendet und in ein tektonisches Gesamtmodel integriert, welches nähere Erkenntnisse über die Zusammenführung Gondwanas und die Entwicklung der neoproterozoischen tektonischen Gürtel liefern soll.

Geologische, geochronologische und isotopengeochemische Untersuchungen des Nico Pérez Terrans weisen zum größten Teil auf ein episodisches Krustenwachstum im Archaikum hin, wobei die Kruste während mehrerer Ereignisse im Proterozoikum wiederaufgearbeitet wurde. Im Gegensatz dazu besteht das Piedra Alta Terran aus jüngerer, paläoproterozoischer kontinentaler Kruste. Das Nico Pérez Terran ist somit allochthon zum Río de la Plata Kraton. Die Krustensignatur des Nico Pérez Terrans ähnelt der afrikanischen sehr und wäre ein weiteres Indiz für eine Provenienz aus dem südwestlichen Congo Kraton. Die Ähnlichkeit zwischen archaischen und proterozoischen Ereignissen, die sich im Grundgebirge des Nico Pérez Terrans und den darüber liegenden Metasedimenten des südwestlichen Dom Feliciano Gürtels abzeichnen, ist ein weiterer Beleg für eine afrikanische Provenienz.

Der Verformungsbeginn der Sarandí del Yí Scherzone, die zu dextraler Scherung führte, kann in dieser Studie auf den Zeitraum 630-625 Ma eingegrenzt werden und fand somit zeitgleich mit dem Beginn der Deformation, Metamorphose und Exhumation des Dom Feliciano Gürtels statt. Diese Prozesse sind auf die Folgen der Kollision des Río de la Plata und Congo Kratons und

der darauffolgenden Verlagerung des Nico Pérez Terrans zum Rand des Río de la Plata Kratons zurückzuführen. Hinweise auf postkollisionale Prozesse (Exhumation, Deformation, Magmatismus) reichen im Dom Feliciano Gürtel bis zu 600 Ma zurück. Um ca. 600-580 Ma trat eine sinistrale Scherung entlang der Sarandí del Yí Scherzone sowie der NNO-streichenden Scherzonen des Dom Feliciano Gürtels auf, welche aus dem konvergierenden Kalahari Kratons mit den bereits verschmolzenen Río de la Plata und Congo Kratonen resultierte. Die von dem Kalahari Kraton eingetragenen Sedimente beschränken sich auf das obere Ediacarium des südöstlichen Dom Feliciano Gürtels. Dies weist auf eine der Akkretion des Kalahari Kratons vorhergehende Verschmelzung der Congo - Río de la Plata Kratone hin.

Wie im Fall der Sarandí del Yí Scherzone sind Kollisionsphasen bis 600 Ma entlang transregionaler Scherzonen, die entlang des Transbrasiliano-Kandi Lineaments nach Norden zu verfolgen sind, erkennbar. Diese Phasen führten zur initialen Bildung West-Gondwanas. Gleichzeitig fanden mit der Öffnung des Iapetus Ozeans zwischen Laurentia, Baltica und Amazonas die letzten Züge des Zerbrechens Rodinias statt. Anschließend fand eine Kollisionsphase des Ostafrikanisch-Antarktischen Orogens um 580-550 Ma statt. Durch diese letzte Kollision wurden West- und Ost-Gondwana zusammengeführt, obwohl der Kalahari Kraton anschließend im oberen Ediacarium-unterem Kambrium zu Gondwana verschmolzen wurde.

Somit ist festzustellen, dass mit der Entstehung Gondwanas eine langwierige Verschmelzung von Krustenblöcken zwischen ca. 630 und 530 Ma einhergeht. Ebenso wird die Existenz des Superkontinents Pannotia ausgeschlossen, da Gondwana erst im unteren Kambrium die finale Konfiguration erreichte, die dem Laurentia-Amazonas Rifting nachfolgte.

-TABLE OF CONTENTS-

-CHAPTER 1-

General Introduction

1.1. Aim of the thesis

The goal of this work is to characterize the tectonic evolution of the Sarandí del Yí Shear Zone and adjacent blocks (Uruguay), namely the Piedra Alta and Nico Pérez terranes and the Dom Feliciano Belt, and to establish their role during Gondwana evolution. A multidisciplinary study was thus carried out, considering several specific objectives that can be summed up in the following:

-To define the age and isotopic signature of the Piedra Alta and Nico Pérez terranes. The autochthonous/allochthonous nature of the Nico Pérez Terrane regarding the Río de la Plata Craton and its crustal affinity are thus evaluated.

-To determine the detrital zircon pattern and provenance of the metasedimentary sequences of the southwestern Dom Feliciano Belt.

-To constrain the tectonothermal evolution of the Sarandí del Yí Shear Zone: structure, kinematics, deformation mechanisms and conditions, and timing of deformation. Based on this thorough analysis, strain localization processes during shear zone nucleation and evolution as well as the application of multiple geochronometers in mylonitic rocks are also discussed.

-To characterize the structural architecture and timing of deformation and metamorphism of the Dom Feliciano Belt. The role of shear zones is emphasized and, consequently, temporal and spatial strain variations at the orogen scale are analysed.

-To provide a unified tectonic model for the history of amalgamation of the main crustal blocks of Western Gondwana and the evolution of major mobile belts during the Neoproterozoic.

1.2. From Rodinia break-up to Gondwana amalgamation

The term *Gondwana* was first used by Medlicott (1872, apud Feistmantel, 1876) to refer to a plant-bearing series in India and was afterwards extended to the Gondwana system (Feistmantel, 1876; Medlicott and Blanford, 1879). Based on similarities in the Paleozoic-Mesozoic geological and fossiliferous record of India and other continental masses, Suess (1885) proposed the existence of a supercontinent and coined the name *Gondwanaland*, which was extended to South America, Australia and Antarctica by Wegener (1915).

The evolution of Gondwana was strongly linked to Rodinia break-up, although the participation of some African and South American blocks in Rodinia is controversial (Kröner and Cordani, 2003; Tohver et al., 2006; Evans, 2009). After amalgamation during the late Mesoproterozoic, Rodinia break-up occurred diachronously during the Cryogenian and Ediacaran (Li et al., 2008; Johansson, 2014). Rifting started at ca. 800-700 Ma at the margin of Laurentia and the Kalahari Craton with the Australia-East Antarctica and South China cratons, and was succeeded by rifting at ca. 600 Ma at the Laurentia-Amazonas Craton margin (Fig. 1.1; Jacobs et al., 2008; Li et al., 2008). This late extensional event was almost coeval with the amalgamation of Western Gondwana, which includes most of the South American and African crustal blocks (e.g., Brito Neves et al., 1999; Cordani et al., 2003). However, the Kalahari Craton and the Eastern Gondwana blocks were not amalgamated with the rest of Gondwana till the early Cambrian (Fig. 1.2; Meert, 2003; Jacobs and Thomas, 2004; Collins and Pisarevsky, 2005; Li et al., 2008).
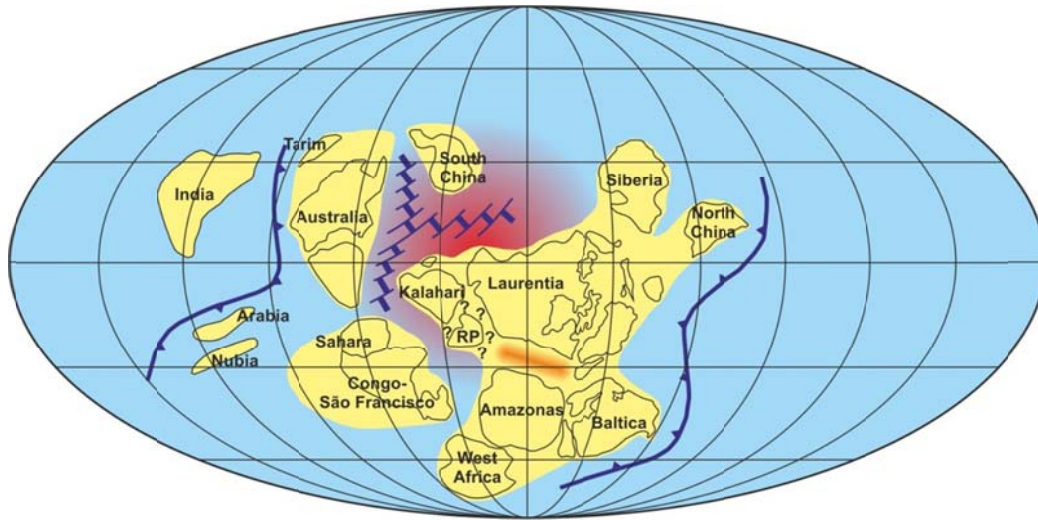
Fig. 1.1: Schematic paleogeography showing main crustal block distribution during Rodinia break-up at ca. 720 Ma (modified after Li et al., 2008). Subduction zones and spreading ridges are indicated in blue, whereas the red area indicates the possible location of a mantle plume. The rifting zone at ca. 600 Ma between Laurentia and Amazonas is shown in orange. Question marks indicate the uncertain location of the Río de la Plata (RP) in Rodinia, as outlined by Kröner and Cordani (2003) and Tohver et al. (2006).
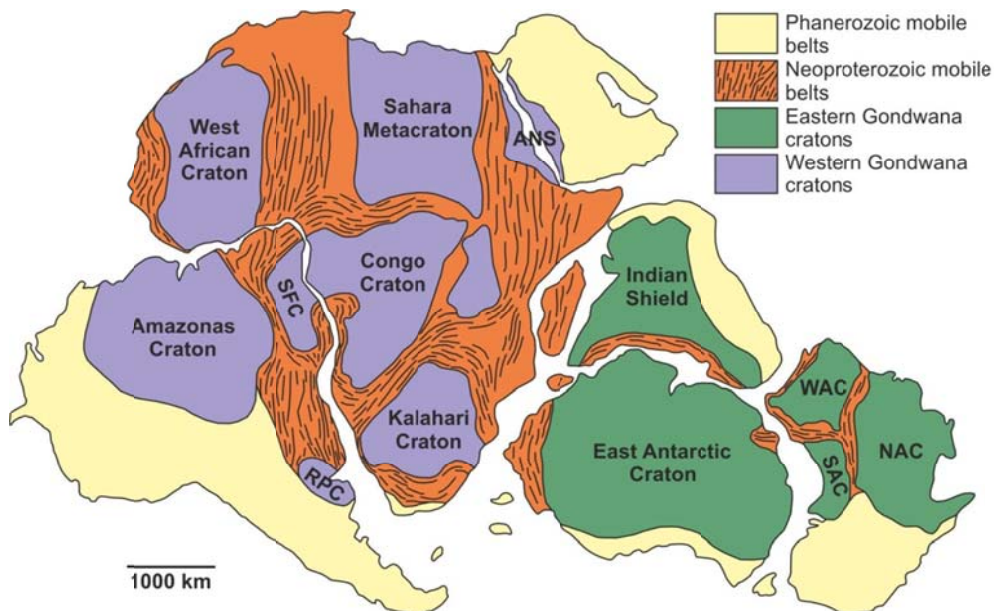
Fig. 1.2: Gondwana map showing main crustal fragments and orogenic belts during the late Neoproterozoic–early Paleozoic (modified after Gray et al., 2008). RPC: Río de la Plata Craton, SFC: São Francisco Craton, ANS: Arabian-Nubian Shield, WAC: West Australian Craton, NAC: North Australian Craton, SAC: South Australian Craton.

1.2. The Brasiliano–Pan-African Orogeny

The Neoproterozoic Brasiliano–Pan-African Orogeny is ubiquitous in South America and Africa and represents a protracted amalgamation of major crustal blocks along several mobile belts, giving rise to the accretion of Gondwana after Rodinia break-up (Almeida et al., 1973; Brito Neves et al., 1999; Cordani et al., 2003; Kröner and Stern, 2004). Particularly, the juxtaposition of the Río de la Plata, Kalahari and Congo cratons together with other minor continental fragments such as the Nico Pérez Terrane took place in Western Gondwana (Basei et al., 2005; Goscombe et al., 2005a; Gray et al., 2008; Foster et al., 2009; Frimmel et al., 2011; Oyhantçabal et al., 2011a, 2011b; Rapela et al., 2011).

The Río de la Plata Craton comprises the Piedra Alta Terrane in Uruguay and the Tandilia Belt in Argentina (Cingolani, 2011, Oyhantçabal et al., 2011a). This Paleoproterozoic block is bounded to the west by the late Ediacaran-Cambrian Pampean Orogen (e.g., Rapela et al., 1998, 2007; Siegesmund et al., 2010), whereas the Sarandí del Yí Shear Zone represents its eastern margin (Oyhantçabal et al., 2011a). The Dom Feliciano Belt is located to the east of this crustal-scale shear zone and reworks several Archean and Paleoproterozoic minor crustal blocks (Oyhantçabal et al., 2011a; Rapela et al., 2011). On the other hand, both Congo and Kalahari cratons comprise mostly Archean and Paleoproterozoic rocks, although Mesoproterozoic rocks are widespread in the Kalahari Craton as well (Fig. 1.3; e.g., Hanson, 2003; McCourt et al., 2013). The western Congo and Kalahari cratons are bounded by the Kaoko and Gariep belts, respectively (Fig. 1.3; Hälbich and Alchin, 1995; Dürr and Dingeldey, 1996; Frimmel and Frank, 1998; Goscombe et al., 2003a, 2003b, 2005a, 2005b; Konopásek et al., 2005; Goscombe and Gray, 2008, 2009; Foster et al., 2009), whereas the Damara Belt represents the boundary between both cratons (Gray et al., 2006, 2008; Foster et al., 2015; Lehmann et al., 2015).
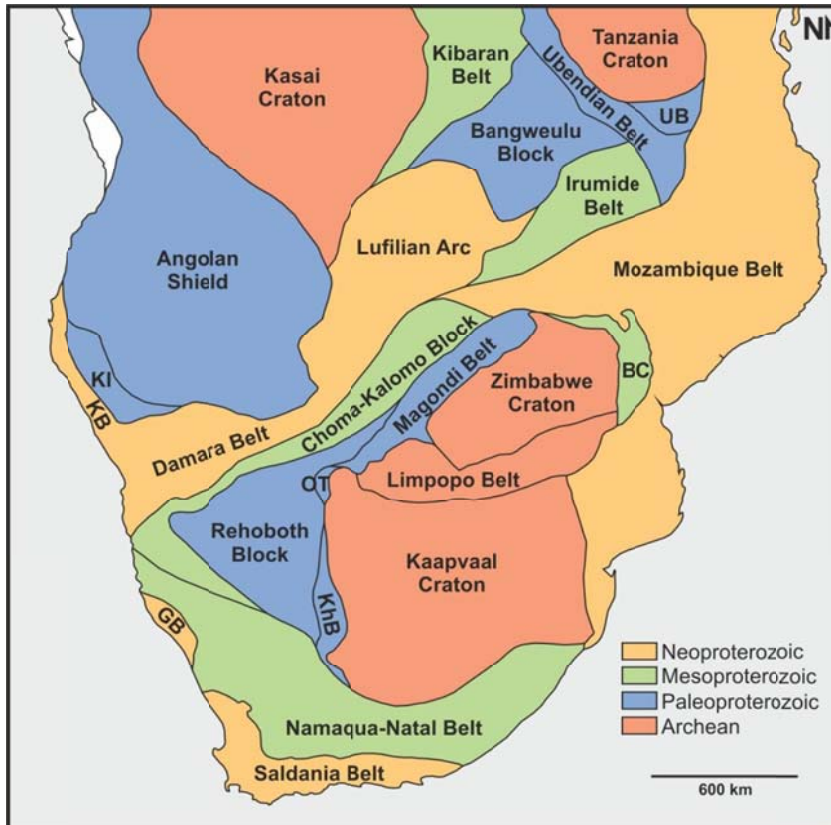
Fig. 1.3: Geological map of the Precambrian of Africa modified after Hanson (2003) and McCourt et al. (2013). UB: Usagaran Belt, KhB: Kheis Belt, OT: Okwa Terrane, KI: Kamanjab Inlier, BC: Báruè Complex, KB: Kaoko Belt, GB: Gariep Belt.

1.4. Geological setting

1.4.1. Tectonostratigraphic units

The Piedra Alta and the Nico Pérez terranes as well as the Dom Feliciano Belt represent the main tectonostratigraphic units that can be recognized in the Precambrian of Uruguay (Fig. 1.4; Oyhantçabal et al., 2011a). The Piedra Alta Terrane is located in western Uruguay and represents a part of the Paleoproterozoic Río de la Plata Craton (Almeida et al., 1973; Dalla Salda et al., 1988), which also includes the Buenos Aires Complex of the Tandilia Belt in Argentina (Cingolani, 2011 and references therein). The craton boundaries are dominantly covered by younger sediments and were thus only recognized through borehole and geophysical information (Booker et al., 2004; Rapela et al. 2007, 2011; Pángaro and Ramos, 2012).
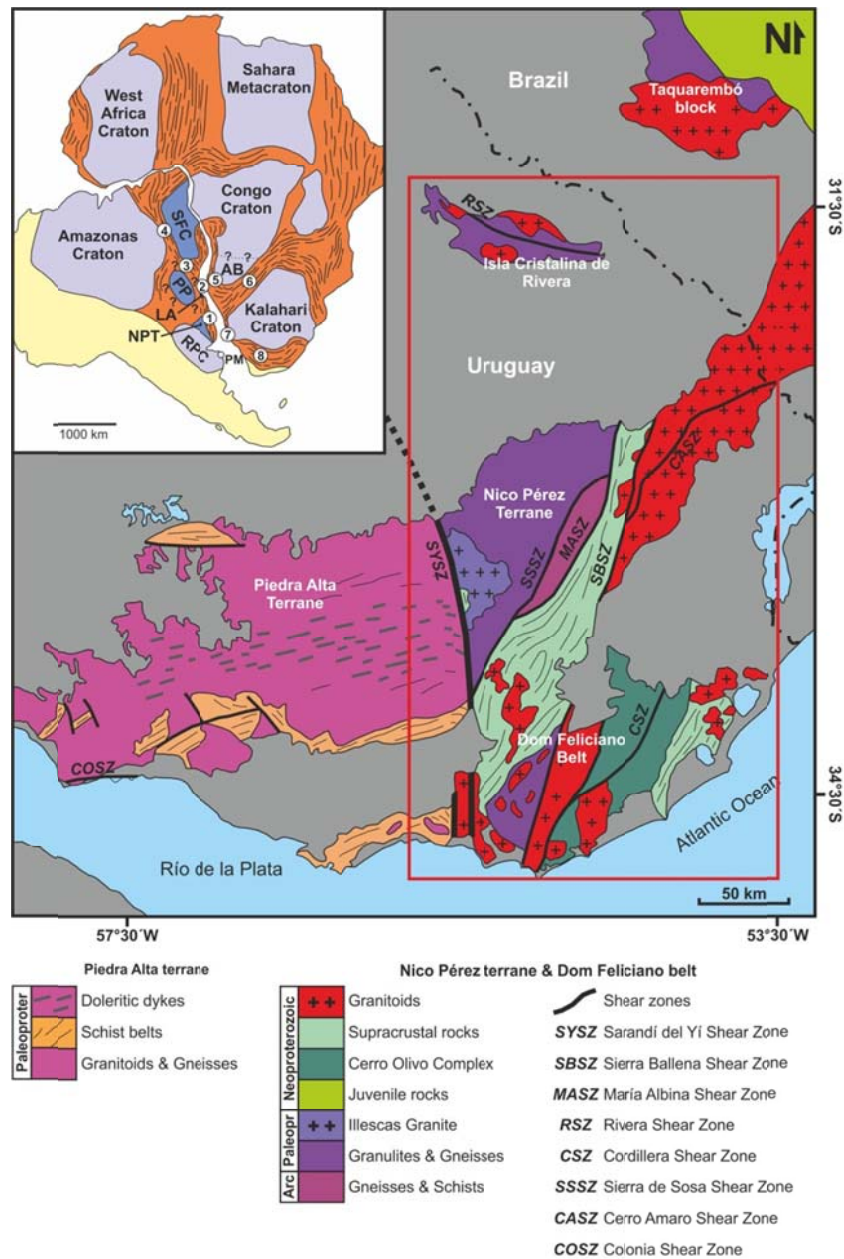
Fig. 1.4: Geological map of the Precambrian of Uruguay modified after Oyhantçabal et al. (2011a) and references therein. The inset shows the distribution of main crustal fragments and Neoproterozoic orogenic belts in South America and Africa, modified after Gray et al. (2008). The study area is indicated in red. African blocks in South America are shown in blue (NPT: Nico Pérez Terrane, PP: Paranapanema Block, SFC: São Francisco Craton). RPC: Río de la Plata Craton, AB: Angola Block. 1: Dom Feliciano Belt, 2: Ribeira Belt, 3: Brasilia Belt, 4: Araçuaí Belt, 5: Kaoko Belt, 6: Damara Belt, 7: Gariep Belt, 8: Saldania Belt. The location of the Punta Mogotes borehole (PM), which represents the southeastern margin of the Río de la Plata Craton, is also indicated (Rapela et al., 2011).

The Nico Pérez Terrane crops out in central Uruguay. It is an Archean-Paleoproterozoic block that shows strong Neoproterozoic reworking (Ellis, 1998; Oyhantçabal et al., 2011a, 2012). It also includes the Isla Cristalina de Rivera in northern Uruguay (Ellis, 1998) and the Taquarembó block in southern Brazil (Oyhantçabal et al., 2011a). The basement of the Nico Pérez Terrane is made up of the Pavas Block, the Valentines-Rivera Granulitic Complex and the Campanero Unit. The Pavas Block comprises Archean orthogneisses, mafic and ultramafic rocks and metasediments (Preciozzi et al., 1979; Hartmann et al., 2001), whereas the Valentines-Rivera Granulitic Complex is constituted by 2.2-2.0 Ga granulites and orthogneisses (Oyhantçabal et al., 2011a, 2012), which are intruded in the west by the 1.7 Ga Illescas rapakivi granite (Campal and Schipilov, 1995). The Campanero Unit comprises migmatites, amphibolites, BIFs, micaschists and orthogneisses with zircon ages of 1.7 Ga and is exposed as a basement inlier of the Dom Feliciano Belt (Sánchez Bettucci et al., 2003, 2004; Oyhantçabal, 2005; Mallmann et al., 2007). Likewise, Neoproterozoic granitoids and metasediments are widespread and indicate a significant reworking related to the evolution of the Dom Feliciano Belt (Oyhantçabal et al., 2011a, 2012).

The Dom Feliciano Belt represents a Neoproterozoic transpressional orogen, which is located in eastern Uruguay and south-eastern Brazil. It can be divided into three main geotectonic units: the granite belt, the schist belt and foreland basins (Basei et al., 2000). The granite belt is made up of the Pelotas and Florianópolis Batholith in Brazil and the Aigúa Batholith in Uruguay (Basei et al., 2000). On the other hand, the schist belt comprises deformed metavolcano-sedimentary sequences such as the Lavalleja, Porongos and Brusque groups, whereas the foreland belt includes post-collisional volcano-sedimentary successions (Basei et al., 2000, 2008). Likewise, it includes a series of pre-Brasiliano basement inliers (Sánchez Bettucci, 1998; Preciozzi et al., 1999; Mallmann et al., 2007; Basei et al., 2011a; Rapela et al., 2011; Saalmann et al., 2011). Due to similarities in the tectonomagmatic evolution, the Dom Feliciano Belt was alternatively correlated

with the Kaoko and Gariep belts in Africa (e.g., Basei et al., 2005, 2008, 2011a; Gross et al., 2009; Oyhantçabal et al., 2009a, 2009b, 2011b; Lenz et al., 2011; Rapela et al., 2011).

1.4.2. Shear zones

The main tectonostratigraphic units of the basement of Uruguay are bound and cross-cut by several major shear zones (Fig. 1.4). In particular, the Sarandí del Yí and the Sierra Ballena shear zones represent the main structural features.

The Sarandí del Yí Shear Zone separates the Paleoproterozoic Piedra Alta Terrane from the adjacent Nico Pérez Terrane and Dom Feliciano Belt (Oyhantçabal et al., 2011a; Rapela et al., 2011) and was proposed as the easternmost boundary of the Río de la Plata Craton (Oyhantçabal et al., 2011a). Due to the lack of structural studies of this shear zone, its evolution is still controversial (Oyhantçabal et al., 1993, 2011a; Gaucher et al., 2011a), even though it represents a key element for the understanding of the amalgamation of Western Gondwana.

On the other hand, the Sierra Ballena Shear Zone represents the boundary between the Nico Pérez Terrane and the Cerro Olivo Complex, i.e., the Punta del Este Terrane (Basei et al., 2011a; Oyhantçabal et al., 2011a; Rapela et al., 2011). Further to the north, the Sierra Ballena was correlated with the Dorsal de Canguçú/Cordilheira and Major Gercino shear zones from southern Brazil (Fernandes et al., 1992; Fernandes and Koester, 1999; Oyhantçabal et al., 2009b, 2011b; Passarelli et al., 2010, 2011) as well as with the Purros Shear Zone of the Kaoko Belt in Namibia (Oyhantçabal et al., 2011b).

Shear zones of the Piedra Alta Terrane present typically E-ENE strike and strike-slip sinistral shearing (Fig. 1.4). Among them, the Colonia and Mosquitos shear zones yield K-Ar muscovite ages of 2.05-1.78 Ga (Oyhantçabal et al., 2006; Gianotti et al., 2010), indicating tectonic activity related to the Paleoproterozoic evolution of the Río de la Plata Craton. The same E-ENE

structural grain can be recognized elsewhere within the Piedra Alta Terrane due to the distribution of gneissic-granitic and metavolcano-sedimentary belts and the Florida dyke swarm (Fig. 1.4; Oyhantçabal et al., 2011a). Furthermore, comparable E-striking Paleoproterozoic shear zones such as the Azul Shear Zone crop out in the Tandilia Belt (Frisicale et al., 2005, 2012).

Between the Sarandí del Yí and Sierra Ballena shear zones, several mylonitic belts are present within the basement of the Nico Pérez Terrane and the southwestern Dom Feliciano Belt (Fig. 1.4). The Rivera Shear Zone cross-cuts the Valentines-Rivera Granulitic Complex, whereas the Sierra de Sosa and María Albina shear zones separate different lithostratigraphical units (Oyhantçabal et al., 2011a, 2012). Likewise, several NE-striking shear zones such as the Cerro Amaro and Cordillera shear zones are present to the east of the Sierra Ballena Shear Zone (Oyhantçabal, 2005; Oyhantçabal et al., 2011a).

-CHAPTER 2-

Methodology

2.1. Geological mapping

The starting point of this research was the geological mapping of the study area (Fig. 1.4), which was based on field work, available geological maps, aerial photographs and satellite images. A total of four months of field work was divided into several campaigns between 2011 and 2014. Geological and structural data were collected thorough the study area and key areas were mapped in detail (ca. 1:20000). Field data were integrated with all available maps from publications, data from the Geological Survey of Uruguay (DINAMIGE), Landsat images and 1:20000 aerial photographs from the Servicio Geográfico Militar, Uruguay.

Based on the mapping, key units were sampled for laboratory analyses (thin sections, quartz crystallographic preferred orientation analyses, geochronological and isotopic studies). In turn, preliminary laboratory results were checked during subsequent field work.

2.2. Petrography

About 160 thin sections were analysed using classical optical microscopy. Petrographic observations included lithological and modal characterization, determination of critical parageneses to constrain metamorphic conditions and microstructural analysis. Microstructural analysis was carried out in order to assess deformation mechanisms and conditions, and was integrated with quartz crystallographic preferred orientation data in the case of mylonitic rocks.

2.3. Quartz crystallographic preferred orientation patterns

Samples of mylonites were collected to analyse the crystallographic preferred orientation (CPO) of quartz (Appendix 1). Sections parallel to the lineation and perpendicular to the foliation

were studied with electron backscatter diffraction (EBSD). The reference structural frame is presented in all pole figures. The sections were polished additionally with a high pH silica solution (40 nm particle size) in order to remove damage from the previous polishing steps. The SEM was a Leo (now Zeiss) Gemini 1530 with a Schottky emitter run at 30 keV accelerating voltage and a beam current of about 8 nA, and is located at the Bayerisches Geoinstitut of the Universität Bayreuth. EBSD patterns were recorded with a Nordlys 2 camera and indexed with the Channel software package, both from Oxford Instruments. Areas of about 40 mm^2 were mapped with a step size of 10 µm yielding between 20000 and 70000 indexed points for quartz depending on the sample. The discrete orientation points were clustered with a 5° circle and then smoothed with a 10° FWHM for representation in the pole figures.

2.4. Geochronology

2.4.1. U-Pb geochronology

Samples were crushed and sieved and, afterwards, the mineral fractions were separated using conventional heavy liquid and isodynamic techniques. Sample locations are presented in Appendix 2. For several samples, not only zircons but also other mineral phases were also concentrated for geochronology (Appendix 2). Measurements were carried out at the Geochronological Research Centre of the University of São Paulo, Brazil (U-Pb SHRIMP and LA-ICP-MS) and the Central Analytical Facility of the Stellenbosch University, South Africa (U-Pb LA-ICP-MS).

Age determinations by SHRIMP were performed at the Geochronological Research Centre of the University of São Paulo, according to standard procedures (Compston et al., 1984; Stern, 1998; Williams, 1998; Sircombe, 2000). Zircons from each sample were arranged in rows with Temora 2 zircon reference standard, cast into epoxy resin grain mounts with a diameter of 2.54

cm, and polished to reveal grain centers. Prior to analysis, cathodoluminescence (CL) and transmitted images were obtained so that sites for analysis could be chosen. The SHRIMP IIe setup is described below:

- Primary beam analytical conditions: Kohler aperture = 120 μm, spot size = 30 μm, and O_2^- beam density = ~2.5-7 ηA (depending on brightness aperture).

- Secondary beam analytical conditions: source slit = 80 μm; mass resolutions for $^{196}(Zr_2O)$, ^{206}Pb, ^{207}Pb, ^{208}Pb, ^{238}U, $^{248}(ThO)$ and $^{254}(UO)$ ranging between 5,000 and 5,500 (1%), and residues < 0.025; energy slit = open.

During acquisition, raster time was 2-3 minutes with spot size = 50 μm, plus 0.5 minutes of burning time fixed at the center. Analytical rate among standard and sample is 1 standard to 4 zircon samples.

The Pb^+ ionization efficiency is about a factor of two higher than U^+, and so the $^{206}Pb^+/^{238}U^+$ ratio must be calibrated using a standard material (Williams, 1998). Measured $^{206}Pb^+/^{238}U^+$ varies with the measured UO^+/U^+ to define a calibration line of known age, in this case 416.78 Ma for the Temora 2 zircon. The age of an unknown sample can then be determined by the ratio of $^{206}Pb^+/U^+$ in the unknown to that ratio in the standard at the common UO/U value. For additional information, see Williams (1998). SHRIMP softwares are LabVIEW 8.5 and SHRIMP SW 2.90. Data was reduced using SQUID 1.06. Common lead corrections use ^{204}Pb according to Stacey and Kramer (1975). Temora 2 is used as $^{206}Pb/^{238}U$ age reference (416.78 Ma; Black et al., 2004), and SL13 (238 ppm) is used as U composition reference. More details about analytical procedures and data acquisition and processing are presented by Sato et al. (2014).

On the other hand, zircon and titanite LA-ICP-MS analyses performed at the Geochronological Research Centre of the University of São Paulo were carried out using a Neptune inductively coupled plasma-mass spectrometer (ICP–MS) and an excimer laser ablation (LA)

system. Table 2.1 provides the cup and ICP-MS configuration as well as the laser parameters used during the analysis. The U-Pb analysis was used to measure the materials in the following order: two blanks, two NIST standard glasses, three external standards, 13 unknown samples, two external standards and two blanks. Each experiment consisted of 40 cycles with 1 s/cycle. The ^{204}Hg interference for ^{204}Pb was corrected using ^{202}Hg, as ^{204}Hg/^{202}Hg = 4.350360. The ^{207}Pb/^{206}Pb ratio was used to normalize both the NIST and external standards, whereas the ^{238}U/^{206}Pb ratio was used to normalize the external standard. The standard GJ-1 was used for the zircon analyses (Elhlou et al., 2006). Zircon typically contains low concentrations of common Pb. Thus, the reliability of the measured ^{207}Pb/^{206}Pb and ^{238}U/^{206}Pb ratios critically depends on accurately assessing the common Pb component. The residual common Pb was corrected based on the measured ^{204}Pb concentration using the known terrestrial composition (Stacey and Kramers, 1975). The uncertainty introduced by laser-induced fractionation of elements and mass instrumental discrimination was corrected using a reference zircon standard (GJ-1; Jackson et al., 2004). The isotope ratios and interelement fractionation of data collected using the ICP-MS instrument were evaluated by interspersing the GJ-1 zircon standard in each set of thirteen zircon spots. The GJ-1 standard meets the requirements for the methods used in the laboratory, and the ratios ^{238}U/^{206}Pb*, ^{207}Pb*/^{206}Pb* and ^{232}Th/^{238}U were homogeneous throughout application of the bracket technique. External errors were calculated using error propagation for the individual measurements of the standard GJ-1 and the individual zircon sample measurements (spots).

Most of the data plot close to concordant ages. Results are represented in concordia and Tera Wasserburg plots generated by the program Isoplot/Ex (Ludwig, 2003). Data were filtered prior to plotting, to remove analyses with the most disturbed radiogenic Pb and with higher ^{206}Pb of common origin, calculated from measured ^{204}Pb using Cumming and Richards (1975) Pb evolution curves for common Pb compositions.

Cup configuration and interferences							
IC3	IC4	L4	IC6	L3	Axial	H2	H4
^{202}Hg	^{204}Pb	^{206}Pb	^{207}Pb	^{208}Pb	~219,59	^{232}Th	^{238}U

Instrument operating parameters				
MC-ICP-MS		Laser ablation		
Model	ThermoFinnigan Neptune	Type	193 nm Ar-F excimer laser	
Forward power	952 W	Model	Analyte G2-Photon Machines	
Mass resolution	Low (400)	Repetition rate	6 Hz	
		Laser fluence	8.55 J/m^2	
		Spot size	32 µm	
Gas flows-laser ablation		Data reduction		
Cool/plasma (Ar)	16 L/min			
Auxiliary (Ar)	0.80 L/min	Interference correction	^{202}Hg/^{204}Hg	4.35036
Sample cell gas (He)	~1 L/min			

Table 2.1: Cup configuration and instrument operating parameters.

U–Pb age data obtained at the Central Analytical Facility of the Stellenbosch University were, in turn, acquired by laser ablation-single collector-magnetic sector field-inductively coupled plasma-mass spectrometry (LA-SF-ICP-MS) employing a ThermoFinnigan Element2 mass spectrometer coupled to a NewWave UP213 laser ablation system. All age data were obtained by single spot analyses with a spot diameter of 30 µm and a crater depth of approximately 15-20 µm. The methods employed for analysis and data processing are described in detail by Gerdes and Zeh (2006) and Frei and Gerdes (2009). For quality control, the Plešovice (Sláma et al., 2008) and M127 (Nasdala et al., 2008; Mattinson, 2010) zircon reference materials were analysed, and the results were consistently in excellent agreement with the published ID-TIMS ages. The calculation of concordia ages and plotting of concordia diagrams were performed using Isoplot 3.0 (Ludwig, 2003). Results are presented in relative probability curves recalculated from the number of zircon analyses for each age class.

2.4.2. ^{40}Ar/^{39}Ar

^{40}Ar/^{39}Ar step-heat analyses were carried out in hornblende and mica separates (Appendix 2). Measurements were carried out at the Geochronology Laboratory of the University of Alaska Fairbanks and the Argonlab Freiberg.

In the case of ^{40}Ar/^{39}Ar determinations conducted at the Geochronology Laboratory of the University of Alaska Fairbanks, the mineral MMhb-1 (Samson and Alexander, 1987) with an age of 513.9 Ma (Lanphere and Dalrymple, 2000) was used to monitor neutron flux and to calculate the irradiation parameter (*J*). The samples and standards were wrapped in aluminium foil and loaded into aluminium cans of 2.5 cm in diameter and 6 cm in height. The samples were irradiated in position 5c of the uranium enriched research reactor of the McMaster University in Hamilton, Ontario, Canada for 20 MW h.

Upon their return from the reactor, the samples and monitors were loaded into 2 mm diameter holes in a copper tray that was then loaded in an ultra-high vacuum extraction line. The monitors were fused and the samples heated, using a 6 W argon-ion laser following the technique described in York et al. (1981), Layer et al. (1987) and Layer (2000). Argon purification was achieved using a liquid nitrogen cold trap and a SAES Zr-Al getter at 400°C. The samples were analysed in a VG-3600 mass spectrometer at the Geophysical Institute, University of Alaska, Fairbanks. The measured argon isotopes were corrected for system blank and mass discrimination, as well as calcium, potassium, and chlorine interference reactions following procedures outlined in McDougall and Harrison (1999). System blanks generally were 2×10^{-16} mol ^{40}Ar and 2×10^{-18} mol ^{36}Ar, which are 10 to 50 times smaller than fraction volumes. Mass discrimination was monitored by running both calibrated air shots and a zero-age glass sample. These measurements were made on a weekly to monthly basis to check for changes in mass discrimination.

Ages are quoted to the ±1σ level and calculated using the constants of Steiger and Jaeger (1977). The integrated age is given by the total gas measured and is equivalent to a K-Ar age. The

spectrum provides a plateau age if three or more consecutive fractions represent at least 50% of the total gas release and are within two standard deviations of each other (MSWD < 2.5).

On the other hand, $^{40}Ar/^{39}Ar$ step-heat analyses were conducted at the Argonlab in Freiberg Germany as well. Sample packets (2-3 mg multigrain) were placed along with fluence monitors on Al discs, and irradiated for 6.5 hours in the LVR-15 research reactor of the Nuclear Research Institute in Řež, Czech Republic. The thermal neutron fluence was ~5x10^{13} n/cm^{2}s and the thermal-to-fast neutron ratio was ~2.2. Step heating was performed using an energy-controlled floating 30W CO_2 laser system at 10.6 μm wavelength and a defocused beam of 3 mm diameter. Gas purification was achieved by two AP10N getter pumps, one operated at room temperature and the other at 400°C. Laser-heating time was 5 minutes per step. Cleaning time per step was 10 minutes. Argon isotope compositions were measured in static mode on a GV instruments ARGUS noble gas-mass spectrometer equipped with five Faraday cups. Typical blank levels are 2.5x10^{-16} mol ^{40}Ar and 8.1x10^{-18} mol ^{36}Ar. Measurement time was 7.5 minutes per step comprising 45 scans of 10 seconds integration time. Mass bias was corrected assuming a linear mass-dependent isotope fractionation and an atmospheric $^{40}Ar/^{36}Ar$ ratio of 295.5. Raw-data reduction and time-zero intercept calculations were carried out with an in-house developed Matlab® software. Isochron, inverse isochron, and plateau ages were calculated with ISOPLOT 3.7 (Ludwig, 2008). All ages are based on Fish Canyon sanidine as flux monitor (28.305 ± 0.036 Ma) and the decay constant (λ_{tot}=(5.5492 ± 0.0093)x10^{-10} a^{-1}) reported by Renne et al. (2010). The age uncertainties are reported at the ±1σ confidence level. Interfering Ar isotopes were corrected using $(^{36}Ar/^{37}Ar)_{Ca}$ = 0.000227 ± 0.000002, $(^{39}Ar/^{37}Ar)_{Ca}$ = 0.000602 ± 0.000006, $(^{38}Ar/^{39}Ar)_K$ = 0.01211 ± 0.00061, $(^{40}Ar/^{39}Ar)_K$ = 0.00183 ± 0.00009.

2.4.3. K-Ar

The mica minerals were enriched by a mica-jet as described by Wemmer (1991) and other standard techniques like magnetic separation and hand picking. Purified micas were ground in pure alcohol to remove alteration rims that might have suffered a loss of Ar or K. The argon isotopic composition was measured in a pyrex glass extraction and purification line coupled to a Thermo Scientific ARGUS VI noble gas mass spectrometer operating in static mode at the Geoscience Centre of the Georg-August-Universität Göttingen. The amount of radiogenic ^{40}Ar was determined by isotope dilution method using a highly enriched ^{38}Ar spike from Schumacher (1975). The spike is calibrated against the biotite standard HD-B1 (Fuhrmann et al., 1987). The age calculations are based on the constants recommended by the IUGS quoted in Steiger and Jäger (1977).

Potassium was determined in duplicate by flame photometry using a BWB-XP flame photometer. The samples were dissolved in a mixture of HF and HNO_3 according to the technique of Heinrichs and Herrmann (1990). The analytical error for the K-Ar age calculations is given on a 95% confidence level (±2σ). Further details of argon and potassium analyses for the laboratory in Göttingen are given in Wemmer (1991).

2.4.4. Rb-Sr

Rb-Sr analyses were carried out at the Geoscience Centre of the Georg-August-Universität Göttingen (Appendix 2). Whole-rock (WR) and muscovite separates (~50 mg) were transferred into Savillex beakers and mixed with a calibrated ^{87}Rb-^{84}Sr spike. Samples were mixed with 2.0 ml of 40% HF and 2.0 ml of 65% HNO_3. After a period of cold reaction, the solution was evaporated to dryness. A second HF-HNO_3 digestion step was carried out, which was followed by addition of 5.0 ml of 6N HCl, initiating another hot reaction. Afterwards, cooled solutions were heated up for

evaporation. In a last step, 1.5 ml of 2.5 N HCl was added and the solutions were centrifuged for

10 minutes.

Rb and Sr were separated using standard cation exchange procedures. The cation

exchange columns were conditioned with 15 ml of 2.5 N HCl. The samples were diluted in 1.5 ml

2.5 N HCl and the resulting sample solutions were loaded into the columns and washed with 1.5

ml of 2.5 N HCl. The separated elements were dissolved in 2.5 N HCl and homogenized using an

ultrasonic bath for 2 minutes. From each sample, 200 ng were transferred to the center of a

rhenium filament with a loading bed of 2μl of 0.4N H_3PO_4 in order to suppress ionization and to

enable measurement with a stable signal. The prepared sample filaments and additional standard

filaments were put onto a sample wheel, which was mounted into the sample chamber. Samples

were ionized and measured under vacuum using a ThermoFinnigan Triton TI mass spectrometer

(TIMS).

2.5. Hf isotopy

All Lu-Hf zircon analyses were carried out at the Geochronological Research Centre of the

University of São Paulo on a Neptune multicollector inductively coupled plasma mass

spectrometer equipped with a laser-ablation Photon system. Analyses were performed in the

same zircon grains that were previously dated by LA-ICP-MS (Appendix 2). The ablation time was

60 s; repetition rate of 7 Hz, and He was used as carrier gas. $^{176}Hf/^{177}Hf$ ratios were normalized to

$^{179}Hf/^{177}Hf = 0.7325$. Cup configuration and instrument operating parameters are presented in

Table 2.2. The isotopes ^{172}Yb, ^{173}Yb, ^{175}Lu, ^{177}Hf, ^{178}Hf, ^{179}Hf, ^{180}Hf and $^{176}(Hf+Yb+Lu)$ were collected

simultaneously on Faraday cups. $^{176}Lu/^{175}Lu$ ratio of 0.02669 was used to calculate $^{176}Lu/^{177}Hf$.

Mass bias corrections of Lu-Hf isotopic ratios were calculated using the variations of GJ-1 standard.

A decay constant for ^{176}Lu of 1.867×10^{-11} a^{-1} (Söderlund et al., 2004), the present-day chondritic

ratios of ^{176}Hf/^{177}Hf = 0.282772 and ^{176}Lu/^{177}Hf=0.0332 (Blichert-Toft and Albarède, 1997) were adopted to calculate ε_{Hf} values. A two-stage continental model (T_{DM2}) was calculated using the initial ^{176}Hf/^{177}Hf of zircon and the ^{176}Lu/^{177}Hf=0.022 ratio for the lower continental crust (Griffin et al., 2004).

Cup configuration and interferences								
L4	L3	L2	L1	Axial	H1	H2	H3	H4
^{171}Yb	^{173}Yb	^{174}Yb	^{175}Lu	^{176}Hf	^{177}Hf	^{178}Hf	^{179}Hf	^{181}Ta

Instrument operating parameters						
MC-ICP-MS			*Laser ablation*			
Model	ThermoFinnigan Neptune		Type	193 nm Ar-F excimer laser		
Forward power	952 W		Model	Analyte G2-Photon Machines		
Mass resolution	Low (400)		Repetition rate	7 Hz		
			Laser fluence	8.55 J/m^2		
			Spot size	47 µm		
Gas flows-laser ablation			*Data reduction*			
Cool/plasma (Ar)	16 L/min		Mass bias	^{173}Yb/^{171}Yb	1.123456	
				^{179}Hf/^{177}Hf	0.7325	
Auxiliary (Ar)	0.80 L/min		Interference correction	^{176}Yb/^{173}Yb	0.786956	
Sample cell gas (He)	~1 L/min			^{176}Lu/^{175}Lu	0.026549	
Nitrogen	1.4 mL/min			^{174}Yb/^{173}Yb	1.973000	

Table 2.2: Cup configuration and instrument operating parameters, following guidelines from Fisher et al. (2014).

-CHAPTER 3-

The Nico Pérez Terrane

3.1. Introduction

The recognition of terranes as fault-bounded crustal blocks with a geological history that differs significantly from the adjacent blocks is fundamental to understand crustal accretion processes during supercontinent amalgamation (Howell et al., 1985). This was early recognized for the South American Platform, particularly during the Precambrian collisional orogenies that gave rise to the consolidation of this part of Western Gondwana (Almeida et al., 1973; Cordani and Brito Neves, 1982; Ramos, 1988).

The Nico Pérez Terrane of Uruguay was first defined by Bossi and Campal (1992) as a Paleoproterozoic block with Neoproterozoic magmatism and deformation. Archean basement inliers were afterwards recognised (Hartmann et al., 2001), whereas Mesoproterozoic reworking during the Grenville Orogeny was also suggested but not confirmed (Campal and Schipilov, 1999; Bossi and Cingolani, 2009; Gaucher et al., 2011a). Nevertheless, the Nico Pérez Terrane was always understood as the easternmost part of the Paleoproterozoic Río de la Plata Craton (Bossi and Campal, 1992; Mallmann et al., 2007; Gaucher et al., 2011a; Frimmel et al., 2011). In contrast, Oyhantçabal et al. (2011a) separated the Nico Pérez Terrane from the Río de la Plata Craton and considered it an Archean-Paleoproterozoic crustal block with a significant Neoproterozoic reworking related to the Brasiliano Orogeny. Rapela et al. (2011) compared it with the Encantadas, Punta del Este and Mar del Plata terranes, indicating that they all comprise African blocks that were rifted away from the African major cratons during the opening of the Adamastor Ocean at 780-760 Ma.

3.2. Geological setting

The Nico Pérez Terrane is bounded to the west by the Sarandí del Yí Shear Zone, whereas the Sierra Ballena Shear Zone separates it from the Cerro Olivo Complex, which comprises a Neoproterozoic basement inlier within the Dom Feliciano Belt, and the Aiguá Batholith (Fig. 3.1;

Oyhantçabal, 2005; Oyhantçabal et al., 2009b, 2011b). The basement of the Nico Pérez Terrane includes the Archean Pavas Block (Preciozzi et al., 1979) as well as two Paleoproterozoic units, namely the Valentines-Rivera Granulitic Complex and the Campanero Unit (Sánchez Bettucci, 1998; Oyhantçabal et al., 2011a), which are intruded by the Paleoproterozoic Illescas granite and several Neoproterozoic intrusions (Campal and Schipilov, 1995; Oyhantçabal et al., 2011a, 2012). A summary of the available geochronological data for the Nico Pérez Terrane is presented in Table 3.1.
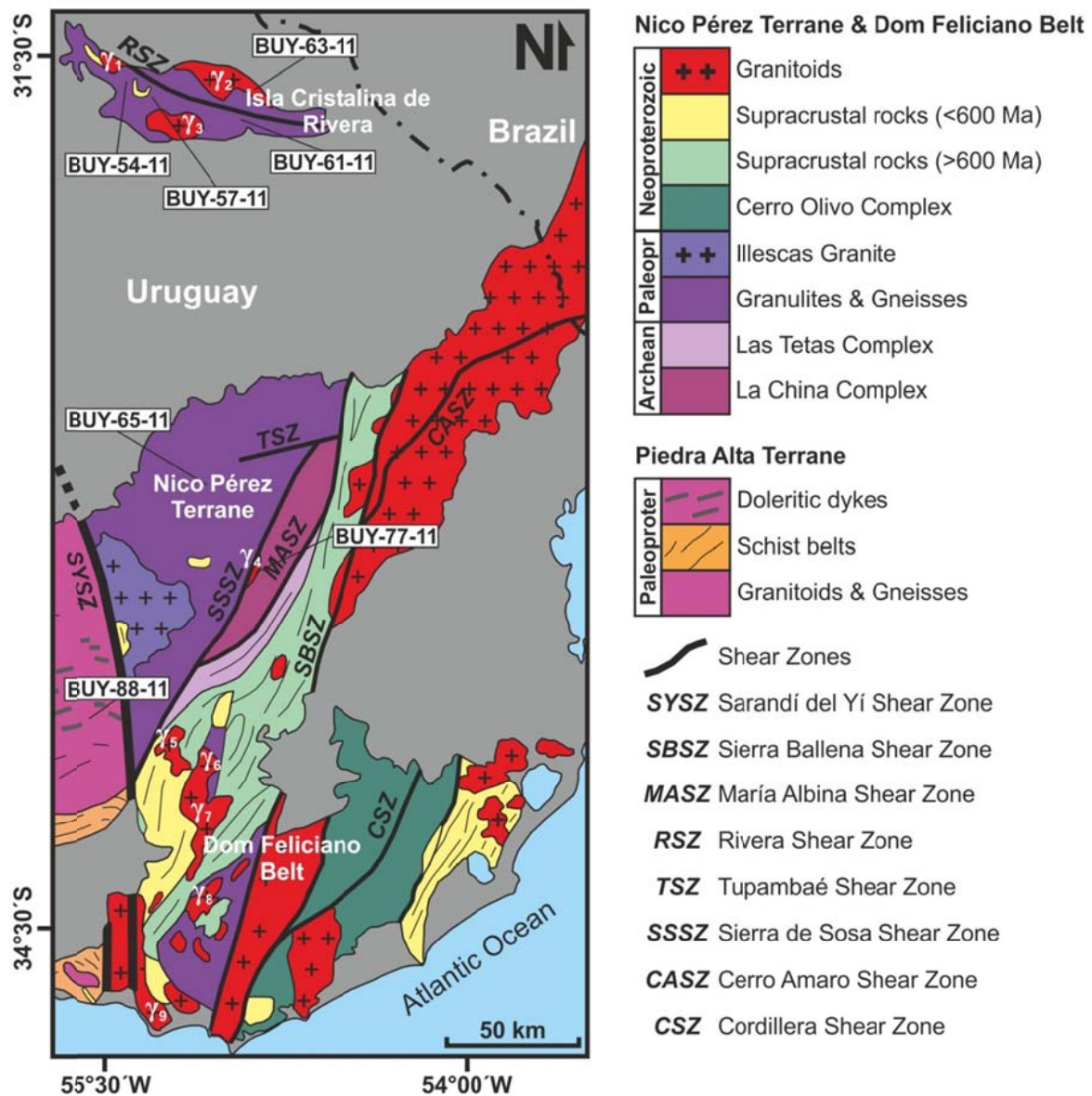
Fig. 3.1: Geological map of the Nico Pérez Terrane and adjacent blocks (modified after Oyhantçabal et al., 2011a, and references therein). Sample locations and Neoproterozoic intrusions (γ_1: Sobresaliente granite, γ_2: Amarillo granite, γ_3: Las Flores granite, γ_4: Zapicán granodiorite, γ_5: Lavaderos granite, γ_6: Arroyo Mangacha granite, γ_7: Puntas del Santa Lucía monzogranite, γ_8: Puntas de Mataojo granodiorite, γ_9: Pan de Azúcar intrusion) are shown.

21

	Unit	Lithology	Age (Ma)	Method	Reference
	La China Complex	Metatonalite	3404 ± 8 (inheritance)	U-Pb SHRIMP Zrn	Hartmann et al. (2001)
		Metatonalite	2721 ± 7 (metamorphic)	U-Pb SHRIMP Zrn	Hartmann et al. (2001)
		Metatonalite	3096 ± 45	U-Pb LA-ICP-MS Zrn	Gaucher et al. (2011a)
	Valentines-Rivera Granulitic Complex	Granulite	2163 ± 22 (magmatic)	U-Pb SHRIMP Zrn	Santos et al. (2003)
		Granulite	2058 ± 3 (metamorphic)	U-Pb SHRIMP Zrn	Santos et al. (2003)
Nico Pérez Terrane	Campanero Unit	Mylonitic granite	1754 ± 7	U-Pb SHRIMP Zrn	Mallmann et al. (2007)
		Amphibolite	564.0 ± 4.1	Ar/Ar Hbl	Oyhantçabal et al. (2007)
	Illescas granite	Rapakivi granite	1760 ± 32	Rb-Sr WR	Bossi and Campal (1992)
	Parque UTE Group	Metarhyolite	1429 ± 21	U-Pb ID-TIMS Zrn	Oyhantçabal et al. (2005)
		Metagabbro	1492 ± 4	U-Pb ID-TIMS Zrn	Oyhantçabal et al. (2005)
	Mina Verdún Group	Metatuff	1433 ± 6	U-Pb LA-ICP-MS Zrn	Gaucher et al. (2011a)
	Neoproterozoic granitoids	Puntas del Santa Lucía monzogranite	633 ± 8	U-Pb SHRIMP Zrn	Hartmann et al. (2002)
		Puntas de Mataojo granodiorite	627 ± 33	U-Pb SHRIMP Zrn	Oyhantçabal et al. (2009a)
		Lavaderos granite	610 ± 3	U-Pb LA-ICP-MS Zrn	Gaucher et al. (2014a)
		Mangacha granite	583 ± 7	U-Pb SIMS Zrn	Gaucher et al. (2008a)
Isla Cristalina de Rivera	Valentines-Rivera Granulitic Complex	Metatrondhjemite	2140 ± 6 (magmatic)	U-Pb SHRIMP Zrn	Santos et al. (2003)
		Metatrondhjemite	2077 ± 6 (metamorphic)	U-Pb SHRIMP Zrn	Santos et al. (2003)
		Mesocratic gneiss	2147 ± 8.7 (magmatic)	U-Pb SHRIMP Zrn	Oyhantçabal et al. (2012)
		Mesocratic gneiss	2113.7 ± 3.1 (magmatic)	U-Pb SHRIMP Zrn	Oyhantçabal et al. (2012)
		Leucocratic gneiss	2171.7 ± 8.4 (magmatic)	U-Pb SHRIMP Zrn	Oyhantçabal et al. (2012)
		Mesocratic gneiss	2094 ± 17 (metamorphic)	Pb-Pb SL Ttn	Oyhantçabal et al. (2012)
		Leucrocratic gneiss	2093 ± 36 (magm/met?)	U-Pb SHRIMP Zrn	Oyhantçabal et al. (2012)
		Mesocratic gneiss	1982 ± 5	Th-U-Pb CHIME-EPMA Mnz	Oyhantçabal et al. (2012)
		Granulitic gneiss	1975 ± 5	Th-U-Pb CHIME-EPMA Mnz	Oyhantçabal et al. (2012)
	Rivera Shear Zone	Mylonite	606 ± 10	Th-U-Pb CHIME-EPMA Mnz	Oyhantçabal et al. (2012)
		Mylonite	606 ± 10	K-Ar Ms	Oyhantçabal et al. (2012)
	Neoproterozoic granitoids	Sobresaliente granite	585 ± 2.5	U-Pb SHRIMP Zrn	Oyhantçabal et al. (2012)
		Las Flores granite	586 ± 2.7	U-Pb SHRIMP Zrn	Oyhantçabal et al. (2012)

Table 3.1: Summary of available geochronological data of the Nico Pérez Terrane (Zrn: zircon, Hbl: hornblende, WR: whole-rock, Ttn: titanite, Mnz: monazite, Ms: muscovite).

The Pavas Block is dominantly characterized by orthogneisses, amphibolites, migmatites, mafic-ultramafic igneous rocks and metasediments with ages between 3.0 and 2.7 Ga (Preciozzi et al., 1979; Hartmann et al., 2001; Gaucher et al., 2011a). Hartmann et al. (2001) separated the Pavas Block into the La China and Las Tetas complexes, which are constituted by amphibolite facies metaigneous and metasedimentary rocks, respectively. The Valentines-Rivera Granulitic Complex is made up of felsic and subordinated mafic granulites with a metasedimentary succession including BIFs, pyroxene fels, micaschists and marbles (Ellis, 1998). On the other hand, the Campanero Unit comprises orthogneisses, scapolite gneisses, amphibolites, micaschists, BIFs and migmatites (Oyhantçabal, 2005).

The Illescas granite represents a rapakivi igneous body that intruded the Valentines-Rivera Granulitic Complex at ca. 1.7 Ga (Campal and Schipilov, 1995). Likewise, Neoproterozoic granitoids are widespread and show ages with a range of ca. 650-570 Ma (Table 3.1).

3.3. Sample description

Eight samples were analysed using U-Pb LA-ICP-MS zircon geochronology, which was carried out at the Geochronological Research Centre of the University of São Paulo (Appendix 2, Appendix 3). Samples BUY-54-11, BUY-57-11, BUY-61-11, BUY-63-11, BUY-65-11 and BUY-77-11 were collected from the Nico Pérez Terrane. On the other hand, BUY-88-11 corresponds to the Cerro Colorado granite in the Piedra Alta Terrane, whereas Nb-66 was obtained from the basement of the Congo Craton in the Kaoko Belt (Fig. 3.2). Sample locations are presented in Appendix 2 and Figure 3.1.

Sample BUY-54-11 corresponds to a mafic granulite of the Valentines-Rivera Granulitic Complex (Fig. 3.3a; Appendix 2). It is mostly made up of plagioclase, orthopyroxene and clinopyroxene, which exhibit granoblastic texture. Garnet and, occasionally, hornblende are present as well. Zircons are prismatic and show homogeneous dark cores with homogeneous bright rims, although oscillatory zoning is sometimes observed in cores (Fig. 3.4).
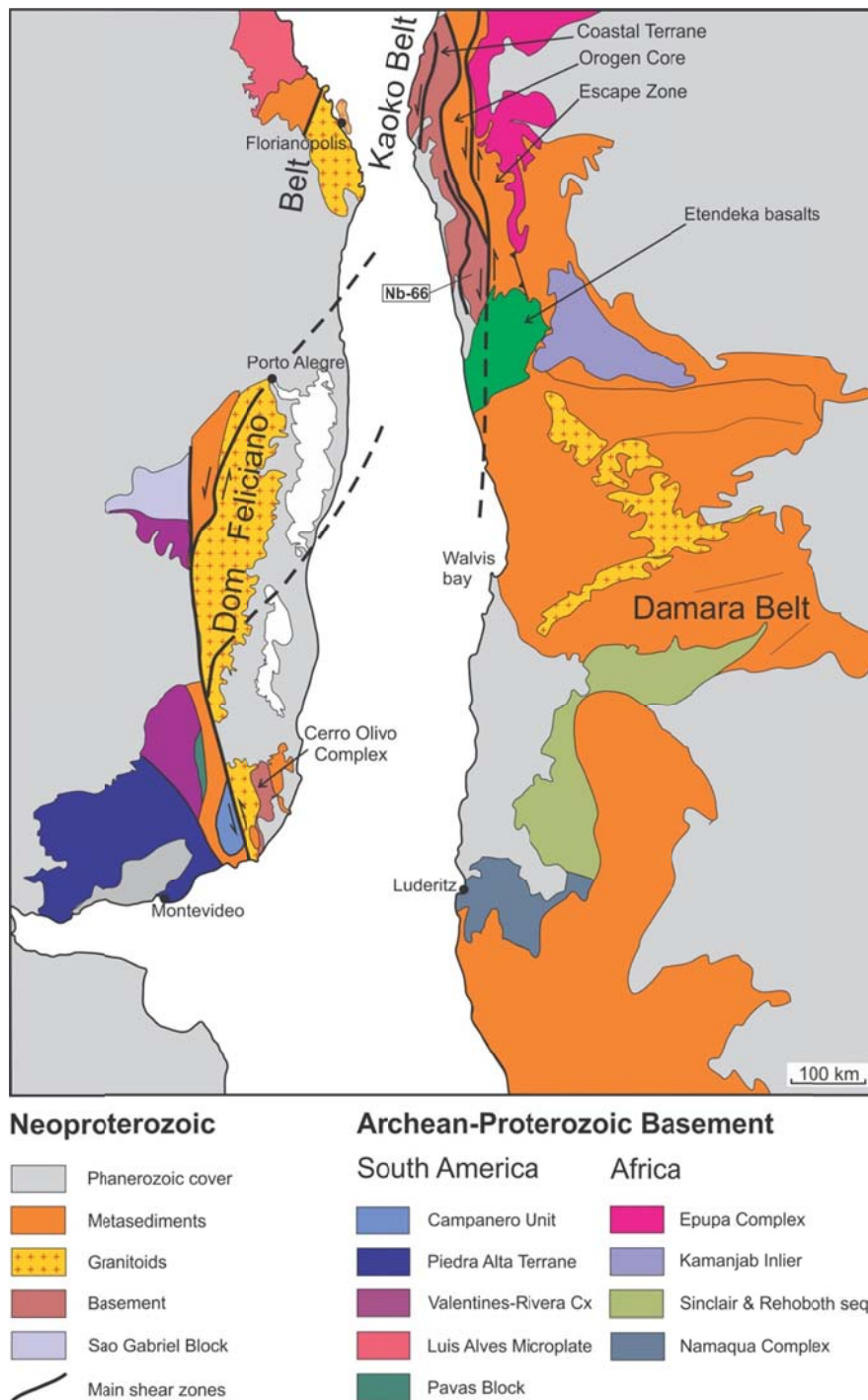
Fig. 3.2: Map of Brasiliano-Pan-African orogens in South America and Africa, respectively (modified after Oyhantçabal et al., 2011b, and references therein). Location of sample Nb-66 is indicated as well.

Sample BUY-57-11 comprises a tonalitic-dioritic orthogneiss of the Valentines-Rivera Granulitic Complex (Appendix 2). Zircons are anhedral and fragmented, and show cores that are either homogeneous or zoned. Homogeneous bright rims are typically observed (Fig. 3.4).

Likewise, samples BUY-61-11 and BUY-65-11 were collected from felsic orthogneisses of the Valentines-Rivera Granulitic Complex (Appendix 2). The orthogneisses are made up of granoblastic K-feldspar and plagioclase, and also exhibit monocrystalline quartz ribbons (Fig. 3.3b). In both samples,

zircons are dominantly prismatic, although rounded crystals are also observable. Both cores and rims dominantly exhibit oscillatory zoning (Fig. 3.4). In the case of BUY-61-11, homogenous dark cores and rims are occasionally observed, whereas homogeneous bright cores are sometimes present in zircons from BUY-65-11.
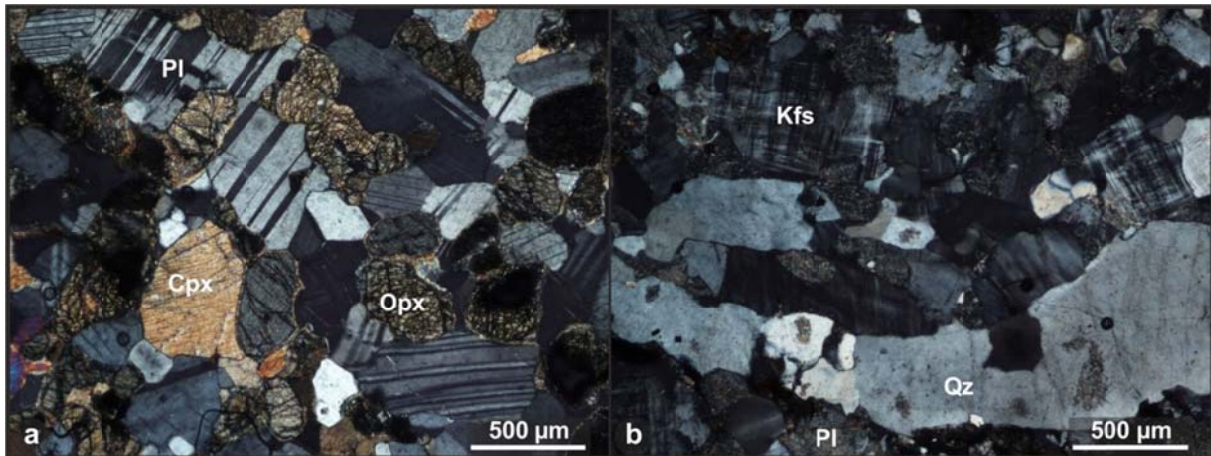
Fig. 3.3: Photomicrographs of studied units (cross-polarized light). a) Mafic granulites with granoblastic plagioclase, orthopyroxene and clinopyroxene. b) Felsic orthogneiss with quartz ribbon.

Sample BUY-63-11 corresponds to the Amarillo granite, which intrudes the basement of the Nico Pérez Terrane in the Isla Cristalina de Rivera (Appendix 2). This equigranular leucocratic granite is constituted by quartz, K-feldspar, plagioclase and scarce biotite. Zircons are prismatic and exhibit oscillatory zoning (Fig. 3.4). In some cases, cores with oscillatory or sector zoning are recognizable as well.

Sample BUY-77-11 was collected from the Zapicán intrusion, which comprises a porphyritic to equigranular tonalitic-granodioritic body (Appendix 2). It is made up of plagioclase, K-feldspar, quartz, hornblende and subordinated biotite. This intrusion is elongated in SW-NE direction and intrudes the orthogneisses of the Pavas Block near the Sierra de Sosa Shear Zone. Zircons are prismatic and exhibit oscillatory zoning (Fig. 3.4). Scarce zoned or homogenous cores are also present.
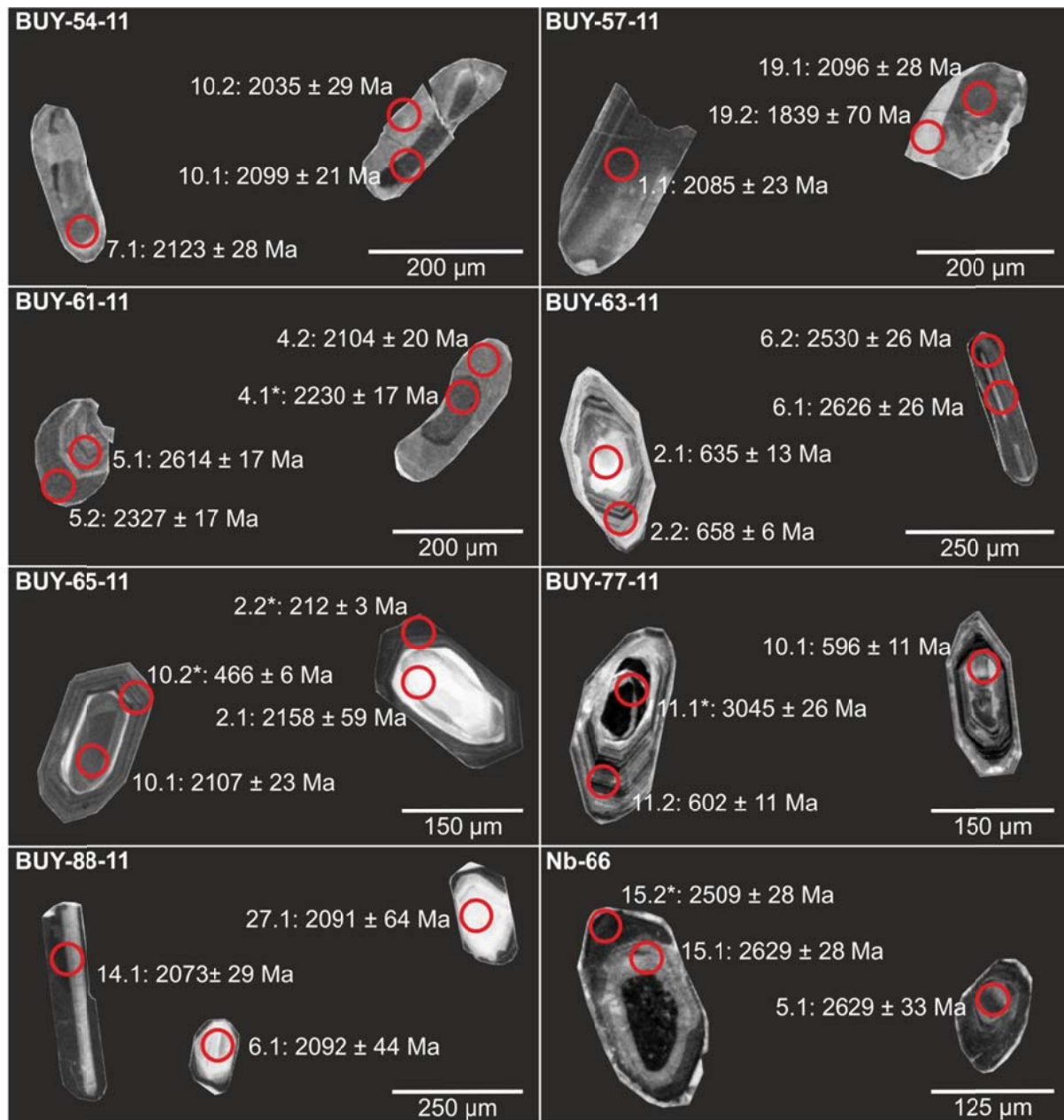
Fig. 3.4: Cathodoluminescence (CL) images of representative zircons. Individual U-Pb ages are shown. Asterisks indicate discordant ages.

One sample, BUY-88-11, was also collected from the Cerro Colorado granite, which comprises a porphyritic intrusion from the Piedra Alta Terrane (Appendix 2). It is made up of K-feldspar, quartz, plagioclase and biotite. Zircons are prismatic and exhibit either oscillatory or sector zoning (Fig. 3.4).

On the other hand, Nb-66 corresponds to an augen gneiss from the basement of the Congo Craton in the Kaoko Belt (Appendix 2). It is made up by quartz, plagioclase, muscovite and biotite.

Zircons are prismatic to round and exhibit oscillatory zoning, although homogeneous or zoned cores are occasionally observable (Fig. 3.4).

3.4. Results

3.4.1. U-Pb geochronology

Two weighted mean $^{207}Pb/^{206}Pb$ ages of 2095 ± 15 Ma (12 out of 26 points) and 2041 ± 24 Ma (4 out of 26 points) were obtained for BUY-54-11 and all concordant data spread between these two values (Fig. 3.5). Highly discordant data were discarded and most of the data show Pb loss. Although youngest ages are observed in rims, they are sometimes present in grain cores as well.

Despite most of the data show Pb loss, a concordia age of 2087.0 ± 7.3 Ma was calculated considering 4 out of 26 points for the sample BUY-57-11 (Fig. 3.5). Additionally, a weighted mean $^{207}Pb/^{206}Pb$ age of 1857 ± 45 Ma (5 out of 26 points) was determined for the rims.

BUY-61-11 presents a weighted mean $^{207}Pb/^{206}Pb$ age of 2069 ± 16 Ma (7 out of 25 points, highly discordant data discarded), while BUY-65-11 shows a concordant age of 2106 ± 21 Ma (3 out of 26 points, discordant data discarded). Both samples present Archean inheritance (Fig. 3.5), being Paleoproterozoic and Archean ages recorded in cores and rims.

In the case of BUY-63-11, a concordia age of 596.0 ± 2.3 Ma was calculated considering 12 out of 26 points (discordant data discarded). Nevertheless, zircons with Archean and Paleoproterozoic ages were also identified (Fig. 3.5). Likewise, a concordant age of 610.4 ± 2.5 Ma was calculated for the Zapicán intrusion (21 out of 26 points), which occasionally shows Paleoproterozoic and Archean ages in cores (Fig. 3.5).

Zircons from the sample BUY-88-11 show a concordia age of 2078.3 ± 4.7 Ma, which was obtained considering 15 out of 39 points (Fig. 3.5; discordant data and older Paleoproterozoic grains discarded). For the sample Nb-66, a concordant age of 2600.2 ± 14.0 Ma was obtained (10 out of 26 points, discordant data discarded). However, one discordant grain may indicate Mesoarchean inheritance (Fig. 3.5).
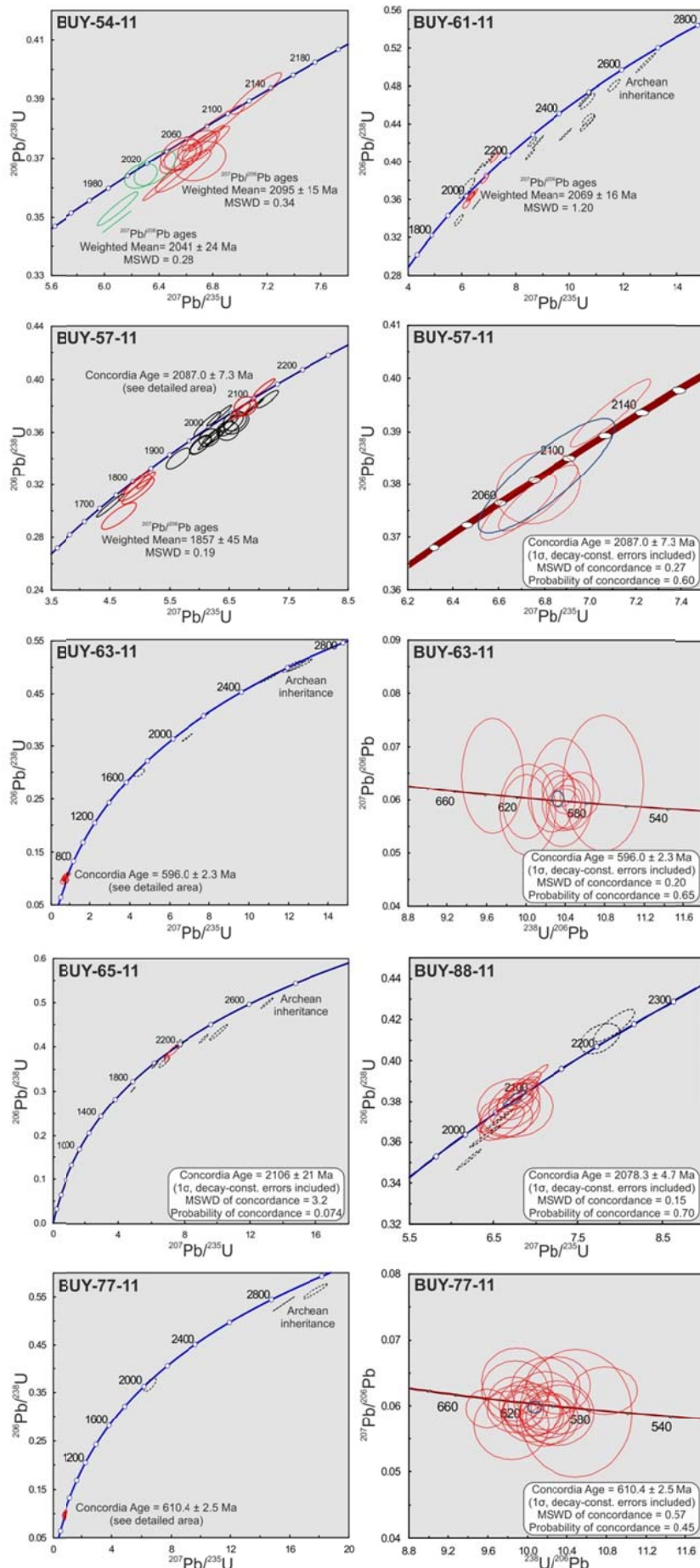
Fig. 3.5: U-Pb diagrams. Red and green ellipses indicate data used for age calculations, whereas black ellipses represent data that were not considered. Blue ellipses show concordia ages. Errors depicted at the 2σ level.
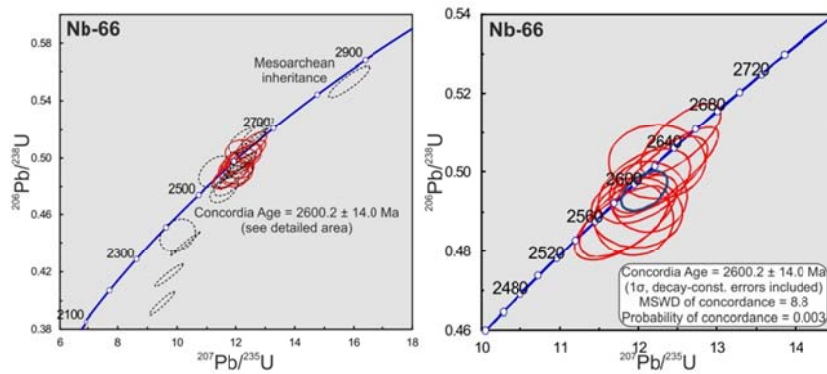
3.4.2. Hf isotopes

All samples from the basement of the Nico Pérez Terrane (BUY-54-11, BUY-57-11, BUY-61-11 and BUY-65-11) show T_{DM} model ages from 2.62 to 3.81 Ga with associated negative to positive ε_{Hf} values between -25.85 and +0.23 (Fig. 3.6; Appendix 4). Likewise, Neoproterozoic intrusions (BUY-63-11 and BUY-77-11) present Archean model ages (2.53-3.56 Ga) and negative ε_{Hf} values between -33.5 and -15.5 as well (Fig. 3.6; Appendix 4). These results represent the first Hf data from the Nico Pérez Terrane.
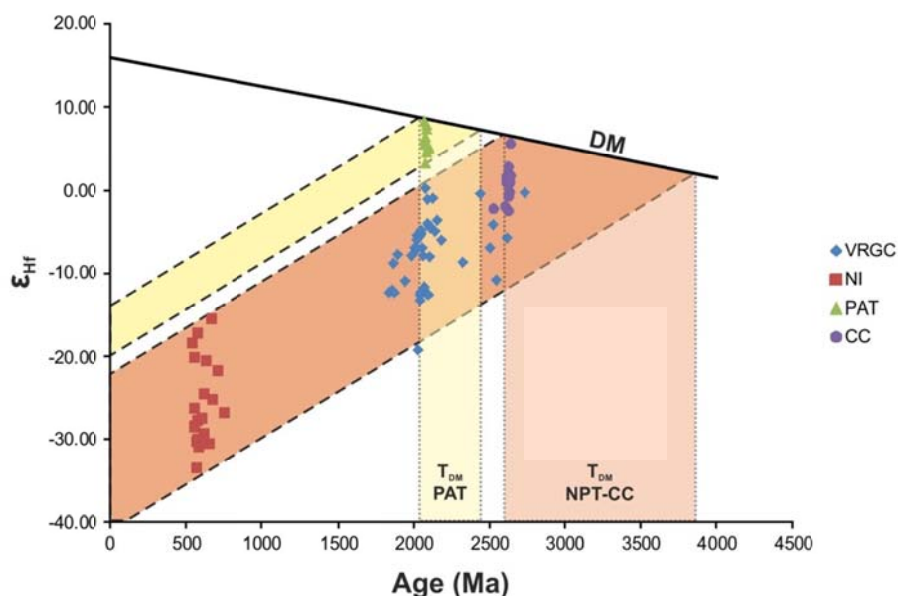
Fig. 3.6: ε_{Hf} vs. zircon age. Model ages (T_{DM}) are also shown. VRGC: Valentines-Rivera Granulitic Complex, NI: Neoproterozoic intrusions of the Nico Pérez Terrane (NPT), PAT: Piedra Alta Terrane, CC: Congo Craton.

In the case of the Congo Craton (sample Nb-66), zircons yield T_{DM} values between 2.71 and 3.22 Ga, and ε_{Hf} values between -2.62 and +5.59 (Fig. 3.6; Appendix 4). In contrast, model ages from

2.10 to 2.43 Ga and positive ε_{Hf} values (+3.22 to +8.30) were obtained for the Cerro Colorado granite zircons (sample BUY-88-11, Fig. 3.6; Appendix 4), which constitute the first reported Hf data for the Piedra Alta Terrane.

3.5. Discussion

3.5.1. Paleo- and Neoproterozoic reworking of Archean crust

Complex textures and U-Pb zircon ages in high-grade metamorphic rocks can result from multiple episodes of recrystallization, presence of a melt, solid-state processes and fluids, among others (Corfu et al., 2003; Kröner et al., 2014; Zhao et al., 2015). In the case of the Valentines-Rivera Granulitic Complex, Santos et al. (2003) and Oyhantçabal et al. (2012) reported ages of magmatism of ca. 2.18-2.11 Ga (Table 3.1). However, ages between 2.10 and 2.05 Ga were alternatively interpreted as the result of high-grade metamorphism (Santos et al., 2003) or multistage magmatism (Oyhantçabal et al., 2012). Similar U-Pb zircon ages were obtained in this work, further supporting Paleoproterozoic ages for the Valentines-Rivera Granulitic Complex, although Archean inheritance is also recorded.

Samples BUY-61-11 and BUY-65-11 show a dominance of prismatic zircon crystals with oscillatory zoning and Th/U > 0.1 (Fig. 4, 5; Appendix 3), allowing to interpret the weighted mean $^{207}Pb/^{206}Pb$ age of 2069 ± 16 Ma and the concordant age of 2106 ± 21 Ma, respectively, as magmatic ages (Hoskin and Schaltegger, 2003, and references therein). On the other hand, ages recorded in mafic granulites (weighted mean $^{207}Pb/^{206}Pb$ ages of 2095 ± 15 Ma and 2041 ± 24 Ma, BUY-54-11) and mesocratic gneisses (concordia age of 2087.0 ± 7.3 Ma, BUY-57-11) show more complex textures, including homogeneous cores rims, evidences of dissolution-precipitation and anhedral crystals with rounded boundaries, particularly in the case of BUY-57-11. These textures could indicate that these zircons record high-grade metamorphism (Corfu et al., 2003; Zhao et al., 2015), although the presence of prismatic zircon crystals with oscillatory zoning and Th/U > 0.1 may indicate

a magmatic origin (Hoskin and Schaltegger, 2003, and references therein). However, Th/U > 0.1 were also reported for zircons in high-grade metamorphic rocks (Santosh et al., 2007; Zhang et al., 2016).

Hence, integration of all geochronological data from the Valentines-Rivera Granulitic Complex reveals multistage magmatism at ca. 2.18-2.10 Ga, as previously indicated by Oyhantçabal et al. (2012). Despite not being conclusive, the event recorded at ca. 2.10-2.02 Ga might be related to granulite facies metamorphism and associated melt presence, accounting for coeval metamorphic and magmatic ages reported by Santos et al. (2003) and Oyhantçabal et al. (2012), respectively. Several authors indicated the role of anatexis during high-grade metamorphism, which is recorded by U-Pb zircon ages (Roberts and Finger, 1997; Schaltegger et al., 1999; Vavra et al., 1999; Rubatto et al., 2001; Hermann and Rubatto, 2003), thus explaining the observed ages. However, U-Pb zircon ages may not necessarily record the age when peak metamorphic conditions were attained but the timing of certain metamorphic reactions that occur due to changes in environmental conditions during high-grade metamorphism (Fraser et al., 1997; Roberts and Finger, 1997; Whitehouse and Platt, 2003; Harley et al., 2007). On the other hand, the high-grade event seems to be also recorded by titanite and monazite ages at ca. 2.1-2.0 Ga (Table 3.1; Oyhantçabal et al., 2012).

In a similar way, concordant ages of 596.0 ± 2.3 Ma (BUY-63-11) and 610.4 ± 2.5 Ma (BUY-77-11) present further evidences of Neoproterozoic magmatism, which is associated with the Dom Feliciano Belt. These results agree with previous ages obtained in the Puntas del Santa Lucía monzogranite (633 ± 8 Ma, U-Pb SHRIMP zircon; Hartmann et al., 2002), the Puntas de Mataojo granodiorite (627 ± 23 Ma, U-Pb SHRIMP zircon, Oyhantçabal et al., 2009a), the Lavaderos granite (610 ± 3 Ma, U-Pb LA-ICP-MS zircon, Gaucher et al., 2014a), the Arroyo Mangacha granite (583 ± 7 Ma, U-Pb SIMS zircon, Gaucher et al., 2008a), the Sobresaliente granite (585 ± 2.5 Ma, U-Pb SHRIMP zircon, Oyhantçabal et al., 2012), the Las Flores granite (586 ± 2.7 Ma, U-Pb SHRIMP zircon, Oyhantçabal et al., 2012) and the Pan de Azucar pluton (579 ± 1.5 Ma, Ar/Ar hornblende, Oyhantçabal et al., 2007; 581.8 ± 3.4 Ma, 574.5 ± 8.1 Ma, U-Pb SHRIMP zircon, Rapalini et al., 2015) (Fig. 3.1).

On the other hand, the Valentines-Rivera Granulitic Complex and the Neoproterozoic intrusions yield negative ε_{Hf} values and Archean model ages (Appendix 4; Fig. 3.6). Similar Archean Sm-Nd model ages were also reported for the Nico Pérez Terrane (Oyhantçabal et al., 2011a). Furthermore, inheritance of Archean zircons is recorded in both the Valentines-Rivera Granulitic Complex and Neoproterozoic intrusions (Fig. 3.5; Santos et al., 2003; Oyhantçabal et al., 2009a), whereas Archean crystallization ages were reported for the La China Complex (Hartmann et al., 2001; Gaucher et al., 2011a).

Despite of the recognition of two distinct Paleo- and Neoproterozoic magmatic events, data reveal that the crust of the Nico Pérez Terrane was mostly generated during the Archean (Fig. 3.6). Likewise, T_{DM} distribution reveals Archean episodic crustal growth with main peaks of crustal generation during the Paleo- and Mesoarchean (Fig. 3.7; Nebel-Jacobsen et al., 2010), indicating that the Nico Pérez Terrane underwent mostly crustal reworking during the Proterozoic. Complete resetting of the U-Pb ages implies total dissolution and reprecipitation of zircons (Mezger and Krogstad, 1997), which is mostly controlled by temperature and composition (Boehnke et al., 2013). Even though the Nico Pérez Terrane underwent high-grade metamorphism during the Paleoproterozoic (Oyhantçabal et al., 2011a, 2012), Paleoproterozoic protoliths of the Valentines-Rivera Granulitic Complex record inheritance. Consequently, relative saturation of zircon in the Proterozoic melts can be inferred (Watson and Harrison, 1983; Miller et al., 2003).
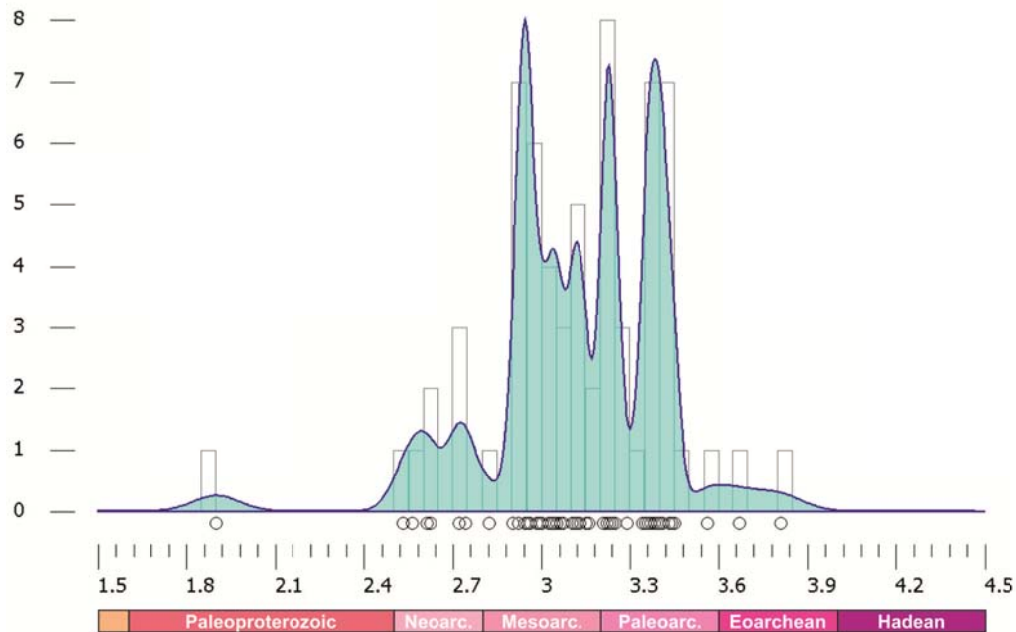
Fig. 3.7: Kernel density estimation curve and histogram of Hf model ages (Ga) of the Nico Pérez Terrane (n=66) plotted using DensityPlotter (Vermeesch, 2012).

3.5.2. Main tectonic events

Ages of orthogneisses of the La China Complex (Hartmann et al., 2001; Gaucher et al., 2011a) together with inherited zircons and Hf model ages in Paleo- and Neoproterozoic units point to Archean episodic crustal growth of the Nico Pérez Terrane. Archean crust was subsequently reworked by Paleoproterozoic multistage magmatism recorded in the Valentines-Rivera Granulitic Complex at 2.18-2.10 Ga, as previously reported by Oyhantçabal et al. (2012). Based on geochemical data (Ellis, 1998; Oyhantçabal et al., 2012), a magmatic arc setting was suggested for this magmatism. This could be further supported by the presence of inheritance-rich magmas and crustal reworking revealed by zircon data, which are frequently related to crustal thickening processes (Watson and Harrison, 1983; Miller et al., 2003). High-grade metamorphism and associated crustal anatexis are subsequently recorded at ca. 2.10-2.02 Ga. Oyhantçabal et al. (2012) reported Th-U-Pb CHIME-EPMA monazite ages of 1.98-1.94 Ga, which were interpreted as evidences of amphibolite facies metamorphism, whereas zircon overgrowths record a weighted mean $^{207}Pb/^{206}Pb$ age of 1857 ± 45 Ma in sample BUY-57-11. Although not conclusive, retrograde metamorphism could be thus constrained at ca. 1.98-1.80 Ga, predating the late Paleoproterozoic magmatism recorded at 1.7 Ga

33

in the Illescas rapakivi granite and the calc-alkaline Campanero Unit (Bossi and Campal, 1992; Oyhantçabal, 2005; Mallmann et al., 2007).

Mesoproterozoic events are also present but so far restricted to metavolcano-sedimentary units such as the Parque UTE and Mina Verdún groups (Poiré et al., 2003; Chiglino et al., 2008). Metavolcanic intercalations yield U-Pb zircon ages of ca. 1.4-1.5 Ga (Oyhantçabal et al., 2005; Gaucher et al., 2011a).

Widespread Neoproterozoic magmatism is recorded between ca. 650-570 Ma, which is related to subduction and collisional processes in the Dom Feliciano Belt (Oyhantçabal et al., 2007, 2009a, 2011a). The collision between the Río de la Plata Craton and the Nico Pérez Terrane is constrained at 630-625 Ma, based on geochronological data of the Sarandí del Yí Shear Zone (Chapter 6).

3.5.3. The Nico Pérez Terrane and its crustal affinity

Despite being traditionally considered as part of the Río de la Plata Craton (Bossi and Campal, 1992; Mallmann et al., 2007; Gaucher et al., 2011a; Frimmel et al., 2011), recent contributions indicated the allochthony of the Nico Pérez Terrane and its docking to the Río de la Plata Craton during the Neoproterozoic (Oyhantçabal et al., 2011a; Rapela et al., 2011). The stabilization of the Río de la Plata was attained during the late Paleoproterozoic (Cingolani, 2011; Oyhantçabal et al., 2011a), whereas the Nico Pérez Terrane shows a much more complex evolution till the Neoproterozoic.

The main characteristic of cratons is their stability through time, which basically implies lack of large-scale pervasive deformation and magmatism (Bates and Jackson, 1980; Pollack, 1986). As craton stability is fundamentally related to the presence of a thick lithospheric mantle (Black and Liégeois, 1993), destabilization is most likely to occur during collisional or post-collisional events (Liégeois et al., 2013). Based on K-Ar muscovite ages, Oyhantçabal et al. (2011a) revealed thermal overprinting of the Nico Pérez Terrane during the Brasiliano–Pan-African Orogeny, which is further

supported by the existence of several Neoproterozoic intrusions (Table 3.1). Coeval deformation and metamorphism reworking basement units were also identified (Rossini and Legrand, 2003; Sánchez Bettucci et al., 2003; Mallmann et al., 2007; Oyhantçabal et al., 2009a, 2012). Hence, the Nico Pérez Terrane achieved stability after cessation of the Brasiliano–Pan-African Orogeny, thus contrasting with Paleoproterozoic cratonisation achieved by the Río de la Plata Craton.

Isotopic data from the Paleoproterozoic Cerro Colorado shows dominant Paleoproterozoic Hf model ages (Fig. 3.5, 3.6; Appendix 4), which are similar to Hf and Sm-Nd model ages from other units of the Río de la Plata Craton (Cingolani, 2011; Oyhantçabal et al., 2011a), and positive ε_{Hf} values. In contrast, the Nico Pérez Terrane shows main crustal growth during the Paleo- and Mesoarchean (Fig. 3.6, 3.7) and only underwent crustal reworking during the Paleo- and Neoproterozoic. Post-collisional underformed intrusions of the Piedra Alta Terrane, such as the Cerro Colorado or Isla Mala granites (Hartmann et al., 2000a), are contemporaneous with metamorphosed intrusions of the Nico Pérez Terrane, providing further evidences of a different evolution of both blocks. On the other hand, Hf model ages from the Nico Pérez Terrane match Hf model ages from Nb-66 from the Congo Craton (Fig. 3.6), and both areas also show Archean basement inliers (Hartmann et al., 2001; McCourt et al., 2013), thus supporting derivation of the Nico Pérez Terrane from the Congo Craton. Moreover, the southwestern Congo Craton presents Paleoproterozoic gneisses of ca. 2.2-2.0 and 1.8-1.7 Ga as well as 1.5-1.4 Ga old igneous rocks in the Kunene Complex (Seth et al., 1998; Kröner et al., 2004; Drüppel et al., 2007; Luft Jr et al., 2011; Ernst et al., 2013; McCourt et al., 2013; Kröner et al., 2015), which in many cases reworked Archean crust (Seth et al., 1998; McCourt et al., 2013). These units would be thus comparable to the gneisses of the Valentines-Rivera Complex and Campanero Unit and Mesoproterozoic metavolcanic rocks of the Nico Pérez Terrane, respectively. These evidences further support previous correlations between the Angolan Shield and the Nico Pérez Terrane (Rapela et al., 2011), as the former comprise the southwestern portion of the Congo Craton (e.g., McCourt et al., 2013).

In contrast, the westernmost Kalahari Craton shows dominance of igneous and metamorphic 1.2-1.0 Ga old rocks from the Namaqua-Natal Belt (Eglington, 2006; Jacobs et al., 2008; Hofmann et al., 2014), which are derived from older Meso- and Paleoproterozoic crust as indicated by Sm-Nd and Hf model ages (e.g., Pettersson et al., 2009; Cornell et al., 2012; Colliston et al., 2015). Even though some Paleoproterozoic basement inliers are present as well, they yield dominant Paleoproterozoic Sm-Nd T_{DM} model ages (Pettersson et al., 2009). Likewise, the Paleoproterozoic Rehoboth Block is located to the north of the western part of the Namaqua Belt and comprises intrusions of 1.7-1.8 Ga (Ziegler and Stoessel, 1991, 1993; Becker et al., 1996; van Schijndel et al., 2014). These intrusions yield Paleoproterozoic Sm-Nd and Hf model ages (Ziegler and Stoessel, 1991; Becker et al., 2000, 2004; van Schijndel et al., 2014). The Nico Pérez Terrane lacks in Namaqua-age rocks and is clearly dominated by Archean Hf model ages, thus allowing to rule out pre-Gondwana connections with the Kalahari Craton.

3.6. Conclusions

New U-Pb and Hf data allow to characterize the Nico Pérez Terrane as a crustal block that originated mostly from Archean episodic crustal growth and underwent crustal reworking during the Proterozoic. In contrast, the Piedra Alta Terrane records Paleoproteorozoic crustal growth, indicating that the Nico Pérez Terrane was allochthonous regarding the Río de la Plata Craton. Based on similarities in terms of tectonostratigraphy, the Nico Pérez Terrane would be thus equivalent to the southwestern Congo Craton.

The Archean crust of the Nico Pérez Terrane underwent multistage magmatism at ca. 2.2-2.1 Ga. Afterwards, a high-grade metamorphic event took place at ca. 2.1-2.0 Ga, prior to magmatism at 1.7 Ga. Metavolcano-sedimentary units indicate the existence of Mesoproterozoic events that could be related to the coeval magmatism of the Kunene Complex. After Cryogenian rifting from the Congo Craton, the Nico Pérez was accreted to the eastern Río de la Plata Craton and underwent further crustal reworking during the evolution of the Dom Feliciano Belt.

-CHAPTER 4-

Provenance of metasedimentary rocks of the southwestern Dom Feliciano Belt

4.1. Introduction

Provenance analyses based on detrital zircon geochronology constitute key elements to understand large-scale tectonic processes (Fedo et al., 2003; Gehrels, 2014). Based on the fingerprint of zircon age populations, characterization of the source rock and maximum sedimentation ages are assessable. Consequently, the history of uplift and erosion can be unravelled and even terrane boundaries can be identified (Fedo et al., 2003; Gehrels, 2014; Lease et al., 2007). Whole-rock geochemistry as well as detrital zircon ages has been applied in metasediments of the Dom Feliciano Belt to support different tectonic models (Basei et al., 2005, 2008, 2011b; Gaucher et al., 2008a; Blanco et al., 2009; Zimmerman, 2011). However, data are still scarce, being the provenance and the tectonic setting of the metasedimentary cover a matter of ongoing debate.

As previously outlined (Section 1.4.1), the Dom Feliciano Belt comprises three tectonic domains, namely the foreland basin, the schist belt and the granite belt, which are developed from west to east (Basei et al., 2000). Nevertheless, the Dom Feliciano Belt in Uruguay shows a singularity, as a second supracrustal assemblage is present on the eastern side of the granite belt. The metasedimentary cover of the southern Dom Feliciano Belt can be thus divided into a western and an eastern domain (Table 4.1).

4.2. Geological setting

Several authors have studied the metasedimentary rocks from the western domain of the Dom Feliciano belt in Uruguay in the last years (e.g., Basei et al., 2008; Gaucher, 2000; Gaucher et al., 2003, 2008a; Frei et al., 2013; Pecoits et al., 2008; Aubet et al., 2014) and different lithostratigraphic units have been proposed for this metasedimentary cover. However, due to non-optimal field exposures, complex deformation structures and scarcity of detailed regional geological maps, there is still no consensus about distribution, correlations and age of most of them (Sánchez Bettucci et al.,

37

2010; Aubet et al., 2014). Due to this controversy, original definitions of sections and formations with geographic continuity are preferred in this contribution over lithostratigraphic units of higher hierarchy, such as the Arroyo del Soldado Group (Gaucher, 2000; Blanco et al., 2009) or the Maldonado Group (Pecoits et al., 2005, 2011). A synthesis of available information about these units is presented in Table 4.1.

In the western Dom Feliciano Belt, the Las Tetas Complex seems to be the only metasedimentary unit that belongs to the pre-Neoproterozoic basement (Hartmann et al., 2001). The Las Tetas Complex is an association of quarzites, micaschists, conglomerates and marbles, which are strongly deformed and affected by amphibolite facies metamorphism as evidenced by parageneses with garnet and sillimanite (Oyhantçabal and Vaz, 1990) and garnet and staurolite (Hartmann et al., 2001). It probably represents remnants of the oldest metasedimentary sequence due to its metamorphism and the absence of detrital zircons younger than ca. 2.7 Ga (Hartmann et al., 2001).

The schist belt in Uruguay includes Neoproterozoic units such as the Zanja del Tigre Complex and the Lavalleja Group (Basei et al., 2000, 2008), which exhibit lower amphibolite to greenschist facies metamorphism. Micaschists, phyllites, marbles and metabasalts are the most frequent lithologies, although criteria for unequivocal distinguishing between these two units are still lacking (Spoturno et al., 2012, and references therein). Some units such as the Yerbal (Gaucher et al., 2008a) and Minas de Corrales formations (Arrighetti et al., 1981; Preciozzi et al., 1985) were also considered by some authors as part of the schist belt (Sánchez Bettucci et al., 2010; Aubet et al., 2014).

Likewise, the metasedimentary association of the western Dom Feliciano Belt also includes several Ediacaran to Cambrian units, which are characterized by better-preserved sedimentary structures and subgreenschist metamorphic facies conditions. This metasedimentary cover comprises the Barriga Negra (Midot, 1984), Piedras de Afilar (Jones, 1956), Playa Hermosa (Masquelin and Sánchez Bettucci, 1993), Arroyo de la Pedrera (Montaña and Sprechmann, 1993) and Las Ventanas formations (Midot, 1984). Available information for these units is summarized in Table 4.1 and their location is presented in Figure 4.1.

Unit	Lithology	Age (fossil content)	Youngest detrital zircon age (Ma, ±1σ)	Other age constraints (Ma, ±1σ)
Western Dom Feliciano Belt				
Arroyo de la Pedrera Formation	Arenites, mudstones, stromatolitic carbonates; Montaña and Sprechmann (1993)	Ediacaran	665 ± 5; Blanco et al. (2009)	
Barriga Negra Formation	Conglomerates, sandstones, pelites; Midot (1984)	Ediacaran	564 ± 9; Blanco et al. (2009)	
Piedras de Afilar Formation	Arenites, pelites, carbonates; Bossi (1966), Spoturno et al. (2004), Pecoits et al. (2008)	Ediacaran	1006 ± 31; Gaucher et al. (2008a)	
Las Ventanas Formation	Conglomerates, sandstones, pelites; Midot (1984), Masquelin and Sánchez Bettucci (1993), Pecoits et al. (2005, 2008)	Ediacaran		Volcaniclastic rocks 573 ± 11; Oyhantçabal et al. (2009a)
Playa Hermosa Formation	Diamictites, rhythmites; Elizalde (1979), Preciozzi et al. (1989), Masquelin and Sánchez Bettucci (1993), Pazos et al. (2011)	Ediacaran	594 ± 8; Rapalini et al. (2015)	
Minas de Corrales Formation	Pelites, arenites, acid volcaniclastic rocks, dolostones, conglomerates; Arrighetti et al. (1981), Preciozzi et al. (1985)	Ediacaran	664 ± 8; this work	
Yerbal Formation	Sandstones, siltstones, cherts, BIFs; Gaucher et al. (2004)	Ediacaran	663 ± 16; Blanco et al. (2009)	K-Ar diagenetic illite 600-570; Aubet et al. (2012)
Polanco Formation	Limestones, dolostones; Gaucher (2000), Gaucher et al. (2004), Aubet et al. (2012)			Sr/Sr and δ^{13}C Ediacaran; Aubet et al. (2012)
Lavalleja Group	Greenschists, marbles, dolomitic slates, phyllites; Bossi (1966), Sánchez Bettucci (1998)		1080 ± 23; this work 715 ± 26; Basei et al. (2008)	
Zanja del Tigre Complex	Micaschists, marbles, felsic volcanic rocks; Sánchez Bettucci (1998)		606 ± 6; this work 1707 ± 68; Basei et al. (2008)	
Las Tetas Complex	Conglomerates, quartzites, micaschists, marbles; Hartmann et al. (2001)		2717 ± 24; Hartmann et al. (2001) 2736 ± 35; this work	
Eastern Dom Feliciano Belt				
San Carlos Formation	Conglomerates, sandstones, pelites, felsic lavas, pyroclastic rocks; Masquelin (1990), Pecoits et al. (2008), Oyhantcabal et al. (2013)		535 ± 7; Gaucher et al. (2014b)	
Cerros de Aguirre Formation	Felsic tuffs, ignimbrites, lavas, sandstones, pelites; Masquelin and Tabó (1988), Campal and Schipilov (2005)			Volcaniclastic rocks 572 ± 11; Hartmann et al. (2002)
Rocha Formation	Sandstones, pelites; Sánchez Bettucci and Burgeño (1993)		596 ± 40; Basei et al. (2005)	

Table 4.1: Summary of available age constraints for metasedimentary sequences (simplified after Oyhantçabal et al., submitted).

On the other hand, the eastern metasedimentary belt comprises the Rocha, Cerros de Aguirre and San Carlos formations (Table 4.1, Fig. 4.1). The Rocha Formation is a folded turbidite sequence, including essentially slates and metaarenites, which were metamorphosed under greenschist facies conditions (Sánchez Bettucci and Burgueño, 1993). Age constraints on sedimentation of the Rocha Formation are the youngest detrital zircon (596 ± 40 Ma, U-Pb SHRIMP zircon, Basei et al., 2005) and the age of the Santa Teresa granite (543 ± 5 Ma U-Pb LA-ICP-MS zircon, Basei et al., 2013a), which intrudes these metasediments. The Cerros de Aguirre Formation consists of felsic volcaniclastic rocks, felsic lavas, sandstones and pelites (Masquelin and Tabó, 1988; Campal and Schipilov, 2005). Hartmann et al. (2002) dated a dacitic pyroclastic rock of this formation at 572 ± 8 Ma (U-Pb SHRIMP zircon). The San Carlos Formation, in turn, comprises fluvial-lacustrine conglomerates, sandstones, pelites and felsic volcanics and volcaniclastic rocks (Masquelin, 1990; Pecoits et al., 2008; Oyhantçabal et al., 2013) and is probably Cambrian, as the youngest detrital zircon presents an age of 535 ± 13 Ma (U-Pb LA-ICP-MS zircon, Gaucher et al., 2014b).

4.3. Sample description

Nine samples from metasedimentary units of the western Dom Feliciano Belt were analysed using U-Pb detrital zircon geochronology. Sample locations are presented in Appendix 2 and Figure 4.1. Two samples were analysed using U-Pb LA-ICP-MS zircon geochronology (BUY-55-11, BUY-76-11), which was carried out at the Geochronological Research Centre of the University of São Paulo (Appendix 2, Appendix 3), whereas seven samples were analysed using U-Pb LA-ICP-MS zircon geochronology at the Central Analytical Facility of the Stellenbosch University (UY-4-13, UY-6-13, UY-8-13, UY-9-13, UY-16-13, UY-22-13, UY-24-13).

Sample BUY-55-11 is a metapelite of the Minas de Corrales Formation. Zircons are 50-150 μm long and present dominance of prismatic crystal faces. Oscillatory zoning is frequent, whereas sector zoning and homogeneous dark rims are sometimes present (Fig. 4.2).

Sample BUY-76-11 is a deformed metaconglomerate from the Las Tetas Complex, which is made up of quartz, muscovite and scarce fuchsite. Zircons comprise typically 100-250 μm long anhedral fragments with bright luminescence (Fig. 4.2). Oscillatory zoning, though not very frequent, is also present in prismatic crystals.

Sample UY-4-13 corresponds to a metapelite of the Lavalleja Group. Prismatic to ovoid 50-150 μm long zircons are the most frequent and present oscillatory zoning (Fig. 4.2).
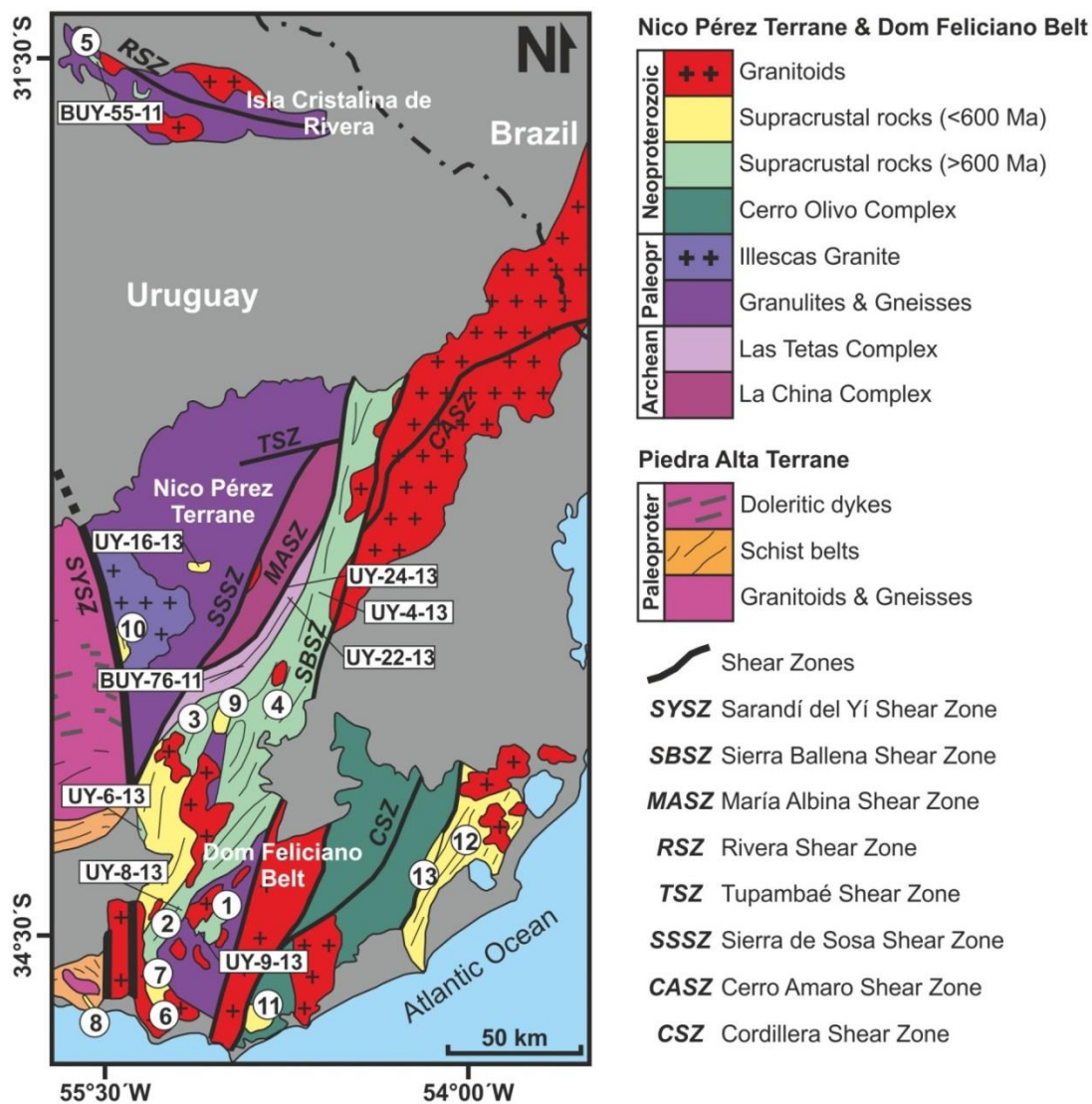
Fig. 4.1: Geological map of the Nico Pérez Terrane and adjacent blocks (modified after Oyhantçabal et al., 2011a, and references therein). Sample locations and metasedimentary sequences (1: Zanja del Tigre Complex, 2: Lavalleja Group, 3: Polanco Formation, 4: Yerbal Formation, 5: Minas de Corrales Formation, 6: Playa Hermosa Formation, 7: Las Ventanas Formation, 8: Piedras de Afilar Formation, 9: Barriga Negra Formation, 10: Arroyo de la Pedrera Formation, 11: San Carlos Formation, 12: Rocha Formation, 13: Cerros de Aguirre Formation) are shown.

41

Sample UY-6-13 corresponds to a garnet-bearing micaschist from an outcrop located ca. 20 km north of the city of Minas. This outcrop area is assumed to correspond to the Zanja del Tigre Complex. Zircons are 50-100 μm long and prismatic, and exhibit oscillatory and subordinated sector zoning (Fig. 4.2).

Sample UY-8-13 is a calcareous schist from the locus typicus of the Lavalleja Group. Prismatic 50-150 μm long zircons with oscillatory zoning dominate (Fig. 4.2). Ovoid, round and fragmented crystals are also present.

Sample UY-9-13 is a fine-grained quartz-sericite schist sampled in the locus typicus of the Zanja del Tigre Complex. Zircons are 50-200 μm long and prismatic crystals with oscillatory zoning are the most frequent, though anhedral crystal fragments and sector zoning are also observable (Fig. 4.2).
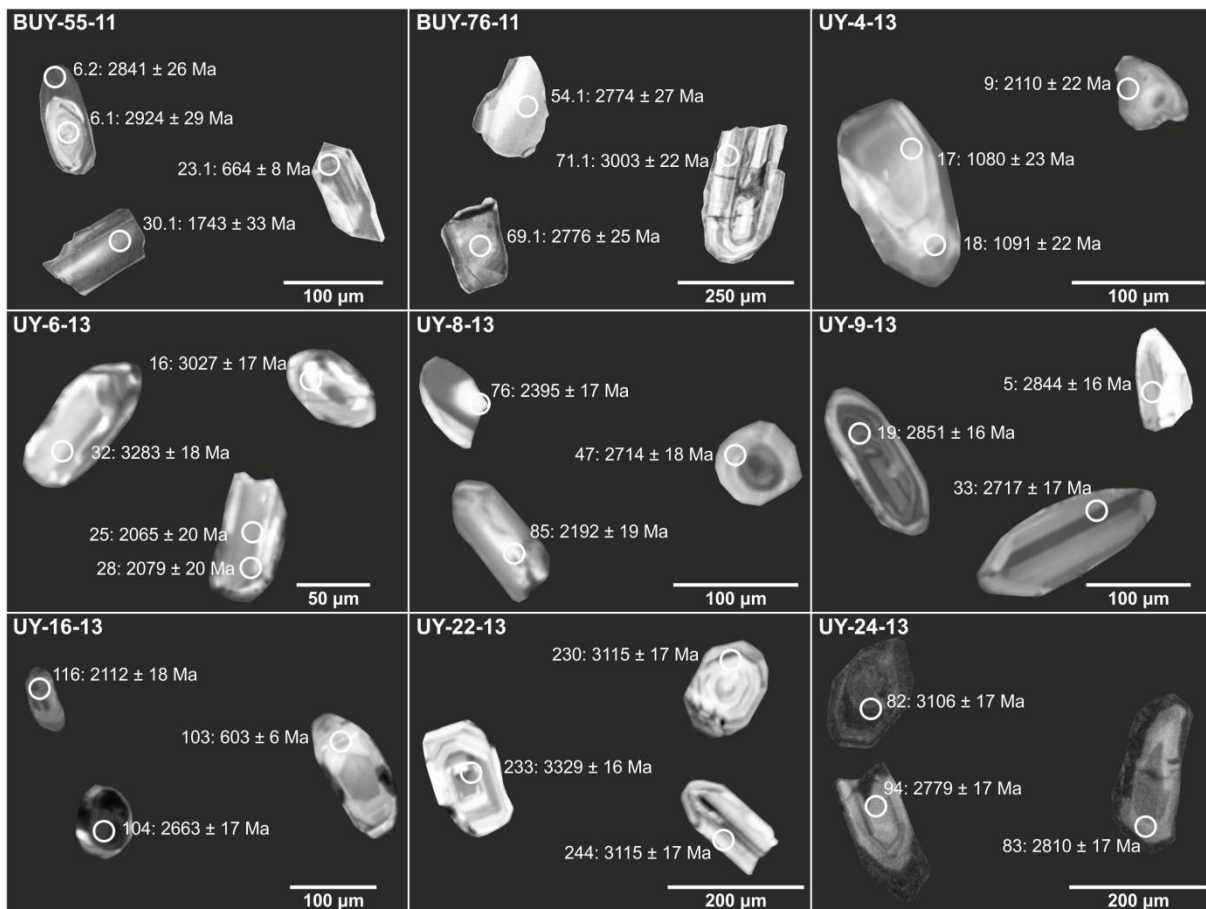
Fig. 4.2: Cathodoluminescence (CL) images of representative zircons. Individual U–Pb ages are shown. Asterisks indicates discordant ages.

Sample UY-16-13 corresponds to a metasandstone from one of the remnants of the foreland basin on the Nico Pérez Terrane. Zircons are up to 200 μm long and typically prismatic, whereas sector zoning is locally present (Fig. 4.2).

Sample UY-22-13 corresponds to a quartz-rich micaschist with muscovite from the Las Tetas Complex. Zircons are 100-200 μm long and present prismatic to ovoid habits with oscillatory zoning (Fig. 4.2).

Sample UY-24-13 is a mylonite of the María Albina Shear Zone constituted by quartz, feldspar and muscovite. The protolith of the mylonites are the metasediments of the Las Tetas Complex. Up to 300 μm long prismatic to ovoid zircons with oscillatory zoning are dominant, though dark overgrowths are recognizable as well (Fig. 4.2).

4.4. Results

4.4.1. U-Pb geochronology

Zircon age populations of the investigated samples are presented in Figure 4.3 as kernel density estimation plots and histograms plotted using DensityPlotter (Vermeesch, 2012). Samples from the Las Tetas Complex present only Archean zircons, which range in age between 3.8 and 2.7 Ga (Fig. 4.3). A main peak at 2.77 Ga is observed in two samples (BUY-76-11 and UY-24-13), whereas sample UY-22-13 shows a main peak at 3.3 Ga.

In comparison, samples from the Neoproterozoic cover (Zanja del Tigre, Lavalleja and Yerbal units) show a dominance of Archean and Paleoproterozoic zircons with scarce contribution of Meso- and Neoproterozoic grains (Fig. 4.3). The most abundant zircon populations are, however, restricted to 3.2-3.0, 2.8-2.6, 2.5-2.4 and 2.2-2.0 Ga. Mesoproterozoic and Statherian peaks are usually subordinated.

The sample of the Minas de Corrales Formation (BUY-55-11) stands out as it shows a main Mesoproterozoic contribution between 1.55 and 1.2 Ga as well as second major Paleoproterozoic peak at 1.8-1.7 Ga. Archean and Neoproterozoic zircons in this sample are subordinated (Fig. 4.3).
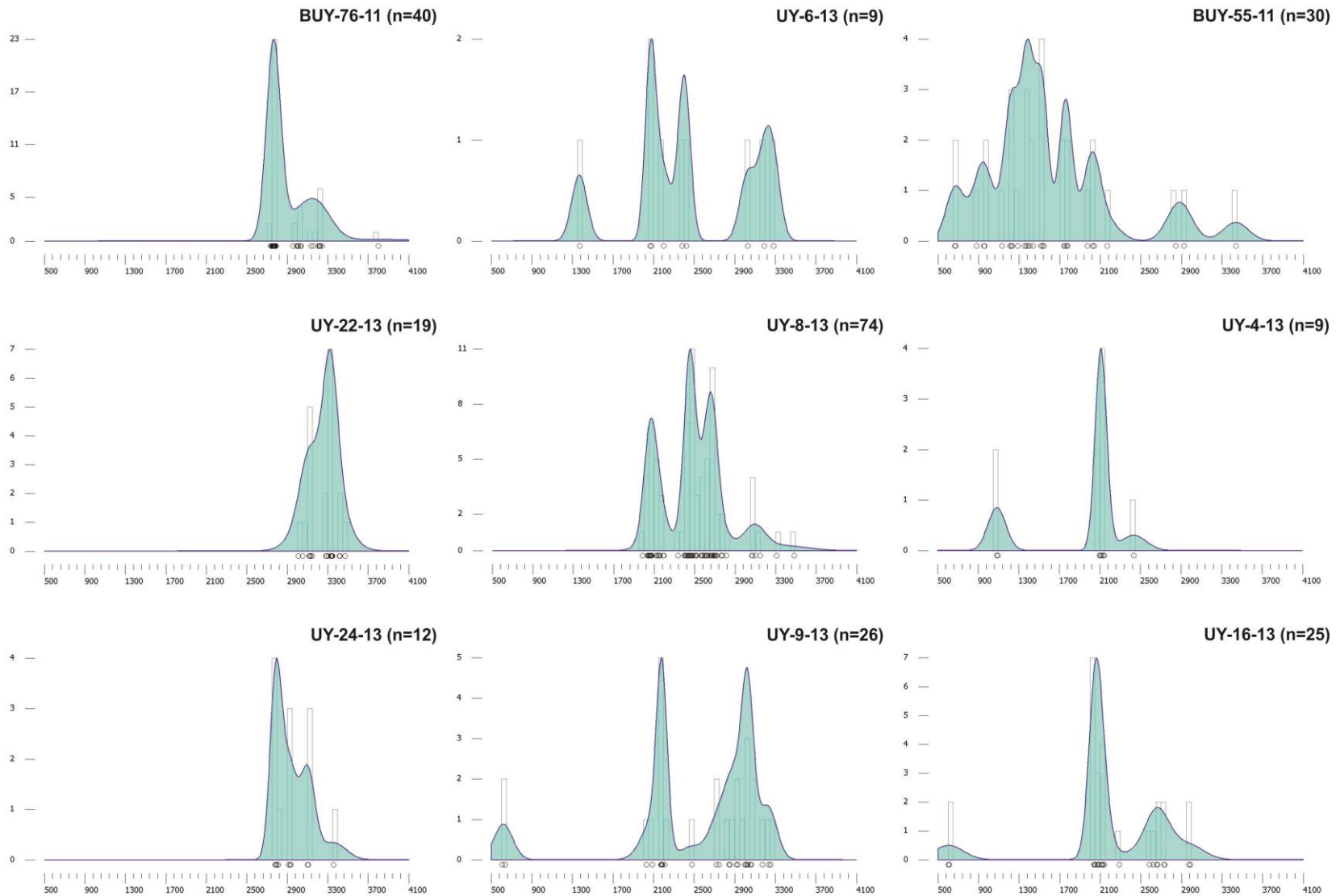
Fig. 4.3: Kernel density estimation plots and histograms plotted using DensityPlotter (Vermeesch, 2012). Plots only include data with ±10% concordance.

4.4.2. Hf isotopes

Archean grains in both samples show T_{DM} model ages from 3.47 to 2.96 Ga with associated ε_{Hf} values between -4.92 and +5.54 (Fig. 4.4; Appendix 4). In the case of Mesoproterozoic grains of sample BUY-55-11, Paleoproterozoic model ages (2.32-1.73 Ga) and dominantly positive ε_{Hf} values between -2.73 and -7.10 are recorded (Fig. 4.4; Appendix 4). Neoproterozoic grains show, in turn, Cryogenian model ages of 0.79-0.77 Ga and highly positive ε_{Hf} values of ca. 12.
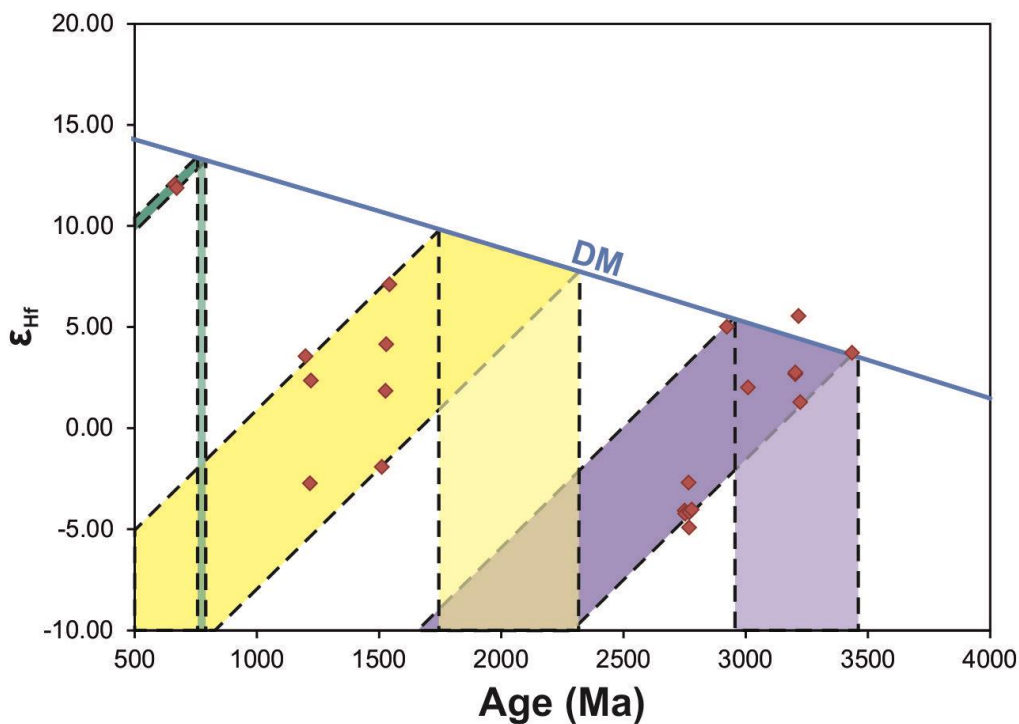
Fig. 4.4: ε_{Hf} vs. zircon age. Model age groups are also shown.

4.5. Discussion

4.5.1. Maximum deposition ages

Table 4.1 shows the constraints for the deposition age of several lithostratigraphic units of the metasedimentary cover of the Dom Feliciano Belt in Uruguay, based on different age constraints. The first implication of these data is that only the Barriga Negra and Playa Hermosa formations show Ediacaran maximum deposition robust ages younger than ca. 600 Ma based on detrital zircon ages. A comparable age can be also interpreted for the Las Ventanas Formation based on intercalated volcaniclastic rocks of 573 ± 11 Ma (Oyhantçabal et al., 2009a). In the case of the Zanja del Tigre

Complex and the Yerbal, Minas de Corrales, Lavalleja and Piedras de Afilar formations, a Neoproterozoic deposition age probably older than ca. 600 Ma is the best constraint considering all parameters. In the case of the Yerbal Formation, this age is further supported by K-Ar data of diagenetic illite (Table 4.1; Aubet et al., 2012). The Polanco Formation, in turn, predates deposition of the Barriga Negra Formation, as the latter lies discordantly over the former (Fambrini et al., 2005, and references therein). Hence, all available data supports models suggesting that the schist belt is older and discordantly overlain by post-collisional Ediacaran foreland deposits (Basei et al., 2000; Fambrini et al., 2005; Almeida et al., 2010).

On the other hand, age constraints of granites intruding the metasedimentary cover indicate that most units are older than Cambrian. This conclusion is also consistent with ages based on the fossil content of some of these units (Gaucher et al., 2003, 2008b; Pecoits et al., 2008).

All samples from Las Tetas Complex (BUY 76-11, UY 22-13 and UY 24-13) are characterized by the absence of Proterozoic detrital zircons in concordance with preliminary data reported by Hartmann et al. (2001). The youngest age in detrital zircon of this unit continues to be 2717 ± 24 Ma (Hartmann et al., 2001), whereas similar ages are reported in this study. The minimum age of this complex, in turn, is constrained by new Ar/Ar data, which indicate an early Ediacaran age for the metamorphism (Chapter 7).

4.5.2. Provenance of the western Dom Feliciano Belt

All new data together with previous results of detrital zircons from the western Dom Feliciano Belt (Mallmann et al., 2007; Basei et al., 2008; Gaucher et al., 2008a; Blanco et al., 2009; Rapalini et al., 2015) are summarized in Figure 4.5. Three main peaks at 2.8-2.7, 2.5-2.4 and 2.2-2.0 Ga are recognizable, whereas subordinated peaks at 3.15-3.00, 1.8-1.7 and 0.65-0.60 Ga and minor Mesoproterozoic contribution are present as well.
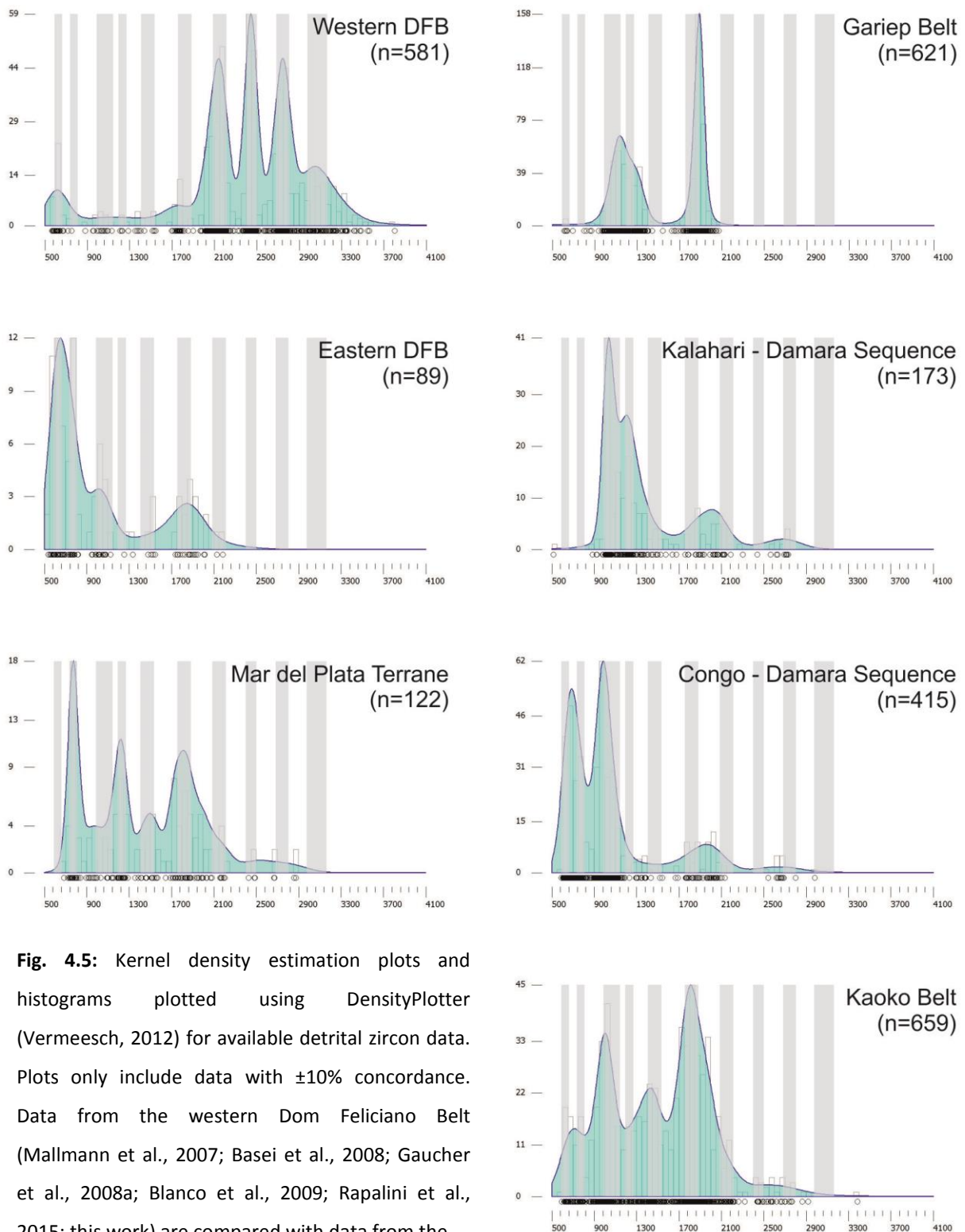
Fig. 4.5: Kernel density estimation plots and histograms plotted using DensityPlotter (Vermeesch, 2012) for available detrital zircon data. Plots only include data with ±10% concordance. Data from the western Dom Feliciano Belt (Mallmann et al., 2007; Basei et al., 2008; Gaucher et al., 2008a; Blanco et al., 2009; Rapalini et al., 2015; this work) are compared with data from the eastern Dom Feliciano Belt (Basei et al., 2005; Gaucher et al., 2014b, 2014c) and the Mar del Plata Terrane (Rapela et al., 2011) on the South American margin, and also with data from the African Damara (Foster et al., 2015), Kaoko (Konopásek et al., 2014) and Gariep belts (Basei et al., 2005; Hofmann et al., 2014).

47

Archean and Paleoproterozoic peaks match ages recorded in the basement of the Nico Pérez Terrane, which underlies the metasedimentary sequences. Archean rocks are present in the Pavas Block (Hartmann et al., 2001; Gaucher et al., 2011a) and 2.2-2.0 Ga ages are recorded in the Valentines-Rivera Granulitic Complex (Santos et al., 2003; Oyhantçabal et al., 2012). Additionally, the Campanero Unit and the Illescas granite account for the 1.8-1.7 Ga detrital ages (Campal and Schipilov, 1995; Mallman et al., 2007). On the other hand, Mesoproterozoic grains may indicate that the Parque Ute Group in the Nico Pérez Terrane (Oyhantçabal et al., 2005; Gaucher et al., 2011a) and/or the Cerro Olivo Complex (Basei et al., 2011b) acted as a minor source during Neoproterozoic sedimentation. Neoproterozoic grains, in turn, may derive from widespread Neoproterozoic magmatism recorded in the area (e.g., Hartmann et al., 2002; Oyhantçabal et al., 2007, 2009, 2012).

Previous contributions attributed the rocks of the Río de la Plata Craton and the Sierras Pampeanas as source for the Archean, Paleo- and Mesoproterozoic zircons of the Arroyo del Soldado Group (Gaucher et al., 2008a; Blanco et al., 2009), though strongly argued by Zimmermann (2011). In contrast, detrital zircons from the Playa Hermosa Formation show a main peak at 2.2-2.0 Ga and a secondary peak at ca. 600 Ma, and lack in Archean, Statherian and Mesoproterozoic ages (Rapalini et al., 2015). The main peak may thus represent ages of the basement of the Río de la Plata Craton (e.g., Cingolani, 2011; Oyhantçabal et al., 2011), which is further supported by SW paleocurrent directions (Pazos et al., 2011). Consequently, the Playa Hermosa Formation may represent the only metasedimentary unit of the western Dom Feliciano Belt that truly reflects provenance from the Río de la Plata Craton, being thus the basement of the Nico Pérez Terrane the dominant source for all other metasedimentary sequences.

As indicated by U-Pb geochronology, Hf data shows a significant contribution of old crust, which was mostly generated during the Paleo- and Eoarchean. Nevertheless, Neo- and Mesoarchean addition is also noticeable. This may reflect the role of the gneisses of the La China Complex as source for the metasediments of the western Dom Feliciano Belt (Hartmann et al., 2001; Gaucher et al., 2011a). Archean and Paleoproterozoic zircon Hf model ages suggest that this was also a major

crustal growth period for the source area. These results are in good agreement with available Sm-Nd data from the western Dom Feliciano Belt metasediments (Mallmann et al., 2007; Blanco et al., 2009; Oyhantçabal et al., submitted) and Hf and Sm-Nd data from the Nico Pérez Terrane basement (Mallmann et al., 2007; Oyhantçabal et al., 2011a; Oriolo et al., 2016a; Chapter 3). In contrast, Hf and Sm-Nd data data indicate a dominance of Paleoproterozoic juvenile crust for the Río de la Plata Craton (Peel and Preciozzi, 2006; Cingolani, 2011; Oyhantçabal et al., 2011; Oriolo et al., 2016a; Chapter 3). On the other hand, the two Cryogenian grains show juvenile Hf isotope compositions. Both the Cerro Olivo Complex and the São Gabriel Block present evidences of Cryogenian magmatism (Saalmann et al., 2005; Basei et al., 2011a; Lenz et al., 2011) and may account as possible sources for the obtained model ages. However, the Cerro Olivo Complex presents Paleo- and Mesoproterozoic xenocrysts, negative ε_{Nd} values and Sm-Nd Paleo- and Mesoproterozoic model ages, indicating that the Cryogenian magmatism reworked much older crust (Basei et al, 2011a; Lenz et al, 2011; Saalmann et al, 2011). The São Gabriel Block, in contrast, is made up of juvenile material (Saalmann et al., 2005; Fortes de Lena et al., 2014) and can be thus interpreted as the source for these grains. This can be further supported by similar detrital zircon patterns observed in some units of the Porongos Group in southernmost Brazil (Pertille et al., 2015a, 2015b).

4.5.3. Regional implications

Archean and Paleoproterozoic zircon Hf model ages suggest that these were the major crustal growth periods for the source areas. Compared with available U-Pb and Hf zircon data (Fig. 4.6), data from the western Dom Feliciano Belt suggest an African signature, either related to the Congo or the Kalahari Craton.

However, the allochthony of the Nico Pérez Terrane and its similitude regarding Archean and Proterozoic events suggests that it may represent a fragment of the Congo Craton separated during the Cryogenian rifting of Rodinia (Rapela et al., 2011; Oyhantçabal et al., 2011a; Oriolo et al, 2016a; Chapter 3). The dominance of Archean and Paleoproterozoic ages in both the Nico Pérez Terrane and

the overlying metasedimentary sequence may support an origin from the Angola Block of the Congo Craton. This could be supported by the juvenile Hf signature of Cryogenian grains, which is restricted to the western Dom Feliciano Belt and the Congo Craton (Fig. 4.6).

Fig. 4.6: Synthesis of available Hf T_{DM} vs. zircon age (this work; Rapela et al., 2011; Frimmel et al., 2013; Hofmann et al., 2014; van Schijndel et al., 2014; Colliston et al., 2015; Cornell et al., 2015; Foster et al., 2015).
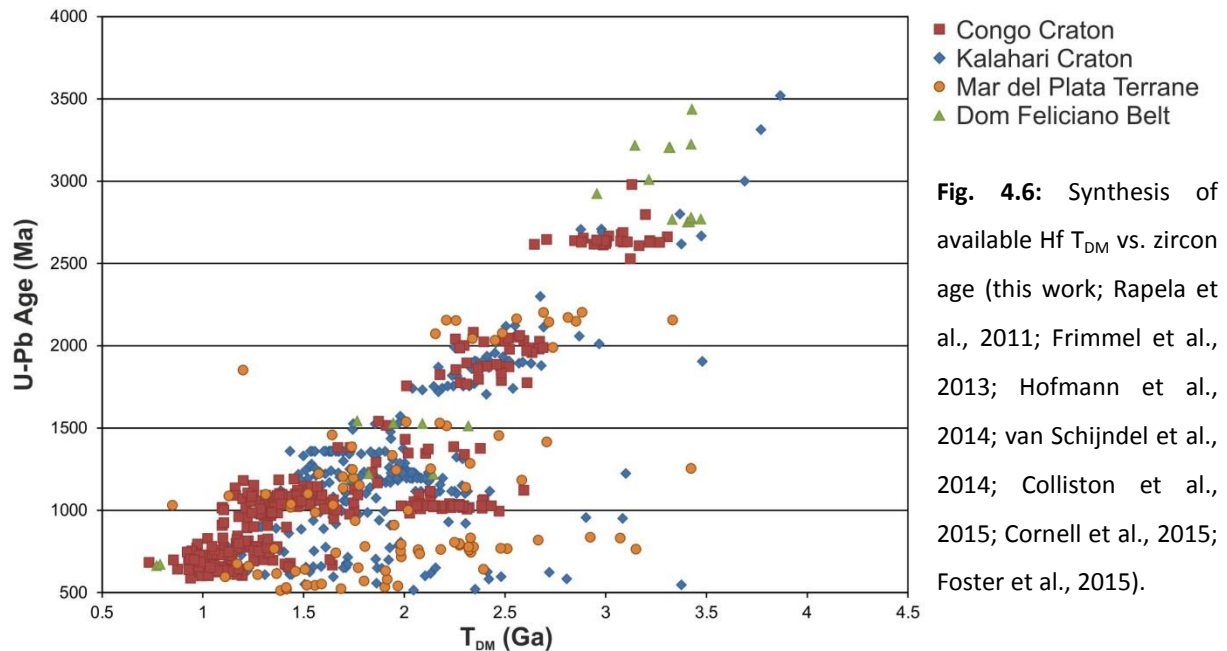
Several differences arise from the comparison between the western and eastern Dom Feliciano Belt in Uruguay (Fig. 4.5). In the eastern Dom Feliciano Belt, main peaks at 1.9-1.7, 1.1-1.0, 0.80-0.75 and 0.65-0.55 Ga are present (Basei et al., 2005; Gaucher et al., 2014b, 2014c). Paleo- and Mesoproterozoic ages coincide with ages recorded in the Gariep Belt (Fig. 4.5; Basei et al, 2005; Hofmann et al, 2014), which indicate provenance from the western Kalahari basement, particularly from the Namaqua-Natal Belt, the Vioolsdrif Granite Group and the Orange River Group (Blanco et al., 2011; Hofmann et al., 2014). Likewise, the 0.65-0.55 and 0.80-0.75 Ga peaks match ages of the Neoproterozoic magmatic rocks and the Cerro Olivo Complex, respectively (Hartmann et al, 2002; Oyhantçabal et al, 2007, 2009a, 2012; Basei et al, 2011b; Lenz et al, 2011). These similarities support the role of the Kalahari Craton basement as source for the sediments of the eastern Dom Feliciano Belt and the Gariep Belt (Basei et al, 2005; Hoffmann et al, 2014), which lacks in the western Dom Feliciano Belt (Fig. 4.5). Comparable peaks are also recorded in the Punta Mogotes Formation of the Mar del Plata Terrane and Damara sequences (Fig. 4.5; Rapela et al., 2011; Foster et al., 2015), providing further evidences of an African fingerprint.

50

It is important to outline that detrital zircon data in the eastern Dom Feliciano Belt of Uruguay are only available for units younger than ca. 590 Ma (Table 4.1). Interestingly, unpublished detrital zircon data from a quartzite of the basement of the eastern Dom Feliciano Belt show a distinct pattern (Nedrebø, 2014), which is similar to the one recorded in the western Dom Feliciano Belt (Fig. 4.5). Consequently, detrital zircon data support models indicating that the accretion of the Río de la Plata and Congo cratons predates the accretion of the Kalahari Craton (Prave, 1996; Rapela et al, 2011; Oriolo et al, 2016b; Chapter 6). Furthermore, detrital zircon data from the Kaoko Belt could reinforce this hypothesis, as the onset of Namaqua-age zircons is only recorded in the upper part of the Neoproterozoic cover (Konopásek et al., 2014). Additionally, similarities between detrital zircon ages from the western Dom Feliciano Belt and data from Nedrebø (2014) may suggest that both areas comprised a single block, in contrast to previous hypothesis (Bossi and Gaucher, 2004; Gaucher et al., 2010; Basei et al., 2011a).

4.6. Conclusions

Detrital zircon ages show late Ediacaran maximum deposition age for the Barriga Negra and Playa Hermosa formations, whereas a Neoproterozoic deposition age older than ca. 600 Ma can be constrained for units of the schist belt. The Neoproterozoic schist belt seems thus to predate the deposition of post-collisional sequences described as part of the foreland basin.

Comparison of U-Pb detrital zircon age distributions and model ages from potential source regions indicates that the Nico Pérez Terrane and not the Río de la Plata Craton was the main source of detritus. The similitude of Archean and Proterozoic events recorded in the Nico Pérez Terrane basement and the overlain metasedimentary cover of the western Dom Feliciano Belt support an African derivation of the former, most probably from the Congo Craton. In contrast, the source area for metasedimentary sequences in the eastern Dom Feliciano Belt was the Kalahari Craton. As this source is only recorded in units younger than ca. 590 Ma, detrital data also suggest that the Congo-

Río de la Plata amalgamation predates the accretion of the Kalahari Craton during Gondwana assembly.

-CHAPTER 5-

Structure of the Sarandí del Yí Shear Zone

5.1. Introduction

Shear zones are common features in the crust that occur on a wide range of scales, P-T conditions and tectonic settings. As they may represent terrane boundaries (e.g., Jégouzo, 1980; van der Pluijm et al., 1994; West, 1998; Höckenreiner et al., 2003; Goodenough et al., 2010; Wong et al., 2011), crustal-scale shear zones are structures with a significant role in the evolution of orogens that can provide irreplaceable information about the timing and mechanisms of accretion and amalgamation of crustal blocks.

Since the early works of Ramsay and Graham (1970), Sibson (1977), Ramsay (1980) and White et al. (1980), contributions about shear zones and associated rocks have diversified. The nucleation and evolution of shear zones related to lithospheric strain localization and, particularly, how these processes operate at different depths have been of particular interest (Grocott, 1977; Sibson, 1983; Hanmer, 1988; Jessel and Lister, 1991; Siegesmund et al., 2008; Platt and Behr, 2011a, 2011b; Montési, 2013).

The Sarandí del Yí Shear Zone is a crustal-scale mylonitic belt located in southern Uruguay (Fig. 5.1). It was first defined as a structural lineament by Preciozzi et al. (1979) and as a dextral structure that separates different tectonostratigraphic terranes by Bossi and Campal (1992). Oyhantçabal et al. (1993) considered it as a pre-Brasiliano dextral shear zone that was subsequently reactivated during the late Neoproterozoic exhibiting a sinistral shear sense. Later, Oyhantçabal et al. (2011a) proposed it as the eastern margin of the Río de la Plata Craton.

The dextral shearing is inferred from the bending of the 1.79 Ga old Florida doleritic dyke swarm (Fig. 5.1; Teixeira et al., 1999, 2013) and of the Paleoproterozoic fabrics of the Piedra Alta Terrane (Oyhantçabal et al., 1993). The subsequent sinistral movement is considered to be Neoproterozoic in age due to the emplacement of the syntectonic Solís de Mataojo Granitic Complex (Oyhantçabal et al., 2001, 2007). Due to the lack of structural and geochronological studies of this

shear zone, its evolution is still controversial (Oyhantçabal et al., 1993, 2011a; Gaucher et al., 2011a), even though it represents a key element for the understanding of the early amalgamation of Western Gondwana.
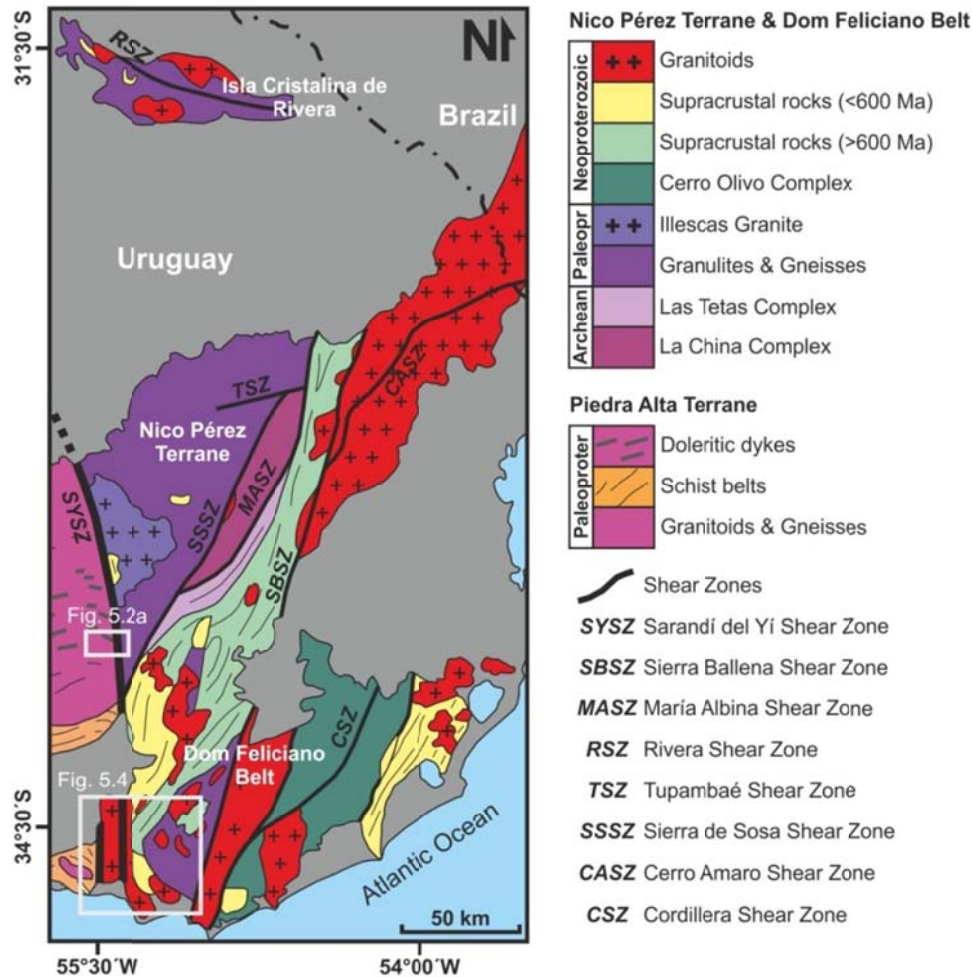
Fig. 5.1.: Geological map of the Precambrian of Uruguay modified after Oyhantçabal et al. (2011a) and references therein. Investigated areas of Figures 5.2a and 5.4 are shown.

5.2. Macro- and mesostructures

5.2.1. Structural domains

On the basis of regional mapping, three main structural domains I, II and III can be recognized in the study area. Domain I corresponds to the Piedra Alta Terrane, domain II comprises the shear zone and associated intrusions and, finally, domain III includes the Dom Feliciano Belt and Nico Pérez Terrane (Fig. 5.1, 5.2). As both domains I and III represent the neighbouring blocks of the Sarandí del Yí Shear Zone, they provide constraints on the relationship between syn- and pre-shearing fabrics.

5.2.2. Domain I: Piedra Alta Terrane

The granitic-gneissic areas, metasediments of the schist belts and shear zones show ages between 2.0 and 1.9 Ga and are dominated by E-ENE subvertical foliations (Oyhantçabal et al., 2006, 2011a). On the other hand, the 1.79 Ga Florida doleritic dyke swarm is made up of subvertical dykes that trend ca. 060° (Halls et al., 2001; Oyhantçabal et al., 2011a; Morales Demarco et al., 2011; Teixeira et al., 2013).
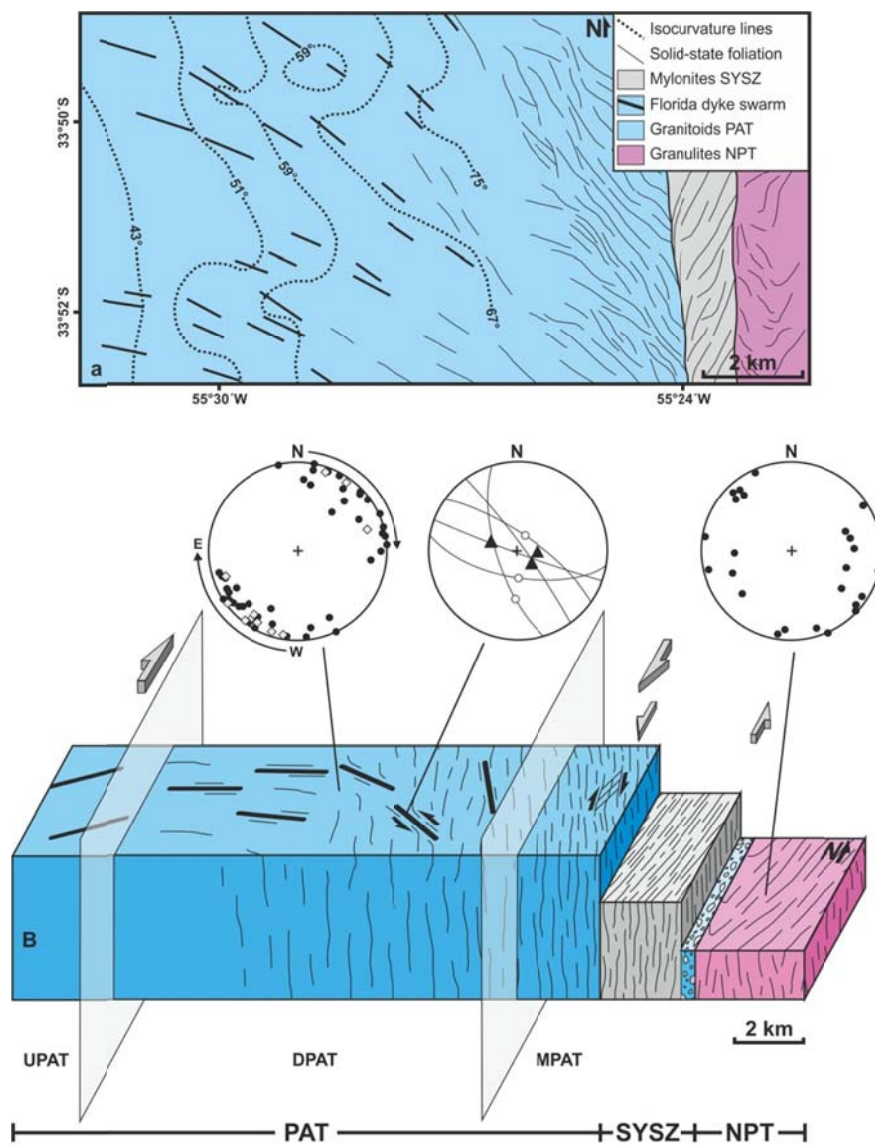
Fig. 5.2: a) Schematic geological map showing the structure of the easternmost Piedra Alta Terrane. Values shown in the isocurvature lines indicate angular differences between the strike of undeformed (060°) and deformed dykes. b) Schematic structural profile summarizing the main structural features in the Piedra Alta Terrane (PAT, domain I), the Sarandí del Yí Shear Zone (SYSZ, domain II) and the Nico Pérez Terrane (NPT, domain III). Strain increase in the Piedra Alta Terrane related to dextral shearing of the Sarandí del Yí Shear Zone is schematized considering three structural subdomains (UPAT: undeformed Piedra Alta Terrane, DPAT: deformed Piedra Alta Terrane and MPAT: mylonites of the Piedra Alta Terrane). Subsequent sinistral shearing and late cataclastic reactivation in the Sarandí del Yí Shear Zone are also shown. Lower hemisphere equal area projections of the orientation of the doleritic dykes (grey diamonds, n=11) and the solid-state foliation in their wall-rock (black dots, n=50) from west to east; foliations (lines, n=5), lineations (white circles, n=3) and fold axes (black triangles, n=3) within the strained doleritic dykes; and high-T foliation in the granulitic gneisses (black dots, n=23) are included.

55
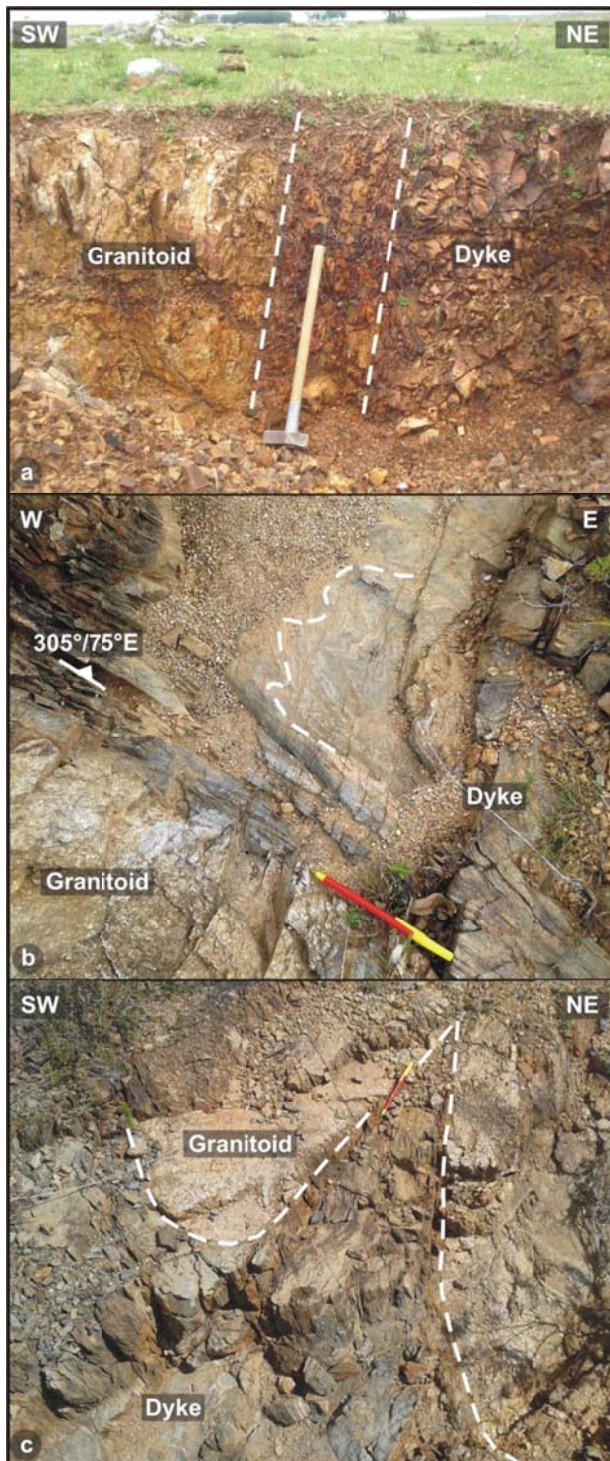
Fig. 5.3: Field photographs of structures in the eastern Piedra Alta Terrane. a) Slightly bent dyke with spaced cleavage subparallel to the contact with the granitic wall-rock. b) Strained and folded dyke. The geometry of the fold is schematically shown. c) Cuspate-lobate fold.

However, detailed mapping of the dykes shows their progressive clockwise rotation about a vertical axis towards the Sarandí del Yí Shear Zone in a ca. 10-km-wide zone (Fig. 5.2). Slightly bent dykes exhibit a spaced cleavage in contact with granitoids and gneisses (Fig. 5.3a), which show both magmatic and local solid-state foliations that strike WNW. Further to the east, the dykes are not only bent but also display a NW-WNW penetrative foliation that is frequently folded or sheared (Fig. 5.3b, 5.3c). Minor drag folds as well as S-C' shear bands in the foliated dykes indicate sinistral shearing. Granitoids show a solid-state foliation that is parallel to the fabric in the dyke along their mutual contacts but strikes NNW further away. Scarce stretching lineations in both dykes and their wall-rock are steeply dipping (Fig. 5.2b).

The easternmost area of the Piedra Alta Terrane is made up of granitic mylonites and protomylonites striking NNW. They are coarser-grained than the mylonites of the Sarandí del Yí Shear Zone and present S-C' shear bands that indicate dextral shearing (Fig. 5.2b).

5.2.3. Domain II: Sarandí del Yí Shear Zone

5.2.3.1. Mylonites

The Sarandí del Yí Shear Zone is a ca. 2-km-wide mylonitic belt that is exposed over at least 200 km in N-S direction (Fig. 5.1). Despite being covered by Phanerozoic rocks, it can be traced further to the north as a marked gravimetric anomaly (Oyhantçabal et al., 2011a). Its regional trend changes from N-S in the south to NNW-SSE in its northern part (Fig. 5.1).

Proto- to ultramylonites constitute the shear zone and present a dominant subvertical NNE-striking foliation with a mean orientation of 184°/81°W and a mean stretching lineation of 182°/06° (Figs. 5.4, 5.5). A transition from proto- to ultramylonites is observed from west to east. S-C' shear bands and σ-type feldspar mantled porphyroclasts are frequent and indicate a sinistral sense of shearing (Fig. 5.6a, 5.6b).

Tight to isoclinal symmetrical folds of the mylonites are typically found in the eastern part of the shear zone (Figs. 5.5, 5.6c). Fold axes with a mean orientation of 024°/01° are subparallel to the lineation, and sometimes a subvertical fold axial plane cleavage is developed (Fig. 5.5). Open folds are extremely rare and, when present, occur in the west. Minor drag folds are also observed (Fig. 5.6d). Parasitic folds are frequently present (Fig. 5.6e).

The eastern margin of the shear zone is cataclastically reworked (Fig. 5.5). Brittle deformation and pseudotachylite veins in the mylonites as well as phyllonites and cataclasites with mylonitic fragments are observed (Fig. 5.6f).

5.2.3.2. Solís de Mataojo Granitic Complex

The Solís de Mataojo Granitic Complex is a N-trending elongate body that intrudes the Sarandí del Yí Shear Zone in its southern portion (Fig. 5.4). The ages of 580 ± 15 Ma (Rb-Sr whole rock, Umpierre and Halpern, 1971) and 584 ± 13 Ma (single-phase Pb-Pb stepwise leaching titanite, Oyhantçabal et al., 2007) are interpreted as the crystallization age.

The wall-rock of this intrusion is made up of mylonites of the Sarandí del Yí Shear Zone, which correspond to the Aguas Blancas and the Arroyo Solís mylonites to the east and to the west, respectively (Fig. 5.5; Oyhantçabal et al., 1993, 2001). On the basis of structural similarities between the Solís de Mataojo Granitic Complex and the mylonites, Oyhantçabal et al. (2001) and Oyhantçabal (2005) inferred that the emplacement of this pluton in the shear zone occurred during sinistral shearing.
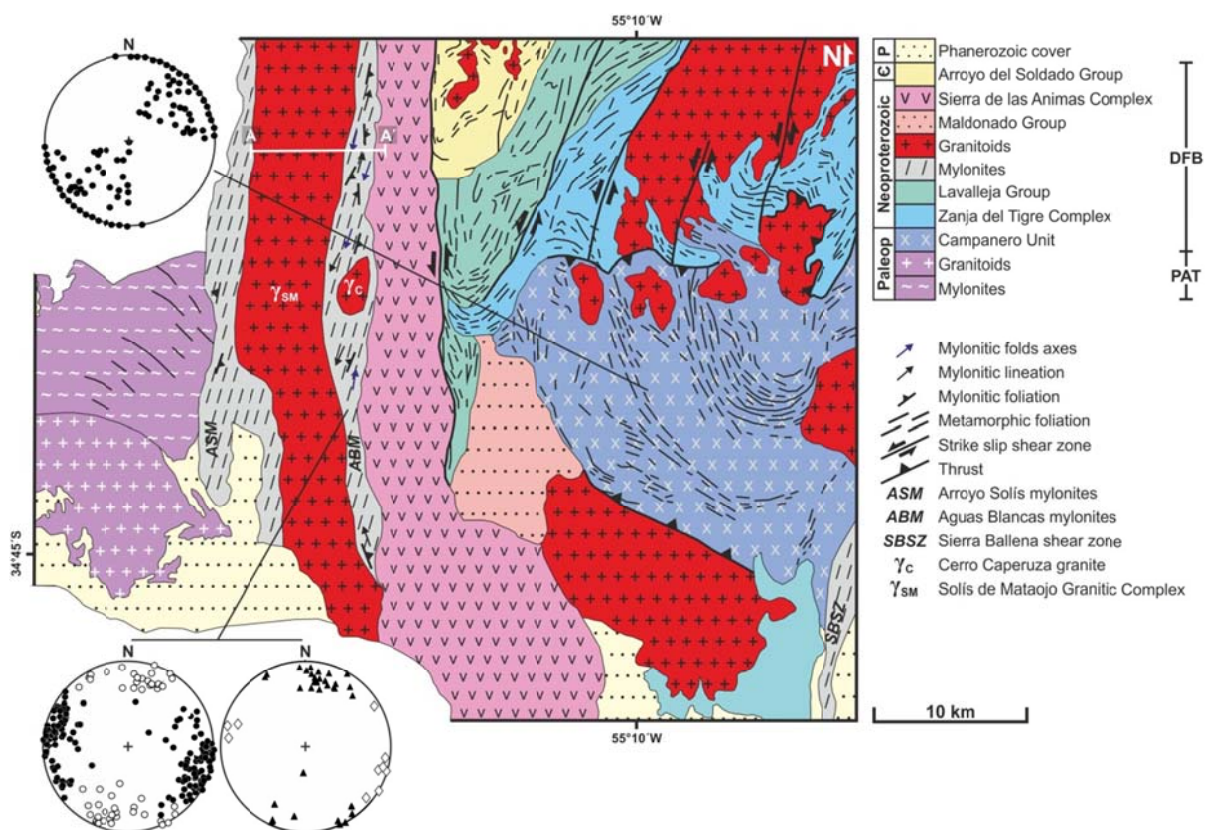
Fig. 5.4: Geological map of the southernmost Sarandí del Yí Shear Zone and adjacent blocks (modified after Oyhantçabal et al., 2001, 2005; Spoturno et al., 2004, 2012). The shear zone includes the Aguas Blancas and Arroyo Solís mylonites. Lower hemisphere equal area projections of foliations (black dots, n=155), lineations (white dots, n=55), fold axial planes (white diamonds, n=11) and fold axes (black triangles, n=36) of the mylonites of the Sarandí del Yí Shear Zone, as well as high-T foliation of the Campanero Unit (data from Oyhantçabal, 2005, n=148), are shown. The location of the structural profile in Fig. 5.5 is also indicated. DFB: Dom Feliciano Belt, PAT: Piedra Alta Terrane.

5.2.3.3. Cerro Caperuza granite

This NNE-SSW elongate intrusion is located in the southern Sarandí del Yí Shear Zone (Fig. 5.4). It is a medium-grained equigranular to porphyritic granite related to the magmatism of the

Sierra de las Ánimas Complex (Oyhantçabal et al., 1993). However, no geochronological or geochemical data are available for this intrusion. Except for quartz veins and fracturing, the Cerro Caperuza granite shows no significant macro-mesoscopic evidence of deformation indicating a late- to post-kinematic emplacement regarding ductile deformation of the Sarandí del Yí Shear Zone.
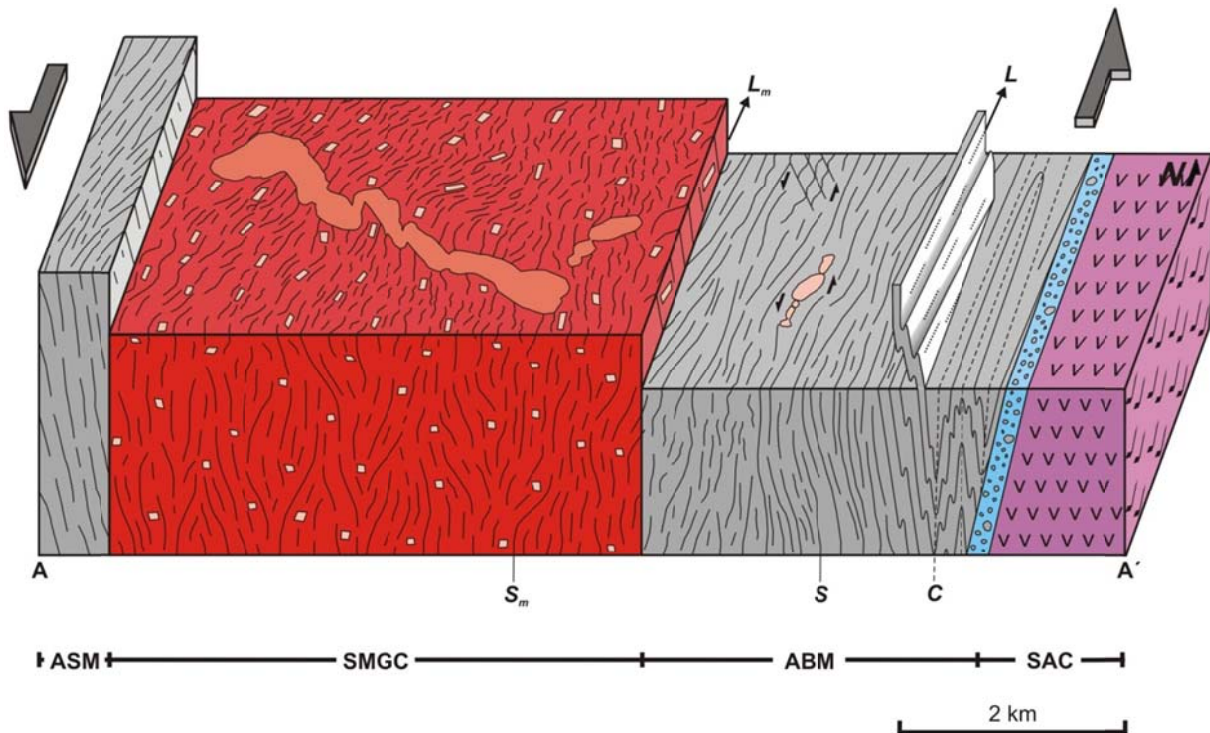
Fig. 5.5: Structural profile of the Sarandí del Yí Shear Zone (SYSZ, see location in Fig. 5.4). The contact between the Arroyo Solís mylonites (ASM) and the Solís de Mataojo Granitic Complex (SMGC) is schematic because it is not observable in the field, whereas the contact between the latter and the Aguas Blancas mylonites (ABM) is transitional. The cataclasites in the easternmost Sarandí del Yí Shear Zone (light blue, schematic orientation) represent the contact with the Sierra de las Ánimas Complex (SAC). Main structural elements of the SMGC (K-feldspar megacrystal fabric, deformed late pegmatitic veins, S_m: magmatic foliation, L_m: magmatic lineation; after Oyhantçabal et al., 2001) and the SYSZ (S: mylonitic foliation, L: stretching lineation, C: axial plane cleavage in chevron folds) are summarized.

5.2.4. Domain III: Nico Pérez Terrane and Dom Feliciano Belt

5.2.4.1. Nico Pérez Terrane

A high-T gneissic foliation can be locally found in the granulites, though without systematic orientation, whereas the Neoproterozoic granitoids show dominant equigranular textures. Therefore, there are no clear deformation patterns in the basement of the Nico Pérez Terrane that

could be related to the Sarandí del Yí Shear Zone. However, gneisses with NNW- to NW-striking foliation and local NNW-trending protomylonitic belts in the westernmost Illescas granite can be found close to the shear zone (Fig. 5.2). The Valentines-Rivera Granulitic Complex also shows cataclastic overprinting towards the Sarandí del Yí Shear Zone.

Fig. 5.6: Field photographs of structures developed in the Sarandí del Yí Shear Zone. a) Sinistral σ-type K-feldspar mantled porphyroclasts in granitic mylonites with mafic enclaves (arrow) that are cross-cut by a post-mylonitic pegmatitic vein. b) Sinistral σ-type feldspar mantled porphyroclasts with recrystallized tails. c) Tight to isoclinal fold with fold axis parallel to the stretching lineation. d) Sinistral drag fold. e) Parasitic folds developed in a tight mylonitic fold. f) Cataclasite of the easternmost Sarandí del Yí Shear Zone with mylonitic fragments. The arrow points to a fine-grained ultramylonitic fragment.

5.2.4.2. Dom Feliciano Belt

The Campanero Unit presents a folded steep high-T foliation, whereas the metasediments are strongly deformed and folded with NNE- or SSW-plunging axes (Fig. 5.4; Oyhantçabal, 2005; Oyhantçabal et al., 2009a; Spoturno et al., 2012). Major NNE-striking sinistral lineaments transect both units.

5.3. Microstructures

5.3.1. Domain I: Piedra Alta Terrane

The wall-rock of the dykes in the easternmost Piedra Alta Terrane comprises mostly granites and granodiorites with equigranular to porphyritic texture. Those granitoids with evidences of solid-state deformation show quartz crystals with interlobate grain boundaries (Fig. 5.7a) and chessboard extinction (Fig. 5.7b). Local recrystallization along the edge of the grains is also observed in feldspars.
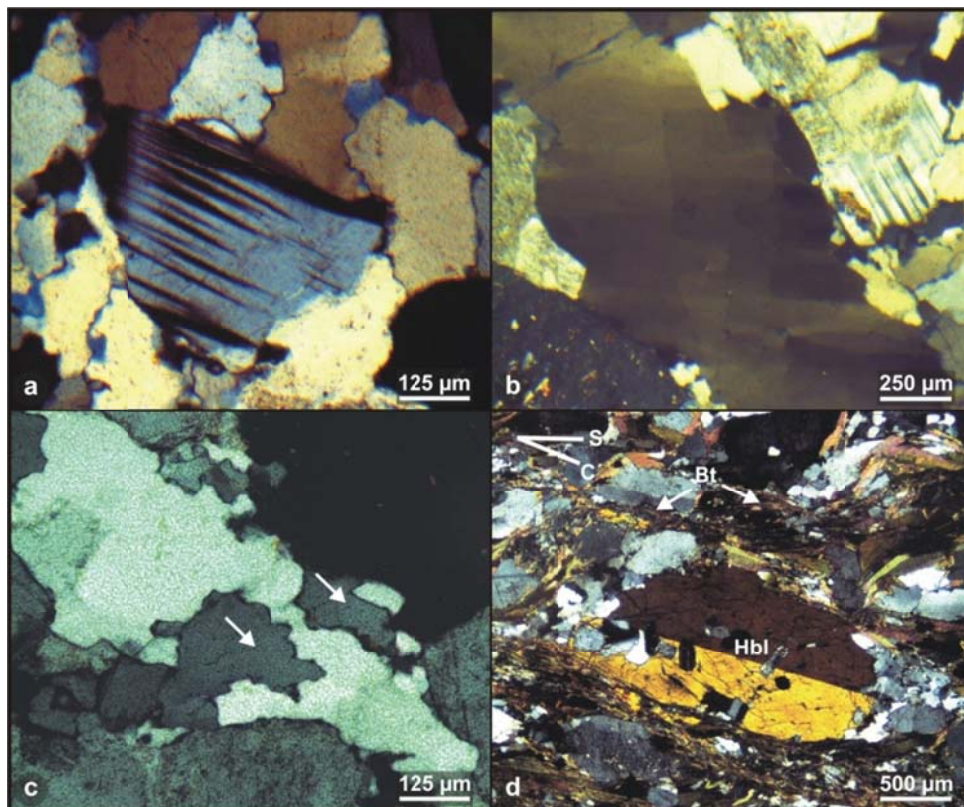
Fig. 5.7: Photomicrographs of microstructures from rocks of the eastern Piedra Alta Terrane (cross-polarized light). a) Mechanical twins in plagioclase and quartz crystals with sutured grain boundaries. b) Chessboard extinction in quartz. c) Interlobate grain boundaries and left-over grains (arrows) in quartz. d) Dextral S-C' shear bands in mylonites with shape-preferred orientation of biotite and hornblende.

The dykes display a significant variation of microstructures from west to east. In the slightly rotated dykes, pyroxenes are partly replaced by hornblende, in some cases as reaction rims. Further to the east, the primary mineral association is strongly replaced by hornblende, plagioclase, chlorite, epidote, clinozoisite, muscovite/sericite, biotite, quartz and opaque minerals.

The NNW-striking mylonites and protomylonites in the easternmost area of the Piedra Alta Terrane are made up of quartz, K-feldspar, plagioclase, biotite and scarce hornblende. Quartz shows sutured grain boundaries with minor chessboard extinction (Fig. 5.7c). Feldspars exhibit local recrystallization along the edge of the grains. Biotite is preferentially oriented in two planes that define the S and C' of dextral shear bands, whereas hornblende presents only minor fracturing (Fig. 5.7d).

5.3.2. Domain II: Sarandí del Yí Shear Zone

5.3.2.1. Mylonites

The protoliths of the Sarandí del Yí Shear Zone are dominantly granitoids, with minor participation of volcanic-subvolcanic and sedimentary rocks. Likewise, sheared quartz and quartz-feldspar veins and veinlets as well as amphibolitic xenoliths are recognizable.

Deformation is heterogeneously distributed with increasing intensity towards the east, which is accompanied by grain size decrease. Kinematic indicators include S-C' shear bands, σ-type feldspar mantled porphyroclasts with asymmetric myrmekites, mica fish and oblique foliation of elongated quartz grains, which support a subhorizontal sinistral sense of shear (Fig. 5.8a, 5.8b).

Quartz grains are mostly sutured (Fig. 5.8c). In some cases, elongate grains of relatively uniform size are developed due to progressive subgrain rotation, particularly in microfolds (Fig. 5.8d). Recrystallization in feldspars is localized at the edges of the grains or within microshear zones. Hornblende exhibits only fracturing (Fig. 5.8e). White mica and minor fine-grained biotite are typically oriented parallel to the S or C' planes.
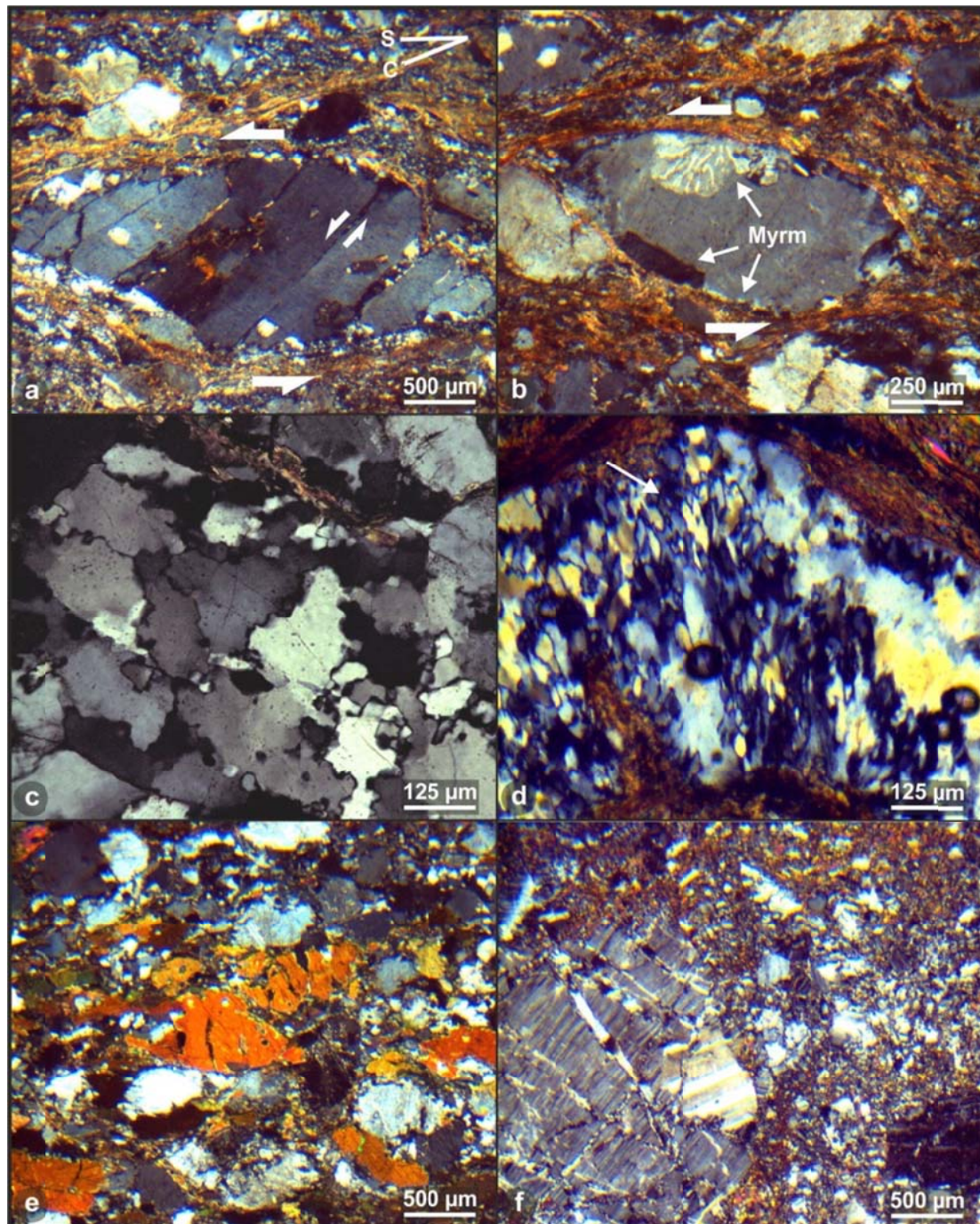
Fig. 5.8: Photomicrographs of microstructures from rocks of the Sarandí del Yí Shear Zone (cross-polarized light). a) Sinistral S-C' shear band and σ-type K-feldspar mantled porphyroclast with anti-bookshelf structure. Synthetic microshear zones with localized recrystallization of feldspar are also indicated. b) Sinistral quarter structure of K-feldspar mantled porphyroclast with asymmetric myrmekites and recrystallized tails. c) Sutured quartz crystals with interfingering grain boundaries. d) Elongate grains parallel to Y of relatively uniform size developed due to subgrain rotation in the hinge of a microfold (YZ section). e) Fractured hornblende crystals. f) Cataclastic texture in sample from the easternmost part of the shear zone. Note the large fragment of a plagioclase crystal showing a cataclastic texture.

The cataclasites located in the easternmost part of the shear zone consist of angular polycrystalline fragments immersed in a very fine-grained matrix of quartz + plagioclase + K-feldspar + epidote + opaque minerals ± clinozoisite ± zoisite ± chlorite ± sericite ± carbonates (Fig. 5.8f). The fragments consist of quartz, plagioclase and K-feldspar with minor participation of micas. They show microstructures similar to those found in the mylonites but significantly overprinted by cataclasis. Locally, phyllonites are also recognizable.

5.3.2.2. Solís de Mataojo Granitic Complex

Microstructures indicate a transition from magmatic to low-T solid-state deformation processes, though a major part of the deformation took place under magmatic and high-T solid-state conditions (Oyhantçabal et al., 2001).

5.3.2.3. Cerro Caperuza granite

The Cerro Caperuza granite is made up of quartz, microcline, plagioclase and biotite with zircon as the main accessory mineral phase. Quartz crystals exhibit undulose extinction and subgrain formation with peripheral bulging and recrystallization. Microcline shows flame perthites, whereas bending and deformation twins are identifiable in plagioclase grains.

5.3.3. Domain III: Nico Pérez Terrane and Dom Feliciano Belt

5.3.3.1. Nico Pérez Terrane

Granulites exhibit granoblastic textures in feldspars and pyroxenes. In the western Nico Pérez Terrane, feldspar shows evidence of localized recrystallization along the edges. Quartz develops sutured boundaries and occasionally triple junctions. Chessboard extinction is frequent, and subgrain formation is sometimes present.

The Illescas granite displays porphyritic to equigranular textures. Quartz exhibits chessboard extinction, whereas plagioclase shows occasionally bent twinning. In the NNW-trending

protomylonitic belts that affect this granitoid in the west, quartz shows recrystallized bulges along grain boundaries with local evidences of subgrain rotation as well as deformation bands and fracturing. Feldspars exhibit only significant fracturing.

5.4. Strain analysis

5.4.1. Passive markers

The Florida doleritic dyke swarm has a regional strike of *ca*. 060° and thus is considered as a passive marker for strain associated with the dextral shearing. The analysis was carried out with the Mohr circle method of Lisle (2014), which is supported by previous models (Ramsay, 1980). Based on the orientation of a deformed and undeformed passive marker and the mylonitic foliation, the method allows obtaining a 2D graphical solution for the shear zone strain. Figure 5.9a shows a schematic representation of the geometrical relationships of the shear zone boundary (x), the orientation of the deformed and undeformed dykes (m' and m, respectively) and the orientation of the mylonitic foliation (S_1).

$S_1=1.69$
$S_2=0.36$
$R_s=4.64$
$d=0.59$
$\gamma=2.03$
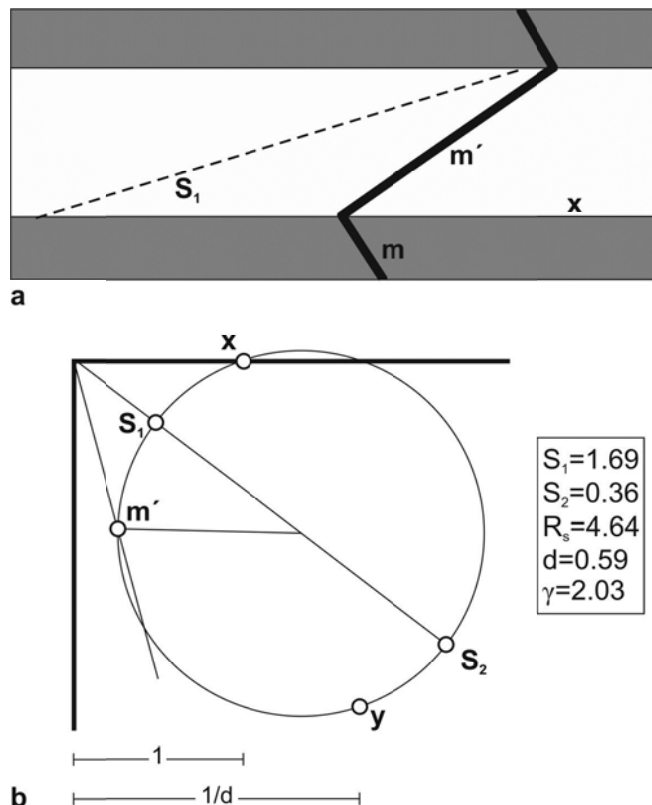
Fig. 5.9: Schematic representation of the dataset (a) and Mohr circle construction (b) used for the strain estimation based on the method of Lisle (2014). The structural elements (x: shear zone boundary; m' and m: orientation of the deformed and undeformed dykes, respectively; S_1: orientation of the mylonitic foliation) as well as the obtained parameters are shown (S_1 and S_2: main stretching axes, R_s: strain ratio, d: proportional volume change, γ: shear strain).

The easternmost outcrops, where both dykes and mylonitic foliation could be measured in the field, were used for the analysis (m^m' = 75°, x^S_1 = 17°, x^m' = 35°). Therefore, values presented herein represent minimum estimates because deformation increases further to the east, where the mylonitic belt is present but no dykes were recognized (Fig. 5.2).

The obtained geometrical solution and the calculated values are presented in Fig. 5.9b. On the basis of these results, a significant deviation from simple shear is observed, with a 41 % volume decrease and a shear strain of 2.03. However, volume loss should be even higher considering the strain within the dykes themselves, whereas shear strain is heterogeneously distributed and even higher towards the shear zone.

5.4.2. S-C´ shear bands

A quantitative strain analysis of the Sarandí del Yí mylonites was carried out on the basis of the method of Kurz and Northrup (2008), which allows to estimate vorticity values in thin sections on the basis of the angle between the mylonitic foliation (S) and the maximum inclined shear band orientation (C'). Within high-strain rocks, the most steeply inclined shear band orientation provides the best estimate of the bulk kinematic vorticity W_k. Consequently, S-C' shear band measurements allow characterizing the coaxiality/non-coaxiality of general shear.

W_k values range between 0.00 and 0.24, considering the maximum inclined shear band orientation for each sample (Fig. 5.10). Since these values indicate a proportion of simple shear lower than 15%, pure-shear dominated deformation related to sinistral shearing of the shear zone is inferred.

5.5. Quartz CPO patterns

Samples of the mylonites were collected to analyse the CPO of quartz. All samples were obtained from the Sarandí del Yí Shear Zone, except AA-12, which corresponds to the mylonites of the easternmost Piedra Alta Terrane. Sample locations are presented in Appendix 1.
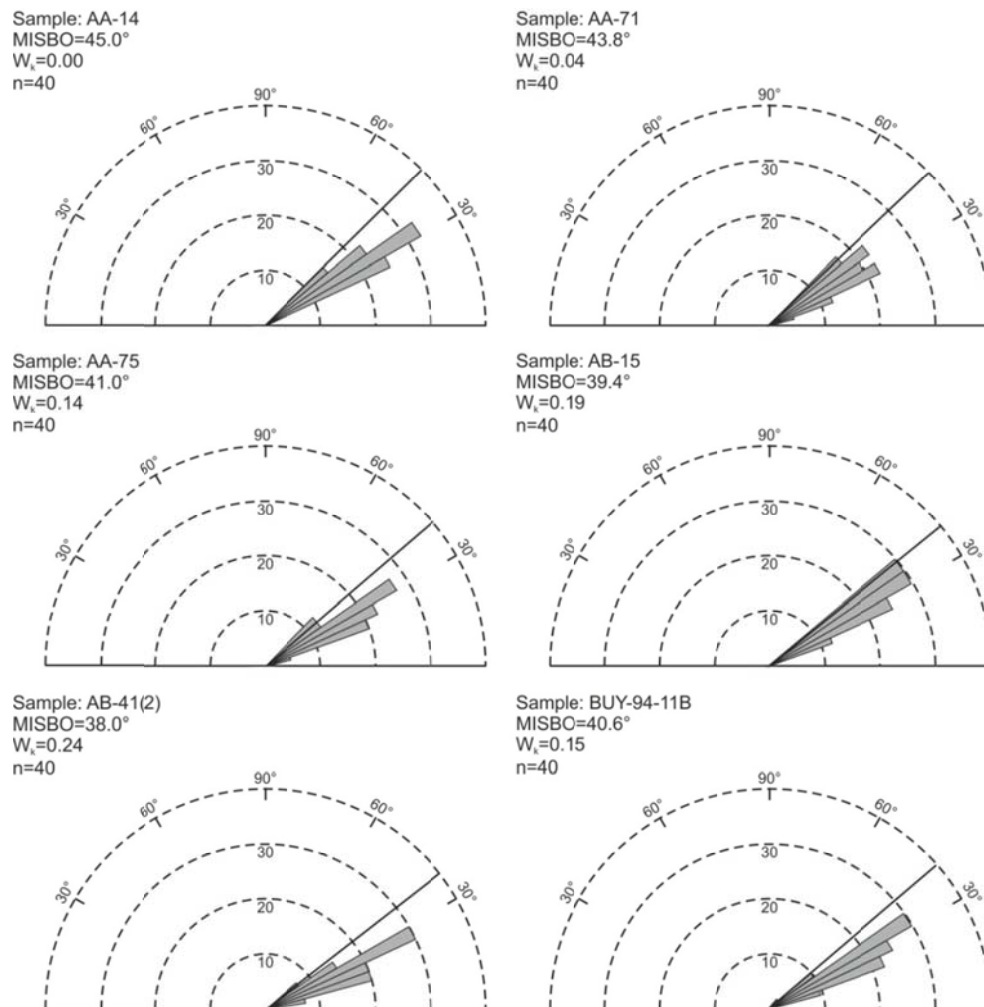
Fig. 5.10: Rose diagrams of synthetic S-C' shear bands orientations according to the method of Kurz and Northrup (2008). Frequency is indicated in percentage. The full line shows the orientation of the maximum inclined shear band orientation (MISBO). W_k: bulk kinematic vorticity, n: number of measurements.

Quartz [c]-axis pole figures show crossed girdles with well-defined maxima subparallel to the Y direction, which are accompanied by girdle distributions of {a}- and {m}-planes perpendicular to Y (Fig. 5.11). These data would account for prism <a> as the main slip system during the mylonitization. Relative symmetric textures indicate pure-shear dominated deformation, according to criteria from Schmid and Casey (1986). However, the weak asymmetry of the [c]-axis pole figure of the sample AA-12 indicates a dextral shear sense. Despite the low reliability of quartz [c]-axis pole figures as shear sense indicators (Killian et al., 2011), these data match kinematic indicators obtained in these mylonites.
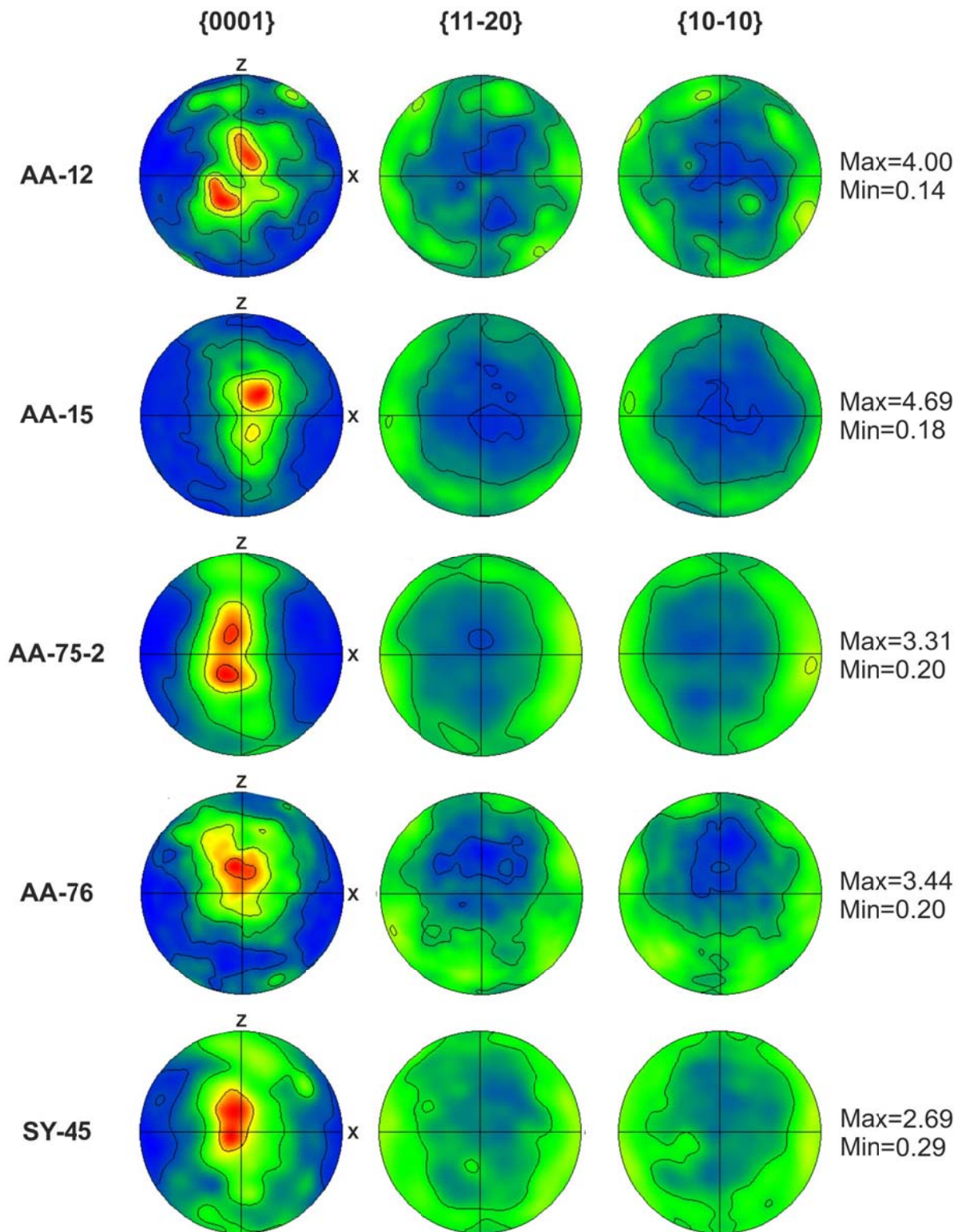
Fig. 5.11: Quartz CPO pole figures from samples of the mylonites. All samples correspond to the Sarandí del Yí Shear Zone, except for AA-12 that represents the mylonites of the easternmost Piedra Alta Terrane. Pole of the foliation (Z) and the lineation (X) are marked. Contour levels are at 0.5, 1, 2 and 3 multiples of uniform distribution (m.u.d.). Colour scaling is from blue (minimum) to red (maximum). Sample locations are indicated in Appendix 1.

5.6. Discussion

5.6.1. Deformation of the eastern Piedra Alta Terrane

On the basis of detailed mapping in the Piedra Alta Terrane, a progressive strain increase towards the east can be identified in its eastern part. This fact is documented by the increase in both the magnitude of the rotation of the dykes and the strain within them and by the presence of mylonites further to the east (Fig. 5.2). The obliquity between the mylonitic foliation and the margins of the belt, S-C' shear bands and the clockwise rotation of the dykes point to dextral shearing. Volume loss (>40%) was associated with the dextral shearing and could result either from metamorphic reactions and/or from vertical extension supported by the scarce subvertical lineations (Fig. 5.2b).

Reaction of pyroxene and plagioclase to hornblende, plagioclase, chlorite, epidote, clinozoisite, muscovite/sericite, biotite, quartz and opaque minerals in the strained dykes indicates maximum amphibolite facies metamorphism during the shearing event. Quartz microstructures observed in the wall-rock account for grain boundary migration recrystallization, probably at temperatures above 600°C due to the presence of chessboard pattern extinction (Kruhl, 1996; Stipp et al., 2002). Recrystallization and formation of subgrains along the edges of feldspars indicate deformation conditions above ca. 550°C (Voll, 1976; Pryer, 1993). Furthermore, quartz microstructures in the mylonites indicating grain boundary migration recrystallization associated with prism <a> slip detected by CPO patterns point to deformation conditions between 500 and 650°C (Mainprice et al., 1986; Stipp et al., 2002). Therefore, the dextral shearing in the eastern margin of the Piedra Alta Terrane is interpreted to occur under middle to upper amphibolite facies conditions (ca. 600-650°C).

5.6.2. Deformation of the Sarandí del Yí Shear Zone

Both macro- and microindicators are indicative of sinistral shear for the Sarandí del Yí Shear Zone. Likewise, the dominance of protomylonites to the west and ultramylonites to the east as well

as the concentration of tight to isoclinal folds in the easternmost shear zone indicates a strain increase towards the east.

No switching in the orientation of the lineation with progressive deformation is observed, suggesting flattening with both vertical and lateral extension (Sengupta and Ghosh, 2004). Pure-shear dominated deformation with flattening is also indicated by the orientation of folds axes and planes (Jones et al., 2004) and supported by the W_k values obtained by the strain analysis of the S-C' shear bands as well as the quartz CPO fabrics (Schmid and Casey, 1986). This is further constrained by strain data from Oyhantçabal et al. (2001), which suggest pure-shear dominated deformation under magmatic conditions during the emplacement of the synkinematic Solís de Mataojo Granitic Complex. Therefore, pure-shear dominated deformation with a subordinated sinistral strike-slip component is interpreted for the Sarandí del Yí Shear Zone.

The abundance of core and mantle structures in feldspars with new grains sometimes also within internal microshear zones accounts for dislocation climb and recrystallization of feldspars at temperatures of 450-550°C (Passchier and Trouw, 2005, and references therein). Quartz microstructures denote dominant diffusion processes and recrystallization due to grain boundary migration, also indicated by quartz CPO data. However, local evidence of subgrain rotation recrystallization, particularly in folds, may support a late activity of this mechanism; hence, deformation conditions probably occurred at grain boundary migration recrystallization conditions near the transition with the subgrain rotation regime (450-550°C; Stipp et al., 2002). On the other hand, formation of synkinematic white mica is interpreted to have taken place due to the breakdown of feldspar, which points to temperatures below 500°C (Wiberley, 1999, and references therein). Deformation conditions during sinistral shearing can thus be constrained to lower amphibolite to upper greenschist facies conditions (*ca*. 550-450°C). Lastly, a significant cataclastic reworking is observed in the Sarandí del Yí Shear Zone. The mineral association indicates greenschist to subgreenschist conditions during this event.

5.6.3. Structural evolution of the Sarandí del Yí Shear Zone

Heterogeneous shear zones are characterized by lateral variations of strain parameters, generally with strain increase towards the core of the shear zone. However, long-lived shear zones may show not only spatial but also temporal variations of strain. Shear zones can thus be classified based on thickness variation with time (Means, 1984, 1995; Hull, 1988; Horsman and Tikoff, 2007; Vitale and Mazzoli, 2008). Increasing and decreasing thickness may be interpreted in terms of strain hardening and softening, respectively, that in turn can result from the combination of different deformation conditions and processes.

Since deformation of the eastern margin of the Piedra Alta Terrane seems to be related to the evolution of the Sarandí del Yí Shear Zone, a polyphase evolution can be interpreted (Fig. 5.12). Cross-cutting relationships indicate retrograde conditions (e.g., mylonitic protoliths in the cataclasites) associated with progressive strain localization towards the east. In this context, a first phase of dextral shearing took place under middle to upper amphibolite facies conditions (Fig. 5.12a). A subsequent sinistral event under lower amphibolite to upper greenschist facies conditions reworked the eastern margin of the shear zone giving rise to the development of the Sarandí del Yí mylonitic belt (Fig. 5.12b). During this stage, more localized strain in the easternmost part of the shear zone gave rise to the development of late folded mylonitic foliation. This high strain zone was then overprinted by cataclasis (Fig. 5.12c).

This evolutionary model is thus comparable with the conceptual model of Sibson (1977, 1983) and natural examples such as the Nordre Strømfjord Shear Zone (Bak et al., 1975), the Great Slave Lake Shear Zone (Hanmer, 1988) and the Imbricate Zone and the Stortrømmen Shear Zone (Smith et al., 2007), among others. Consequently, the Sarandí del Yí Shear Zone represents an example of shear zone with thickness decreasing in time that evolved from upper amphibolite to subgreenschist facies conditions and records a kinematic switch from dextral to sinistral shear at ca. 600-550°C.
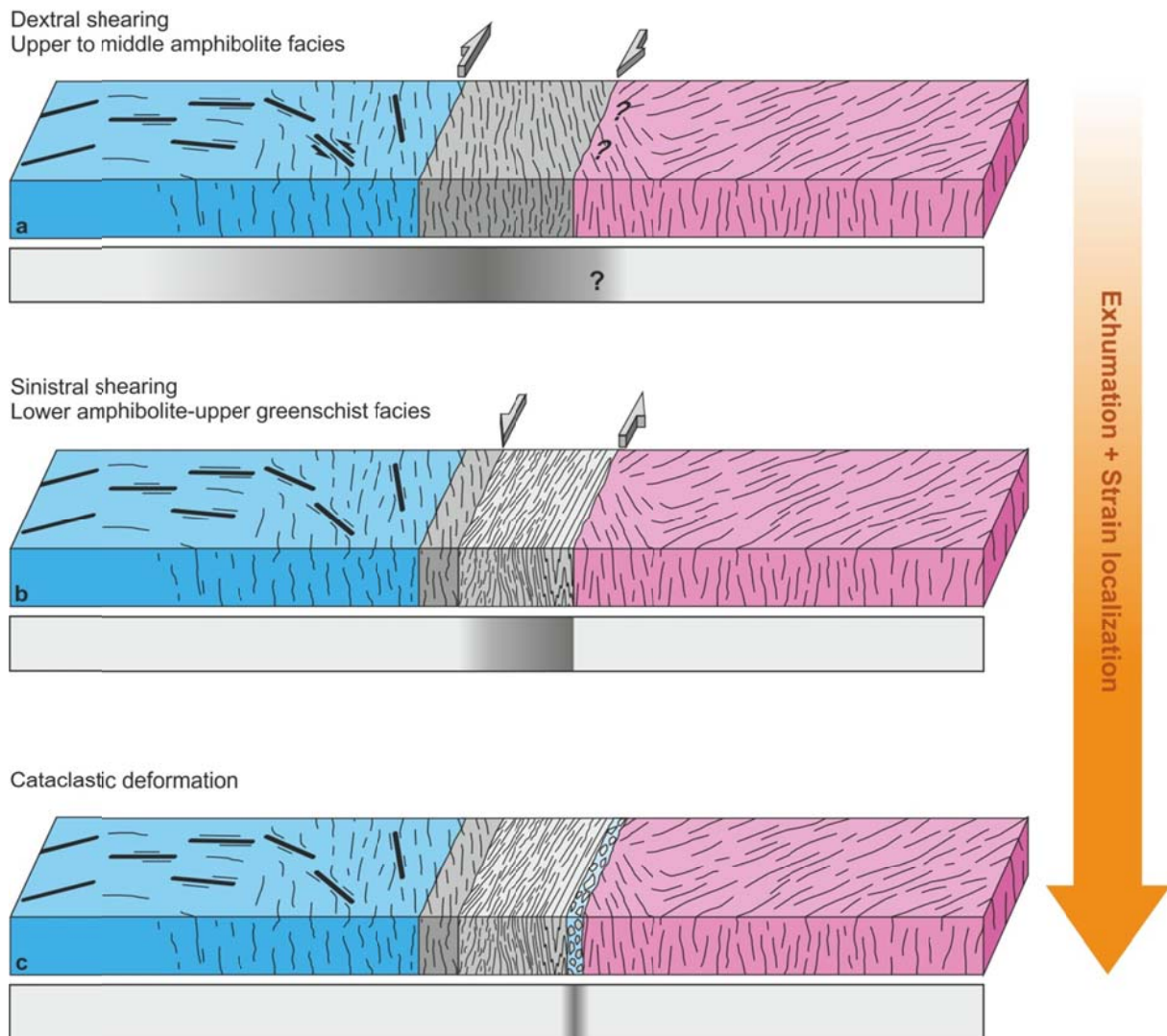
Fig. 5.12: Structural evolution of the Sarandí del Yí Shear Zone related to progressive strain localization under retrograde conditions. Schematic strain distribution is indicated with the grey scale (darker colours indicate higher strain).

The preservation of deformation of the Sarandí del Yí Shear Zone under different conditions is related to progressive strain localization linked to strain softening processes. In this case, the nucleation of the shear zone may be controlled by the presence of a former terrane boundary that started to evolve as a shear zone after continental collision (Oyhantçabal et al., 2011a). Towards the eastern part of the Piedra Alta Terrane, a mylonitic foliation and grain size reduction are observed and can be considered as responsible for the strain softening (Platt and Behr, 2011a; Rennie et al., 2013; Sullivan et al., 2013). Subsequently, the zone with the highest strain was reactivated during exhumation, obliterating the previous fabric that was only preserved in lower strain domains. Such

domains may have experienced only partial annealing but no significant deformation during retrograde conditions, as schematized by Herwegh et al. (2008).

5.7. Conclusions

Integration of macro- to microstructural data indicates that the Sarandí del Yí Shear Zone represents a crustal-scale shear zone that underwent complex long-term deformation. During juxtaposition of the Piedra Alta (Río de la Plata Craton) and Nico Pérez terranes, deformation in the Sarandí del Yí Shear Zone started under upper to middle amphibolite facies conditions with dextral shearing in the easternmost Piedra Alta Terrane. Subsequent lower amphibolite-upper greenschist facies metamorphism was related to pure-shear dominated sinistral shearing, which was accompanied by contemporaneous plutonism reflected by the Solís de Mataojo Granitic Complex. Post-mylonitization magmatism is indicated by the Cerro Caperuza granite. Afterwards, a late cataclastic event took place and reworked the easternmost border of the shear zone.

The evolution of the shear zone reflects progressive strain localization under retrograde metamorphic conditions during crustal exhumation. Furthermore, strain localization also resulted in decrease in the shear zone thickness.

-CHAPTER 6-

Geochronology of the Sarandí del Yí Shear Zone

6.1. Introduction

Exhumed long-lived shear zones represent fundamental structures that allow studying the coupling between crustal exhumation and strain localization processes as well as the timing at which they take place in the lithosphere. However, assessing the age of the deformation is not a simple task, due to the overprinting caused by the youngest events that may reset the isotopic systems that are used as thermochronometers. It is even more complex to integrate geochronological with macro- and microstructural data as well as kinematics in order to create a robust model of the tectonometamorphic evolution of shear zones, which can further constrain the evolution at the orogen-scale.

Several methods can be applied to study the temperature-time (T-t) paths of metamorphic rocks, which are based on closure temperatures of isotopic geochronometers (Table 6.1; Dodson, 1973; Villa, 1998). The most widespread methods to constrain the age of the deformation in shear zones consist in either dating synkinematic intrusions or minerals that were formed during mylonitization, or constraining the T-t paths of adjacent blocks (van der Pluijm et al., 1994). All these methods, though potentially powerful, have some limitations. Dating synkinematic intrusions represents an indirect and interpretative method (van der Pluijm et al., 1994), whereas dating minerals in the mylonites themselves may be limited by the problem of whether these ages represent neocrystallization or cooling ages (Dunlap, 1997; Mulch and Cosca, 2004). On the other hand, establishing T-t paths of neighbouring blocks may be helpful but nevertheless indirect and, in many cases, difficult to obtain due to the lack of equivalent datable minerals associations on both sides of the shear zones.

As previously indicated (Chapter 5), no geochronological data are available for the mylonites of the Sarandí del Yí Shear Zone. Though the sinistral shearing is considered to be Neoproterozoic in age due to the emplacement of the synkinematic Solís de Mataojo Granitic Complex (580 ± 15 Ma,

Rb-Sr whole rock, Umpierre and Halpern, 1971; 584 ± 13 Ma, single phase Pb-Pb stepwise leaching

titanite, Oyhantçabal et al., 2007), the timing of the dextral shearing is not well constrained. This first

event took place prior to the Neoproterozoic sinistral shearing and also postdates the emplacement

of the 1.79 Ga old Florida doleritic dyke swarm (Teixeira et al., 1999, 2013; Halls et al., 2001), as

these dykes are dextrally sheared towards the shear zone (Chapter 5; Oyhantçabal et al., 1993;

Oriolo et al., 2015). Therefore, the onset of the deformation during accretion of the Nico Pérez

Terrane to the eastern margin of the Río de la Plata Craton could be placed at any time between the

late Paleoproterozoic (< 1.79 Ga) and the Ediacaran.

System	Tc (°C)	References
U-Th-Pb zircon	>900	Dahl (1997), Cherniak and Watson (2000)
U-Th-Pb monazite	>750	Heaman and Parrish (1991)
U-Pb xenotime	>650	Heaman and Parrish (1991)
U-Th-Pb allanite	650	Heaman and Parrish (1991)
U-Th-Pb titanite	650 ± 50	Cherniak (1993), Dahl (1997), Frost et al. (2000)
U-Pb rutile	620 ± 20	Cherniak (2000), Vry and Baker (2006), Kooijman et al. (2010)
Sm-Nd garnet	600 ± 30	Mezger et al. (1992)
Rb-Sr muscovite	500 ± 50	Jäger et al. (1967), Jäger (1977)
K-Ar hornblende	530 ± 40	Harrison (1981)
K-Ar phlogopite	440 ± 40	Giletti (1974), Jenkin et al. (2001)
U-Pb apatite	425-500	Dahl (1997), Chamberlain and Bowring (2000)
K-Ar muscovite	350-425	Purdy and Jäger (1976), Harrison et al. (2009)
Rb-Sr biotite	350	Jenkin (1997)
K-Ar biotite	310 ± 40	Harrison et al. (1985)

Table 6.1: Closure temperature (Tc) for different isotopic systems.

6.2. Sample description

Samples AA-13, BUY-81-11, BUY-84-11, BUY-92-11, BUY-93-11 and BUY-94-11 were collected

from mylonites of the Sarandí del Yí Shear Zone itself (Fig. 6.1, Appendix 2). On the other hand, AA-

12 corresponds to a granitic mylonite located in the easternmost Piedra Alta Terrane, which was

deformed during dextral shearing along the shear zone. A sample (UY-22-14) from the Cerro

Caperuza granite was obtained as well (Fig. 5.4), as it intrudes the shear zone and shows no

significant ductile deformation, thus providing a constraint on the end of the mylonitization. Sample

locations and applied methods are presented in Appendix 2.
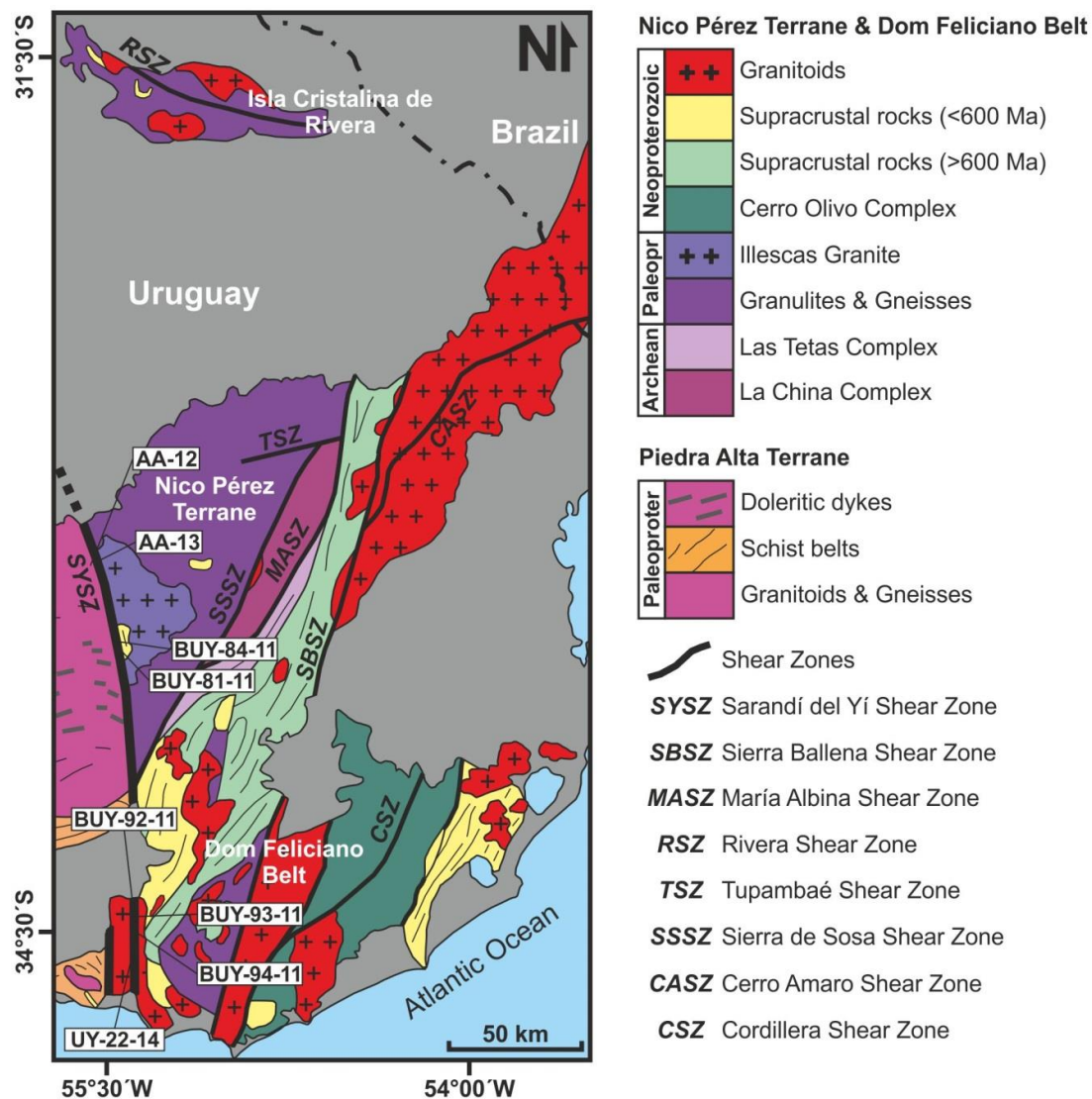
Fig. 6.1: Geological map of the Nico Pérez Terrane and adjacent blocks (modified after Oyhantçabal et al., 2011a, and references therein). Sample locations are shown.

The sample AA-12 corresponds to a mylonite made up of quartz, K-feldspar, plagioclase, hornblende and biotite. Quartz shows interlobate grain boundaries, left-over grains and minor chessboard extinction, which accounts for grain boundary migration recrystallization at temperatures above ca. 600°C (Kruhl, 1996; Stipp et al., 2002). Feldspars exhibit local recrystallization along the edge of the grains, indicating recrystallization temperatures above 550°C (Voll, 1976; Pryer, 1993). Biotite and hornblende are preferentially oriented in two planes that define the S and C' of dextral shear bands, which are also observable at mesoscale. Hornblende crystals are typically euhedral and present only minor fracturing.

The sample AA-13 from a granitic mylonite is made up of quartz, K-feldspar and plagioclase. S-C´ shear bands and feldspar σ-type mantled porphyroclast microstructures indicate sinistral shearing. Sutured grain boundaries point to grain boundary migration recrystallization in quartz, although minor evidences of subgrain rotation recrystallization can be recognized as well, indicating recrystallization temperatures of 450-550°C (Stipp et al., 2002). Feldspars develop core and mantle structures with occasionally anti-bookshelf structures, indicating temperatures of 450-550°C (Passchier and Trouw, 2005, and references therein). Scarce sericite and epidote are also present along shear band planes.

The mylonite of the sample BUY-81-11 is constituted by quartz, K-feldspar, plagioclase and hornblende. Sutured grain boundaries point to grain boundary migration recrystallization at ca. 500-550°C for quartz (Stipp et al., 2002). Core and mantle structures in feldspars reveal sinistral shearing both at meso- and microscale and point to recrystallization temperatures of 450-550°C (Passchier and Trouw, 2005, and references therein). Hornblende crystals present significant fracturing and are sometimes boudinaged parallel to the stretching lineation direction.

The sample BUY-84-11 is an ultramylonite constituted by quartz, feldspar and sericite. Quartz crystals form aggregates with foam textures indicating recovery. Core and mantle structures in feldspars show sinistral shearing and point to recrystallization temperatures of 450-550°C (Passchier and Trouw, 2005, and references therein). Pressure solution is revealed by the presence of opaque-minerals-rich solution seams.

UY-22-14 corresponds to the Cerro Caperuza granite, which presents equigranular texture and is constituted by quartz, K-feldspar, plagioclase and scarce biotite.

The deformed porphyritic felsic intrusion of the sample BUY-93-11 is made up of quartz and feldspar. Sutured grain boundaries point to grain boundary migration recrystallization at ca. 500-550°C for quartz (Stipp et al., 2002). Core and mantle structures in feldspars reveal sinistral shearing and recrystallization temperatures of 450-550°C (Passchier and Trouw, 2005, and references therein).

Both BUY-92-11 and BUY-94-11 correspond to mylonites, which are constituted by quartz, K-feldspar, plagioclase and muscovite. Sinistral shearing is indicated by S-C' shear bands, σ-type feldspar mantled porphyroclasts with asymmetric myrmekites, mica fish and oblique foliation of elongated quartz grains. S-C' shear bands and σ-type feldspar mantled porphyroclasts are also observable at mesoscale. Sutured grain boundaries point to grain boundary migration recrystallization in quartz and recrystallization temperatures of 500-550°C (Stipp et al., 2002). Feldspars develop core and mantle structures, which are sometimes accompanied by microshear zones that show internal recrystallization, indicating temperatures of 450-550°C (Passchier and Trouw, 2005, and references therein). Muscovite typically develops mica fish microstructures and is oriented parallel to the S or C´ planes of the shear bands in the mylonites, suggesting that they are synkinematic minerals. This interpretation is further supported by the lack of muscovite in the protolith of the mylonites, i.e., the Solís de Mataojo Granitic Complex. Locally, solution seams parallel to shear band planes can be recognized as well. They are made up of fine-grained aggregates of biotite and opaque minerals.

6.3. Results

6.3.1. U-Pb geochronology and Hf isotopes

Zircons from the sample AA-12 are typically prismatic to equant and show oscillatory zoning, sometimes with homogeneous bright cores (Fig. 6.2a). A concordant age of 596.0 ± 3.3 Ma was obtained considering 15 out of 24 spots (Fig. 6.3a, data points with low correlation coefficients rejected), which is interpreted as the crystallization age of the magmatic protolith. Titanites, in turn, show a slightly older concordant age of 602.7 ± 4.3 Ma (18 out of 19 points), which seems to reflect the crystallization age of the protolith as well (Fig. 6.4a).

In the case of AA-13, zircons present oscillatory zoning as well as homogeneous dark or bright cores (Fig. 6.2b). A 2048.3 ± 11.0 Ma concordia age is interpreted as the age of the crystallization of the magmatic protolith based on 23 out of 26 data points (Fig. 6.3b, discordant data

rejected). In addition, Hf model ages (T_{DM}) between 2.20 and 2.47 Ga as well as $\varepsilon_{Hf}(t1)$ between +2.26 and +7.23 were obtained for the zircons (Fig. 6.3c, Appendix 4). On the other hand, a concordant titanite age of 588.0 ± 7.1 Ma (7 out of 19 spots, discordant data or with high common ^{206}Pb content rejected) seems to represent the timing of the metamorphism associated with sinistral shearing (Fig. 6.4b), although microstructures indicates deformation temperatures slightly lower than the titanite closure temperature. Inheritance is recorded as well, as two titanite grains yield ^{207}Pb/^{206}Pb ages of ca. 2.05 Ga (Appendix 3).

Zircons from BUY-81-11 are prismatic and, in some cases, fragmented. Cores are dominantly homogeneous (Fig. 6.2c) and present a weighted mean ^{207}Pb/^{206}Pb age of 2025 ± 37 Ma (Fig. 6.3d, 6 spots, discordant data rejected). On the other hand, oscillatory zoning is found in the rims, which show a concordant age of 623.0 ± 5.1 Ma based on 6 out of 15 data points (Fig. 6.3e, data with high U or common ^{206}Pb content rejected).

Zircons from BUY-84-11 are prismatic and occasionally round, and exhibit homogeneous dark cores surrounded by overgrowths with oscillatory zoning (Fig. 6.2d). A concordia age of 2068.9 ± 4.2 Ma considering 6 out of 8 spots is interpreted as the crystallization age of the magmatic protolith, which is recorded in both cores and overgrowths (Fig. 6.3f, discordant data rejected).

In the Cerro Caperuza granite (sample UY-22-14), zircons are prismatic with oscillatory zoning and present a concordant age of 570.9 ± 11.0 Ma considering 5 out of 26 data points (Fig. 6.2e, 6.3g, highly discordant data or with high U or common ^{206}Pb content rejected). Some spots show slightly older concordant ages that may indicate reworking of magmatic zircons with ages between ca. 620-580 Ma (Fig. 6.3g).

Prismatic to slightly rounded zircons with cores that are either homogeneous or zoned were recognized for BUY-93-11. Homogeneous bright cores present a weighted mean ^{207}Pb/^{206}Pb age of 2115 ± 38 Ma (Fig. 6.3h, 7 out of 26 spots). 3 points measured in overgrowths with oscillatory zoning exhibit a concordant age of 589.1 ± 1.5 Ma (Fig. 6.2f, 6.3i, highly discordant data or with high U or common ^{206}Pb content rejected).
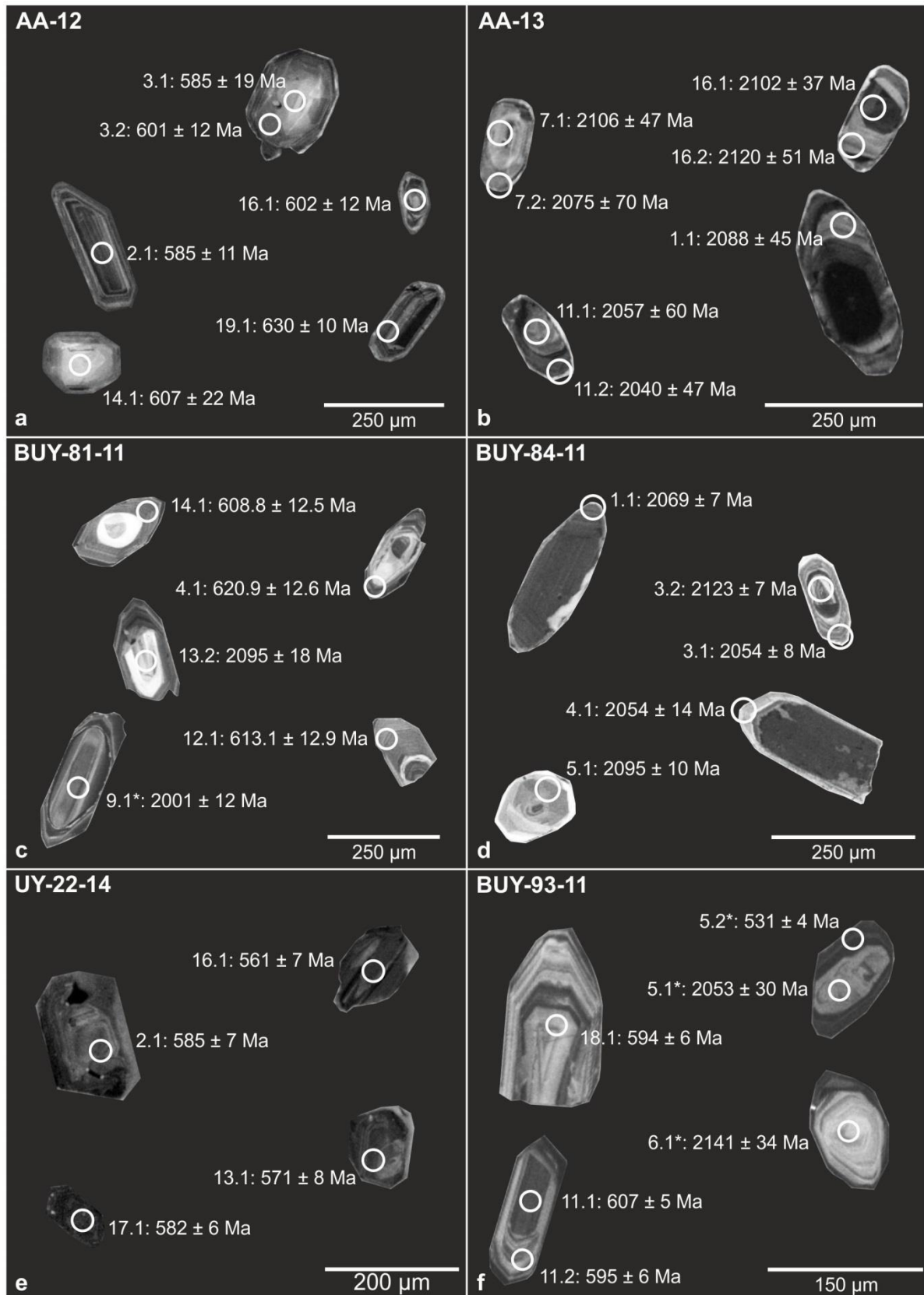
Fig. 6.2: Cathodoluminescence (CL) images of representative zircons. Individual U-Pb ages are shown. Asterisks indicates discordant ages.

Fig. 6.3: U-Pb zircon diagrams. Red ellipses indicate data used for age calculations, whereas dashed ellipses represent data that were not considered. Errors depicted at the 2σ level. ε$_{Hf}$ vs time data from the sample AA-13 is also shown.
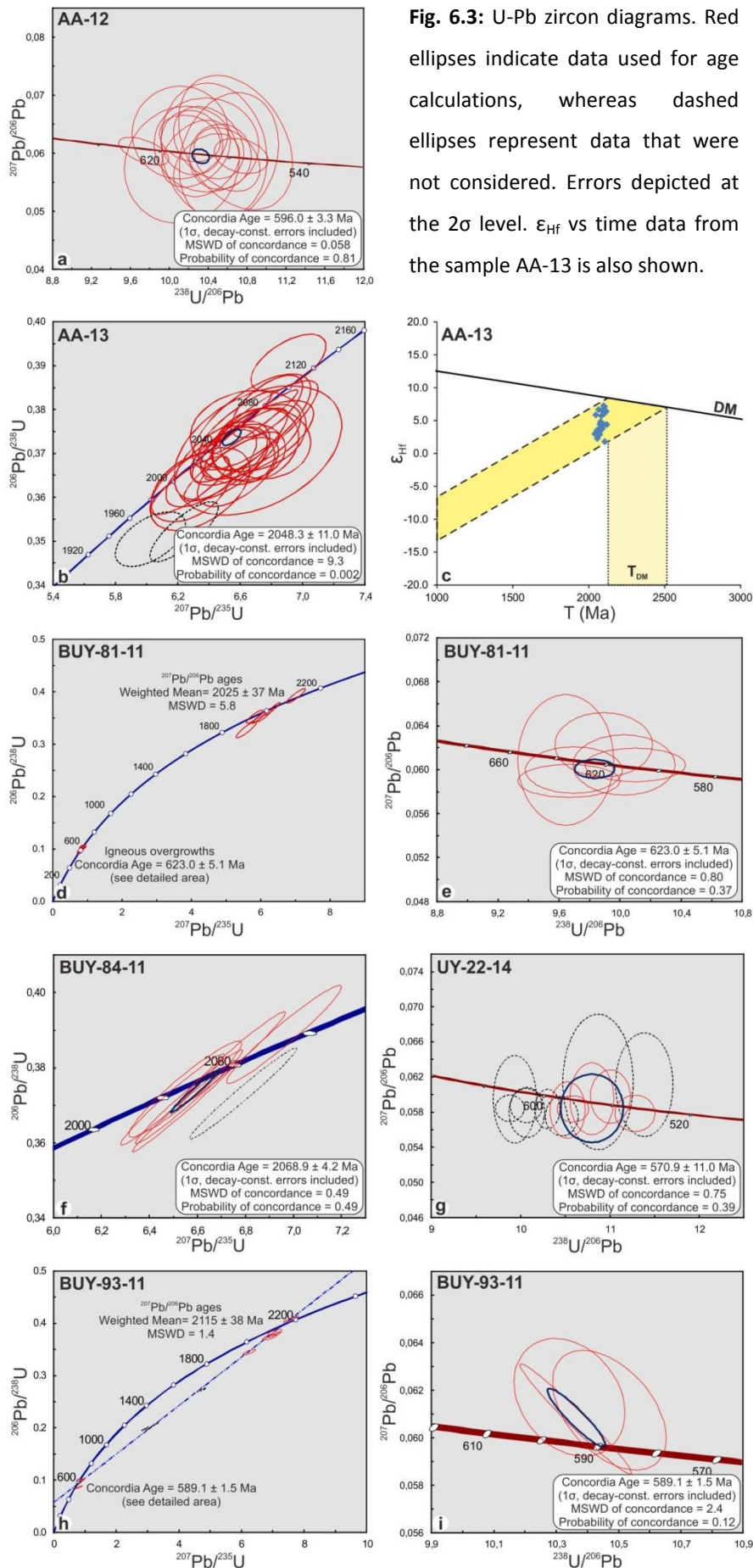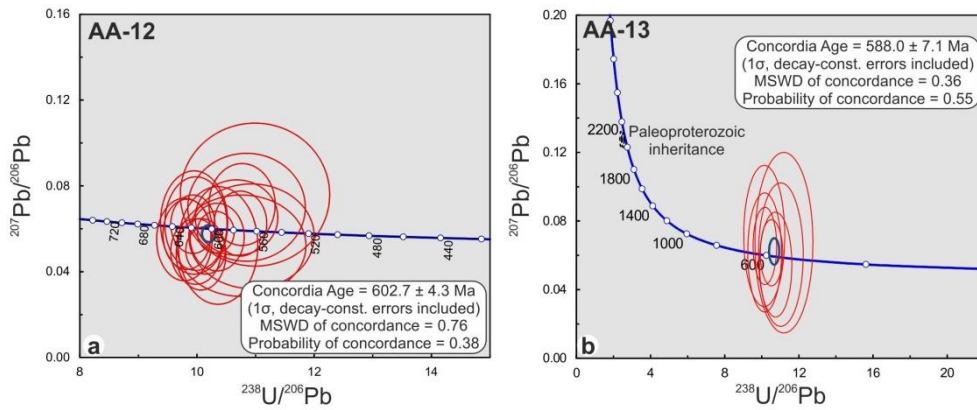
Fig. 6.4: U-Pb titanite diagrams. Red ellipses indicate data used for age calculations, whereas dashed ellipses represent data that were not considered. Errors depicted at the 2σ level.

6.3.2. $^{40}Ar/^{39}Ar$

A hornblende plateau age of 600.1 ± 3.4 Ma was obtained for the sample AA-12, whereas the sample BUY-81-11 presents a hornblende plateau age of 590.2 ± 2.6 Ma (Fig. 6.5a, 6.5b). On the other hand, the white mica concentrates yield plateau ages of 594.41 ± 0.98 Ma and 587.6 ± 1.5 Ma for the samples BUY-92-11 and BUY-94-11, respectively (Fig. 6.5c, 6.5d).
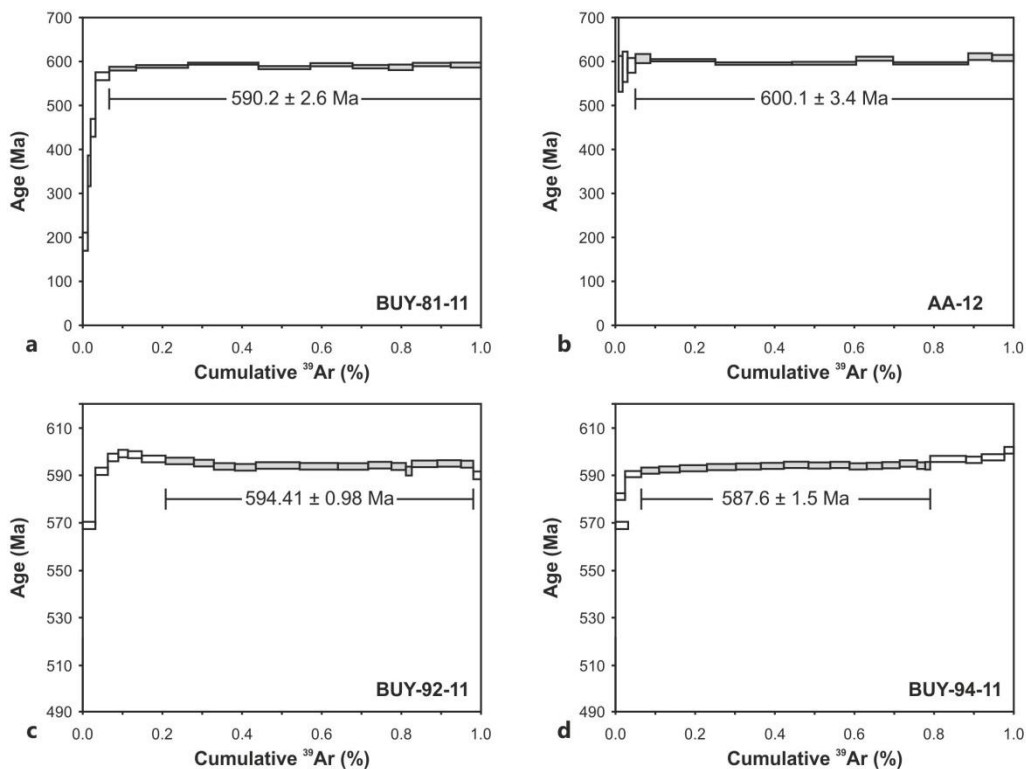
Fig. 6.5: Ar/Ar age spectrum from hornblende and muscovite samples. Plateau steps are colored in grey whereas rejected steps are indicated in white.

82

6.3.3. Rb-Sr

Two Rb-Sr isochrone ages were defined by muscovite and WR concentrates from the same muscovite samples that were analysed using the ^{40}Ar/^{39}Ar method. The sample BUY-92-11 shows an age of 566.1 ± 2.9 Ma, whereas the sample BUY-94-11 presents an age of 566.6 ± 2.9 Ma (Appendix 5).

6.4. Discussion

6.4.1. Protolith petrogenesis

U-Pb zircon data reveal two protoliths generated during the Paleo- and the Neoproterozoic. However, no significant textural differences are observed between both zircon groups. Zircons are prismatic and occasionally round with oscillatory zoning and Th/U > 0.1 (Fig. 6.2, Appendix 3), which is indicative of a magmatic origin (Hoskin and Schaltegger, 2003, and references therein). As deformation conditions along the Sarandí del Yí Shear Zone did not surpass amphibolite facies conditions (Chapter 5), U-Pb zircon ages are interpreted to represent the age of the magmatic protolith rather than a direct age constraint on the deformation along the shear zone.

Two concordant ages of 2048.3 ± 11.0 Ma (sample AA-13) and 2068.9 ± 4.2 Ma (sample BUY-84-11) as well as two ^{207}Pb/^{206}Pb weighted mean ages of 2025 ± 37 Ma (sample BUY-81-11) and 2115 ± 38 Ma (sample BUY-93-11) provide evidence of a late Rhyacian-early Orosirian magmatic event and are equivalent to ages of granitoids and gneisses of the basement of the Piedra Alta Terrane (Fig. 6.3; Hartmann et al., 2000a; Santos et al., 2003; Peel and Preciozzi, 2006). Hf isotopes from the zircons of the sample AA–13 yield a T_{DM} age range from 2.20 to 2.47 Ga as well as $\varepsilon_{Hf}(t_1)$ between +2.26 and +7.23 (Fig. 6.3c), which indicates contribution of Paleoproterozoic juvenile continental crust. Hf isotopes from the Cerro Colorado granite (eastern Piedra Alta Terrane) are identical (Fig. 3.6) and similar Sm-Nd model ages were obtained in different intrusions of the Piedra Alta Terrane as well (Peel and Preciozzi, 2006), thus supporting a crustal affinity of the mylonitic protolith with the Piedra Alta Terrane.

On the other hand, Neoproterozoic concordant ages of 596.0 ± 3.3 Ma (sample AA-12), 623.0 ± 5.1 Ma (sample BUY-81-11) and 589.1 ± 1.5 Ma (sample BUY-93-11) were obtained in three samples (Fig. 6.3). The zircons of AA-12 yield only Neoproterozoic ages, but BUY-81-11 and BUY-93-11 also show inheritance of Paleoproterozoic zircons (Fig. 6.3, Appendix 3). In addition, Neoproterozoic ages in BUY-81-11 zircons were only detected in overgrowths, whereas BUY-93-11 contains Neoproterozoic neoformed zircons as well (Fig. 6.2). Consequently, obtained Neoproterozoic ages may have resulted from both re-equilibration of inherited Paleoproterozoic crystals and neocrystallization in the presence of a melt (Bea et al., 2007; Geisler et al., 2007).

6.4.2. Tectonometamorphic evolution of the Sarandí del Yí Shear Zone

Despite previous works suggested a Mesoproterozoic age for the onset of the deformation (Bossi and Cingolani, 2009; Gaucher et al., 2011a), new results provide solid evidence of Neoproterozoic nucleation for the Sarandí del Yí Shear Zone (Fig. 6.6a). The only previous constraint for the dextral shearing was the bending of the 1.79 Ga old Florida doleritic dyke swarm, which provides a maximum age for this event. Results obtained for the sample AA-12 indicate dextral shearing up to 596 Ma. Similar zircon, titanite and hornblende ages together with hornblende microstructures point to emplacement and fast cooling of this intrusion below ca. 500°C during dextral shearing. Likewise, the oldest concordant age of 623.0 ± 5.1 Ma (sample BUY-81-11) represents a maximum age for magmatism related to deformation along the shear zone. This value is thus interpreted as syn- to early post-collisional magmatism related to the amalgamation of the Nico Pérez Terrane and the Río de la Plata Craton along the Sarandí del Yí Shear Zone. As this sample shows evidence of sinistral shearing at temperatures of 450-550°C, which are similar to the closure temperature for amphibole, the significantly younger ^{40}Ar/^{39}Ar plateau age of 590.2 ± 2.6 Ma from strongly deformed hornblende crystals may indicate reworking of these rocks and resetting of the K-Ar system at ca. 590 Ma. This is also supported by structural evidence indicating progressive strain localization towards the east (Chapter 5).

The onset of deformation along the Sarandí del Yí Shear Zone at 630-625 Ma constrains the age of the amalgamation of the Nico Pérez Terrane and the Río de la Plata Craton. These results support models from Oyhantçabal et al. (2011a) and Rapela et al. (2011) considering juxtaposition of both crustal blocks during the Neoproterozoic, previously constrained by the 584 ± 13 Ma age of the Solís de Mataojo Granitic Complex (Rapela et al., 2011). Contrasting cooling age patterns on both sides of the shear zone reinforce this interpretation (Fig. 6.6c; Oyhantçabal et al., 2011a).
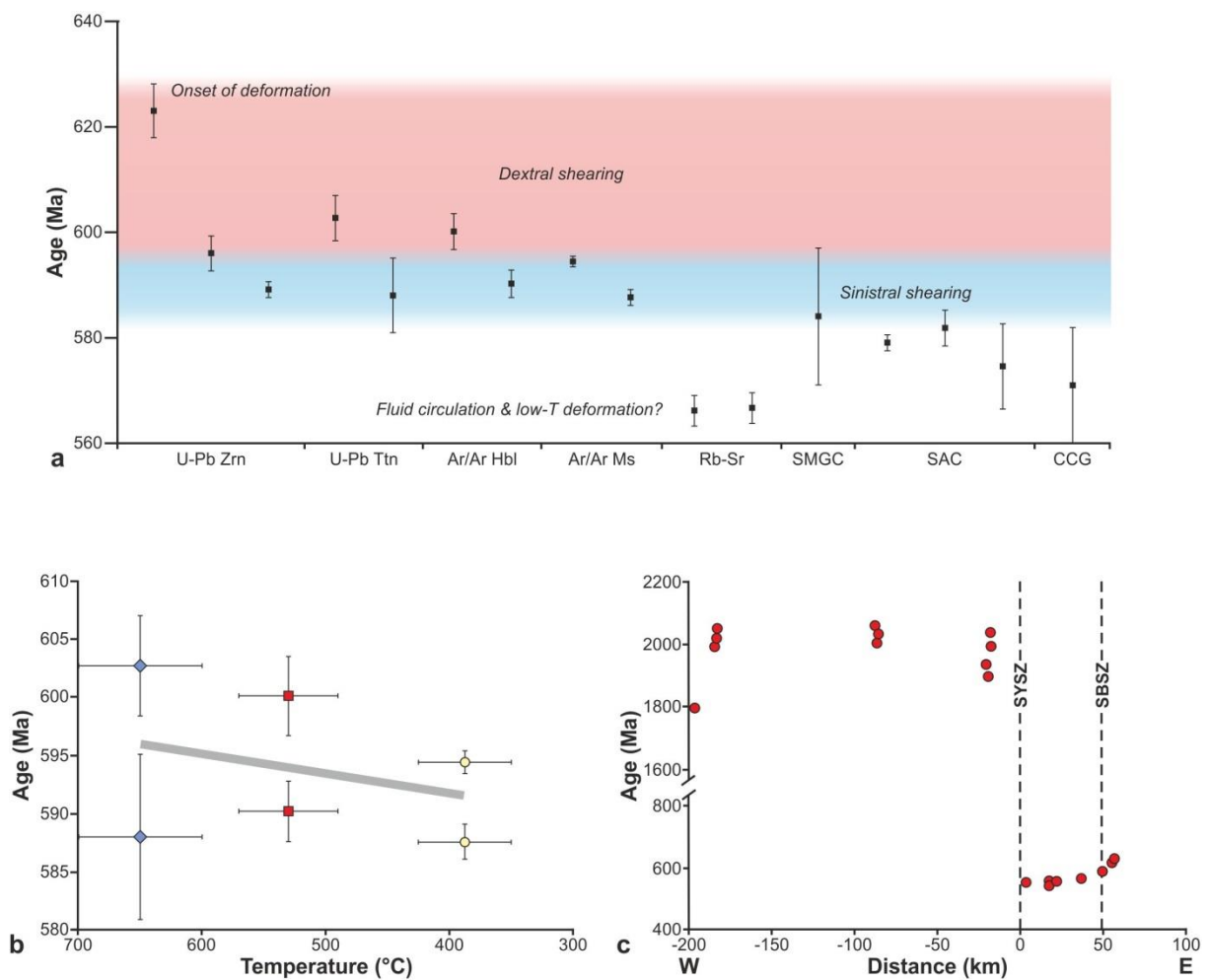
Fig. 6.6: a) Summary of geochronological data from the Sarandí del Yí Shear Zone. Ages of associated intrusions are also shown (SMGC: Solís de Mataojo Granitic Complex, Oyhantçabal et al., 2007; SAC: Sierra de las Ánimas Complex, Oyhantçabal et al., 2007; Rapalini et al., 2015; CCG: Cerro Caperuza granite, this work). The age of the dextral (red) and the sinistral shearing (blue) are indicated as well. b) t vs T plots based on titanite (blue diamonds), hornblende (red squares) and muscovite (yellow circles) data with average cooling path. Closure temperatures after references from Table 6.1. c) West-east K-Ar muscovite profile across the Piedra Alta Terrane, the Nico Pérez Terrane and the Dom Feliciano Belt (modified after Oyhantçabal et al., 2011). The position of the Sarandí del Yí Shear Zone (SYSZ) and the Sierra Ballena Shear Zone (SBSZ) are presented.

The subsequent sinistral movement was previously constrained by the age of the synkinematic Solís de Mataojo Granitic Complex (Fig. 5.4; Oyhantçabal et al., 2001, 2007). The U-Pb zircon concordant age of 589.1 ± 1.5 Ma and the titanite concordant age of 588.0 ± 7.1 Ma together with the ^{40}Ar/^{39}Ar hornblende plateau age of 590.2 ± 2.6 Ma of sinistrally-sheared mylonites and ^{40}Ar/^{39}Ar plateau ages of 594.41 ± 0.98 Ma and 587.6 ± 1.5 Ma of synkinematic muscovites constrain the sinistral shearing at ca. 594-584 Ma. As temperature conditions for the sinistral shearing are constrained at 450-550°C, which are above the closure temperature of the K-Ar system for muscovites, muscovite ages probably reflect cooling after synkinematic crystallization (Mulch and Cosca, 2004; Rolland et al., 2008).

Rb-Sr data are significantly younger than the respective ^{40}Ar/^{39}Ar muscovite ages. As the latter match other geochronological data as well as geological evidences (e.g., intrusion of the Cerro Caperuza granite postdating the ductile deformation along the shear zone), Rb-Sr data may not reflect true cooling stories (Jenkin, 1997). As indicated by Eberlei et al. (2015), deformation strongly affects the Rb-Sr geochronometer at <500°C. Likewise, Bozkurt et al. (2011) demonstrated that fluid-assisted deformation under cataclastic conditions may reopen this isotopic system. Local cataclastic reworking, pressure-solution and associated fluid circulation are recorded in these samples, which could account for reequilibration of the Rb-Sr system during low-temperature fluid-assisted deformation. However, ^{40}Ar/^{39}Ar muscovite ages seem to remain unaffected by these processes, which may suggest that Sr presents an unlikely more effective diffusivity than Ar under similar conditions. Alternatively, a more plausible explanation could be that the Rb-Sr system has remained closed for the muscovites, but was affected for the whole rock system, giving rise to whole rock-muscovite isochron ages that are younger than expected.

On the basis of titanite, hornblende and muscovite geochronological data, a cooling rate of ca. 60°C Ma^{-1} between ca. 597-592 Ma can be estimated for the Sarandí del Yí Shear Zone (Fig. 6.6b). This cooling rate may have resulted from fast exhumation during sinistral shearing. Vertical extrusion related to pure shear dominated deformation along the Sarandí del Yí Shear Zone could account for

this process (Chapter 5). Comparable cooling rates related to shearing and rapid exhumation were also reported from the Carthage-Colton Mylonite Zone of the Adirondack Mountains (Bonamici et al., 2014).

Nevertheless, the estimated cooling rates have to be considered carefully due to the complexity of the processes involved in the shearing. Particularly, the existence of several intrusions during deformation appears to be one of the most significant processes affecting isotopic systems, as the existence of magmatism reset the chronometers and true cooling paths cannot be calculated (Fig. 6.6a). In addition, strain localization during exhumation of the shear zone also induces local reworking of the mylonitic belt and consequent reset of the thermochronometers (Mulch et al., 2006). Comparison of titanite and hornblende data from the dextrally and sinistrally sheared domains show younger ages in the latter, supporting progressive strain localization towards the east inferred from structural data (Chapter 5). Consequently, recrystallization-related processes such as strain and fluids as well as magmatism play a major role in the closure of isotopic systems in mylonites, being temperature not the only significant variable, as outlined by Villa (1998).

The age of 570.9 ± 11 Ma for the Cerro Caperuza granite together with the age of the alkaline plutonic-volcanic Sierra de las Ánimas Complex (Fig. 5.4; 579 ± 1.5 Ma, Ar/Ar hornblende, Oyhantçabal et al., 2007; 581.8 ± 3.4 Ma, 574.5 ± 8.1 Ma, U-Pb SHRIMP zircon, Rapalini et al., 2015) provide a solid constraint for the end of the ductile deformation in the shear zone (Fig. 6.6a). Likewise, the Rb-Sr ages of the mylonites can be interpreted as the result of the reequilibration of the Rb-Sr isotopic system due to fluid circulation, probably associated with low temperature deformation that is recognizable in both mylonites and the Cerro Caperuza granite (Chapter 5). It can be thus inferred that cataclastic deformation in the easternmost shear zone started after 570 Ma. Moreover, the Arroyo de la Pedrera Formation is folded and affected by low-T shear zones and faults near the cataclasites of the Sarandí del Yí Shear Zone in the western Nico Pérez Terrane (Fig. 4.1; Montaña and Sprechmann, 1993; Oriolo et al., 2015). As this unit did not achieve metamorphic conditions higher than lower greenschist facies (Gaucher, 2000; Blanco et al., 2009; Sánchez Bettucci et al.,

2010) and may present a late Ediacaran-lower Cambrian age (Montaña and Sprechmann, 1993; Blanco et al., 2009; Gaucher et al., 2004, 2011b), deformation of these sequences may be related to late Ediacaran-Cambrian cataclastic deformation along the shear zone. Furthermore, Rapalini and Sánchez Bettucci (2008) interpreted a post-folding remagnetization event in the Arroyo de la Pedrera Formation as evidence for an early Cambrian event. Consequently, brittle deformation in the Sarandí del Yí Shear Zone can be characterized as a long-term process that took place between the late Ediacaran and the Cambrian.

The existence of collisional events between ca. 625-600 Ma in South America can be further traced to the north along the Transbrasiliano Lineament (Ganade de Araujo et al., 2014a, 2014b). This crustal-scale structure has been correlated with the easternmost Pampean Belt in the Sierras Pampeanas, mostly based on geophysical data (e.g., Rapela et al., 2007; Peri et al., 2015). Nevertheless, the collisional phase of the Pampean Belt was placed at the lower Cambrian (Rapela et al., 1998, 2007; Siegesmund et al., 2010), which is considerably younger than the collision recorded along the Transbrasiliano Lineament (Ganade de Araujo et al., 2014a, 2014b). The Sarandí del Yí Shear Zone, in contrast, shows both timing of deformation and kinematics, which are comparable with those recorded along the Transbrasiliano Lineament. Consequently, the amalgamation of the Gondwanic domains in the South American Platform (Brito Neves and Fuck, 2014) was completed at ca. 600 Ma and resulted from the accretion of African blocks to the eastern margin of the South American older nuclei, i.e., the Amazonas and Río de la Plata cratons, along crustal-scale shear zones.

6.5. Conclusions

Multithermochronometric and structural data from the mylonites combined with geochronological information from shear zone-related magmatism as well as cooling ages of the adjacent blocks were integrated to constrain the tectonometamorphic evolution of the Sarandí del Yí shear Zone. The onset of the deformation is related to the collision of the Río de la Plata and Nico Pérez Terrane at 630-625 Ma, giving rise to dextral shearing up to 596 Ma along the Sarandí del Yí

Shear Zone under upper to middle amphibolite conditions in a post-collisional setting. Subsequent sinistral shearing took place between 594-584 Ma under lower amphibolite to upper greenschist facies conditions, which was followed by emplacement of the Sierra de las Ánimas Complex and the Cerro Caperuza granite. Further deformation under brittle conditions was recorded after ca. 570 Ma.

Additionally, the obtained data reveal the complexity in assessing the age of deformation of long-lived shear zones. Strain partitioning and localization with time, magma emplacement and fluid circulation were identified as the main processes affecting the isotopic systems. Therefore, multiple geochronometers from the mylonitic belts and their adjacent blocks as well as detailed structural analysis have to be integrated in order to establish solid tectonothermal models of crustal-scale shear zones.

-CHAPTER 7-

Structure and geochronology of the Dom Feliciano Belt

7.1. Introduction

Harland (1971) defined transpression as a combination of compression and transcurrence that results from oblique plate convergence at crustal scale. This term was then extended by Sanderson and Marchini (1984), who considered transpression as deformation developed between two undeformed blocks resulting from both simple and pure shear, independently of the scale. Subsequent contributions presented deviations from these first models and demonstrated the 3D complexity of transpressional orogens (Fossen et al., 1994; Dewey et al., 1998; Fossen and Tikoff, 1998; Jones et al., 1997, 2004; Fernández and Díaz-Azpiroz, 2009; Fernández et al., 2013; Massey and Moecher, 2013), especially when related to strain partitioning (Lister and Williams, 1983; Tikoff and Teyssier, 1994; Jones and Tanner, 1995; Teyssier et al., 1995). Although strain partitioning refers to heterogeneous spatial distribution of deformation, changes with time are also frequent (Lister and Williams, 1983). Among others, shear zone nucleation due to strain localization is one of the most common consequences of temporal strain variations (e.g., Hobbs et al., 1990; Jessell and Lister, 1991; Platt and Behr, 2011).

Although the regional structure of the Pan-African mobile belts was thoroughly investigated (Hälbich and Alchin, 1995; Goscombe et al., 2003, 2005; Konopásek et al., 2005; Goscombe and Gray, 2008; Ulrich et al., 2011; Lehmann et al., 2016), contributions regarding structural aspects of the Dom Feliciano Belt focused mostly on the Major Gercino-Sierra Ballena shear zone system (Fernandes et al., 1992; Fernandes and Koester, 1999; Oyhantçabal et al., 2009b, 2011b; Passarelli et al., 2010, 2011). Likewise, constraints on the timing of deformation and metamorphism are scarce (Oyhantçabal et al., 2009a, 2009b, 2011b), thus being the tectonothermal evolution of the belt still elusive.

7.2. Structural architecture of the Dom Feliciano Belt

7.2.1. Introduction

The Dom Feliciano Belt in Uruguay can be divided into two domains, which are separated by the Sierra Ballena Shear Zone. The western domain is dominated by metavolcano-sedimentary units, whereas the eastern domain is mostly made up of granitoids (Fig. 7.1). In order to assess the macro- and mesostructural aspects of both domains, two key areas were studied in detail (Fig. 7.2, 7.3).
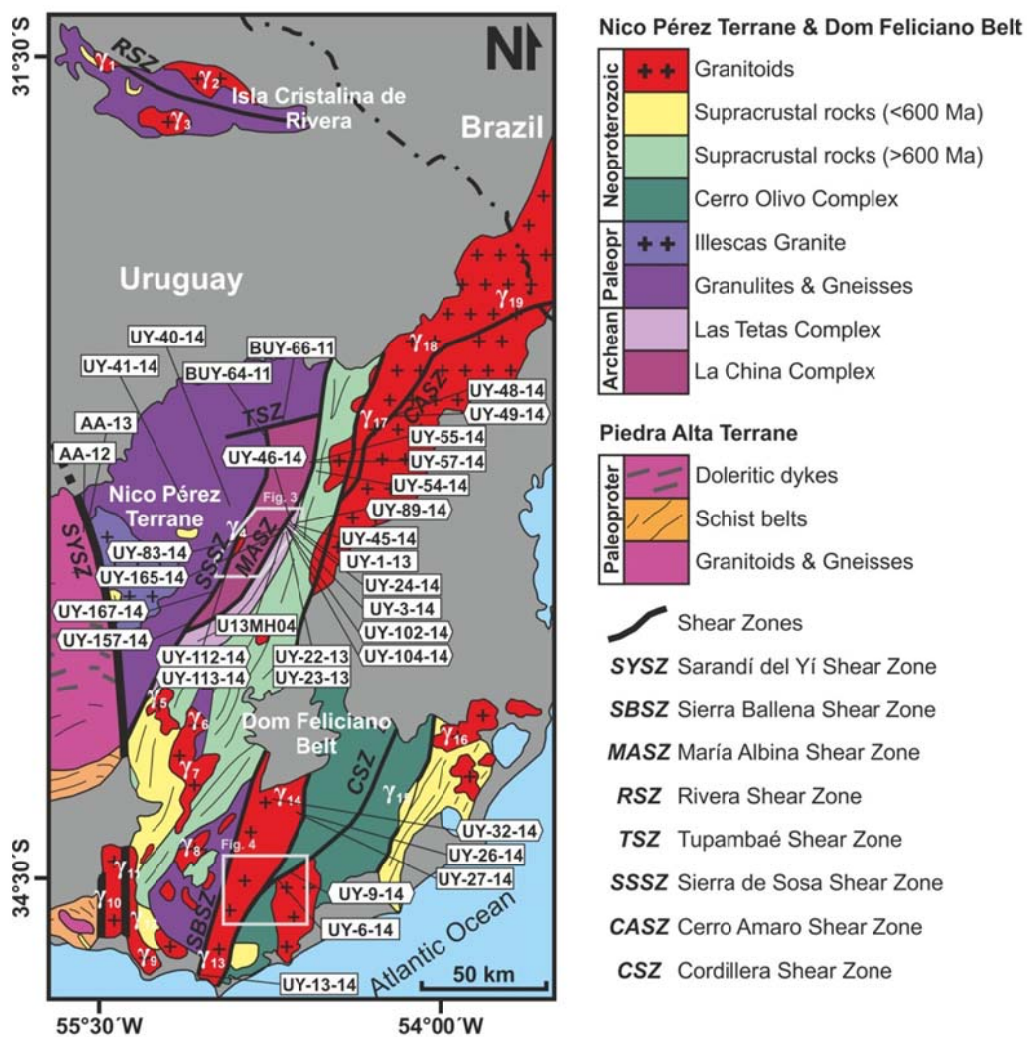
Fig. 7.1: Geological map of the Precambrian of Uruguay (modified after Oyhantçabal et al., 2011a and references therein). Detailed areas of Fig. 7.2 and 7.3 are shown. Geochronological and quartz CPO samples are indicated with rectangles and prisms, respectively. Magmatic units are indicated as well (γ_1: Sobresaliente granite, γ_2: Amarillo granite, γ_3: Las Flores granite, γ_4: Zapicán granodiorite, γ_5: Lavaderos granite, γ_6: Arroyo Mangacha granite, γ_7: Puntas del Santa Lucía monzogranite, γ_8: Puntas del Mataojo granodiorite, γ_9: Pan de Azucar intrusion, γ_{10}: Solís de Mataojo Granitic Complex, γ_{11}: Sierras de las Ánimas Complex, γ_{12}: Las Ventanas Formation, γ_{13}: Maldonado granite, γ_{14}: Valdivia granite, γ_{15}: Cerro Aguirre dacite, γ_{16}: Santa Teresa granite, γ_{17}: Cerro Amaro granite, γ_{18}: Arroyo Malo granite, γ_{19}: Sarandí del Yaguarón granite).

91
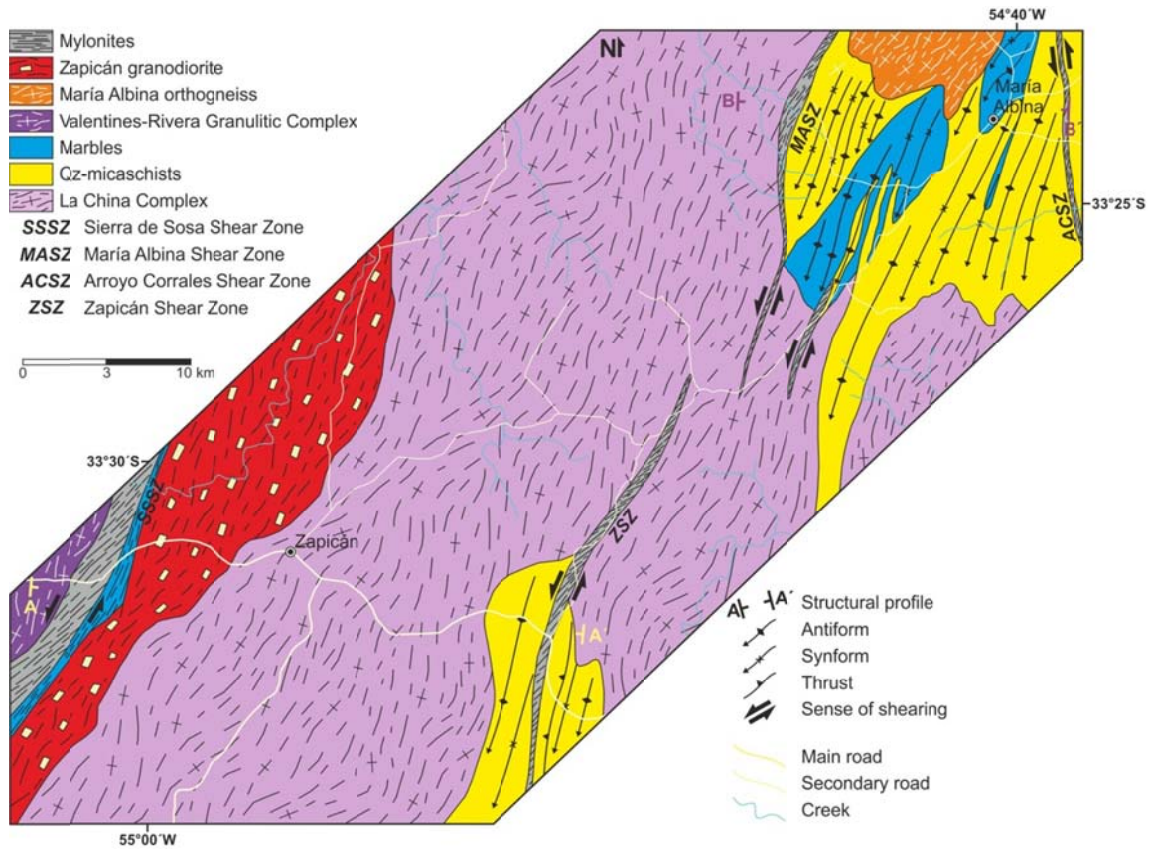
Fig. 7.2: Detailed geological map of the western Dom Feliciano Belt (modified after Preciozzi, 1987; Hartmann et al., 2001). Locations of structural profiles of figures 7.4 (A-A´) and 7.5 (B-B´) are shown as well.

Fig. 7.3: Detailed geological map of the eastern Dom Feliciano Belt (modified after Spoturno et al., 2012).
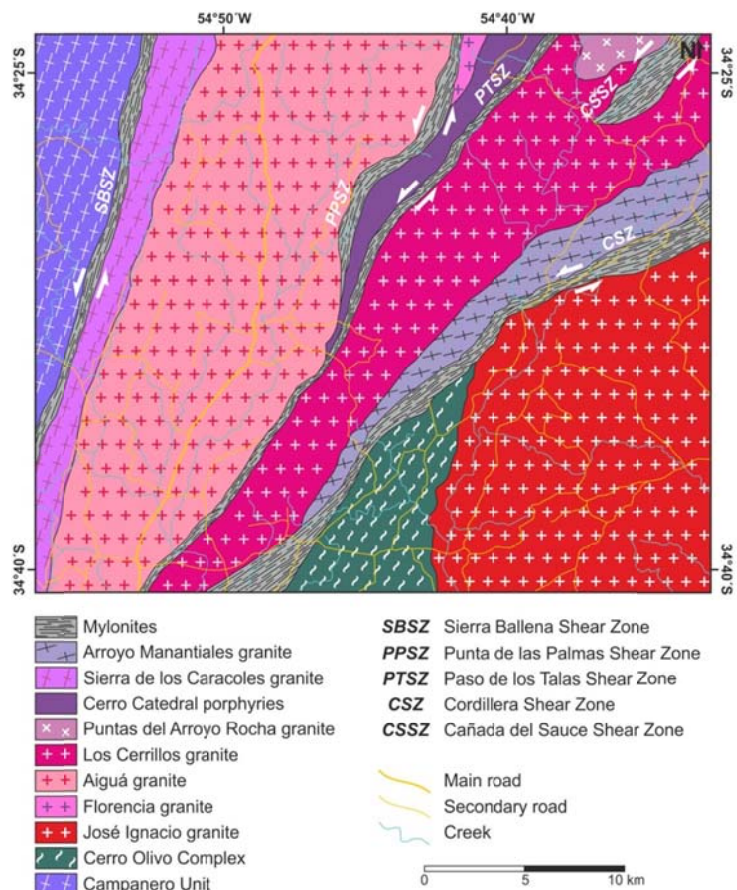
7.2.2. Western domain

The northwestern area of the western domain is constituted by the Paleoproterozoic Valentines-Rivera Granulitic Complex, which represents the basement of the Nico Pérez Terrane and is affected by Neoproterozoic magmatism and shear zones (Fig. 7.1; Oyhantçabal et al., 2011a, 2012). Minor NNW-striking protomylonitic belts were recognized in the western Nico Pérez Terrane and are related to the Sarandí del Yí Shear Zone (Oriolo et al., 2015). Likewise, oblique shear zones are also recognizable. The dextral Tupambaé Shear Zone affects the Valentines-Rivera Granulitic Complex in the northern Nico Pérez Terrane, whereas the sinistral Rivera Shear Zone cross-cuts the same unit in the Isla Cristalina de Rivera (Fig. 7.1).

The Valentines-Rivera Granulitic Complex is bounded to the southeast by the Sierra de Sosa Shear Zone, which separates it from the La China Complex. The former comprises felsic and subordinated intermediate to mafic granulites and orthogneisses, whereas the latter is mostly made up of amphibolite facies felsic orthogneisses with mafic to ultramafic intercalations (Hartmann et al., 2001; Oyhantçabal et al., 2011a, 2012; Spoturno et al., 2012). The Sierra de Sosa Shear Zone presents a mean mylonitic foliation of 219°/70°W and a mean stretching lineation of 225°/15° (Fig. 7.4). The gneisses of the Valentines-Rivera Granulitic Complex show a dominant subvertical NE-striking foliation towards the shear zone, which may indicate Neoproterozoic reworking due to shearing. Likewise, the marbles located to the east show a foliation with a mean orientation of 207°/76°W, whereas the Zapicán granodiorite present a dominant NE-striking subvertical magmatic foliation defined by the shape preferred orientation of feldspars (Fig. 7.4). Structural data indicate that the deformation of the marbles and the emplacement of the Zapicán granodiorite took place during the evolution of the Dom Feliciano Belt, which is further supported by geochronological data of the intrusion (Chapter 3; Oriolo et al., 2016a). In contrast, felsic orthogneisses and associated mafic rocks of the Archean La China Complex present a higher complexity. High-T and migmatic foliations are frequent in the orthogneisses and show no clear relationship with the structure of the adjacent units (Fig. Fig. 7.4, 7.5, 7.6a), being thus probably related to the pre-Brasiliano evolution of these rocks.

Mafic rocks are frequently emplaced parallel to the foliation of the felsic orthogneisses but show in many cases equigranular textures (Fig. 7.6b). Further to the east, scarce outcrops of folded quartz-micaschists point to a dominant vergence to the SE and are cross-cut by the sinistral Zapicán Shear Zone, which exhibits a mean mylonitic foliation of 193°/19°W and a mean lineation of 211°/09° (Fig. 7.4). Thrusts are recognizable within the quartz-micaschists and also support vergence to the SE (Fig. 7.6c).
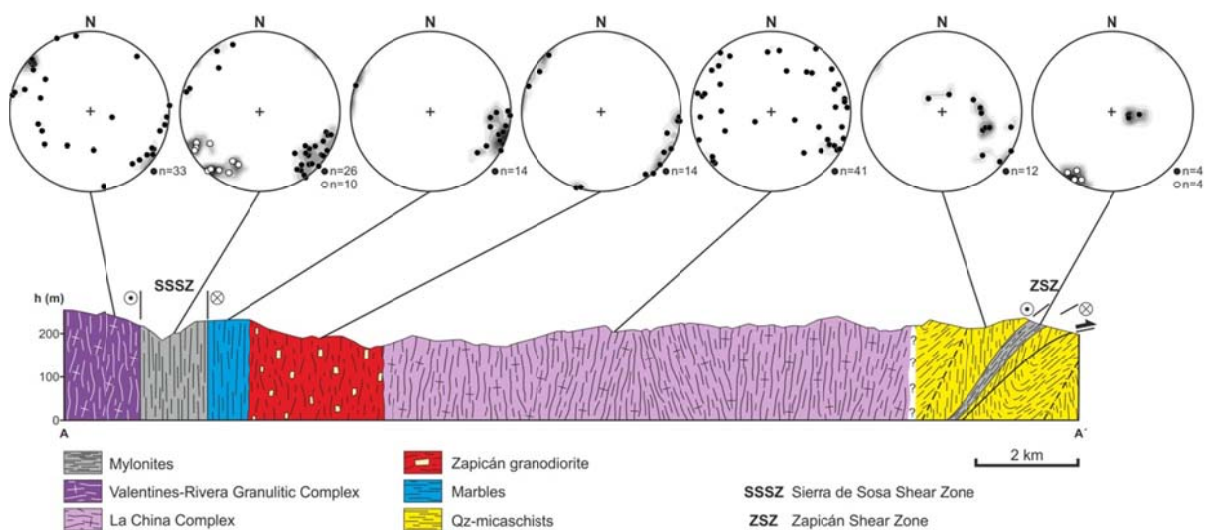
Fig. 7.4: Structural profile A-A´. Lower hemisphere equal area projection of foliations (black dots) and lineations (white dots). Diagrams were obtained using Stereonet 8 (Allmendinger et al., 2012).

On the other hand, the La China Complex is separated from the Las Tetas Complex by the María Albina Shear Zone (Fig. 7.5). However, orthogneisses are occasionally found to the east of the shear zone (e.g., María Albina orthogneiss), whereas the Las Tetas Complex is mostly made up in this area by folded quartz-micaschists and marbles, which present a mean stretching lineation of 194°/18° and 194°/17°, respectively (Fig. 7.5, 7.7a). Folds display a typically inclined to overturned similar geometry and, despite being dominantly close, tight to isoclinal folds are frequent in the marbles. Cleavage is oblique to fold axes and fold axial planes and transects clockwise the folds. Fold axes are subparallel to stretching lineations excepting in some marbles, which exhibit slightly curvilinear hinge lines. NW-vergence is dominant, although SE-vergence can be recognized towards

the ESE (Fig. 7.5, 7.7b). Minor subvertical ENE-striking dextral shear zones cross-cut the metasediments (Fig. 7.7c).
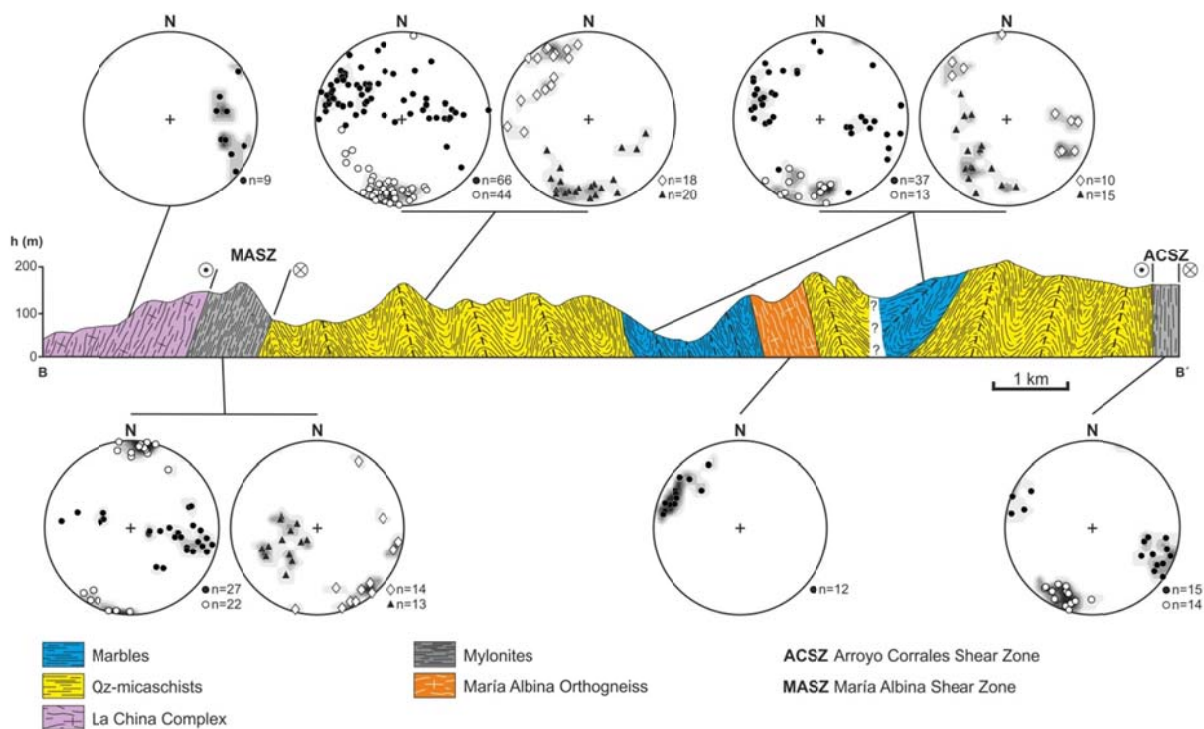
Fig. 7.5: Structural profile B-B´. Lower hemisphere equal area projection of foliations (black dots), lineations (white dots), fold axes (black triangles) and fold axial planes (white diamonds). Diagrams were obtained using Stereonet 8 (Allmendinger et al., 2012).

The María Albina Shear Zone shows a mean mylonitic foliation of 192°/48°E and a mean stretching lineation of 017°/06° (Fig. 7.5). Likewise, mylonitic folds present a mean axis of 244°/56° and a mean axial plane of 223°/76°W (Fig. 7.5, 7.7d). Sinistral shearing can be recognized on the basis of shear bands and feldspar mantle porphyroclasts. The western part of the mylonitic belt is cataclastically overprinted.

To the east of the María Albina Shear Zone, a second sinistral mylonitic shear zone can be recognized, namely the Arroyo Corrales Shear Zone, which presents a mean mylonitic foliation of 199°/80°E and a mean stretching lineation of 203°/14° (Fig. 7.5). Likewise, discontinuous outcrops of mylonites with similar orientations of fabric elements can be identified further to the southwest, indicating that the María Albina, Arroyo Corrales and Zapicán shear zones comprise a complex system of anastomosing shear zones that cross-cut the metasediments.
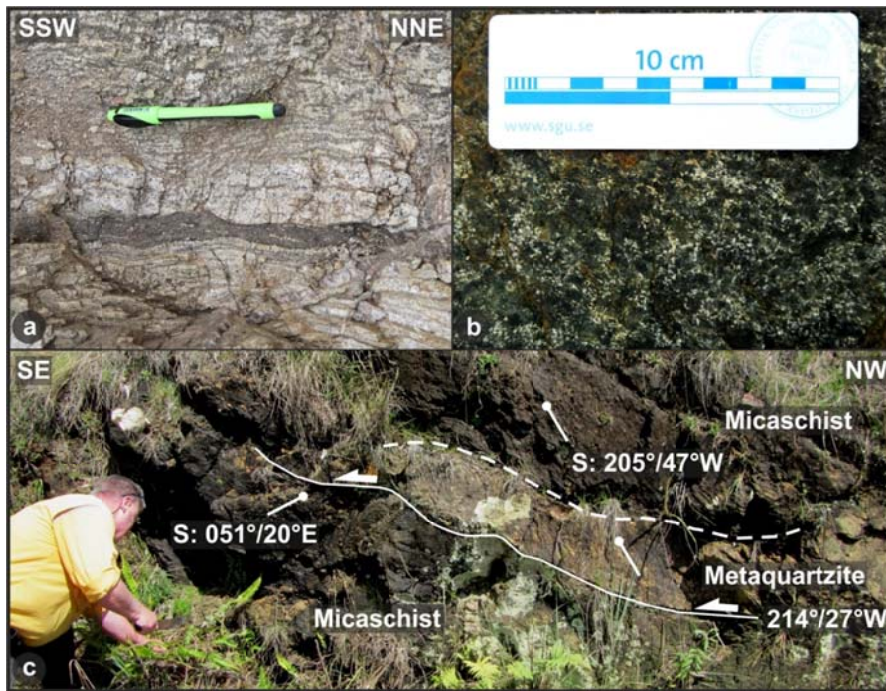
Fig. 7.6: Field photographs along the structural profile of Figure 7.4. a) Migmatic foliation in orthogneisses of the La China Complex. b) Equigranular texture in mafic rocks of the La China Complex. c) Minor SE-vergent thrust within metasediments.

Fig. 7.7: Field photographs along the structural profile of Figure 7.5. a) Lineation in micaschist of the Las Tetas Complex with transecting cleavage. b) Folded quartz-micaschists. Fold axial plane cleavage (FAPC) is indicated. c) ENE-striking dextral shear zone cross-cutting marbles of the Las Tetas Complex. d) Folded mylonitic foliation of the María Albina Shear Zone. Axial plane is indicated (AP).
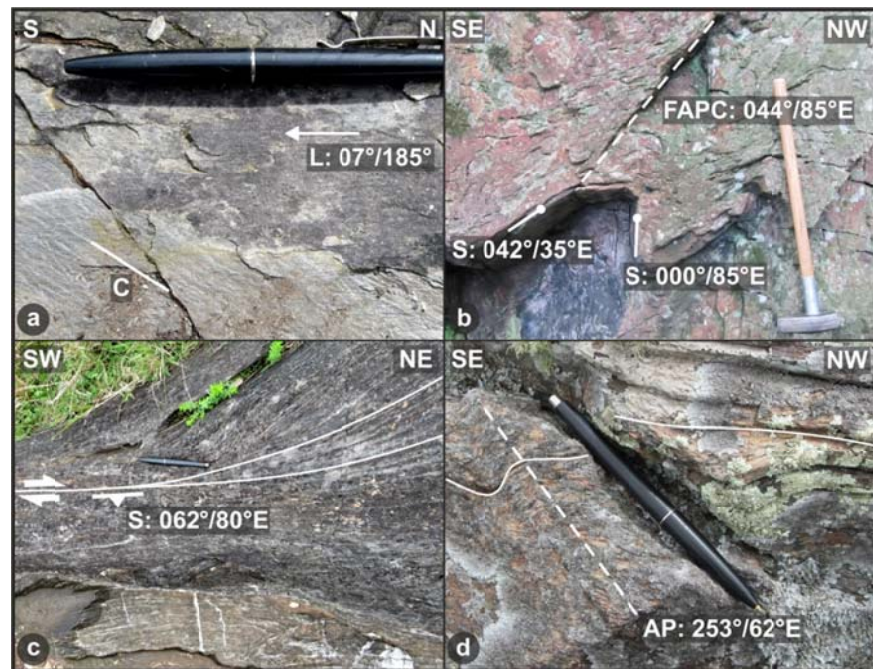
7.2.3. Eastern domain

The area located to the east of the Sierra Ballena Shear Zone is fundamentally made up of Neoproterozoic granitoids and subordinated subvolcanic rocks (Fig. 7.1, 7.3; Spoturno et al., 2012). These granitoids present either equigranular textures or magmatic to high-T solid-state foliations.

Solid-state foliations are subvertical and strike NE (Fig. 7.8a), and are particularly frequent close to shear zones.

Several sinistral shear zones are also distinguishable. The Cordillera Shear Zone is the most outstanding one and reworks the northern margin of the José Ignacio granite, separating this intrusion from the Los Cerrillos granite, and exhibits a mean mylonitic foliation of 220°/71°E and a mean stretching lineation of 217°/19° (Fig. 7.8b). However, a relictic lineation that predates the latter is occasionally present and plunges moderately to the WNW. Scarce fold axes plunge moderate to steeply towards the WSW (Fig. 7.8b). Similar structural features can be recognized in the Puntas de las Palmas, Paso de los Talas and Cañada del Sauce shear zones, which constitute NE- to NNE-trending shear zones that separate different magmatic bodies as well (Fig. 7.3; Spoturno et al., 2012). Subvolcanic synkinematic dykes (Cerro Catedral porphyries) are emplaced between the Puntas de las Palmas and Paso de los Talas shear zones.

Further to the north, the Cerro Amaro Shear Zone cross-cuts the Aiguá Batholith (Fig. 7.1). It shows a mean mylonitic foliation of 215°/70°W and a mean stretching lineation of 037°/04°.
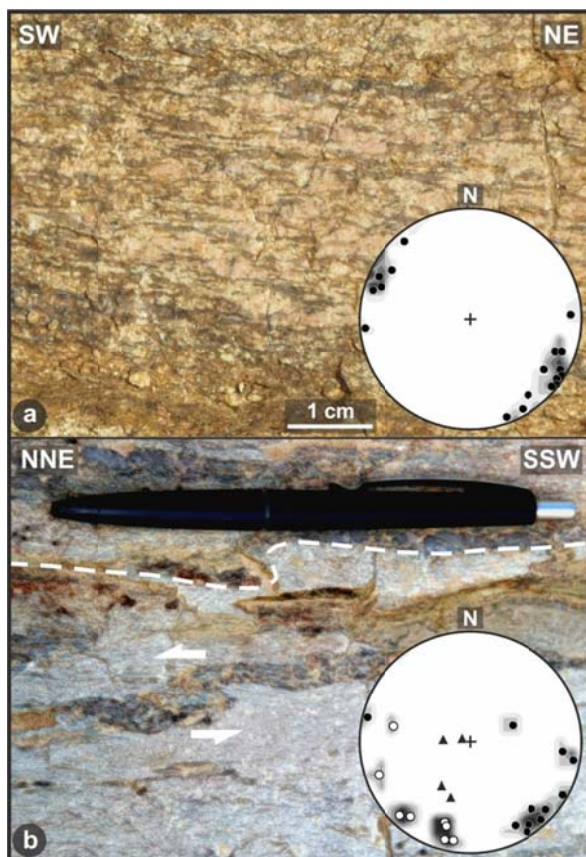
Fig. 7.8: Field photographs of the eastern Dom Feliciano Belt. a) Solid-state foliation in granitoids. Lower hemisphere equal area projection of foliations (black dots, n=18). b) Folded mylonitic foliation in the Cordillera Shear Zone. Lower hemisphere equal area projection of mylonitic foliations (black dots, n=11), lineations (white dots, n=8) and fold axes (black triangles, n=4).

7.3. Microstructures

7.3.1. Western domain

7.3.1.1. Tupambaé Shear Zone

The Tupambaé Shear Zone is made up of granitic mylonites. Oblique foliation in quartz and σ-type feldspar mantled porphyroclasts with tensional microfractures indicate a dextral sense of shear (Fig. 7.9a).

Scarce sutured coarse-grained crystals are present, although quartz typically constitutes polycrystalline aggregates of homogeneous fine-grained elongated crystals (Fig. 7.9a). These aggregates locally develop an oblique foliation. Feldspar porphyroclasts present microfracturing and cataclasis as well as recrystallization only localized in tails. Flame perthites are common in K-feldspar and bent twins are sometimes present in plagioclase.

A secondary paragenesis of fine-grained biotite + epidote + sericite + opaque minerals is observable within local cataclastic bands that rework the mylonites, particularly in areas with oblique foliation of quartz. These bands present Y and P shears, which support dextral shearing also under brittle conditions (Fig. 7.9a).

7.3.1.2. Sierra de Sosa Shear Zone

The Sierra de Sosa Shear Zone is made up of granitic and scarce quartz mylonites. S-C´ shear bands as well as δ- and σ-type feldspar mantled porphyroclasts reveal a sinistral sense of shear (Fig. 7.9b).

Microstructures in the Sierra de Sosa Shear Zone are highly variable. Sutured quartz crystals are recognizable, but aggregates of fine- to medium-grained elongated crystals are more frequent. In some samples, large elongated relictic crystals with deformation lamellae, undulose extinction and subgrain formation are observable (Fig. 7.9c). In these cases, recrystallization is restricted to bulges along grain boundaries. Foam structures are present as well and point to subsequent static recrystallization. Feldspar porphyroclasts show recrystallized tails, boudinage and microfracturing,

giving rise in some cases to bookshelf or anti-bookshelf structures (Fig. 7.9b). Flame perthites and assymetric myrmekites are ocasionally recognizable in K-feldspar, whereas secondary twinning and bent twins in plagioclase are frequent.

Likewise, localized deformation bands with significant grain size reduction of quartz and feldspars and associated fine-grained aggregates of sericite + biotite + opaque minerals ± epidote ± chlorite can be observed. These evidences account for pressure solution and cataclasis postdating ductile deformation.
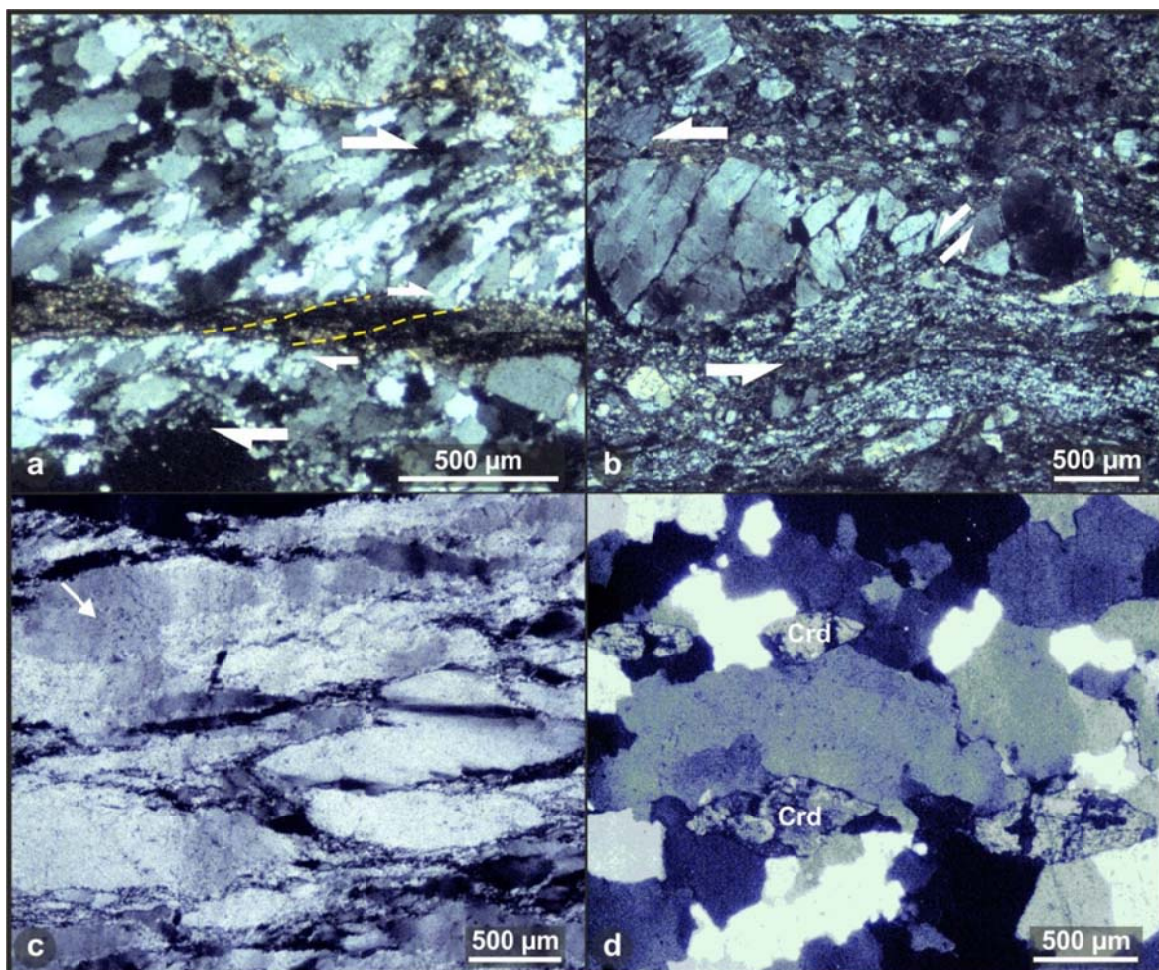
Fig. 7.9: Photomicrographs of microstructures from mylonites of the western Dom Feliciano Belt. a) Oblique foliation in quartz indicating dextral shearing in the Tupambaé Shear Zone. Dextral P shears (yellow lines) within low-grade localized bands constituted by fine-grained biotite + epidote + sericite + opaque minerals. b) Sinistral σ-type K-feldspar mantled porphyroclast in mylonites of the Sierra de Sosa Shear Zone. Synthetic microshear zones are also observed. c) Elongated relictic crystals with deformation lamellae and undulose extinction (arrow). Recrystallization is localized along grain boundaries indicating bulging recrystallization for the Sierra de Sosa Shear Zone. d) Microfracturing and boudinage of cordierite parallel to the stretching lineation direction in the María Albina Shear Zone.

7.3.1.3. María Albina and associated shear zones

The metasediments of the Las Tetas Complex dominantly comprise the protolith of the María Albina and associated mylonitic belts, although detrital zircon data seem to indicate that the Arroyo Corrales Shear Zone affects metasediments of the Lavalleja Group (Oyhantçabal et al., submitted). S-C´ shear bands point to sinistral shearing.

Quartz typically develops sutured grain boundaries, although local subgrain rotation and peripherial bulging are also observable, particularly in the Arroyo Corrales Shear Zone. However, static recrystallization is frequent in quartz, as indicated by foam structures. Muscovite and fuchsite typically develop fish minerals. Cordierite is occasionally present and shows boudinage as well as microfractures perpendicular to the stretching lineation direction (Fig. 7.9d).

The western margin of María Albina Shear Zone is overprinted by cataclastic deformation that also affects the orthogneisses located to the west. Cataclasites constitute minor belts, which are oriented parallel to the mylonitic foliation and are made up of epidote + chlorite + sericite + opaque minerals + quartz.

On the other hand, the María Albina orthogneiss is located to the east of the María Albina Shear Zone (Fig. 7.2) and is constituted by quartz, K-feldspar, plagioclase and muscovite. Quartz presents foam textures, whereas feldspars show mostly microfracturing. Muscovite, in turn, is oriented parallel to the foliation.

7.3.2. Eastern domain

7.3.2.1. Cordillera Shear Zone

The protolith of the Cordillera Shear Zone are granitoids and, to a minor extent, metaquartzites and quartz-micaschists. S-C´ shear bands, σ-type feldspar mantled porphyroclasts and mica fish indicate a dominant sinistral sense of shear, although dextral shear is locally recorded in ENE-striking restraining bends.

Quartz develops polycrystalline aggregates of homogeneous fine-grained elongated crystals. Nevertheless, flattened relictic coarser-grained crystals are frequently preserved, which exhibit subgrain development as well as undulose extinction (Fig. 7.10a). Feldspar porphyroclasts present microfracturing, which is frequently related to boudinage or bookshelf and anti-bookshelf structures. Recrystallization is scarce and restricted to tails. Deformation twins are frequent in plagioclase. Muscovite and biotite are locally present and develop fish structures.

Locally, evidences of pressure solution and cataclasis are observable and overprint the mylonitic features. In some cases, cataclasites are also associated with phyllonites and ultramylonites. The mineral association is typically made up of quartz + sericite + biotite ± epidote ± opaque minerals.

7.3.2.2. Punta de las Palmas Shear Zone

The Punta de las Palmas Shear Zone is made up of granitic mylonites. S-C´shear bands and σ-type feldspar mantled porphyroclasts indicate a sinistral sense of shear.

Although scarce relictic crystals are observable, quartz dominantly develops polycrystalline aggregates of homogeneous fine-grained elongated crystals. However, foam structures are frequent, indicating subsequent static recrystallization. Feldspar porphyroclasts internally present microfracturing and cataclasis, whereas recrystallization is only localized in tails. Bent twins are present in plagioclase (Fig. 7.10b). Boudinage parallel to the direction of the stretching lineation is recognizable in titanites as well as feldspars (Fig. 7.10c).

7.3.2.3. Cerro Amaro Shear Zone

The granitoids of the Aiguá Batholith constitute the protolith of the Cerro Amaro Shear Zone. A sinistral sense of shear can be inferred from S-C´ shear bands and σ-type feldspar mantled porphyroclasts (Fig. 7.10d).

Quartz develops sutured crystals, although recrystallized polycrystalline aggregates of homogeneous fine-grained crystals are locally recognisable as well. Feldspar presents microfracturing, which is sometimes related to bookshelf or anti-bookshelf structures. Recrystallization is restricted to tails (Fig. 7.10d). Deformation twins are frequent in plagioclase, whereas flame perthites are observable in K-feldspar. Muscovite develops mica fish structures with frequent kink bands, microfolding and boudinage.
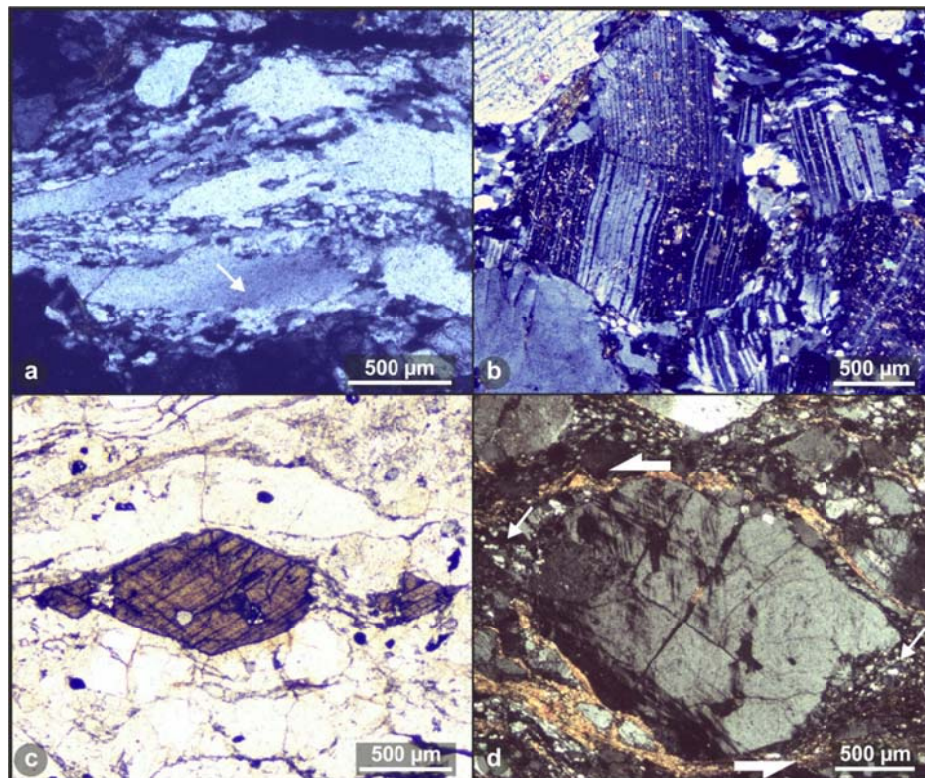
Fig. 7.10: Photomicrographs of microstructures from mylonites of the eastern Dom Feliciano Belt. a) Recrystallized elongated fine-grained and relictic coarse-grained (arrow) quartz crystals in the Cordillera Shear Zone. b) Bent twins and microcataclasis in plagioclase of mylonites of the Puntas de las Palmas Shear Zone. c) Boudinage parallel to the stretching lineation direction in titanites of the Puntas de las Palmas Shear Zone. d) Sinistral σ-type K-feldspar mantled porphyroclast in the Cerro Amaro Shear Zone.

7.4. Quartz CPO patterns

Four samples were obtained from the Sierra de Sosa Shear Zone (Fig. 7.11). Sample UY-112-14 presents asymmetrical single girdles with quartz [c]-axes showing maxima slightly oblique to the Z direction and [a]-axes perpendicular to them. This accounts for dominant basal <a> slip, though a minor contribution of rhomb <a> slip is also observable. UY-113-14, in turns, shows symmetrical

crossed girdles of [c]-axes with two maxima in the YZ plane and [a]-axes developing a slightly defined maximum around X. Rhomb and basal <a> are interpreted to be the main slip systems. In contrast, sample UY-157-14 presents an almost symmetrical single girdle with a well–defined maximum parallel to the Y direction. Quartz [a]-axes are distributed perpendicular to Y and exhibit a maximum subparallel to X. In this case, prism <a> slip seems to be the dominant system, though minor rhomb <a> slip can be also inferred. A similar result was obtained for the sample UY-167-14, although the single girdle for this sample is clearly asymmetrical.

Likewise, samples were collected from the María Albina Shear Zone (Fig. 7.11). Sample UY-83-14 shows asymmetrical crossed girdles of quartz [c]-axes with maxima slightly oblique to the Z direction and [a]-axes perpendicular to them. Basal and minor rhomb <a> slip are thus interpreted as the main slip systems. Samples UY-102-14 presents dominant asymmetrical type I crossed girdles of quartz [c]-axes (Lister, 1977), whereas UY-61-14, UY-104-14 and UY-165-14 show asymmetrical single girdles. In all cases, well-defined maxima close to the Y direction are observed, which are accompanied by girdle distributions of the [a]-axes perpendicular to Y. Prism <a> slip is thus interpreted as the main slip system, although rhomb and basal <a> slip were also active, particularly in the case of UY-104-14.

Sample UY-46-14 from the María Albina orthogneiss shows clearly asymmetrical crossed girdles of quartz [c]-axes with maxima oblique to the Z direction and [a]-axes perpendicular to them. Hence, basal <a> slip is interpreted as the dominant slip system.

Samples UY-89-14-1 and UY-89-14-2 from the Arroyo Corrales Shear Zone present asymmetrical crossed girdles (Fig. 7.11). Quartz [c]-axes maxima are slightly oblique to the Z direction, whereas [a]-axes maxima are dominantly subparallel to X. Consequently, quartz CPO data point to basal and minor rhomb <a> slip.

In the case of shear zones of the eastern domain, three samples were obtained (Fig. 7.11). Sample UY-9-14-2 was collected from the Cordillera Shear Zone and exhibits type I crossed girdles of quartz [c]-axes (Lister, 1977) with well-defined maxima subparallel to the Z direction. Quartz [a]-axes

are distributed perpendicular to Z and exhibit a slightly defined maximum subparallel to X. Basal and minor rhomb <a> slip thus account as slip systems. Sample UY-49-14 from the Cerro Amaro Shear Zone shows a symmetrical single girdle with a well-defined maximum close to the Y direction. Quartz [a]-axes are distributed perpendicular to Y and exhibit a maximum subparallel to X. Prism <a> slip and minor rhomb <a> slip can be thus interpreted. In the case of sample UY-32-14 from the Puntas de las Palmas Shear Zone, a type II crossed girdle with [a]-axes distributed perpendicular to the [c]-axes maximum was obtained. The obtained pole figures seem to be slightly rotated along X, which might result from oblique cutting during sample preparation. Hence, prism <a> slip and subordinated rhomb and basal <a> slip seem to be the slip systems.

Samples from the María Albina and Arroyo Corrales shear zones show dominance of assymetrical textures, which indicate of sinistral simple-shear dominated strain according to criteria from Schmid and Casey (1986). Only sample UY-104-14 shows an opposite sense of shear, pointing to either local dextral shearing (e.g., bents) or flow partitioning (Killian et al., 2011). The María Albina orthogneiss (sample UY-46-14) shows a dextral shear sense as well. In the case of the Sierra de Sosa Shear Zone, samples UY-112-14 and UY-167-14 are also indicative of sinistral simple-shear dominated deformation, whereas samples UY-113-14 and UY-157-14 point to pure-shear dominated strain. This variation may also result from variations of strain along the shear zone (i.e., simple vs pure shear-dominated domains) or flow partitioning at the microscale (Killian et al., 2011). In contrast, shear zones from the eastern domain seem to show a larger contribution of pure-shear strain, as indicated by the dominance of more symmetrical quartz textures (Schmid and Casey, 1986).

7.5. Geochronology

7.5.1. Sample description

In order to constrain the timing of deformation and metamorphism of the Dom Feliciano Belt, several units were analysed using different geochronological systems. Sample locations are shown in Figure 7.1, whereas sample coordinates and applied methods are described in Appendix 2.
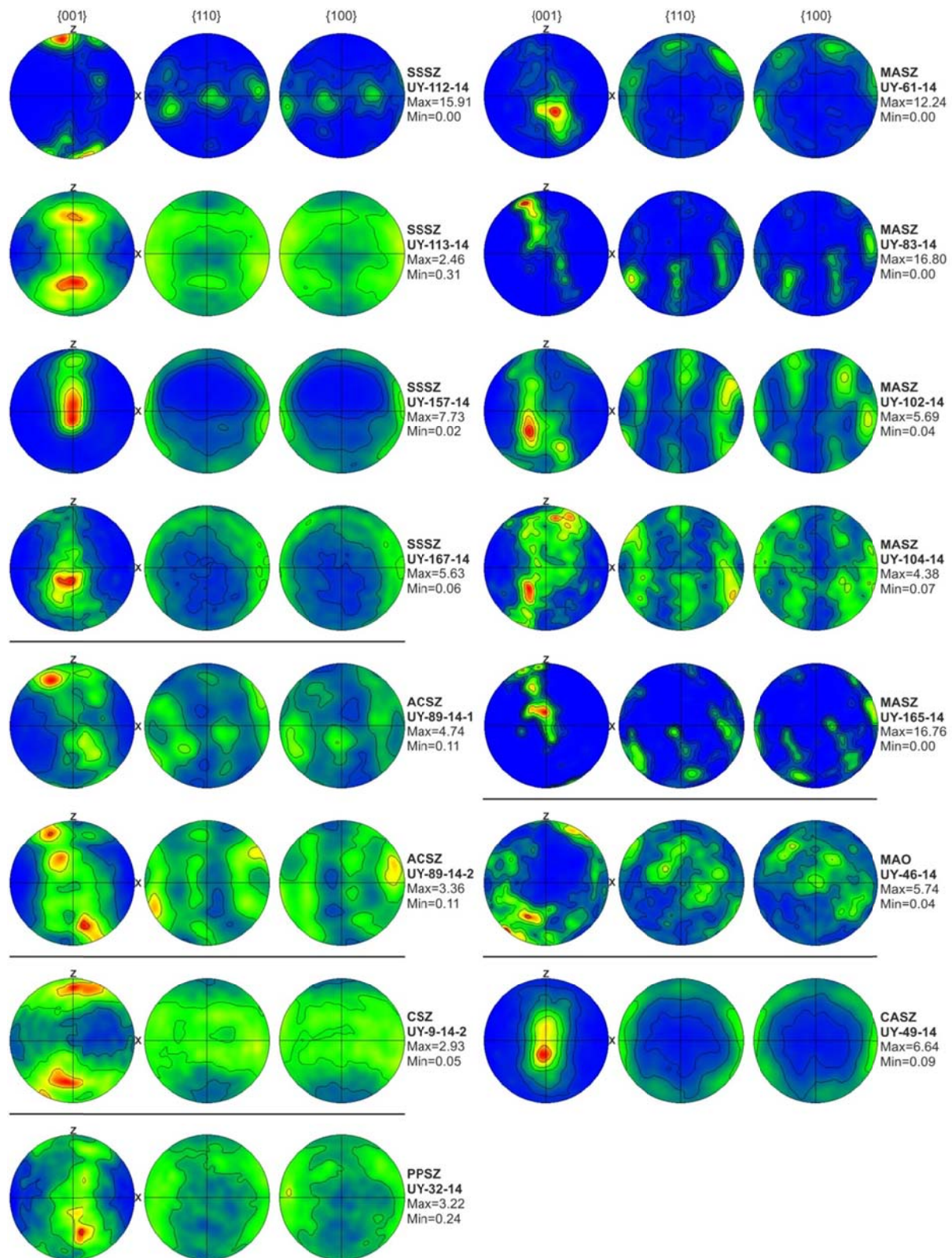
Fig. 7.11: Quartz CPO pole figures. Pole of the foliation (Z) and the lineation (X) are indicated. Contour levels are at 1 intervals up to 15 multiples of uniform distribution (m.u.d.). Colour scaling is from blue (minimum) to red (maximum). Sample locations are indicated in the Appendix 1. SSSZ: Sierra de Sosa Shear Zone, MASZ: María Albina Shear Zone, ACSZ: Arroyo Corrales Shear Zone, MAO: María Albina orthogneiss, CSZ: Cordillera Shear Zone, CASZ: Cerro Amaro Shear Zone, PPSZ: Puntas de las Palmas Shear Zone.

Sample BUY-64-11 comprises a granitic mylonite of the Sierra de Sosa Shear Zone. It is mostly made up of quartz and feldspars, which develop core and mantle structures. Quartz shows interfingering grain boundaries, whereas feldspars show recrystallized tails.

Sample BUY-66-11 corresponds to a granitic mylonite of the Tupambaé Shear Zone. Quartz and feldspars are most frequent minerals. Some quartz grains show interfingering boundaries, although finer-grained elongated crystals seem to dominate. Feldspars, in turn, develop core and mantle structures with recrystallized tails.

Sample UY-13-14 corresponds to a mylonite of the Sierra Ballena Shear Zone, which is made up by quartz, feldspar and minor honblende and sericite. Quartz develops homogeneous fine-grained elongated crystals, whereas feldspars show only microfracturing and cataclasis.

Two samples from the María Albina Shear Zone, namely UY-3-13 and UY-24-13, were collected as well. Both samples are made up of quartz, muscovite, fuchsite and cordierite. Quartz shows typically foam textures indicating recovery. Micas, in turn, develop fish microstructures, which are parallel to the mylonitic foliation.

On the other hand, several samples were collected from basement inliers of the western Dom Feliciano Belt. Samples UY-40-14 and UY-57-14 correspond to amphibolites, which are located to the west of the María Albina Shear Zone and thus probably correspond to the La China Complex. Sample UY-1-13 was collected from a phlogopite-bearing marble of the Las Tetas Complex, whereas UY-22-13, UY-23-13 and U13MH04 were obtained from quartz-micaschists of the same complex. UY-22-13 and U13MH04 are made up of quartz and muscovite, whereas UY-23-13 is constituted by quartz, fuchsite and scarce muscovite. UY-41-14 comprises a schist, which is made up of poikiloblastic cordierite, quartz, muscovite and biotite. It corresponds to an isolated outcrop of metasediments, which is located to the west of the Sierra de Sosa Shear Zone and may correspond to the Las Tetas Complex as well. UY-45-14, in turn, was collected from the María Albina orthogneiss, whereas UY-54-14 and UY-55-14 correspond to undifferentiated micaschists. Finally, one sample (UY-

64-14) was collected from a deformed pegmatite, which intrudes felsic orthogneisses of the La China Complex and is mylonitized together with them.

Likewise, two samples were collected from shear zones of the eastern Dom Feliciano Belt. UY-6-14 was collected from ultramylonites of the Cordillera Shear Zone, which are made up of quartz, feldspars and muscovite. Quartz is typically fine-grained and develops ribbons, whereas feldspars constitute porphyroclasts, which show sometimes boudinage. UY-48-14 corresponds to a granitic mylonite of the Cerro Amaro Shear Zone and is constituted by quartz, feldspars and muscovites. Interfingering grain boundaries are observed in quartz and recrystallization in feldspars is restricted to porphyroclast tails. Fish microstructures and kink bands are recognizable in muscovite, which is typically oriented parallel to the mylonitic foliation.

As reference, two samples were collected to constrain the regional cooling of the eastern Dom Feliciano Belt as well. UY-26-14 was obtained from the Puntas del Arroyo Rocha granite (Fig. 7.3), which is made up of quartz, feldspars and scarce hornblende and muscovite. UY-27-14, in turn, corresponds to a pegmatitic dyke that cross-cuts a mylonitic granitoid.

7.5.2. Results

7.5.2.1. U-Pb geochronology

Zircons of sample BUY-64-11 (Sierra de Sosa Shear Zone) are prismatic and up to 500 µm long. They typically exhibit oscillatory zoning, although some bright homogeneous cores are ocassionally recognizable (Fig. 7.12). A concordia age of 598.1 ± 2.2 Ma was obtained considering 9 out of 26 spots (Fig. 7.13, discordant data or with high common Pb content rejected). Nevertheless, some spots present slightly older concordant ages that may indicate reworking of magmatic zircons with ages between ca. 650-600 Ma (Fig. 7.13, Appendix 3). Additionally, one spot yields a concordant age of ca. 2.7 Ga, indicating Archean inheritance (Appendix 3).

In the case of sample BUY-66-11 (Tupambaé Shear Zone), prismatic and subordinated ovoid zircons up to 300 µm long can be observed (Fig. 7.12). Oscillatory zoning is the most frequent texture

but bright homogeneous cores are sometimes present as well. Zircons yield a concordant age of 549.0 ± 2.9 Ma considering 8 out of 25 spots (Fig. 7.13, Appendix 3, highly discordant data or with high common Pb content rejected). Likewise, a few bright luminescent cores show concordant ages of 1.6-1.7 Ga, which indicates inheritance of Statherian zircons.
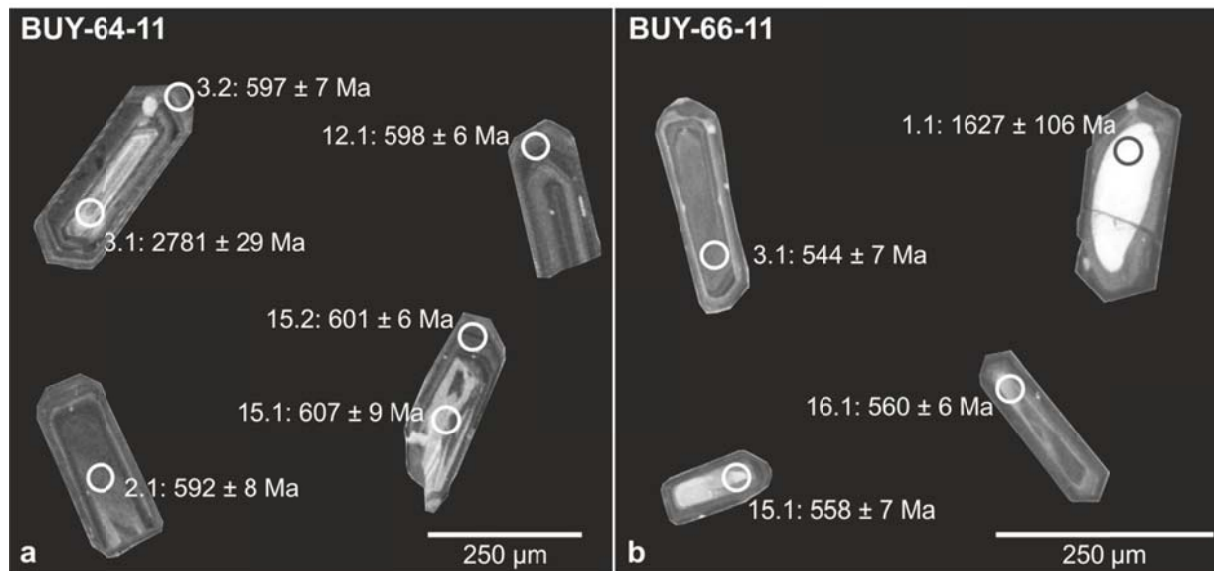
Fig. 7.12: Cathodoluminescence (CL) images of representative zircons. Individual U–Pb ages are shown.
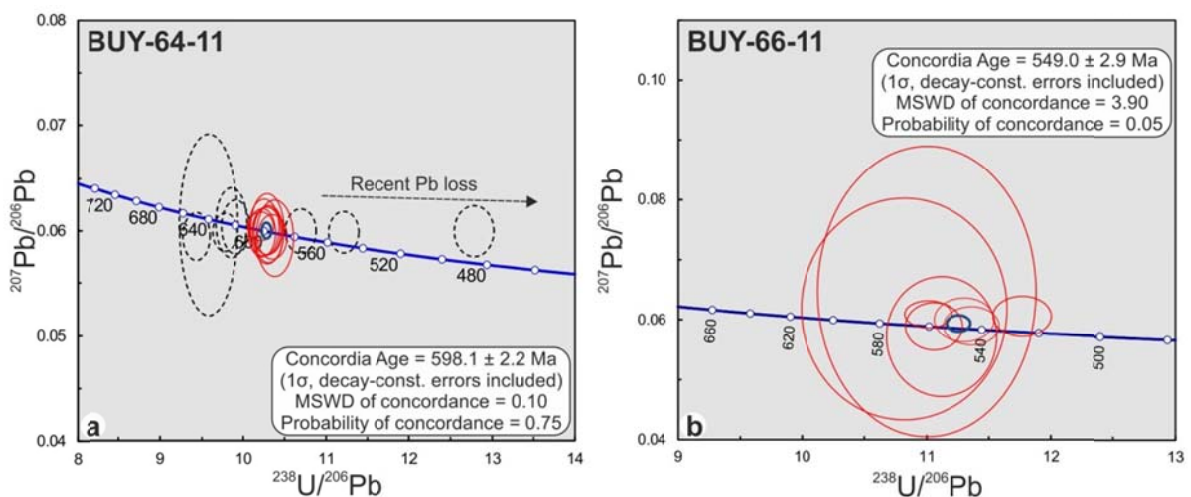
Fig. 7.13: U-Pb diagrams for zircons. Red ellipses indicate data used for age calculations, whereas dashed ellipses represent data that were not considered. Errors depicted at the 2σ level. Analytical data are presented in Appendix 3.

7.5.2.2. ^{40}Ar/^{39}Ar and K-Ar

Amphiboles from sample UY-13-14 (Sierra Ballena Shear Zone) show a significantly disturbed spectrum with a progressive stepping-up pattern (Fig. 7.14a). Inverse isochrones considering only the first or last steps would indicate a maximum age of ca. 420 Ma with excess Ar or a minimum age of ca. 2.0 Ga with subsequent Ar loss, respectively. A combination of these two-end member processes may be also feasible, therefore no further interpretations can be done for this sample. Disturbed spectrums were obtained as well for amphibolite samples of the basement of the western Dom Feliciano Belt (Fig. 7.14b, 7.14c). In the case of UY-40-14, an inverse isochrone shows an age of 604 ± 14 Ma and excess Ar considering steps 7 to 13 (Fig. 7.15). In a similar way, sample UY-57-14 yields an isochrone age (steps 8 to 15) of 639.5 ± 8.8 Ma (Fig. 7.15).

On the other hand, metasediments from the Las Tetas Complex yield ^{40}Ar/^{39}Ar and K-Ar ages between ca. 630 and 600 Ma (Fig. 7.14). Phlogopites from marbles yield a ^{40}Ar/^{39}Ar age of 621.4 ± 1.0 Ma (Fig. 7.14d), although it does not represent a true plateau age. In contrast, muscovite concentrates from quartz-micaschists yield ^{40}Ar/^{39}Ar plateau ages of 600.4 ± 1.1 and 600.9 ± 1.2 Ma (Fig. 7.14e, 7.14f). Two K-Ar ages of 623.9 ± 7.4 and 625.9 ± 7.4 Ma were obtained for fuchsite concentrates of sample UY-23-13. Muscovites of sample UY-41-14, in turn, yield a K-Ar age of 604.9 ± 6.3 Ma.

The María Albina orthogneiss yields a K-Ar muscovite age of 619.4 ± 8.5 Ma (sample UY-45-14), whereas muscovite concentrates from undifferentiated metasediments present K-Ar ages of 623.8 ± 6.6 and 610.4 ± 6.5 Ma (samples UY-54-14 and UY-55-14, respectively). Likewise, muscovites from sample UY-64-14 yield a K-Ar age of 618.1 ± 7.6 Ma.

In the case of the María Albina Shear Zone, two ^{40}Ar/^{39}Ar plateau ages were obtained for muscovite concentrates (Fig. 7.14g, 7.14h). Sample UY-3-13 yields an age of 596.8 ± 1.1 Ma, whereas an age of 597.2 ± 3.2 Ma was obtained for sample UY-24-13.

In the eastern Dom Feliciano Belt, the Puntas del Arroyo Rocha granite (sample UY-26-14) presents a K-Ar muscovite age of 589.7 ± 6.2 Ma, muscovite concentrates from sample UY-27-14 of a

pegmatitic dyke yields an age of 605.0 ± 7.2 Ma. On the other hand, K-Ar muscovites ages of 632.7 ±

6.1 and 615.2 ± 6.6 Ma were obtained for the Cordillera and Cerro Amaro shear zones, respectively

(UY-6-14 and UY-48-14).
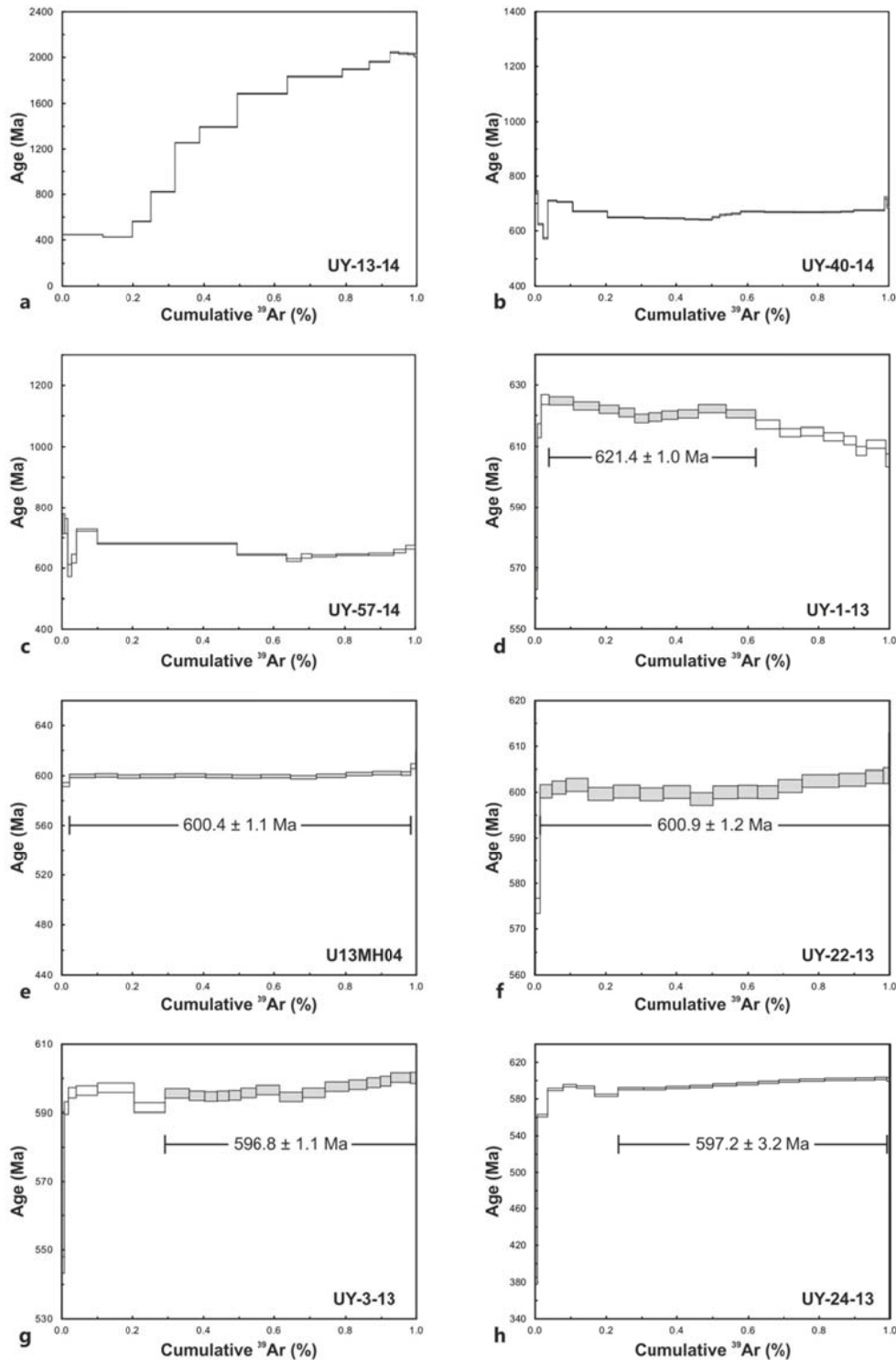
Fig. 7.14: Ar/Ar age spectrum from hornblende (UY-13-14, UY-40-14, UY-57-14), phlogopite (UY-1-13) and muscovite (UY-22-13, U13MH04, UY-3-13, UY-24-13) samples. Steps used for age calculations are colored in grey, whereas rejected steps are indicated in white.
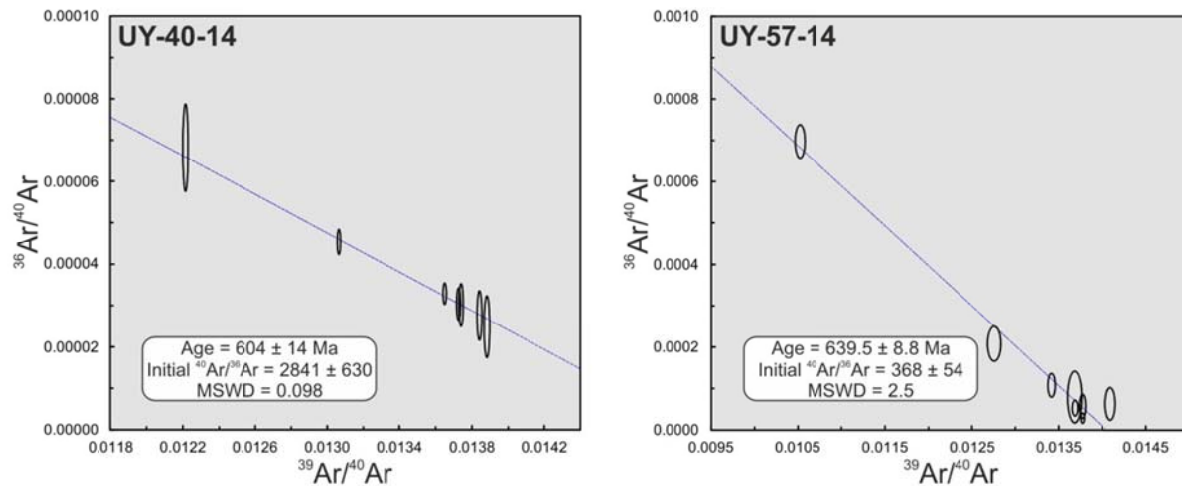
Fig. 7.15: Ar/Ar inverse isochrones for hornblende samples.

7.5.2.3. Rb-Sr

Two samples from the Las Tetas Complex were analysed using Rb-Sr mica and whole-rock (WR) isochrones. The sample UY-1-13 yields a phlogopite-WR isochrone age of 550.5 ± 2.7 Ma, whereas a muscovite-WR isochrone age of 590 ± 11 Ma was obtained for the sample U13MH04 (Appendix 5).

7.6. Discussion

7.6.1. Shear zone deformation mechanisms and conditions

Integration of microstructural and CPO data from rock-forming minerals has been widely applied to constrain deformation mechanisms and conditions in different minerals. Among them, quartz stands out due to its ubiquity and the existence of both experimental and natural calibrations (e.g., Mainprice et al., 1986; Hirth and Tullis, 1992; Okudaira et al., 1995; Kruhl, 1996; Stipp et al., 2002; Stipp and Tullis, 2003). Despite having some limitations (Law, 2014), thermometry based on quartz CPO textures and microstructures represents a useful tool, especially when combined with microstructures of other mineral phases in polycrystalline rocks (Dollinger and Blacic, 1975; Voll, 1976; Fitz Gerald and Stünitz, 1993; Pryer, 1993; Berger and Stünitz, 1996; Heidelbach et al., 2000; Rosenberg and Stünitz, 2003; Díaz Aspiroz et al., 2007).

In the case of the Tupambaé Shear Zone, quartz microstructures are indicative of subgrain rotation as the main dynamic recrystallization mechanism (Hirth and Tullis, 1992; Stipp et al., 2002), although the existence of larger sutured crystals may suggest conditions closer to the grain boundary migration zone. Quartz microstructures together with microfracturing, flame perthites, bent twins and recrystallization localized in tails recorded in feldspars may indicate deformation conditions of ca. 400-550°C (Voll, 1976; Passchier, 1985; Pryer, 1993; Stipp et al., 2002).

Microstructures and CPO data of the Sierra de Sosa Shear Zone reveal variable deformation conditions. Sutured quartz crystals and associated CPO textures revealing dominance of prism <a> slip point to deformation conditions in the grain boundary migration zone, probably near the transition to subgrain rotation (Passchier, 1985; Hirth and Tullis, 1992; Stipp et al., 2002), which are further supported by feldspar microstructures (Voll, 1976; Passchier, 1985; Pryer, 1993; Passchier and Trouw, 2005, and references therein). Nevertheless, the existence of large elongated relictic crystals with deformation lamellae, undulose extinction and only local subgrain formation reveal bulging recrystallization as the main mechanism in some samples, which would also account for the recorded basal <a> slip. In this case, deformation conditions can be thus constrained at ca. 300-400°C (Lloyd and Freeman, 1994; Hongn and Hippertt, 2001; Stipp et al., 2002).

In a similar way, higher conditions observed for the María Albina Shear Zone correspond to the grain boundary migration zone, as indicated by the presence of sutured grain boundaries and prism <a> as the main slip system (Passchier, 1985; Hirth and Tullis, 1992; Stipp et al., 2002). Nevertheless, subgrain rotation and bulging recrystallization are observable in some samples and may account for the recorded basal and rhomb <a>, as in the Arroyo Corrales Shear Zone and the María Albina orthogneiss, indicating lower grade deformation conditions as well (Hirth and Tullis, 1992; Lloyd and Freeman, 1994; Hongn and Hippertt, 2001; Stipp et al., 2002).

On the other hand, microstructures from the Cordillera Shear Zone are indicative of deformation conditions below ca. 450°C, as quartz seems to be dominated recrystallized by bulging and subgrain rotation recrystallization, whereas feldspar shows only microfracturing (Voll, 1976;

Hirth and Tullis, 1992; Pryer, 1993; Lloyd and Freeman, 1994; Hongn and Hippertt, 2001; Stipp et al., 2002; Passchier and Trouw, 2005, and references therein; Sinha et al., 2010). This interpretation is further supported by the dominance of basal <a> recorded in one sample, which account for conditions at the boundary between subgrain rotation and bulging recrystallization zones. Comparable conditions for the Cordillera Shear Zone were also obtained by Oyhantçabal (2005) based on quartz CPO neutron diffraction data.

In contrast, the Cerro Amaro Shear Zone shows microstructures that indicate grain boundary migration and local subgrain rotation recrystallization (Hirth and Tullis, 1992; Stipp et al., 2002), whereas microfracturing and recrystallized tails in feldspars may suggest deformation at ca. 450-550°C (Voll, 1976; Passchier, 1985; Pryer, 1993; Passchier and Trouw, 2005, and references therein). Hence, deformation took place probably in the grain boundary migration zone close to the transition to the subgrain rotation recrystallization zone, as further supported by prism and minor rhomb <a> slip recorded by quartz CPO data (Passchier, 1985; Hirth and Tullis, 1992; Stipp et al., 2002).

Relictic quartz crystals in the Punta de las Palmas Shear Zone may indicate early grain boundary migration recrystallization, which was lately overprinted by subgrain rotation recrystallization. Despite subsequent static recrystallization partially overprinted quartz microstructures, this interpretation is further supported by quartz CPO data indicating conditions close to the transition between grain boundary migration and subgrain rotation recrystallization zones (Passchier, 1985; Hirth and Tullis, 1992; Stipp et al., 2002). Feldspar microstructures, in turn, point to deformation conditions of ca. 450-550°C (Voll, 1976; Pryer, 1993; Passchier and Trouw, 2005, and references therein).

Based on field observations, microstructural analysis and quartz CPO data, variable deformation conditions are documented for shear zones of the Dom Feliciano Belt. The dominance of grain boundary migration recrystallization, diffusion processes and prism <a> slip in quartz (Passchier, 1985; Jessel, 1987; Hirth and Tullis, 1992; Stipp et al., 2002; Passchier and Trouw, 2005) together with localized recrystallization and dislocation climb in feldspars (Voll, 1976; Pryer, 1993;

Passchier and Trouw, 2005, and references therein) point to maximum deformation conditions of ca. 450-550°C. Subsequent lower grade conditions between ca. 300-450°C are recorded by subgrain rotation and bulging recrystallization with associated basal and rhomb <a> slip in quartz as well as by microfracturing, twinning and dislocation glide and creep recorded in feldspars (Voll, 1976; Pryer, 1993; Lloyd and Freeman, 1994; Hongn and Hippertt, 2001; Hirth and Tullis, 1992; Stipp et al., 2002; Passchier and Trouw, 2005, and references therein; Sinha et al., 2010). Conditions below 300°C are observed as well, since most shear zones present local cataclastic reworking, pressure solution and phyllonite development (Rutter, 1983; Gibson, 1990; Shimizu, 1995; Stipp et al., 2002; Jefferies et al., 2006). Based on cross-cutting relationships indicating local lower grade deformation overprinting larger areas of higher grade deformation conditions, the variability of deformation conditions in shear zones can be interpreted as the result of progressive strain localization during exhumation and associated retrograde metamorphism (e.g., Sibson, 1977, 1983; Smith et al., 2007; Herwegh et al., 2008; Toy et al., 2008; Oriolo et al., 2015).

7.6.2. Strain partitioning and timing of deformation in the Dom Feliciano Belt

Despite variations of strain with time operate at all scales (Lister and Williams, 1983; Schulmann et al., 2003; Leever et al., 2011; Carreras et al., 2013), most documented examples of shear zones developed within transpressional orogens only consider strain partitioning processes, i.e., simultaneous heterogeneous deformation of different domains (e.g., Sanderson and Marchini, 1985; Teyssier et al., 1995; Fossen et al., 1994; Fossen and Tikoff, 1998; Jones et al., 1997, 2004; Sullivan and Law, 2007; Fernández et al., 2013; Massey and Moecher, 2013). One of the main problems may arise from the difficulty to assess the age of deformation, as it is difficult to be directly dated and geochronological data cannot be easily interpreted in terms of deformation processes (van der Pluijm et al., 1994; Dunlap, 1997; Mulch and Cosca, 2004). Hence, a methodological approach combining 3D macro- to microstructural data and geochronological data from different structural

domains is compulsory to provide robust evolutionary models of orogens (van der Pluijm et al., 1994; Carreras et al., 2013; Oriolo et al., 2016b; Wang et al., 2016).

Quartz-micaschists and marbles may comprise mostly metasediments of the Las Tetas Complex based on detrital zircon data (Hartmann et al., 2001; Oyhantçabal et al., submitted; Chapter 4), although the easternmost outcrops of quartz-micaschists near the Arroyo Corrales Shear Zone may represent remnants of the Lavalleja Group (Oyhantçabal et al., submitted; Chapter 4). Structural data from these units reflect double vergence, transected folds and associated gently-dipping lineations towards the SSE (Fig. 7.4, 7.5), which are similar to results obtained by Rossini and Legrand (2003) in the Zanja del Tigre Complex. Double vergence has been typically reported for transpressional settings (e.g., Cunningham et al., 1996; Giambiagi et al., 2011; Ellero et al., 2015), whereas transected folds may indicate a non-coaxial component of deformation during or after folding (Treagus and Treagus, 1992). Lineation orientations and fold geometries, in turn, point to pure-shear dominated deformation and orogen-parallel extension or lateral extrusion (Jones et al., 1997, 2004; Sengupta and Ghosh, 2004). Minor thrusts might be associated with fold development, although neither clear field relationships nor geochronological data are available.

In contrast, fold geometries, lineation orientations and the dominance of relative asymmetric CPO quartz [c]-axis textures indicate strike-slip dominated deformation for most shear zones (Fig. 7.4, 7.5; Schmid and Casey, 1986; Jones et al., 2004; Sengupta and Ghosh, 2004). Nevertheless, quartz [c]-axis textures observed in the shear zones of the eastern Dom Feliciano Belt show more symmetric textures, which may indicate a larger component of coaxial deformation (Schmid and Casey, 1986).

Amphibole Ar/Ar data from sample UY-57-14 show the oldest cooling age of the western Dom Feliciano Belt at ca. 640-630 Ma, which is well agreement with the oldest Ar/Ar and K-Ar mica data based on the expected cooling temperatures. Within error, this age probably indicates the onset of deformation and metamorphism at ca. 630 Ma based on comparison with all available data from the Dom Feliciano Belt (Fig. 7.16), which would be further supported by the Ar/Ar amphibole age of

604 ± 14 Ma of sample UY-40-14. Alternatively, this could be related to a metamorphic event at ca.

650Ma, which is well recorded in the basement of the eastern Dom Feliciano Belt (Oyhantçabal et al.,

2009a; Basei et al., 2011a; Lenz et al., 2011) and was not reported so far for the western Dom

Feliciano Belt. The disturbed spectrum of this sample prevents from doing further interpretations

and more data are required to evaluate the potential presence of a metamorphic event at ca. 650 Ma

in the western Dom Feliciano Belt.
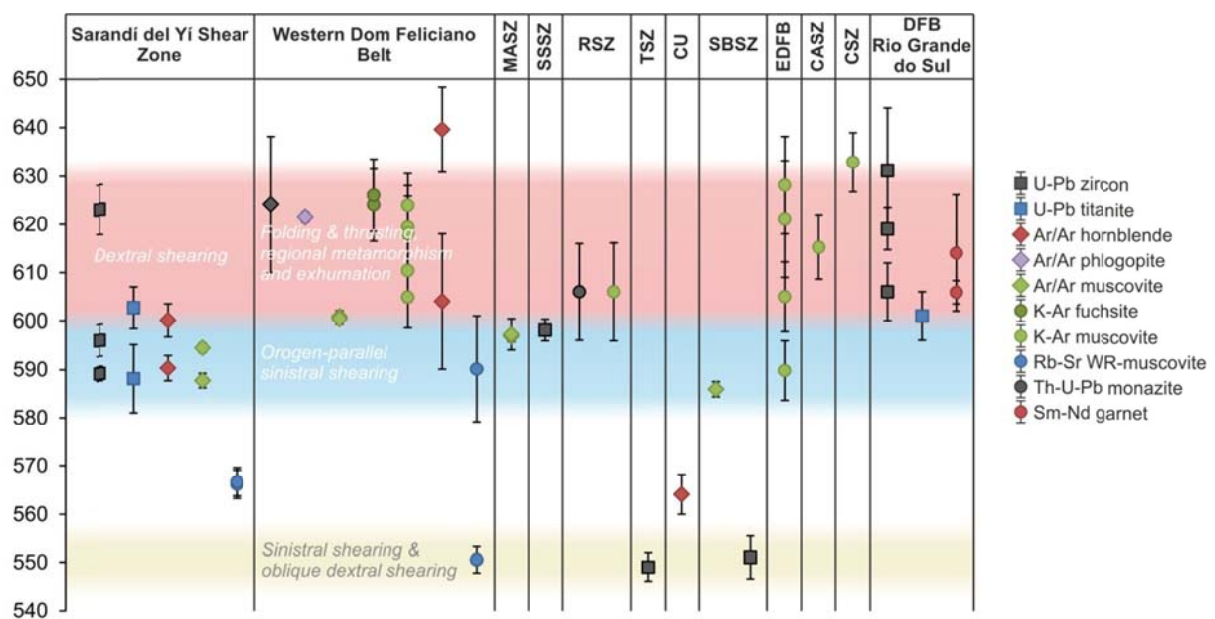
Fig. 7.16: Summary of geochronological constraints of the Dom Feliciano Belt of Uruguay after new and
available data from the literature (U-Pb rutile, Passarelli et al., 2009; Campanero Unit and two K-Ar muscovite
eastern Dom Feliciano Belt, Oyhantçabal et al., 2009a; Sierra Ballena Shear Zone Ar/Ar muscovite, Oyhantçabal
et al., 2009b; Sierra Ballena Shear Zone U-Pb zircon, Oyhantçabal et al., 2011b; Rivera Shear Zone, Oyhantçabal
et al., 2012). Geochronological data from the Dom Feliciano Belt in southernmost Brazil (Río Grande do Sul
area) are included as well. U-Pb zircon metamorphic overgrowth data after da Silva et al. (1999), Chemale Jr. et
al. (2011) and Philipp et al. (2015); U-Pb titanite data after Chemale Jr. et al. (2011) and Sm-Nd WR garnet data
after Gross et al. (2006). MASZ: María Albina Shear Zone, SSSZ: Sierra de Sosa Shear Zone, RSZ: Rivera Shear
Zone, TSZ: Tupambaé Shear Zone, CU: Campanero Unit, SBSZ: Sierra Ballena Shear Zone, CASZ: Cerro Amaro
Shear Zone, CSZ: Cordillera Shear Zone. Data from the western and eastern (EDFB) Dom Feliciano in Uruguay
and from the Dom Feliciano Belt in Rio Grande do Sul correspond to the timing of regional metamorphism and
deformation.

On the other hand, the K-Ar fuchsite age is equivalent to the Ar/Ar phlogopite age and older than most K-Ar and Ar/Ar muscovite ages, excepting sample UY-54-14 (Fig. 7.16; Appendix 6). Both fuchsite and phlogopite samples were obtained from the Las Tetas Complex in close areas, whereas sample UY-54-14 was collected ca. 40 km to the NNE (Appendix 2). Although neither experimental nor theoretical constraints on Ar diffusion in fuchsite are available, these data suggest that the closure temperature for K/Ar in fuchsite may be slightly higher than in muscovite, probably close to the closure temperature of phlogopite for this system (Table 6.1). K-Ar and Ar/Ar muscovite ages, in turn, spread between ca. 624-600 Ma, which may indicate slightly differential cooling below muscovite closure temperature (Table 6.1) along the belt during exhumation and deformation (e.g., folding and thrusting of metasediments). Structural data from the Zapicán intrusion indicating emplacement during deformation of the belt further constraints regional deformation between ca. 630-600 Ma, as indicated by the 610.4 ± 2.5 Ma U-Pb LA-ICP-MS zircon age of the pluton (Oriolo et al., 2016a). This time span is equivalent to the timing of dextral shearing reported for the Sarandí del Yí Shear Zone (Fig. 7.16, 7.17; Chapter 6; Oriolo et al., 2016b), whereas coeval shearing along the Rivera Shear Zone at 606 ± 6 Ma was documented as well (Fig. 7.1, 7.16; Oyhantçabal et al., 2012). Furthermore, K-Ar data from the María Albina orthogneiss (sample UY-45-14, 619.4 ± 8.5 Ma) together with structural data indicating deformation during metasediment folding (Fig. 7.5) and CPO data asymmetry seem to indicate that a dextral shearing component might be also present during folding of the belt.

As late Neoproterozoic magmatism is widespread in the eastern Dom Feliciano Belt and may reset isotopic systems, the timing of metamorphism and regional metamorphism in this region is more difficult to assess. Nevertheless, K-Ar muscovite ages of ca. 630-620 Ma were obtained in pegmatites intruding the Cerro Olivo Complex (Oyhantçabal et al., 2009a), whereas a K-Ar muscovite age of 589.7 ± 6.2 Ma was obtained for the Puntas del Arroyo Rocha granite (Fig. 7.16). Muscovites from a pegmatitic dyke that cross-cuts a mylonitic granitoid yield a K-Ar age of 605.0 ± 7.2 Ma (Fig. 7.16), indicating deformation prior to pegmatite emplacement and subsequent cooling. Hence,

117

regional cooling of the eastern Dom Feliciano Belt below muscovite closure temperature might extend between ca. 630-590 Ma.

The María Albina Shear Zone yields Ar/Ar muscovite ages of 596.8 ± 11 and 597.2 ± 3.2, whereas the Sierra de Sosa Shear Zones present a U-Pb LA-ICP-MS zircon age of 598.1 ± 2.2 Ma (Fig. 7.16). Maximum deformation conditions constrained for the María Albina Shear Zone were higher than the closure temperature for the K-Ar system in muscovite, and ages thus represent cooling after shearing. In the case of the Sierra de Sosa Shear Zone, the age seems to represent the crystallization age of the magmatic protolith, as zircons show dominance of prismatic habits with oscillatory zoning and Th/U > 0.1 (Hoskin and Schaltegger, 2003, and references therein). According to deformation conditions constrained for the shear zone, shearing probably took place shortly after emplacement of the protolith. In both cases, shearing might also predate the obtained ages, despite not being recorded by geochronological data, but similar ages were reported for sinistral shearing along the Sierra Ballena and the Sarandí del Yí shear zones (Fig. 7.16; Oyhantçabal et al., 2009b; Oriolo et al., 2016b). Sample UY-13-14 does not provide any clear constrain for deformation along the Sierra Ballena Shear Zone due to the strongly disturbed spectrum. Consequently, orogen-parallel sinistral shearing was active between ca. 598-584 Ma and clearly postdates regional deformation and metamorphism of the belt (Fig. 7.17). In the case of the eastern Dom Feliciano Belt, shear zone activity may also postdate the onset of regional deformation but might start prior to 600 based on the K-Ar of the Cerro Amaro and Cordillera shear zone. However, these shear zones show a large component of pure-shear, thus also supporting that deformation at ca. 630-600 Ma was dominated by pure shear as in the western Dom Feliciano Belt. However, more geochronological data are required to assess the timing of sinistral shearing in the eastern Dom Feliciano Belt.

A second event of shearing seems to be documented in the Tupambaé Shear Zone, indicating that oblique ENE-striking dextral shear zones were active at ca. 550 Ma (Fig. 7.16, 7.17). As in the case of the Sierra de Sosa Shear Zone, the age may represent the crystallization age of the magmatic protolith due to zircon habits, textures and Th/U ratios (Hoskin and Schaltegger, 2003, and

references therein). According to deformation conditions, deformation took place shortly after protolith emplacement. Contemporaneous shearing was documented for the Sierra Ballena Shear Zone (Oyhantçabal et al., 2011b), whereas cataclastic deformation since ca. 570 Ma up to the Cambrian was indicated for the Sarandí del Yí Shear Zone (Oriolo et al., 2015, 2016b). As in the latter, tectonic activity along other shear zones might be plausible during the late Ediacaran as well, but are probably not recorded by geochronological data. Evidences of cataclasis, pressure solution processes and phyllonite development could thus account for low-T deformation after shearing under ductile conditions constrained by geochronological data. Although Rb-Sr data from the folded metasediments do not reflect cooling paths as ages are younger than expected from closure temperatures, they may reflect resetting of the system during the two shearing events (Fig. 7.16). On the other hand, the Campanero Unit was probably exhumed during these late stages of the orogen, as indicated by the $^{40}Ar/^{39}Ar$ hornblende age of 564.0 ± 4.1 Ma (Fig. 16; Oyhantçabal et al., 2009a). Coeval low-grade metamorphism and subsequent cooling is recorded during the late Ediacaran in phyllites of the Lavalleja Group (545 ± 6 and 556 ± 8 Ma, K-Ar illite fine-fraction, Oyhantçabal et al., 2009a).
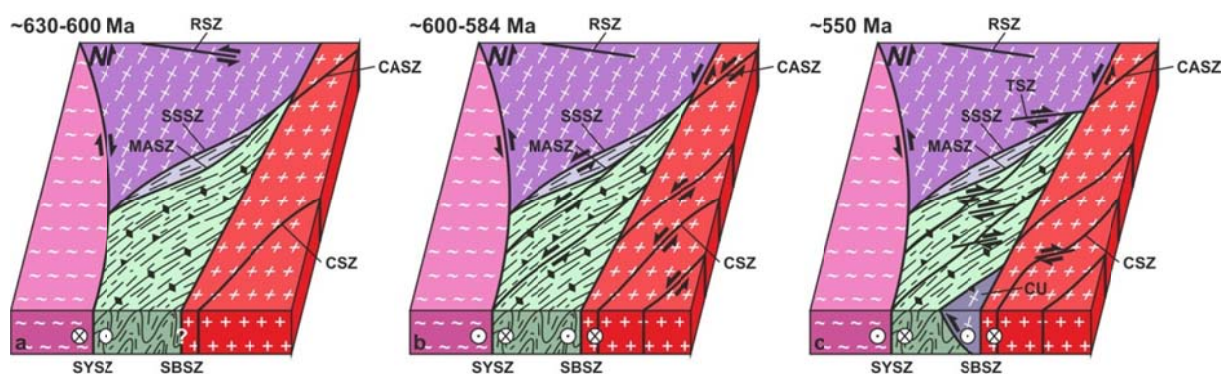
Fig. 7.17: Schematic structural evolution of the Dom Feliciano Belt (SYSZ: Sarandí del Yí Shear Zone, SBSZ: Sierra Ballena Shear Zone, RSZ: Rivera Shear Zone, SSSZ: Sierra de Sosa Shear Zone, MASZ: María Albina Shear Zone, CASZ: Cerro Amaro Shear Zone, CSZ: Cordillera Shear Zone, TSZ: Tupambaé Shear Zone). a) Main phase of regional metamorphism and deformation of the Dom Feliciano Belt (e.g., folding of the metasedimentary units) coeval with dextral shearing along the Sarandí del Yí Shear Zone. b) Sinistral shearing along N- to NNE-striking shear zones. c) Dextral shearing along ENE-striking shear zones and further sinistral shearing along N- to NNE-striking shear zones.

7.6.3. Structural evolution and regional implications

Structural data from the Dom Feliciano Belt indicate inclined transpression with partitioning into different deformational domains (Jones et al., 1997, 2004). Nevertheless, regional metamorphism and deformation in the Dom Feliciano Belt clearly predates deformation along localized shear zones. Hence, pure shear-dominated deformation related to crustal shortening was probably succeeded by strike-slip simple shear-dominated deformation, being the evolution of the Dom Feliciano Belt thus comparable with the Chongshan Shear Zone in the Himalayas (Zhang et al., 2010) and the eastern Pyrenees in the Cap de Creus area (Carreras and Druguet, 1994). Moreover, this model might account for the development of transected folds (Treagus and Treagus, 1992). Although strike-slip simple shear-dominated deformation is recorded along most shear zones of the Dom Feliciano Belt, coeval pure-shear dominated deformation was reported for the Sierra Ballena and Sarandí del Yí shear zones (Oyhantçabal et al., 2009b; Oriolo et al., 2015), indicating strain partitioning to some extent. On the other hand, late deformation along oblique ENE-striking dextral shear zones, which are antithetic regarding sinistral shearing along main N- to NNE-striking shear zones, also matches proposals that indicate late activation of antithetic oblique structures regarding orogen-parallel structures (Cembrano et al., 2005).

New and available geochronological data from the Dom Feliciano Belt places the onset of deformation and metamorphism at ca. 630 Ma (Fig. 7.16). These results match the onset of the collision between the Río de la Plata craton and the Nico Pérez Terrane/Congo Craton system along the Sarandí del Yí Shear Zone at 630-625 Ma (Chapter 6; Oriolo et al., 2016b) as well as ages of metamorphism and syncollisional magmatism reported for the Dom Feliciano Belt in Río Grande do Sul in southernmost Brazil (Fig. 7.16; da Silva et al., 1999; Gross et al., 2006; Chemale Jr. et al., 2011; Philipp et al., 2013, 2016). The collisional phase of the Dom Feliciano Belt in the Santa Catarina region, in turn, was alternatively placed between ca. 650 and 600 Ma (Basei et al., 2008; Chemale Jr. et al., 2012; Florisbal et al., 2012). Likewise, post-collisional magmatism since ca. 630 Ma is

ubiquitously recorded along the belt (Oyhantçabal et al., 2007; Florisbal et al., 2009, 2012; Sacks de

Campos et al., 2012; de Oliveira et al., 2015).

7.7. Conclusions

The Dom Feliciano Belt records inclined transpression and strain partitioning processes. The

main phase of deformation, metamorphism and associated exhumation below muscovite closure

temperature conditions is recorded between 630 and 600 Ma, which is related to the collision of the

Río de la Plata and Congo cratons. Subsequent sinistral shearing along N- to NNE-striking shear zones

gave rise to further deformation up to ca. 584 Ma. These shear zones record progressive strain

localization and retrograde conditions of deformation during crustal exhumation. Dextral ENE-

striking shear zones were subsequently active at ca. 550 Ma, coeval with further sinistral shearing

along N- to NNE-striking shear zones to some extent.

-CHAPTER 8-

Discussion: Implications for the tectonic evolution of Western Gondwana

8.1. Pre-Gondwana configuration

Several contributions attempted to elucidate the Mesoproterozoic paleogeography (e.g., Powell et al., 1993; Dalziel et al., 2000; Kröner and Cordani, 2003; Pisarevsky et al., 2003; Tohver et al., 2006; Li et al., 2008; Evans, 2009), which represents a key point to understand the history of Gondwana amalgamation. Despite most authors agree on the fact that the Amazonas and West African cratons were part of Rodinia (Dalziel et al., 2000; Tohver et al., 2006; Li et al., 2008; Evans, 2009), the participation of southwestern Gondwanic blocks is still under discussion. Kröner and Cordani (2003) indicated that the Río de la Plata and Congo-São Francisco cratons were not part of Rodinia, which was further supported by Tohver et al. (2006) and Rapalini et al. (2013). In contrast, Evans (2009) included both blocks within Rodinia. In the case of the Río de la Plata Craton, the pre-Brasiliano geological record is restricted to the Paleoproterozoic (Cingolani, 2011; Oyhantçabal et al., 2011a), pointing to lack of Mesoproterozoic events and isolation of the Río de la Plata Craton during Rodinia evolution. The Congo-São Francisco Craton, in turn, exhibits several distinct Mesoproterozoic magmatic events at ca. 1.50, 1.38 and 1.10 Ga (Ernst et al., 2013). Although the youngest event is almost coeval with the timing of Rodinia assembly, it is unclear if it is related to a convergent or an intraplate setting (Ernst et al., 2013; Debruyne et al., 2015). A different situation can be observed in the Kalahari Craton, which was clearly part of Rodinia based on the existence of the Namaqua-Natal Belt (e.g., Thomas et al., 1994; Dalziel et al., 2000; Cornell et al., 2006; Eglington, 2006; Spencer et al., 2015). In any case, most reconstructions do not consider Mesoproterozoic connections of the Congo-São Francisco and Kalahari cratons, even if the former was part of Rodinia (Evans, 2009), which is further supported by detrital zircon data from the Damara Belt (Foster et al., 2015) and paleomagnetic data (Bartholomew, 2008). Hence, the Río de la Plata, Congo-São Francisco and Kalahari cratons did not interact with each other prior to their incorporation into Gondwana, being only the latter part of Rodinia.

On the other hand, new data presented herein further supports the allochtony of the Nico Pérez Terrane regarding the Río de la Plata Craton and its derivation from the Congo Craton, previously suggested by Oyhantçabal et al. (2011a) and Rapela et al. (2011). The oldest Neoproterozoic record in the southern Dom Feliciano Belt, in turn, is constituted by the high-grade rocks of the Cerro Olivo Complex, which contains zircons yielding U-Pb concordant ages of ca. 800-750 Ma (Hartmann et al., 2002; Oyhantçabal et al., 2009a; Basei et al., 2011a; Lenz et al., 2011). Due to similar ages reported in the Coastal Terrane of the Kaoko Belt (Kröner et al., 2004; Konopásek et al., 2008), both regions were correlated and these ages were interpreted as the timing of rifting-related magmatism during the Rodinia break-up (Kröner et al., 2004; Oyhantçabal et al., 2009a; Basei et al., 2011a; Frimmel et al., 2011; Rapela et al., 2011; Konopásek et al., 2014), although some contributions indicated a convergent setting for this event (Lenz et al., 2013; Koester et al., 2016). Hence, the African crustal affinity of the Nico Pérez Terrane together with correlations between the Cerro Olivo Complex and the Coastal Terrane point to Cryogenian rifting of the Nico Pérez Terrane from the Congo Craton margin as indicated by Rapela et al. (2011), in contrast to contributions interpreting the Cerro Olivo Complex as the basement of a distinct terrane (Bossi and Gaucher, 2004; Gaucher et al., 2010; Basei et al., 2011a). Similarities in the detrital zircon pattern of the southwestern Dom Feliciano Belt metasediments (Chapter 4) and a quartzite of the southeastern Dom Feliciano Belt basement (Nedrebø, 2014) would further support that the underlying Nico Pérez Terrane basement and the Cerro Olivo Complex, respectively, comprised a single African block.

Further to the north, the Nico Perez Terrane extends up to the Taquarembó block in Río Grande do Sul, southeastern Brazil (Fig. 1.4; Oyhantçabal et al., 2011a). To the east of this block, isolated outcrops of gneisses of the Encantadas Complex within the Pelotas Batholith record Paleoproterozoic magmatism at ca. 2.3-2.0 Ga (Hartmann et al., 2000b, 2003a; Leite et al., 2000; Saalmann et al., 2011), which is comparable to magmatism recorded in the Nico Pérez Terrane in Uruguay (Chapter 3) and the Taquarembó Block. Sm-Nd model ages in the area are mostly Archean and Paleoproterozoic (Gastal et al., 2005), being also similar to those recorded in the Nico Pérez

Terrane (Oyhantçabal et al., 2011a). Cryogenian magmatism is recorded as well (da Silva et al., 1999; Hartmann et al., 2000a; Koester et al., 2016). Archean-Paleoproterozoic magmatism with Archean Hf and Sm-Nd model ages is also recorded in the Camboriú Complex in the Santa Catarina region (Hartmann et al., 2000c, 2003b; Basei et al., 2013b), thus allowing possible correlations with the Nico Pérez Terrane. Independently of whether Archean-Paleoproterozoic basement inliers of the Dom Feliciano Belt comprised a single block or not, the existence of Cryogenian magmatism may suggest that all these blocks were rifted during Rodinia break-up from the southwestern Congo Craton (Rapela et al., 2011). If so, the first rifting phase reported by Li et al. (2008) also extended up to the Congo Craton margin (Fig. 8.1).
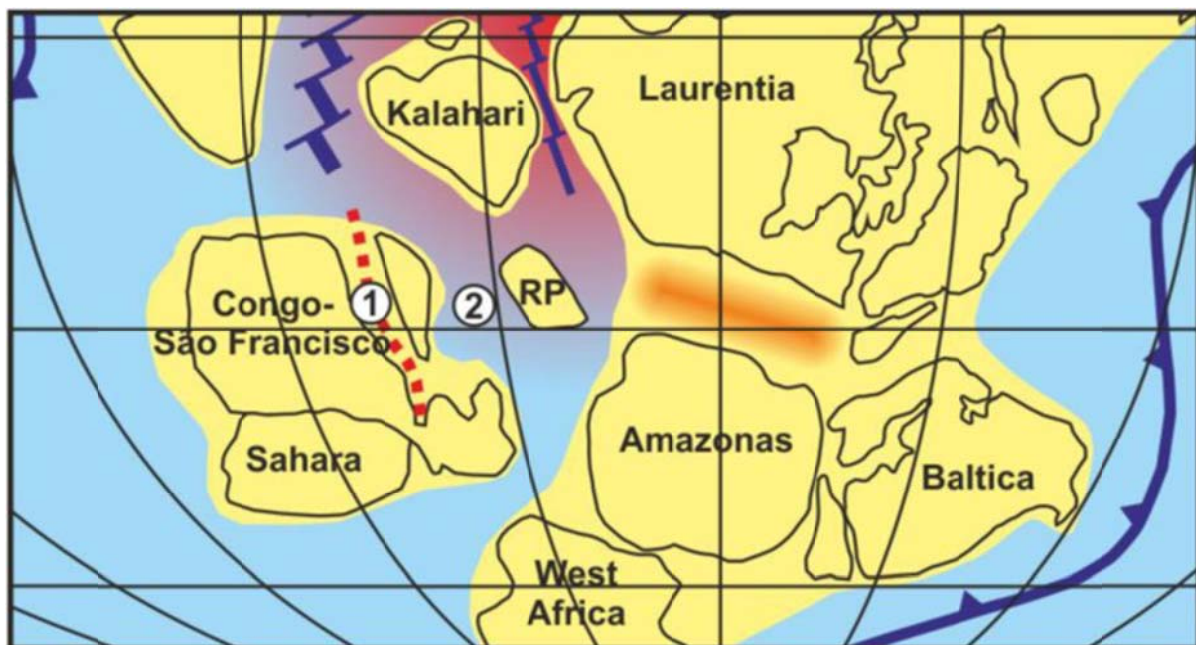
Fig. 8.1: Schematic paleogeography showing main crustal block distribution during Rodinia break-up at ca. 720 Ma (see Fig. 1.1 for comparison; modified after Li et al., 2008). The red line shows the position of the rifting of Congo-derived blocks amalgamated to the Río de la Plata Craton margin during the Ediacaran (e.g., Nico Pérez Terrane). Two possible positions after the redefinition of the Adamastor Ocean are presented as well (1: proto-Adamastor developed during Cryogenian crustal extension after Rapela et al., 2011; 2: Adamastor as a pre-Cryogenian remnant ocean separating the Río de la Plata Craton and the Congo-derived blocks after Cordani et al., 2003). Subduction zones and spreading ridges are indicated in blue, whereas the red area indicates the possible location of a mantle plume. The rifting zone at ca. 600 Ma between Laurentia and Amazonas is shown in orange.

Rapela et al. (2011) considered that the rifting gave rise to the opening of the Adamastor Ocean. Nevertheless, the Adamastor Ocean was originally defined by Hartnady et al. (1985) for the ocean closed during the evolution of the Gariep and Damara belts, and was afterwards extended to the Dom Feliciano Belt (Fragoso Cesar, 1991). Fragoso Cesar (1991) considered that the Adamastor Ocean separated the Río de la Plata and Kalahari cratons prior to the collisional phase of the Dom Feliciano Belt, which gave rise to the closure of the oceanic basin. Considering new and available evidences summarized in this work (e.g., Chapter 3, 6, 7; Section 8.2), this phase was related to the Río de la Plata and Congo collision, which also included the amalgamation of minor crustal blocks such as the Nico Pérez Terrane. Likewise, the definition of the Río de la Plata Craton after Oyhantçabal et al. (2011a) also differs from the definition considered by Fragoso Cesar (1991), as the Sarandí del Yí Shear Zone comprises its eastern boundary. Hence, the existence of the Adamastor Ocean can be questioned, or it should be at least redefined. If the Adamastor is regarded as the ocean located to the east of the Río de la Plata Craton as indicated by Fragoso Cesar (1991), it may thus represent a probable pre-Cryogenian remnant ocean (Fig. 8.1; Cordani et al., 2003), rulling out that its opening was related to the beginning of a "Brasiliano Wilson Cycle" (Fragoso Cesar, 1991) or to Cryogenian rifting (Rapela et al., 2011). On the other hand, if Cryogenian magmatism records crustal extension that triggered the ocean development, the Adamastor would have separated the Congo Craton from the Congo-rifted blocks (Fig. 8.1), and not from the Río de la Plata Craton as originally defined by Fragoso Cesar (1991). However, no evidences of Cryogenian oceanic crust generation were founded so far as Cryogenian rocks show Sm-Nd Paleo- to Mesoproterozoic T_{DM} ages, and some contributions even indicated that this magmatism could be associated with a convergent setting (Lenz et al., 2013; Koester et al., 2016). In order to test the validity of these hypotheses, more data are nevertheless required.

8.2. The Brasiliano–Pan-African Orogeny in southwestern Gondwana

Since early contributions recognized the existence of late Neoproterozoic tectonic events in South America and Africa and first correlations across the Atlantic Ocean were established (Almeida et al., 1973, 1981; Miller, 1983; Porada, 1985, 1989; Brito Neves and Cordani, 1991; Fragoso Cesar, 1991), works focused on the Brasiliano–Pan-African Orogeny have diversified. Nevertheless, the amalgamation of Western Gondwana and the evolution of the Dom Feliciano Belt are a matter of ongoing debate. Some hypotheses have linked the Dom Feliciano with the Gariep Belt, thus indicating that tectonic processes recorded in both areas were related to convergence and subsequent collision between the Río de la Plata and Kalahari cratons (Basei et al., 2005; Frimmel et al., 2011, 2013). Other proposals, in contrast, have indicated first assembly of the Río de la Plata and Congo cratons, favoring correlations between the Dom Feliciano and Kaoko belts (Prave, 1996; Alkmim et al., 2001; Goscombe and Gray, 2007; Oyhantçabal et al., 2011b; Rapela et al., 2011; Konopásek et al., 2014; Oriolo et al., 2016b).

New and available data point to collision at ca. 630 Ma of the Río de la Plata and Congo Craton, which also implied the amalgamation of minor blocks located at the attenuated Congo Craton margin (i.e., the Nico Pérez Terrane and the Cerro Olivo Complex/Coastal Terrane; Chapter 3, 6, 7). Several contributions demonstrated the correlation between the Coastal Terrane in Africa and the Cerro Olivo Complex in Uruguay (Gross et al., 2009; Oyhantçabal et al., 2009a; Basei et al., 2011a; Lenz et al., 2011; Rapela et al., 2011; Konopásek et al., 2014), as they both record Cryogenian rifting-related magmatism and high-grade metamorphism at ca. 650 Ma (Hartmann et al., 2002; Kröner et al., 2004; Konopásek et al., 2008; Oyhantçabal et al., 2009a; Basei et al., 2011a; Lenz et al., 2011). Goscombe and Gray (2007, 2008) and Konopásek et al. (2014) indicated an arc/barck-arc domain at ca. 650-630 Ma at the attenuated Congo Craton margin, implying subduction towards the east and a trench located to the west of the Coastal Terrane. Consequently, metamorphic conditions of the Cerro Olivo Complex and the Coastal Terrane could be explained by arc-related high-grade metamorphism and magmatism followed by the accretion of the Nico Pérez Terrane and the Río de

la Plata Craton (Fig. 8.2a, 8.2b). Similar P-T conditions in arc settings were reported by Tibaldi et al. (2013) and Maki et al. (2014) in the Famatinian arc (Western Sierras Pampeanas) and the Higo metamorphic terrane (central Kyushu), respectively.
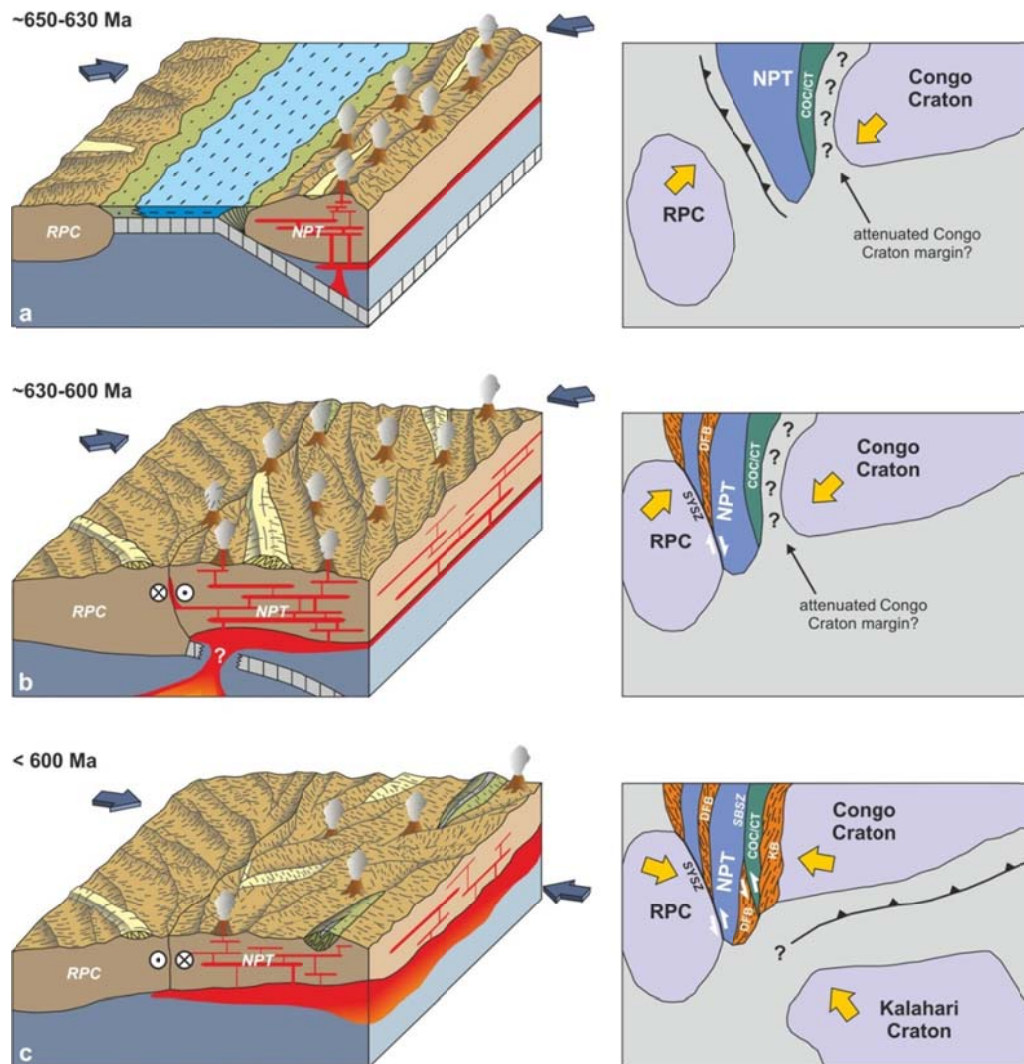
Fig. 8.2: Tectonic evolution model for the Sarandí del Yí Shear Zone and adjacent crustal blocks. The paleogeographic framework is schematized on the right. RPC: Río de la Plata Craton, NPT: Nico Pérez Terrane, COC/CT: Cerro Olivo Complex/Coastal Terrane, DFB: Dom Feliciano Belt, KB: Kaoko Belt, SYSZ: Sarandí del Yí Shear Zone, SBSZ: Sierra Ballena Shear Zone. a) Subduction under the Nico Pérez Terrane, which was probably part of the attenuated margin of the Congo Craton margin. b) Juxtaposition of the Río de la Plata Craton and the Nico Pérez Terrane and consequent onset of deformation along the Sarandí del Yí Shear Zone at ca. 630 Ma. During the post-collisional phase and associated slab break-off, dextral shearing along the shear zone was coeval with deformation, metamorphism and magmatism in the Dom Feliciano Belt. c) Sinistral shearing in the Sarandí del Yí Shear Zone after ca. 600 Ma. Further post-collisional magmatism and sinistral shearing along the shear zones of the Dom Feliciano Belt are also recorded. The switch to sinistral shearing was related to the onset of the convergence of the Kalahari Craton.

Oblique collision and associated deformation, metamorphism and exhumation extended up to ca. 600 Ma in the Dom Feliciano Belt, as indicated by geochronological data (Fig. 7.16). The Kaoko Belt, in turn, records this phase since 580 Ma as it comprised a foreland domain, indicating deformation and exhumation migration towards the east (Goscombe et al., 2005a; Konopásek et al., 2005; Goscombe and Gray, 2007, 2008; Foster et al., 2009; Ulrich et al., 2011). This is further supported by docking of the Coastal Terrane to the Kaoko Belt western margin at 645-580 Ma (Goscombe and Gray, 2007).

Widespread post-collisional magmatism is recorded in the Nico Pérez Terrane and the Dom Feliciano Belt after ca. 630 Ma (Oyhantçabal et al., 2007; Florisbal et al., 2009, 2012; Sacks de Campos et al., 2012; de Oliveira et al., 2015). Likewise, minor post-collisional magmatism is recorded in the Piedra Alta Terrane at 587.1 ± 7.9 Ma (Cingolani et al., 2012), whereas hydrothermal activity at ca. 620-590 Ma was reported for the Tandilia Belt (Martínez et al., 2013). Asthenospheric upwelling due to slab break-off after collision could account for this process (Figure 8.2b; Oyhantçabal et al., 2007), as in the Western Kunlun orogenic belt in the Tibet Plateau (Ye et al., 2008) and the Alps (von Blanckenburg and Davies, 1998), giving rise to thinning of the lithospheric mantle under the Nico Pérez Terrane and consequent thermal desestabilization (Black and Liégeois, 1993; Liégeois et al., 2013), which is supported by cooling age patterns (Figure 6.6c; Oyhantçabal et al., 2011a). Moreover, significant post-collisional synkinematic magmatism is recorded along the Sarandí del Yí Shear Zone (Figure 6.6a) and is thus comparable with the magmatism along the Periadriatic Lineament (Steenken et al., 2000; Rosenberg, 2004; Stipp et al., 2004), which also represents a first-order tectonic boundary (Schmid et al., 1989).

The switch from dextral to sinistral shearing along the Sarandí del Yí Shear Zone together with sinistral shearing along NNE-striking shear zones of the Dom Feliciano point to a geodynamic change at ca. 600 Ma (Fig. 6.6a, 7.16; Oyhantçabal et al., 2009b; Oriolo et al., 2016b), postdating the main crustal shortening and metamorphism phase. In a similar way, sinistral shearing along main shear zones in the Kaoko Belt was recorded after ca. 570-550 Ma (Goscombe et al., 2005; Konopásek

et al., 2005; Goscombe and Gray, 2007, 2008; Foster et al., 2009; Ulrich et al., 2011), providing further evidences of deformation migration towards the foreland.

The onset of convergence between the Kalahari and Río de la Plata-Congo cratons along the Damara Belt at ca. 600 Ma provides a satisfactory explanation for ubiquitous sinistral shearing in the Dom Feliciano Belt (Figure 8.2c; Lehmann et al., 2015; Oriolo et al., 2016b). This plate reorganization could be further supported by the sudden change in the apparent polar wander path of the Congo Craton observed after ca. 590 Ma (Moloto-A-Kenguemba et al., 2008). Consequently, the assembly of the Río de la Plata and Congo cratons clearly predates the incorporation of the Kalahari Craton in Western Gondwana, which is further supported by detrital zircon data of the eastern Dom Feliciano and Kaoko belts (Section 4.5.3). In the Dom Feliciano Belt, the final incorporation of the Kalahari Craton gave rise to the closure of the Rocha basin, which was located at the southeastern margin of the Dom Feliciano Belt and represented the western counterpart of the Gariep basin (Basei et al., 2005; Blanco et al., 2009; Frimmel et al., 2011, 2013).

8.3. The diachronous assembly of Gondwana

Comparison of available data allows characterizing the amalgamation of the Río de la Plata and Congo cratons as the earliest collisional phase recorded during the Brasiliano–Pan-African Orogeny (Fig. 8.3, 8.4a), indicating that they probably comprised the first Gondwana nucleus. Subsequent collisional processes up to 600 Ma are recognizable further to the north along the Transbrasiliano-Kandi Lineament (Ganade de Araujo et al., 2014a, 2014b, 2014c; Ganade et al., 2016), the Ribeira and Brasilia belts (Bento dos Santos et al., 2010; Campos Neto et al., 2010) and the LATEA metacraton (Berger et al., 2014). This implied the incorporation of the Amazonas and West African cratons as well as of the Saharan Metacraton into Gondwana during this period (Fig. 8.3, 8.4b), revealing that the first stages of Gondwana assembly are contemporaneous with the last events related to Rodinia break-up, which were related to the opening of the Iapetus Ocean at 610-

600 Ma (Fig. 8.3; Cawood et al., 2001; Hartz and Torsvik, 2002; Li et al., 2008; O´Brien and van der Pluijm, 2012; Johansson, 2014; Lubnina et al., 2014).

Interestingly, all collisional orogens between 630 and 600 Ma show some similarities. Although the timing of collision is slightly diachronous, they are all bounded to the west by crustal-scale dextral shear zones, namely the Transbrasiliano-Kandi Lineament (Ganade de Araujo et al., 2014a, 2014b, 2014c) and the Sarandí del Yí Shear Zone (Chapter 5, 6; Oriolo et al., 2015, 2016b), which separate them from cratonic areas (i.e., West African, Amazonas and Río de la Plata cratons). They also record Cryogenian magmatism and subsequent arc/back-arc magmatism with subduction to the east since ca. 660 Ma up to the collisional phase, probably implying the existence of one of the largest collisional zones in the geological history (Fig. 8.4a; Goscombe and Gray, 2007, 2008; Rapela et al., 2011; Berger et al., 2014; Ganade de Araujo et al., 2014c; Konopásek et al., 2014; Ganade et al., 2016; Oriolo et al., 2016b). The subsequent collision gave rise to the birth of Western Gondwana and the consequent amalgamation of African-derived crustal blocks to the South American Archean-Proterozoic nuclei (Fig. 8.4b; Rapela et al., 2011; Chapter 3).

Available O and Hf isotopic data combined with geological evidences reveal that juvenile continental crustal addition took place to some extent during Tonian to Cryogenian subduction, mostly related to island arc or back-arc systems associated with northwestern Gondwanic cratons (Fig. 8.5; Matteini et al., 2010; Fortes de Lena et al., 2014; Ganade de Araujo et al., 2014c; Ali et al., 2015). In contrast, coeval magmatism recorded in southwesternmost Gondwanic blocks show higher $\delta^{18}O$ values and Meso- to Paleoproterozoic Hf model ages, indicating a dominant crustal source (Rapela et al., 2011; Frimmel et al., 2013). However, Archean to Mesoproterozoic Hf model ages and high $\delta^{18}O$ values in zircons younger than ca. 650 Ma reveal that the timing of Gondwana amalgamation was ubiquitously dominated by crustal reworking processes (Fig. 8.5). This is further supported by geological evidences, as deformation, metamorphism and voluminous post-collisional magmatism and shear zone activity that reworked basement units were elsewhere recognized (Abdesalam et al., 2002; Liégois et al., 2003; Neves, 2003; da Silva et al., 2005; Oyhantçabal et al.,

2007, 2011a, 2011b, 2012; Teixeira et al., 2010; Berger et al., 2014; Ganade de Araujo et al., 2014a), indicating the importance of metacratonization processes during Gondwana assembly (Fig. 8.4b; Liégois et al., 2013). This also agrees with proposals indicating that accretional tectonics favour crustal growth in comparison with collisional tectonics, which are dominated by crustal reworking processes (Collins et al., 2011).

As previously outlined, the Kalahari Craton was lately incorporated into Western Gondwana, as indicated by the timing of collision in the Gariep, Saldania, Damara and Zambezi belts (Fig. 8.3, 8.4d, 8.4e; Frimmel and Frank, 1998; John et al., 2004; Gray et al., 2006; Frimmel et al., 2011, 2013; Schmitt et al., 2012). However, the onset of the Kalahari convergence with the already amalgamated Western Gondwana is recorded since ca. 600-590 Ma in both Damara and Dom Feliciano belts (Section 8.2; Lehmann et al., 2016; Oriolo et al., 2016b).
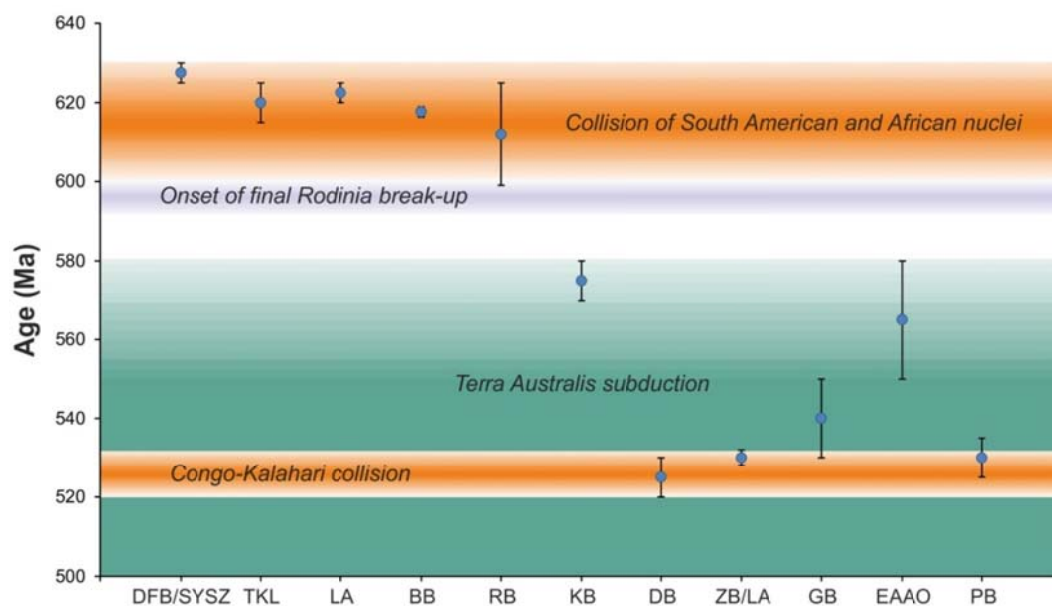
Fig. 8.3: Timing of Gondwana-related collisional events summarized from available data. DFB/SYSZ: Dom Feliciano Belt/Sarandí del Yí Shear Zone (this work), TKL: Transbrasiliano-Kandi Lineament (Ganade de Araujo et al., 2014a, 2014b, 2014c), LA: LATEA Metacraton (Berger et al., 2014), BB: Brasilia Belt (Campos Neto et al., 2010), RB: Ribeira Belt (Bento dos Santos et al., 2010), KB: Kaoko Belt (Goscombe et al., 2005; Goscombe and Gray, 2007, 2008; Foster et al., 2009), DB: Damara Belt (Gray et al., 2006; Schmitt et al., 2012), Zambezi Belt/Lufillian Arc (John et al., 2004), GB: Gariep Belt (Frimmel and Frank, 1998; Frimmel et al., 2011), EAAO: East African-Antarctic Orogen (Jacobs and Thomas, 2004; Viola et al., 2008), PB: Pampean Belt (Rapela et al., 1998, 2007; Siegesmund et al., 2010). Onset of final Rodinia break-up after Li et al. (2008) and subduction along the Terra Australis Orogen after Cawood (2005) and Cawood and Buchan (2007) are shown as well. See text for further explanations.

Collisional processes at 580-550 Ma were reported in the East African-Antartic Orogen (Fig. 8.4d; Jacobs and Thomas, 2004; Viola et al., 2008; Fritz et al., 2013), indicating that the assembly of Western and Eastern Gondwana predates the final incorporation of the Kalahari Craton into the former. Nevertheless, the accretion of the juvenile Arabian-Nubian Shield to the Congo Craton/Saharan Metacraton margin was constrained at ca. 650-620 Ma (Fig. 8.4a; Fritz et al., 2013).
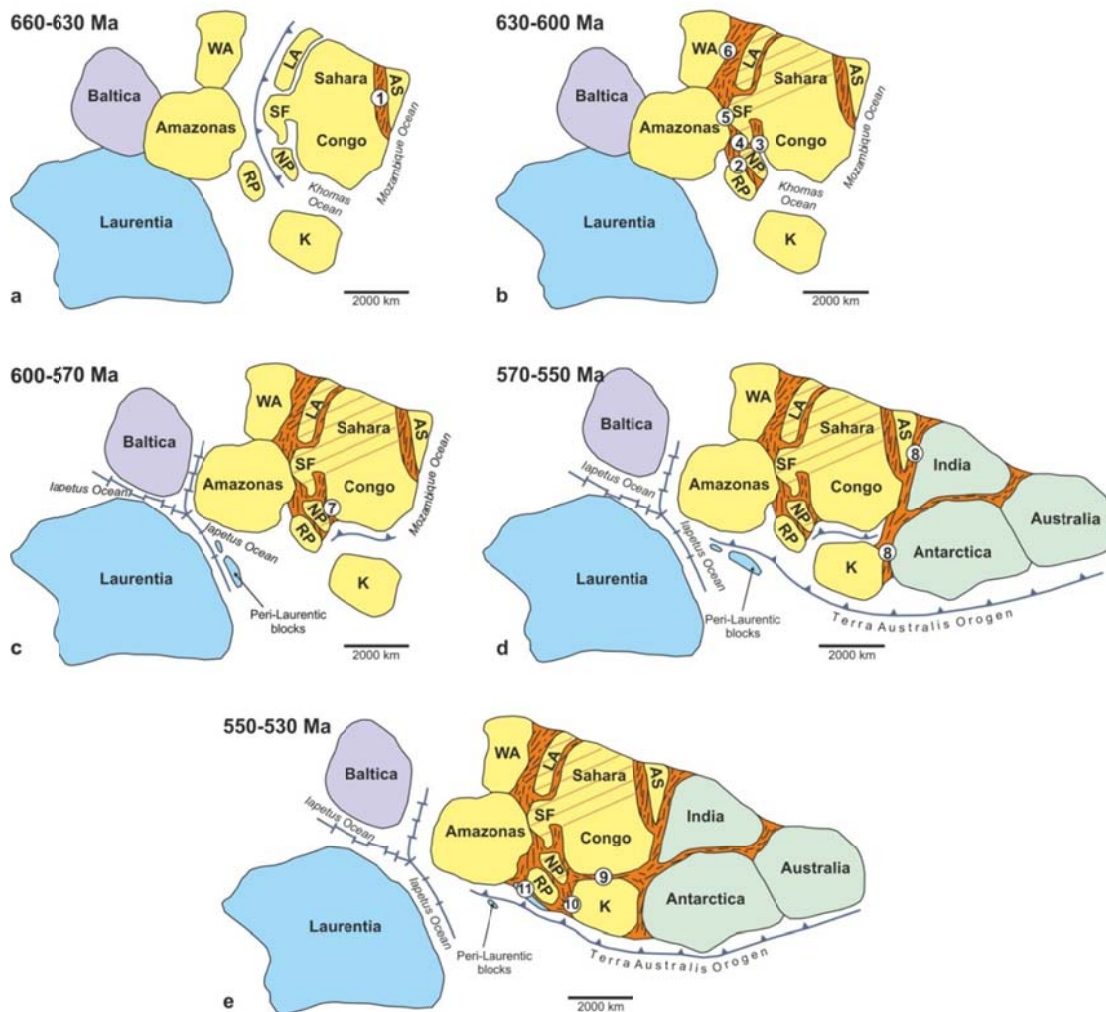
Fig. 8.4: Schematic tectonic and paleogeographic evolution of main crustal blocks (WA: West Africa, RP: Río de la Plata, K: Kalahari, NP: Nico Pérez, SF: São Francisco, LA: LATEA, AS: Arabian-Nubian Shield). Gondwana reconstructions modified after Meert and Lieberman (2004), Collins and Pisarevsky (2005), Tohver et al. (2006), Li et al. (2008), Pisarevsky et al. (2008), Pradhan et al. (2009) and Johansson (2014). Evolution of Laurentia, Baltica and Iapetus Ocean after Cawood et al. (2001), Hartz and Torsvik (2002), O´Brien and van der Pluijm (2012) and Lubnina et al. (2014). Terra Australis Orogen after Cawood (2005) and Cawood and Buchan (2007). See text for further explanations. Red dashed lines indicate areas that underwent metacratonization. 1: northern East African Orogen, 2: Dom Feliciano Belt, 3: Ribeira Belt, 4: Brasilia Belt, 5: Transbrasiliano Lineament, 6: Kandi Lineament, 7: Kaoko Belt, 8: East African-Antarctic Orogen, 9: Damara Belt, 10: Gariep and Saldania belts, 11: Pampean Belt.

On the southeastern margin of Western Gondwana, late Ediacaran-Cambrian subduction is recorded along the Terra Australis Orogen, which also extended up to the southern Eastern Gondwana margin (Cawood, 2005; Cawood and Buchan, 2007). Along this margin, several peri-Laurentic blocks were rifted away during the opening of the Iapetus Ocean and subsequently juxtaposed to the Gondwana margin during the Paleozoic (e.g., Dalla Salda et al., 1992; Dalziel et al., 1994). Among them, Pampia was one of the first amalgamated blocks (Ramos et al., 2010), which collided with the Río de la Plata Craton during the early Cambrian Pampean Orogeny (Fig. 8.3, 8.4e; Rapela et al., 1998, 2007; Siegesmund et al., 2010).

8.4. Implications for the supercontinent cycle

Late Neoproterozoic-Cambrian collisions leading to the final Gondwana assembly and coeval subduction along the Terra Australis Orogen suggest a coupling between internal collisional and marginal subduction processes, as indicated by Cawood and Buchan (2007). Likewise, these processes seemed to be strongly linked to the final stages of Rodinia break-up, particularly to the opening of the Iapetus Ocean (Pisarevsky et al., 2008). Hence, the evolution of Gondwana emphasizes the need to reevaluate the classical concept of supercontinent cycle (Nance *et al.*, 2014, and references therein), as supercontinent assembly and break-up do not necessarily represent alternating episodic processes but may overlap in time (Condie and Aster, 2013). As a first conclusion, the proposed Gondwana evolution (Fig. 8.4) allows ruling out the existence of the supercontinent Pannotia (Powell and Young, 1995; Dalziel, 1997), as Laurentia, Western and Eastern Gondwana were not part of a single supercontinent during the late Neoproterozoic. Indeed, Laurentia and Amazonas connections just represented remnants of the Rodinia assembly.
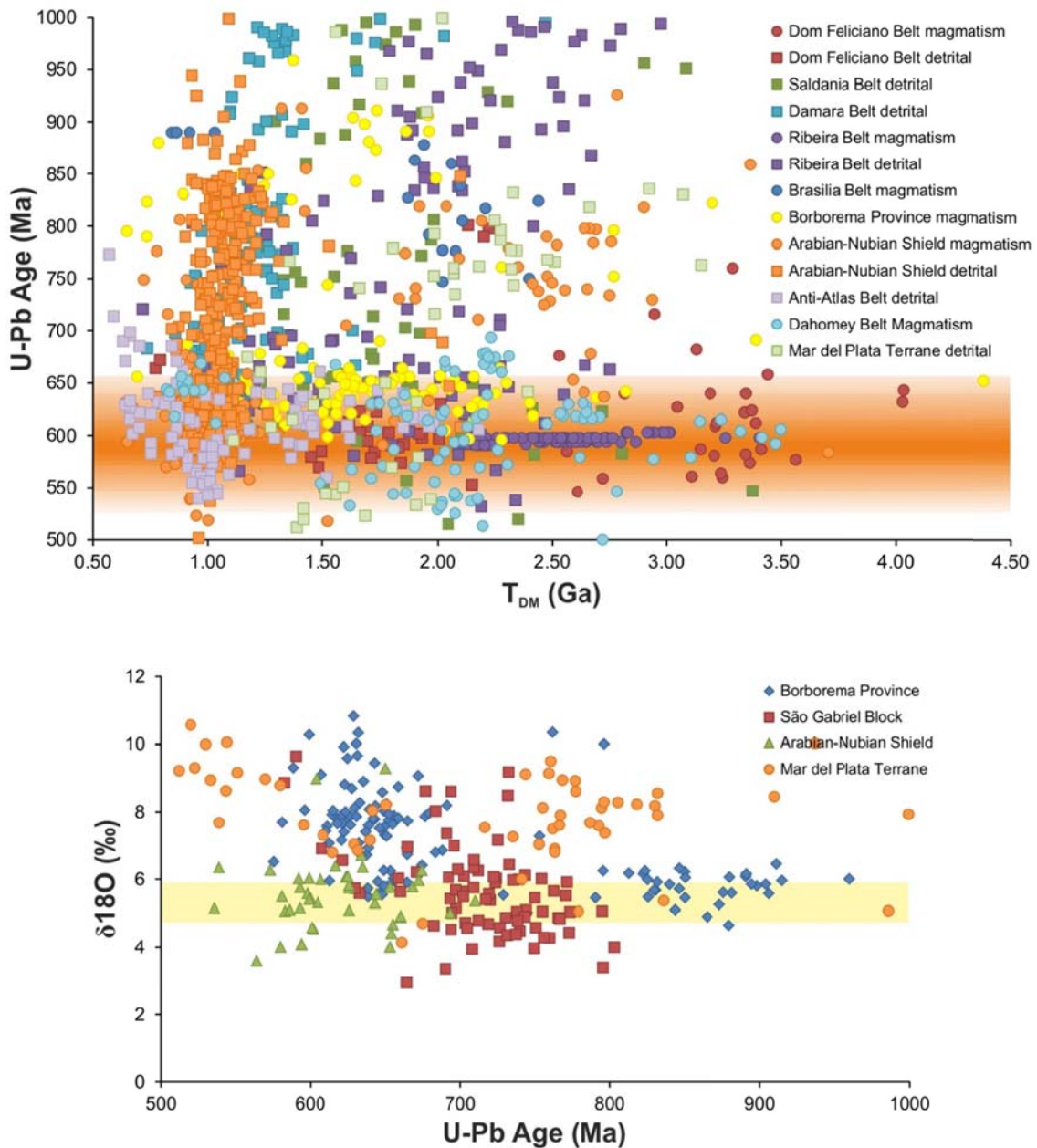
Fig. 8.5: Synthesis of available isotopic data from Neoproterozoic zircons of Brasiliano–Pan-African belts. a) Hf T_{DM} vs. U-Pb data after this work, Be'eri-Shlevin et al. (2010), Matteini et al. (2010), Morag et al. (2011), Rapela et al. (2011), Abati et al. (2012), Ali et al. (2012, 2013, 2015), Basei et al. (2013b), Frimmel et al. (2013), Ganade de Araujo et al. (2014c), Fernandes et al. (2015), Foster et al. (2015), Janasi et al. (2015), Pertille et al. (2015b) and Ganade et al. (2016). The timing of Gondwana amalgamation is indicated in orange. b) U-Pb vs. $\delta^{18}O$ data after Rapela et al. (2011), Ganade de Araujo et al. (2014c), Fortes de Lena et al. (2014) and Ali et al. (2015).

Two end-member processes were proposed for the formation of supercontinents, namely introversion and extroversion, depending on whether internal or external oceans of a supercontinent are closed to form the next one, respectively (Fig. 8.6; Nance et al., 1988; Hartnady, 1991; Hoffman,

1991; Murphy and Nance, 2003, 2005, 2013; Mitchell et al., 2012; Evans et al., 2016). In terms of paleogeography, introversion implies that the location of a supercontinent is the same of its predecessor, whereas the successor is located in the opposite hemisphere in the case of extroversion (Mitchell et al., 2012). For this purpose, large databases of U-Pb, Hf, Sm-Nd and O isotopic data have been typically analyzed (Murphy and Nance, 2003, 2005; Kemp et al., 2006; Collins et al., 2011; Roberts, 2012; Condie and Aster, 2013), as internal oceans comprise juvenile crust that formed after break-up of the previous supercontinent and external oceanic crust predates the previous supercontinent (Murphy and Nance, 2003, 2005). In the particular case of Gondwana, an extroversion model was proposed (Murphy and Nance, 2003, 2005, 2013; Evans et al., 2016).
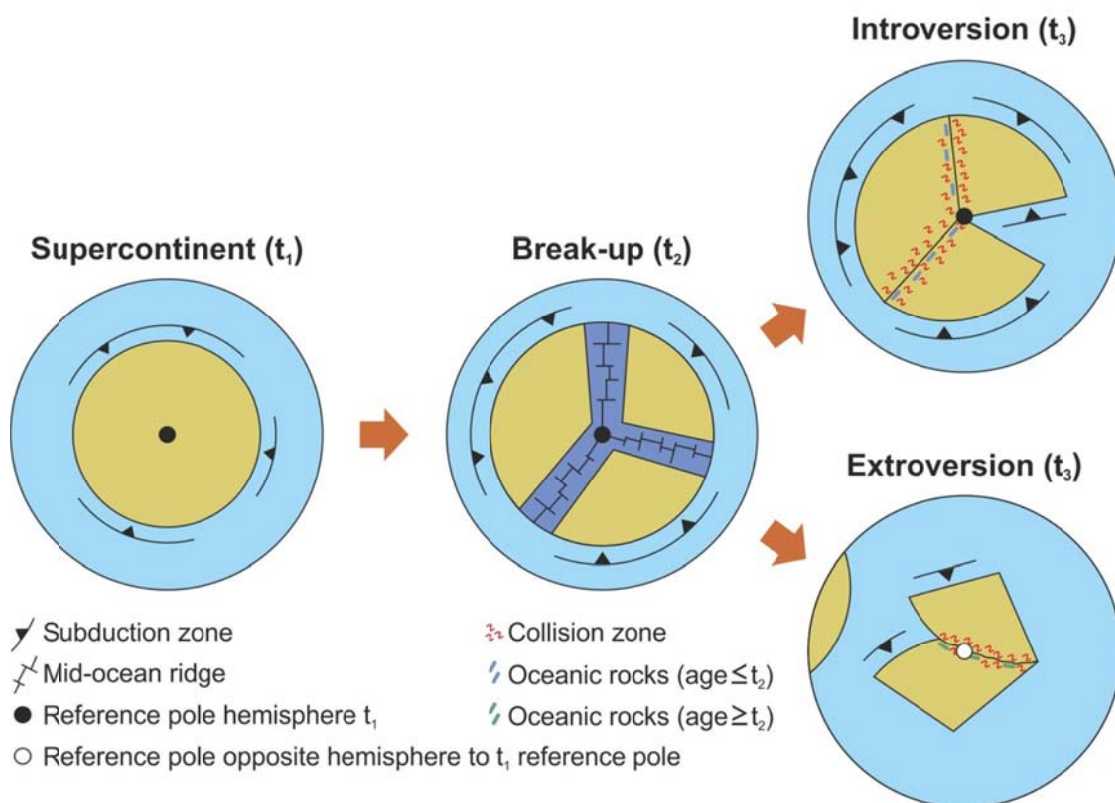
Fig. 8.6: Cartoons illustrating two end-member processes for the formation of supercontinents (modified after Murphy and Nance, 2003).

However, some points regarding Gondwana evolution have to be carefully considered. Though scarce, Tonian-Cryogenian mafic and ultramafic rocks showing ε_{Nd} values between ca. +3.5 and +7 are recorded between western Gondwanic blocks and indicate post-Rodinia oceanic crust

formation (Pedrosa-Soares et al., 1998; Saalmann et al., 2005; Paixão et al., 2008), although in some cases older remnants of oceanic crust are spatially associated as well (Pimentel et al., 2006). The presence of oceanic lithosphere older than the Cryogenian Rodinia break-up could be explained by geological evidences supporting that neither the Río de la Plata nor the Congo-São Francisco Craton was part of Rodinia (Fig. 8.1), thus being possible that the age of oceanic rocks predates Rodinia break-up. On the other hand, all paleogeographic reconstructions indicate that the amalgamation of Western Gondwana cratons took place in almost the same place where they were positioned since Rodinia break-up (Li et al., 2008; Evans, 2009; Evans et al., 2016). Hence, the amalgamation of Western Gondwana resulted from introversion, although extroversion can still be considered valid for the amalgamation of Western and Eastern Gondwana based on paleogeographic reconstructions (Tohver et al., 2006; Li et al., 2008; Evans, 2009) as originally indicated by Hoffman (1991). Consequently, the assembly of Gondwana resulted from a combination of introversion and extroversion.

-CHAPTER 9-

General conclusions

Based on the aims presented in Section 1.1, the main conclusions are summarized in this chapter. These results and interpretations are partially included in contributions that resulted from this work, and are thus integrated herein.

The Nico Pérez Terrane mostly originated from Archean episodic crustal growth and underwent crustal reworking during the Proterozoic, which is recorded by the dominance of Archean Hf model ages and several Proterozoic magmatic events. In contrast, U-Pb and Hf data reveal that the Piedra Alta Terrane (i.e., Río de la Plata Craton) is made up of juvenile Paleoproterozoic continental crust, thus supporting the allochthony of the Nico Pérez Terrane regarding the Río de la Plata Craton. The Archean crust of the Nico Pérez Terrane underwent multistage magmatism at ca. 2.2-2.0 Ga and subsequent high- to medium grade metamorphism, prior to magmatism at 1.7 Ga. Metavolcano-sedimentary units indicate the existence of Mesoproterozoic events, which could be related to intracontinental magmatism. During the Brasiliano–Pan-African Orogeny, the Nico Pérez Terrane underwent further crustal reworking recorded by widespread late Neoproterozoic magmatism, metamorphism and deformation. Based on similarities in terms of tectonostratigraphy as well as isotopic fingerprint, the Nico Pérez Terrane shows an African crustal affinity and probably derived from the southwestern margin of the Congo Craton. After Cryogenian rifting from the Congo Craton, the Nico Pérez was accreted to the eastern Río de la Plata Craton and underwent further crustal reworking during the evolution of the Dom Feliciano Belt.

Detrital zircon data from the metasedimentary sequences of the southwestern Dom Feliciano Belt indicate a Neoproterozoic deposition age older than ca. 600 Ma for the schist belt, predating deposition of late Ediacaran post-collisional sequences of the foreland basin. U-Pb

137

detrital zircon age distributions and model ages indicate that the basement of the Nico Pérez Terrane was the main source of both sequences. Similarities of Archean and Proterozoic events recorded in the Nico Pérez Terrane basement and the overlying metasedimentary cover of the western Dom Feliciano Belt further support an African derivation. Comparison with available detrital zircon data from the southeastern Dom Feliciano Belt suggests that the Congo-Río de la Plata amalgamation predates the accretion of the Kalahari Craton during Gondwana assembly, as the input of Kalahari-derived detritus is only recorded during the late Ediacaran in the southeasternmost post-collisional sequences.

The evolution of the Sarandí del Yí Shear Zone records progressive strain localization under retrograde metamorphic conditions during crustal exhumation. The onset of the deformation is related to the collision of the Río de la Plata and Nico Pérez Terrane at 630-625 Ma, giving rise to dextral shearing up to 596 Ma along the Sarandí del Yí Shear Zone under upper to middle amphibolite conditions in a post-collisional setting. Subsequent sinistral shearing took place between 594-584 Ma under lower amphibolite to upper greenschist facies conditions, which was followed by emplacement of the Sierra de las Ánimas Complex and the Cerro Caperuza granite. Further deformation under brittle conditions was recorded after ca. 570 Ma. On the other hand, strain partitioning and localization, magmatism and fluid circulation were identified as key processes that have to be evaluated when assessing the timing of deformation of crustal-scale shear zones.

The Dom Feliciano Belt records inclined transpression and strain partitioning. The main phase of deformation, metamorphism and associated exhumation is recorded at ca. 630-600 Ma, resulting from to the collision of the Río de la Plata and Congo cratons. Subsequent sinistral shearing along N- to NNE-striking shear zones gave rise to further deformation up to ca. 584 Ma, and is also contemporaneous with sinistral shearing along the Sarandí del Yí Shear Zone. All these

shear zones record progressive strain localization and retrograde conditions of deformation during crustal exhumation. The onset of sinistral shearing in the Dom Feliciano Belt is related to the onset of convergence between the Kalahari Craton and Río de la Plata-Congo cratons, which is well-documented in the Damara Belt. The Kaoko Belt comprised the foreland domain of the Dom Feliciano Belt and its evolution resulted from deformation migration towards the foreland. Therefore, the Kaoko Belt also records sinistral shearing postdating the main phase of crustal shortening, being both phases younger than their respective counterparts in the Dom Feliciano Belt.

An integral model for the amalgamation of Gondwana is presented based on available geological, geochronological, isotopic and paleomagnetic data. The amalgamation of the Río de la Plata and Congo cratons at ca. 630 Ma gave rise to the first Gondwana nucleus and was succeeded by the assembly of the Amazonas and West African cratons up to 600 Ma. These first collisional phases were coeval with the beginning of the Iapetus Ocean opening during late stages of Rodinia break-up. The Kalahari Craton was lately incorporated into Western Gondwana, succeeding collisional orogenies along the East African/Antartic Orogen between Western and Eastern Gondwana since 580 Ma. The latter took place contemporaneously with the onset of subduction along the Terra Australis Orogen, which implied the accretion of several peri-Laurentic blocks to the margin of Gondwana during the Paleozoic. As a corollary, the existence of Pannotia can be ruled out, as the final amalgamation of Gondwana postdates latest Laurentia-Gondwana connections.

-References-

Abati, J., Aghzer, A.M., Gerdes, A., Ennih, N. 2012. Insights on the crustal evolution of the West African Craton from Hf isotopes in detrital zircons from the Anti-Atlas belt. Precambrian Res. 212-213, 263-274.

Abdesalam, M.G., Liégeois, J.-P., Stern, R.J. 2002. The Saharan Metacraton. J. Afr. Earth Sci. 34, 119-136.

Ali, K., Andresen, A., Manton, W.I., Stern, R.J., Omar, S.A., Maurice, A.E. 2012. U-Pb zircon dating and Sr-Nd-Hf isotopic evidence to support a juvenile origin of the ~634 Ma El Shalul granitic gneiss dome, Arabian-Nubian Shield. Geol. Mag. 149, 783-797.

Ali, K.A., Wilde, S.A., Stern, R.J., Moghazi, A.-K.M., Ameen, S.M.M. 2013. Hf isotopic composition of single zircons from Neoproterozoic arc volcanics and post-collision granites, Eastern Desert of Egypt: Implications for crustal growth and recycling in the Arabian-Nubian Shield. Precambrian Res. 239, 42-55.

Ali, K.A., Zoheir, B.A., Stern, R.J., Andresen, A., Whitehouse, M.J., Bishara, W.W. 2015. Lu-Hf and O isotopic compositions on single zircons from the North Eastern Desert of Egypt, Arabian-Nubian Shield: Implications for crustal evolution. Gondwana Res. 32, 181-192.

Alkmim, F.F., Marshak, S., Fonseca, M.A. 2001. Assembling West Gondwana in the Neoproterozoic: Clues from the São Francisco craton region, Brazil. Geology 29, 319-322.

Allmendinger, R.W., Cardozo, N., Fisher, D. 2012. Structural geology algorithms: Vectors and tensors in structural geology. Cambridge University Press, Cambridge.

Almeida, F.F.M., Amaral, G., Cordani, U.G., Kawashita, K. 1973. The Precambrian evolution of the South American cratonic margin, South of Amazonas River. In: Nairn, A.C.M., Kanes, W.H., Stehli, F.G. (eds.) The Ocean Basins and Margins. Plenum, New York, 411-446.

Almeida, F.F.M., Hasui, Y., Brito Neves, B.B., Fuck, R.A. 1981. Brazilian structural provinces: an introduction. Earth-Sci. Rev. 17, 1-29.

Almeida, R.P., Janikian, L., Fragoso-Cesar, A.R.S., Fambrini, G.L. 2010. The Ediacaran to Cambrian Rift System of Southeastern South America: Tectonic Implications. J. Geol. 118, 145-161.

Arrighetti, R., Pena, S., Rossi, P., Vaz Chávez, N. 1981. Estudio Geológico y Minero de la Región de Minas. Dirección Nacional de Minería y Geología, Montevideo.

Aubet, N., Pecoits, E., Bekker, A., Gingras, M.K., Zwingmann, H., Veroslavsky, G., de Santa Ana, H., Kunhauser, K.O. 2012. Chemostratigraphic constraints on early Ediacaran carbonate ramp dynamics, Río de la Plata Craton, Uruguay. Gondwana Res. 22, 1073-1090.

Aubet, N., Pecoits, E., Heaman, L.M., Veroslavsky, G., Gingras, M.K., Kunhauser, K.O. 2014. Ediacaran in Uruguay: Facts and controversies. J. South Am. Earth Sci. 55, 43-57.

Bak, J., Kortsgård, J., Sørensen, K. 1975. A major shear zone within the Nagssugtoqidian of west Greenland. Tectonophysics 27, 191-209.

Bartholomew, L.T. 2008. Paleomagnetism of Neoproteozoic intraplate igneous rocks in the southwest Kalahari Craton, Namibia and South Africa. M.Sc. Thesis, University of Texas at Austin.

Basei, M.A.S., Siga Jr, O., Masquelin, H., Harara, O.M., Reis Neto, J.M., Preciozzi, F. 2000. The Dom Feliciano Belt (Brazil-Uruguay) and its Foreland (Río de la Plata Craton): framework, tectonic evolution and correlations with similar terranes of southwestern Africa. In: Cordani, U., Milani, E., Thomaz Filho, A., Campos, D. (eds.) Tectonic evolution of South America. 31° International Geological Congress, Rio de Janeiro, 311-334.

Basei, M.A.S., Frimmel, H.E., Nutman, A.P., Preciozzi, F., Jacob, J. 2005. A connection between the Neoproterozoic Dom Feliciano (Brazil/Uruguay) and Gariep (Namibia/South Africa) orogenic belts - evidence from a reconnaissance provenance study. Precambrian Res. 139, 195-221.

Basei, M.A.S., Frimmel, H.E., Nutman, A.P., Preciozzi, F. 2008. West Gondwana amalgamation based on detrital zircon ages from Neoproterozoic Ribeira and Dom Feliciano belts of South America and comparison with coeval sequences from SW Africa. In: Pankhurst, R.J., Trouw, R.A.J., Brito Neves,

B.B., de Wit, M.J. (eds.) West Gondwana: Pre-Cenozoic correlations across the South Atlantic region. Geol. Soc. Spec. Publ., London, 294, 239-256.

Basei, M.A.S., Peel, E., Sánchez Bettucci, L., Preciozzi, F., Nutman, A.P. 2011a. The basement of the Punta del Este Terrane (Uruguay): an African Mesoproterozoic fragment at the eastern border of the South American Río de la Plata craton. Int. J. Earth Sci. 100, 289-304.

Basei, M.A.S., Campos Neto, M.C., Castro, N.A., Nutman, A.P., Wemmer, K., Yamamoto, M.T., Hueck, M., Osako, L., Siga, O., Pasarelli, C.R. 2011b. Tectonic evolution of the Brusque Group, Dom Feliciano belt, Santa Catarina, Southern Brazil. J. South Am. Earth Sci. 32, 324-350.

Basei, M.A.S., Sánchez Bettucci, L., Peel, E., Muzio, R. 2013a. Geocronología U-Pb-LA-ICP-MS en circones del Complejo Granítico Santa Teresa, Terreno Punta del Este. 7° Congreso Uruguayo de Geología, Montevideo.

Basei, M.A.S., Campos Neto, M.C., Pacheco Lopes, A., Nutman, A.P., Liu, D. 2013b. Polycyclic evolution of Camboriú Complex migmatites, Santa Catarina, Southern Brazil: integrated Hf isotopic and U-Pb age zircon evidence of episodic reworking of a Mesoarchean juvenile crust. Braz. J. Geol. 43, 427-443.

Bates, R.L., Jackson, J.A. 1980. Glossary of geology, 2nd edition. American Geological Institute, Virginia.

Bea, F., Montero, P., González-Lodeiro, F., Talavera, C. 2003. Zircon inheritance reveals exceptionally fast crustal magma generation processes in Central Iberia during the Cambro-Ordovician. J. Petrol. 48, 2327-2339.

Becker, T., Hansen, B.T., Weber, K., Wiegand, B. 1996. U-Pb and Rb-Sr isotopic data for the Mooirivier Complex, Weener Igneous Suite and Gaub Valley Formation (Rehoboth Sequence) in the Nauchas area and their significance for Paleoproterozoic crustal evolution in Namibia. Communs. Geol. Surv. Namibia 11, 33-48.

Becker, T., Diedrichs, B., Hansen, B.T., Weber, K. 2000. Weener Igneous Complex: geochemistry and implications for the evolution of the Palaeoproterozoic Rehoboth basement inlier; Namibia. Communs. Geol. Surv. Namibia 12, 43-55.

Becker, T., Wiegand, B., Hansen, B.T., Weber, K. 2004. Sm/-Nd, Rb/-Sr and U/-Pb data from the Rehoboth Basement Inlier, Namibia: Evidence of a Paleoproterozoic magmatic arc. Communs. Geol. Surv. Namibia 13, 75-84.

Be'eri-Shlevin, Y., Katzir, Y., Blichert-Toft, J., Kleinhanns, I., Whitehouse, M.J. 2010. Nd-Sr-Hf-O isotope provinciality in the northernmost Arabian-Nubian Shield: implications for crustal evolution. Contrib. Mineral. Petrol. 160, 181-201.

Bento dos Santos, T.M., Muhná, J.M., Tassinari, C.C.G., Fonseca, P.E., Dias Neto, C. 2010. Thermochronology of central Ribeira Fold Belt, SE Brazil: Petrological and geochronological evidence for long-term high temperature maintenance during Western Gondwana amalgamation. Precambrian Res. 180, 285-298.

Bento dos Santos, T.M., Tassinari, C.C.G., Fonseca, P.E. 2015. Diachronic collision, slab break-off and long-term high thermal flux in the Brasiliano–Pan-African orogeny: Implications for the geodynamic evolution of the Mantiqueira Province. Precambrian Res. 260, 1-22.

Berger, A., Stünitz, H. 1996. Deformation mechanisms and reaction of hornblende: examples from the Bergell tonalite (Central Alps). Tectonophysics 257, 149-174.

Berger, J., Ouzegane, K., Bendaoud, A., Liégois, J.-P., Kiénast, J.-K., Bruguier, O., Caby, R. 2014. Continental subduction recorded by Neoproterozoic eclogite and garnet amphibolites from Western Hoggar (Tassendjanet terrane, Tuareg Shield, Algeria). Precambrian Res. 247, 139-158.

Black, R., Liégeois, J.-P. 1993. Cratons, mobile belts, alkaline rocks and continental lithospheric mantle: the Pan-African testimony. J. Geol. Soc. London 150, 89-98.

Black, L. P., Kamo, S.L., Allen, C.M., Davis, D.W., Alenikoff, J.N., Valley, J.W., Mundif, R., Campbell, I.H., Korsch, R.J., Williams, I.S., Foudoulis, C. 2004. Improved $^{206}Pb/^{238}U$ microprobe geochronology by the monitoring of trace element related matrix effect; SHRIMP, ID-TIMS, ELA-ICP-MS and oxygen isotope documentation for a series of zircon standards. Chem. Geol. 205, 115-140.

Blanco, G., Rajesh, H.M., Gaucher, C., Germs, G.J.B., Chemale Jr, F. 2009. Provenance of the Arroyo del Soldado Group (Ediacaran to Cambrian, Uruguay): Implications for the paleogeographic evolution of southwestern Gondwana. Precambrian Res. 171, 57-73.

Blanco, G., Germs, G.J.B., Rajesh, H.M., Chemale Jr, F., Dussin, I.A., Justino, D. 2011. Provenance and paleogeography of the Nama Group (Ediacaran to early Palaeozoic, Namibia): Petrography, geochemistry and U-Pb detrital zircon geochronology. Precambrian Res. 187, 15-32.

Blichert-Toft, J., Albarède, F. 1997. The Lu-Hf isotope geochemistry of chondrites and the evolution of the mantle-crust system. Earth Planet. Sci. Lett. 148, 243-258.

Boehnke, P., Watson, E.B., Trail, D., Harrison, T.M., Schmitt, A.K. 2013. Zircon saturation re-revisited. Chem. Geol. 351, 324-334.

Bonamici, C.E., Kozdon, R., Ushikubo, T., Valley, J.W. 2014. Intragrain oxygen isotope zoning in titanite by SIMS: cooling rates and fluid infiltration along the Carthage-Colton Mylonite Zone, Adirondack Mountains, NY, USA. J. Metamorph. Geol. 32, 71-92.

Booker, J.R., Favetto, A., Pomposiello, M.C. 2004. Low electrical resistivity associated with plunging of the Nazca flat slab beneath Argentina. Nature 429, 399-403.

Bossi, J. 1966. Geología del Uruguay. Departamento de Publicaciones de la Universidad de la República, Colección Ciencias, Montevideo.

Bossi, J., Campal, N. 1992. Magmatismo y tectónica transcurrente durante el Paleozoico inferior del Uruguay. In: Gutiérrez, J., Saavedra, J., Rábano, I. (eds.) Paleozoico Inferior de Ibero-América. Universidad de Extremadura, Alicante, 343-356.

Bossi, J., Gaucher, C. 2004. The Cuchilla Dionisio Terrane, Uruguay: An allochtonous block accreted in the Cambrian to SW-Gondwana. Gondwana Res. 7, 661-674.

Bossi, J., Cingolani, C. 2009. Extension and general evolution of the Río de la Plata Craton. In: Gaucher, C., Sial, A.N., Halverson, G.P., Frimmel, H.E. (eds.) Neoproterozoic-Cambrian tectonics, global change and evolution: a focus on southwestern Gondwana. Elsevier, Amsterdam, 73-85.

Bozcurt, E., Satir, M., Buğdaycioğlu, Ç. 2011. Surprisingly young Rb/Sr ages from the Simav extensional detachment fault zone, northern Menderes Massif, Turkey. J. Geodyn. 52, 406-431.

Brito Neves, B.B., Cordani, U.G. 1991. Tectonic evolution of South America during the Late Proterozoic. Precambrian Res. 53, 23-40.

Brito Neves, B.B., Fuck, R.A. 2013. Neoproterozoic evolution of the South-American platform. J. South Am. Earth Sci. 47, 72-89.

Brito Neves, B.B., Fuck, R.A. 2014. The basement of the South American platform: Half Laurentian (N-NW) + half Gondwanic (E-SE) domains. Precambrian Res. 244, 75-86.

Brito Neves, B.B., da Costa Campos Neto, M., Fuck, R.A. 1999. From Rodinia to Western Gondwana: An approach to the Brasiliano-Pan African Cycle and orogenic collage. Episodes 22, 155–166.

Campal, N., Schipilov A. 1995. The Illescas bluish quartz rapakivi granite (Uruguay-South America): some geological features. Symposium rapakivi granites and related rocks, Belem.

Campal, N., Schipilov, A. 1999. The eastern edge of the Río de la Plata Craton: A history of tangential collisions. In: Sinha, A.K. (ed.). Basement Tectonics 13, Springer, Dordrecht, 33-48.

Campal, N., Schipilov, A. 2005. La Formación Cerros de Aguirre: evidencias de magmatismo Vendiano en el Uruguay. Lat. Am. J. Sedimentol. Basin Anal. 12, 161-174.

Campos Neto, M.C., Cioffi, C.R., Moraes, R., Gonçalves da Motta, R., Siga Jr., O., Basei, M.A.S. 2010. Structural and metamorphic control on the exhumation of high-P granulites: the Carvalhos Klippe

example, from the oriental Andrelândia Nappe System, southern portion of the Brasilia Orogen, Brazil. Precambrian Res. 180, 125-142.

Carreras, J., Druguet, E. 1994. Structural zonation as a result of inhomogeneous non-coaxial deformation and its control on syntectonic intrusions: an example from the Cap de Creus area, eastern Pyrenees. J. Struct. Geol. 16, 1525-1534.

Carreras, J., Cosgrove, J.W., Druguet, E. 2013. Strain partitioning in banded and/or anisotropic rocks: Implications for inferring tectonic regimes. J. Struct. Geol. 50, 7-21.

Cawood, P.A. 2005. Terra Australis Orogen: Rodinia breakup and development of the Pacific and Iapetus margins of Gondwana during the Neoproterozoic and Paleozoic. Earth-Sci. Rev. 69, 249-279.

Cawood, P.A., Buchan, C. 2007. Linking accretionary orogenesis with supercontinent assembly. Earth-Sci. Rev. 82, 217-256.

Cawood, P.A., McCausland, P.J.A., Dunning, G.R. 2001. Opening Iapetus: Constraints from the Laurentian margin in Newfoundland. Geological Society of America Bulletin 113, 443-453.

Cembrano, J., González, G., Arancibia, G., Ahumada, I., Olivares, V., Herrera, V. 2005. Fault zone development and strain partitioning in an extensional strike-slip duplex: A case study from the Mesozoic Atacama fault system, Northern Chile. Tectonophysics 400, 105-125.

Chamberlain, K.R., Bowring, S.A. 2000. Apatite-feldspar U-Pb thermochronometer: a reliable, mid-range (~450°C), diffusion-controlled system. Chem. Geol. 172, 173-200.

Chemale Jr., F., Philipp, R.P., Dussin, I.A., Formoso, M.L.L., Kawashita, K., Berttotti, A.L. 2011. Lu-Hf and U-Pb age determination of Capivarita Anorthosite in the Dom Feliciano Belt, Brazil. Precambrian Res. 186, 114-126.

Chemale Jr., F., Mallmann, M., Bitencourt, M.F., Kawashita, K. 2012. Time constraints on magmatism along the Major Gercino Shear Zone, southern Brazil: Implications for West Gondwana reconstructions. Gondwana Res. 22, 184-199.

Cherniak, D.J. 1993. Lead diffusion in titanite and preliminary results on the effects of radiation damage on Pb transport. Chem. Geol. 110, 177-194.

Cherniak, D.J. 2000. Pb diffusion in rutile. Contrib. Mineral. Petrol. 139, 198-207.

Cherniak, D.J., Watson, E.B. 2000. Pb diffusion in zircon. Chem. Geol. 172, 5-24.

Chiglino, L., Gaucher, C., Sial, A.N., Bossi, J., Ferreira, V.P. 2008. Chemostratigraphy of Mesoproterozoic carbonates in the Nico Pérez Terrane (Río de la Plata Craton). 33° International Geological Congress, Oslo.

Cingolani, C.A. 2011. The Tandilia System of Argentina as a southern extension of the Río de la Plata craton: an overview. Int. J. Earth Sci. 100, 221-242.

Cingolani, C.A., Basei, M.A.S., Bossi, J., Piñeiro, D., Uriz, N.J. 2012. U-Pb (LA-ICP-MS) zircon age of the La Paz Granite (Pando Belt, Uruguay): an Upper Neoproterozoic magmatic event in the Río de la Plata Craton. 8° South American Symposium on Isotope Geology, Medellín.

Collins, A.S., Pisarevsky, S. 2005. Amalgamating eastern Gondwana: The evolution of the Circum-Indian orogens. Earth-Sci. Rev. 71, 229-270.

Collins, W.J., Belousova, E., Kemp, A.I.S., Murphy, B. 2011. Two contrasting Phanerozoic orogenic systems revealed by hafnium isotope data. Nature Geoscience 4, 333-337.

Colliston, W.P., Cornell, D.H., Schoch, A.E., Praekelt, H.E. 2015. Geochronological constraints on the Hartbees River Thrust and Augrabies Nappe: New insights into the assembly of the Mesoproterozoic Namaqua-Natal Province of Southern Africa. Precambrian Res. 265, 150-165.

Compston, W., Williams, I.S., Meyer, C. 1984. U-Pb geochronology of zircons from lunar breccia 73217 using a sensitive high mass-resolution ion microprobe. J. Geophys. Res. 89(S02), B525-B534.

Condie, K.C., Aster, R.C. 2013. Refinement of the supercontinent cycle with Hf, Nd and Sr isotopes. Geosci. Frontiers 4, 667-680.

Cordani, U.G., Brito Neves, B.B. 1982. The geologic evolution of South America during the Archaean and Early Proterozoic. Rev. Bras. Geociências 12, 78-88.

Cordani, U.G., D'Agrella-Filho, M.S., Brito Neves, B.B., Trindade, R.I.F. 2003. Tearing up Rodinia: the Neoproterozoic palaeogeography of South American cratonic fragments. Terra Nova 15, 350-359.

Corfu, F., Hanchar, J.M., Hoskin, P.W.O., Kinny, P. 2003. Atlas of zircon textures. In: Hanchar, J.M., Hoskin, P.W.O. (eds.) Zircon. Reviews in Mineralogy & Geochemistry, Mineralogical Society of America, Washington 53, 469-500.

Cornell, D.H., Thomas, R.J., Gibson, R., Moen, H.F.G., Moore, J.M., Reid, D.L. 2006. Namaqua-Natal Province. In: Johnson, M.R., Anhaeusser, C.R., Thomas, R.J. (eds.) The geology of South Africa. Geological Society of South Africa and Council for Geoscience, Johannesburg and Pretoria, 325-379.

Cornell, D.H., Pettersson, Å., Simonsen, S.L. 2012. Zircon U-Pb emplacement and Nd-Hf crustal residence ages of the Straussburg granite and Friersdale charnockite in the Namaqua-Natal Province, South Africa. S. Afr. J. Geol. 115, 465-484.

Cornell, D.H., van Schijndel, V., Simonsen, S.L., Frei, D. 2015. Geochronology of Mesoproterozoic hybrid intrusions in the Konkiep Terrane, Namibia, from passive to active continental margin in the Namaqua-Natal Wilson Cycle. Precambrian Res. 265, 166-188.

Cumming, G.L., Richards, J.R. 1975. Ore lead isotope ratios in a continuously changing Earth. Earth Planet. Sci. Lett. 28, 155-171.

Cunningham, W.D., Windley, B.F., Dorjnamjaa, D., Badamgarov, G., Saandar, M. 1996. A structural transect across the Mongolian Western Altai: Active transpressional mountain building in central Asia. Tectonics 15, 142-156.

da Silva, L.C., Hartmann, L.A., McNaughton, N.J., Fletcher, I.A. 1999. SHRIMP U/Pb zircon dating of Neoproterozoic granitic magmatism and collision in the Pelotas Batholith, southernmost Brazil. Int. Geol. Rev. 41, 531-551.

da Silva, L.C., McNaughton, N.J., Armstrong, R., Hartmann, L.A., Fletcher, I.R. 2005. The Neoproterozoic Mantiqueira Province and its African connections: a zircon-based U-Pb geochronologic subdivision for the Brasiliano/Pan-African systems of orogens. Precambrian Res. 136, 203-240.

Dahl, P.S. 1997. A crystal-chemical basis for Pb retention and fission-track annealing systematics in U-bearing minerals, with implications for geochronology. Earth Planet. Sci. Lett. 150, 277-290.

Dalla Salda, L., Bossi, J., Cingolani, C.A. 1988. The Río de la Plata cratonic region of southwestern Gondwanaland. Episodes 11, 263–269.

Dalla Salda, L.H., Dalziel, I.W.D., Cingolani, C.A., Varela, R. 1992. Did the Taconic Appalachians continue into southern South America?. Geology 20, 1059-1062.

Dalziel, I.W.D. 1997. Neoproterozoic-Paleozoic geography and tectonics: Review, hypothesis, environmental speculation. Geol. Soc. Am. Bull. 109, 16-42.

Dalziel, I.W.D., Dalla Salda, L.H., Gahagan, L.M. 1994. Paleozoic Laurentia-Gondwana interaction and the origin of the Appalachian-Andean mountain system. Geol. Soc. Am. Bull. 106, 243-252.

Dalziel, I.W.D., Mosher, S., Gahagan, L.M. 2000. Laurentia-Kalahari collision and the assembly of Rodinia. J. Geol. 108, 499-513.

de Oliveira, D.S., Sommer, C.A., Philipp, R.P., Fernandes de Lima, E., Basei, M.A.S. 2015. Post-collisional subvolcanic rhyolites associated with the Neoproterozoic Pelotas Batholith, southern Brazil. J. South Am. Earth Sci. 63, 84-100.

Debruyne, D., Hulsbosch, N., Van Wilderode, J., Balcaen, L., Vanhaecke, F., Muchez, P. 2015. Regional geodynamic context for the Mesoproterozoic Kibara Belt (KIB) and the Karagwe-Ankole Belt: Evidence from geochemistry and isotopes in the KIB. Precambrian Res. 264, 82-97.

Díaz-Azpiroz, M., Lloyd, G.E., Fernández, C. 2007. Development of latice preferred orientation in clinoamphiboles deformed under low-pressure metamorphic conditions. A SEM/EBSD study of metabasites from the Aracena metamorphic belt (SW Spain). J. Struct. Geol. 29, 629-645.

Dodson, M.H. 1973. Closure temperature in cooling geochronological and petrological systems. Contrib. Mineral. Petrol. 40, 254-274.

Dollinger, G., Blacic, J.D. 1975. Deformation mechanisms in experimentally and naturally deformed amphiboles. Earth Planet. Sci. Lett. 26, 409-416.

Drüppel, K., Littmann, S., Romer, R.L., Okrusch, M. 2007. Petrology and isotope geochemistry of the Mesoproterozoic anorthosite and related rocks of the Kunene Intrusive Complex, NW Namibia. Precambrian Res. 156, 1-31.

Dürr, S.B., Dingeldey, D.P. 1996. The Kaoko belt (Namibia): Part of a late Neoproterozoic continental-scale strike-slip system. Geology 24, 503-506.

Dunlap, W.J. 1997. Neocrystallization or cooling? $^{40}Ar/^{39}Ar$ ages of white micas from low-grade mylonites. Chem. Geol. 143, 181-203.

Eberlei, T., Habler, G., Wegner, W., Schuster, R., Körner, W., Thöni, M., Abart, R. 2015. Rb/Sr isotopic and compositional retentivity of muscovite during deformation. Lithos 227, 161-178.

Eglington, B.M. 2006. Evolution of the Namaqua-Natal Belt, southern Africa - A geochronological and isotope geochemical review. J. Afr. Earth Sci. 46, 93-111.

Elhlou, S., Belousova, E., Griffin, W.L., Pearson, N.J., O´Reilly, S.Y. 2006. Trace element and isotopic composition of GJ-red zircon standard by laser ablation. Geochim. Cosmochim. Acta 70, A158, doi: 10.1016/j.gca.2006.06.1383.

Elizalde, G. 1979. Carta Geológica de la Costa. Conservación y Mejora de Playas. Ministerio de Transporte y Obras Publicas, Programa de las Naciones Unidas para el Desarrollo y UNESCO, Montevideo, 101-235.

Ellero, A., Ottria, G., Marroni, M., Pandolfi, L., Cemal Göncüoğlu, M. 2015. Analysis of the North Anatolian Shear Zone in Central Pontides (northern Turkey): Insight for geometries and kinematics of deformation structures in a transpressional zone. J. Struct. Geol. 72, 124-141.

Ellis, J. 1998. The Precambrian supracrustal rocks of the Isla Cristalina de Rivera in northern Uruguay and their ore deposits. Heidelberger Geowissenschaftliche Abhandlungen, Heidelberg.

Ernst, R.E., Pereira, E., Hamilton, M.A., Pisarevsky, S.A., Rodriques, J., Tassinari, C.C.G., Teixeira, W., Van-Dunem, V. 2013. Mesoproterozoic intraplate magmatic "barcode" record of the Angola portion of the Congo Craton: newly dated magmatic events at 1505 and 1110 Ma and implications for Nuna (Columbia) supercontinent reconstructions. Precambrian Res. 230, 103-118.

Evans, D.A.D. 2009. The palaeomagnetically viable, long-lived and all-inclusive Rodinia supercontinent reconstruction. In: Murphy, J.B., Keppie, J.D., Hynes, A.J. (eds.) Ancient orogens and modern analogues. Geol. Soc. Spec. Publ., London, 327, 371-404,.

Evans, D.A.D., Li, Z.-X., Murphy, J.B. 2016. Four-dimensional context of Earth´s supercontinents. In: Li, Z.X., Evans, D.A.D., Murphy, J.B. (eds.) Supercontinent cycles through Earth history. Geol. Soc. Spec. Publ., London, 424, doi: 10.1144/SP424.12.

Fambrini, G.L., Fragoso-Cesar, A.R.S., Almeida, R.P., Riccomini, C. 2005. A Formaçao Barriga Negra (Ediacarano do Uruguai): caracterizaçao estratigráfica e correlaçao com unidades do estado do Rio Grande do Sul, Brasil. Rev. Bras. Geociências 35, 515-524.

Fedo, C.M., Sircombe, K.N., Rainbird, R.H. 2003. Detrital zircon analysis of the sedimentary record. In: Hanchar, J.M., Hoskin, P.W.O. (eds.) Zircon. Reviews in Mineralogy & Geochemistry, Mineralogical Society of America, Washington, 277-303.

Feistmantel, O. 1876. Notes on the age of some fossils of India. Rec. Geol. Soc. India 9, 28-42.

Fernandes, L.A.D., Koester, E. 1999. The Neoproterozoic Dorsal de Canguçu strike-slip shear zone: its nature and role in the tectonic evolution of southern Brazil. J. Afr. Earth Sci. 29, 3-24.

Fernandes, L.A.D., Tommasi, A., Porcher, C.C. 1992. Deformation patterns in the southern Brazilian branch of the Dom Feliciano Belt: a reappraisal. J. South Am. Earth Sci. 5, 77-96.

Fernandes, G.L.F., Schmitt, R.S., Bongiolo, E.M., Basei, M.A.S., Mendes, J.C. 2015. Unraveling the tectonic evolution of a Neoproterozoic-Cambrian active margin in the Ribeira Orogen (Se Brazil): U-Pb and Lu-Hf provenance data. Precambrian Res. 266, 337-360.

Fernández, C., Czeck, D.M., Díaz-Azpiroz, M. 2013. Testing the model of oblique tranpression with oblique extrusion in two natural cases: Steps and consequences. J. Struct. Geol. 54, 85-102.

Fisher, C.M., Vervoort, J.D., Hanchar, J.M. 2014. Guidelines for reporting zircon Hf isotopic data by LA-MC-ICPMS and potential pitfalls in the interpretation of these data. Chem. Geol. 363, 125-133.

Fitz Gerald, J.D., Stünitz, H. 1993. Deformation of granitoids at low metamorphic grade. I: Reactions and grain size reduction. Tectonophysics 221, 269-297.

Florisbal, L.M., Bitencourt, M.F., Nardi, L.V.S., Conceiçao, R.V. 2009. Early post-collisional granitic and coeval mafic magmatism of medium- to high-K tholeiitic affinity within the Neoproterozoic Southern Brazilian Shear Belt. Precambrian Res. 175, 135-148.

Florisbal, L.M., Janasi, V.A., Bitencourt, M.F., Heaman, L.M. 2012. Space-time relation of post-collisional granitic magmatism in Santa Catarina, southern Brazil: U-Pb LA-MC-ICP-MS zircon geochronology of coeval mafic-felsic magmatism related to the Major Gercinho Shear Zone. Precambrian Res. 216-219, 132-151.

Fortes de Lena, L.O., Pimentel, M.M., Philipp, R.P., Armstrong, R., Sato, K. 2014. The evolution of the Neoproterozoic São Gabriel juvenile terrane, southern Brazil based on high spatial resolution U-Pb ages and $\delta^{18}O$ data from detrital zircons. Precambrian Res. 247, 126-138.

Fossen, H., Tikoff, B. 1998. Extended models of transpression and transtension, and application to tectonic settings. In: Dewey, J.F., Holdsworth, R.E., Strachan, R.A. (eds.) Continental transpressional and transtensional tectonics. Geol. Soc. Spec. Pub., London, 135, 15-33.

Fossen, H., Tikoff, B., Teyssier, C. 1994. Strain modelling of transpressional and transtensional deformation. Norsk Geol. Tidsskr. 74, 134-145.

Foster, D.A., Goscombe, B.D., Gray, D.R. 2009. Rapid exhumation of deep crust in an obliquely convergent orogeny: The Kaoko Belt of the Damara Orogen. Tectonics 28, TC4002.

Foster, D.A., Goscombe, B.D., Newstead, B., Mapani, B., Mueller, P.A., Gregory, L.C., Muvangua, E. 2015. U-Pb age and Lu-Hf isotopic data of detrital zircons from the Neoproterozoic Damara sequence: Implications for Congo and Kalahari before Gondwana. Gondwana Res. 28, 179-190.

Fragoso Cesar, A.R.S. 1991. Tectônica de placas no ciclo Brasiliano: as orogenias dos cinturões Dom Feliciano e Ribeira no Rio Grande do Sul. Ph.D. Thesis, Universidade de São Paulo.

Fraser, G., Ellis, D., Eggins, S. 1997. Zirconium abundance in granulite-facies minerals, with implications for zircon geochronology in high-grade rocks. Geology 25, 607-610.

Frei, D., Gerdes, A. 2009. Precise and accurate in situ U-Pb dating of zircon with high sample throughput by automated LA-SF-ICP-MS. Chem. Geol. 261, 261-270.

Frei, R., Gaucher, C., Stolper, D., Canfield, D.E. 2013. Fluctuations in late Neoproterozoic atmospheric oxidation - Cr isotope chemostratigraphy and iron speciation of the late Ediacaran lower Arroyo del Soldado Group (Uruguay). Gondwana Res. 23, 797-811.

Frimmel, H.E., Frank, W. 1998. Neoproterozoic tectono-thermal evolution of the Gariep Belt and its basement, Namibia and South Africa. Precambrian Res. 90, 1-28.

Frimmel, H.E., Basei, M.A.S., Gaucher, C. 2011. Neoproterozoic geodynamic evolution of SW-Gondwana: a southern African perspective. Int. J. Earth Sci. 100, 323-354.

Frimmel, H.E., Basei, M.A.S., Correa, V.X., Mbangula, N. 2013. A new lithostratigraphic subdivision and geodynamic model for the Pan-African western Saldania Belt, South Africa. Precambrian Res. 231, 218-235.

Frisicale, M.C., Martínez, F.J., Dimieri, L.V., Dristas, J.A. 2005. Microstructural analysis and P-T conditions of the Azul megashear zone, Tandilia, Buenos Aires province, Argentina. J. South Am. Earth Sci. 19, 433-444.

Frisicale, M.C., Dimieri, L.V., Dristas, J.A., Araujo, V., Fortunatti, N. 2012. Microstructural and geochemical analysis of Paleoproterozoic pseudotachylytes in Río de la Plata craton, Tandilia belt, Argentina. Geol. Acta 10, 85-101.

Fritz, H., Abdesalam, M., Ali, K.A., Bingen, B., Collins, A.S., Fowler, A.R., Ghebreab, W., Hauzenberger, C.A., Johnson, P.R., Kusky, T.M., Macey, P., Muhongo, S., Stern, R.J., Viola, G. 2013. Orogen styles in the East African Orogen: A review of the Neoproterozoic to Cambrian tectonic evolution. J. Afr. Earth Sci. 86, 65-106.

Frost, B.R., Chamberlain, K.R., Schumacher, J.C. 2000. Sphene (titanite): phase relations and role as a geochronometer. Chem. Geol. 172, 131-148.

Fuhrmann, U., Lippolt, H.J., Hess, J.C. 1987. Examination of some proposed K-Ar standards: $^{40}Ar/^{39}Ar$ analyses and conventional K-Ar-data. Chem. Geol. 66, 41-51.

Ganade, C.E., Cordani, U.G., Agbossoumounde, Y., Caby, R., Basei, M.A.S., Weinberg, R.F., Sato, K. 2016. Tightening-up NE Brazil and NW Africa connections: New U-Pb/Lu-Hf zircon data of a complete plate tectonic cycle in the Dahomey belt of the West Gondwana Orogen in Togo and Benin. Precambrian Res. 276, 24-42.

Ganade de Araujo, C.E., Weinberg, R.F., Cordani, U.G. 2014a. Extruding the Borborema Province (NE-Brazil): a two-stage Neoproterozoic collision process. Terra Nova 26, 157-168.

Ganade de Araujo, C.E., Rubatto, D., Hermann, J., Cordani, U.G., Caby, R., Basei, M.A.S. 2014b. Ediacaran 2500-km-long synchronous deep continental subduction in the West Gondwana Orogen. Nature Communications 5, 5198, doi: 10.1038/ncomms6198.

Ganade de Araujo, C.E., Cordani, U.G., Weinberg, R.F., Basei, M.A.S., Armstrong, R., Sato, K. 2014c. Tracing Neoproterozoic subduction in the Borborema Province (NE-Brazil): Clues from U-Pb geochronology and Sr-Nd-Hf-O isotopes on granitoids and migmatites. Lithos 202-203, 167-189.

Gastal, M.C.P., Lafon, J.M., Hartmann, L.A., Koester, E. 2005. Sm-Nd isotopic compositions as a proxy for magmatic processes during the Neoproterozoic of the southern Brazilian shield. J. South Am. Earth Sci. 18, 255-276.

Gaucher, C. 2000. Sedimentology, palaeontology, and stratigraphy of the Arroyo del Soldado Group (Vendian to Cambrian, Uruguay). Beringeria 26, 1-120.

Gaucher, C., Boggiani, P.C., Sprechmann, P., Sial, A.N., Fairchild, T. 2003. Integrated correlation of the Vendian to Cambrian Arroyo del Soldado and Corumbá Groups (Uruguay and Brazil): palaeogeographic, palaeoclimatic and palaeobiologic implications. Precambrian Res. 120, 241-278.

Gaucher, C., Chiglino, L., Pecoits, E. 2004. Southernmost exposures of the Arroyo del Soldado Group (Vendian to Cambrian, Uruguay): Palaeogeographic implications for the amalgamation of W-Gondwana. Gondwana Res. 7, 701-714.

Gaucher, C., Finney, S.C., Poiré, D.G., Valencia, V.A., Grove, M., Blanco, G., Pamoukaghlián, K., Gómez Peral, L. 2008a. Detrital zircon age of Neoproterozoic sedimentary successions of Uruguay and Argentina: Insights into the geological evolution of the Río de la Plata Craton. Precambrian Res. 167, 150-170.

Gaucher, C., Blanco, G., Chiglino, L., Poiré, D., Germs, G.J.B. 2008b. Acritarchs of Las Ventanas Formation (Ediacaran, Uruguay): Implications for the timing of coeval rifting and glacial events in western Gondwana. Gondwana Res. 13, 488-501.

Gaucher, C., Frimmel, H.E., Germs, G.J.B. 2010. Tectonic events and palaeogeographic evolution of southwestern Gondwana in the Neoproterozoic and Cambrian. In: Gaucher, C., Sial, A.N., Halverson, G.P., Frimmel, H.E. (eds.) Neoproterozoic-Cambrian tectonics, global change and

evolution, a focus on southwestern Gondwana. Developments in Precambrian Geology, Elsevier, 295-318.

Gaucher, C., Frei, R., Chemale Jr, F., Frei, D., Bossi, J., Martínez, G., Chiglino, L., Cernuschi, F. 2011a. Mesoproterozoic evolution of the Río de la Plata Craton in Uruguay: at the heart of Rodinia?. Int. J. Earth Sci. 100, 273-288.

Gaucher, C., Frei, R., Sial, A.N., Cabrera, J. 2011b. Contrasting Sr isotope composition of Paleo- and Neoproterozoic high-Sr limestone successions from the Nico Pérez Terrane, Uruguay. Gondwana 14, abstracts.

Gaucher, C., Sial, A.N., Frei, R., Ferreira, V.P., Frei, D., Bossi, J., Cabrera, J. 2014a. Magmatismo anorogénico ediacárico. In: Bossi, J., Gaucher, C. (eds.) Geología del Uruguay, Tomo 1: Predevónico. Universidad de la República, Montevideo, 283-298.

Gaucher, C., Frei, R., Frei, D., Blanco, G. 2014b. Edad, proveniencia y paleogeografía de la Formación San Carlos. In: Bossi, J., Gaucher, C. (eds.) Geología del Uruguay, Tomo 1: Predevónico. Universidad de la República, Montevideo, 409-418.

Gaucher, C., Bossi, J., Frei, R., Remus, M., Piñeyro, D. 2014c. Terreno Cuchilla Dionisio: bloque septentrional. In: Bossi, J., Gaucher, C. (eds.) Geología del Uruguay, Tomo 1: Predevónico. Universidad de la República, Montevideo, 377-400.

Gehrels, G. 2014. Detrital zircon U-Pb geochronology applied to tectonics. Annu. Rev. Earth Planet. Sci. 42, 127-149.

Geisler, T., Schaltegger, U., Tomaschek, F. 2007. Re-equilibration of zircon in aqueous fluids and melts. Elements 3, 43-50.

Gerdes, A., Zeh, A. 2006. Combined U-Pb and Hf isotope LA-(MC-)ICP-MS analyses of detrital zircons: comparison with SHRIMP and new constraints for the provenance and age of an Armorican metasediment in Central Germany. Earth Planet. Sci. Lett. 249, 47-61.

Giambiagi, L., Mescua, J., Bechis, F., Martínez, A., Folguera, A. 2011. Pre-Andean deformation of the Precordillera southern sector, southern Central Andes. Geosphere 7, 219-239.

Gianotti, V., Oyhantçabal, P., Spoturno, J., Wemmer, K. 2010. Caracterización geológico-estructural y estudio microtectónico de las zonas de cizalla de Colonia. 6° Congreso Uruguayo de Geología, Lavalleja.

Gibson, R.G. 1990. Nucleation and growth of retrograde shear zones: an example from the Needle Mountains, Colorado, U.S.A. J. Struct. Geol. 12, 339-350.

Giletti, B.J. 1974. Studies in diffusion I: Argon in phlogopite mica. In: Hofmann, A.W., Giletti, B.J., Yoder Jr., H.S., Yund, R.A. (eds.) Geochemical transport and kinetics. Carnegie Institution of Washington, Washington, 634, 107-116.

Goodenough, K.M., Park, R.G., Krabbendam, M., Myers, J.S., Wheeler, J., Loughlin, S.C., Crowley, Q.G., Friend, C.R.L., Beach, A., Kinny, P.D., Graham, R.H. 2010. The Laxford Shear Zone: an end-Archean terrane boundary?. In: Law, R.D., Butler, R.W.H., Holdsworth, R.E., Krabbendam, M., Strachan, R.A. (eds.) Continental Tectonics and Mountain Building: The Legacy of Peach and Horne. Geol. Soc. Spec. Pub., London, 335, 103-120.

Goscombe, B., Gray, D.R. 2007. The Coastal Terrane of the Kaoko Belt, Namibia: Outboard arc-terrane and tectonic significance. Precambrian Res. 155, 139-158.

Goscombe, B., Gray, D.R. 2008. Structure and strain variation at mid-crustal levels in a transpressional orogen: A review of Kaoko Belt structure and the character of West Gondwana amalgamation and dispersal. Gondwana Res. 13, 45-85.

Goscombe, B., Gray, D.R. 2009. Metamorphic responses in orogens of different obliquity, scale and geometry. Gondwana Res. 15, 151-167.

Goscombe, B., Hand, M., Gray, D., Mawby, J. 2003a. The metamorphic architecture of a transpressional orogen: the Kaoko Belt, Namibia. J. Petrol. 44, 679-711.

Goscombe, B., Hand, M., Gray, D. 2003b. Structure of the Kaoko Belt, Namibia: progressive evolution of a classical transpressional orogen. J. Struct. Geol. 25, 1049-1081.

Goscombe, B., Gray, D.R., Armstrong, R., Foster, D.A., Vogl, J. 2005a. Event geochronology of the Pan-African Kaoko Belt, Namibia. Precambrian Res. 140, 103.e1-103.e41.

Goscombe, B., Gray, D., Hand, M. 2005b. Extrusional tectonics in the core of a transpressional orogen; the Kaoko Belt, Namibia. J. Petrol. 46, 1203-1241.

Gray, D.R., Foster, D.A., Goscombe, B.D., Passchier, C.W., Trouw, R.A.J. 2006. ^{40}Ar/^{39}Ar thermochronology of the Pan-African Damara Orogen, Namibia, with implications for tectonothermal and geodynamic evolution. Precambrian Res. 150, 49-72.

Gray, D.R., Foster, D.A., Meert, J.G., Goscombe, B.D., Armstrong, R., Trouw, R.A.J., Passchier, C.W. 2008. A Damara orogeny perspective on the assembly of southwestern Gondwana. In: Pankhurst, R.J., Trouw, R.A.J., Brito Neves, B.B., de Wit, M.J. (eds.) West Gondwana: Pre-Cenozoic correlations across the South Atlantic region. Geol. Soc. Spec. Publ., London, 294, 257-278.

Griffin, W.L., Belousova, E.A., Shee, S.R., Pearson, N.J., O´Reilly, S.Y. 2004. Archean crust evolution in the northern Yilgarn Craton: U-Pb and Hf-isotope evidence from detrital zircons. Precambrian Res. 131, 231-282.

Grocott, J. 1977. The relationship between Precambrian shear belts and modern fault systems. J. Geol. Soc. London 133, 257-262.

Gross, A.O.M.S., Droop, G.T.R., Porcher, C.C., Fernandes, L.A.D. 2009. Petrology and thermobarometry of mafic granulites and migmatites from the Chafalote Metamorphic Suite: new insights into the Neoproterozoic P-T evolution of the Uruguayan-Sul-Rio-Grandense Shield. Precambrian Res. 170, 157-174.

Hälbich, I.W., Alchin, D.J. 1995. The Gariep belt: stratigraphic-structural evidence for obliquely transformed grabens and back-folded thrust stacks in a combined thick-skin thin-skin structural setting. J. Afr. Earth Sci. 21, 9-33.

Halls, H.C., Campal, N., Davis, D.W., Bossi, J. 2001. Magnetic studies and U-Pb geochronology of the Uruguayan dike swarm, Rio de la Plata Craton, Uruguay: paleomagnetic and economic implications. J. South Am. Earth Sci. 14, 349-361.

Hanmer, S. 1988. Great Slave Lake Shear Zone, Canadian Shield: reconstructed vertical profile of a crustal-scale shear zone. Tectonophysics 149, 245-264.

Hanson, R.E. 2003. Proterozoic geochronology and tectonic evolution of southern Africa. In: Yoshida, M., Windley, B.F., Dasgupta, S. (eds.) Proterozoic East Gondwana: Supercontinent assembly and breakup. Geol. Soc. Spec. Publ., London, 206, 427-463.

Harley, S.L., Kelly, N.M., Möller, A. 2007. Zircon behaviour and the thermal histories of mountain chains. Elements 3, 25-30.

Harrison, T.M. 1981. Diffusion of ^{40}Ar in hornblende. Contrib. Mineral. Petrol. 78, 324-331.

Harrison, T.M., Duncan, I., McDougall, I. 1985. Diffusion of ^{40}Ar in biotite: Temperature, pressure and compositional effects. Geochim. Cosmochim. Acta 49, 2461-2468.

Harrison, T.M., Célérier, J., Aikman, A.B., Hermann, J., Heizler, M.T. 2009. Diffusion of ^{40}Ar in muscovite. Geochim. Cosmochim. Acta 73, 1039-1051.

Hartmann, L.A., Piñeyro, D., Bossi, J., Leite, J.A.D., McNaughton, N.J. 2000a. Zircon U-Pb SHRIMP dating of Palaeoproterozoic Isla Mala granitic magmatism in the Río de la Plata Craton, Uruguay. J. South Am. Earth Sci. 13, 105-113.

Hartmann, L.A., Leite, J.A.D., da Silva, L.C., Remus, M.V.D., McNaughton, N.J., Groves, D.I., Fletcher, I.R., Santos, J.O.S., Vasconcellos, M.A.Z. 2000b. Advances in SHRIMP geochronology and their impact

on understanding the tectonic and metallogenic evolution of southern Brazil. Aust. J. Earth Sci. 47, 829-844.

Hartmann, L.A., Santos, J.O.S., McNaughton, N.J., Vasconcellos, M.A.Z., da Silva, L.C. 2000c. Ion microprobe (SHRIMP) dates complex granulite from Santa Catarina, southern Brazil. An. Acad. Bras. Ci. 72, 559-572.

Hartmann, L.A., Campal, N., Santos, J.O.S., McNaughton, N.J., Bossi, J., Schipilov, A., Lafon, J.-M. 2001. Archean crust in the Río de la Plata Craton, Uruguay. J. South Am. Earth Sci. 14, 557-570.

Hartmann, L.A., Santos, J.O.S., Bossi, J., Campal, N., Schipilov, A., McNaughton, N.J. 2002. Zircon and titanite U-Pb SHRIMP geochronology of Neoproterozoic felsic magmatism on the eastern border of the Río de la Plata Craton, Uruguay. J. South Am. Earth Sci. 15, 229-236.

Hartmann, L.A., Santos, J.O.S., Leite, J.A.D., Porcher, C.C., McNaughton, N.J. 2003a. Metamorphic evolution and U-Pb zircon SHRIMP geochronology of the Belizário ultramafic amphibolite, Encantadas Complex, southernmost Brazil. An. Acad. Bras. Ci. 75, 393-403.

Hartmann, L.A., Bitencourt, M.F., Santos, J.O.S., Mc Naughton, N.J., Rivera, C.B., Betiollo, L. 2003b. Prolonged Paleoproterozoic magmatic participation in the Neoproterozoic Dom Feliciano belt, Santa Catarina, Brazil, based on zircon U-Pb SHRIMP geochronology. J. South Am. Earth Sci. 16, 477-492.

Hartnady, C.J.H. 1991. About turn for supercontinents. Nature 352, 476-478.

Hartz, E.H., Torsvik, T.H. 2002. Baltica upside down: A new plate tectonic model for Rodinia and the Iapetus Ocean. Geology 30, 255-258.

Heaman, L., Parrish, R.R. 1991. U-Pb geochronology on accessory minerals. In: Heaman, L., Ludden, J.N. (eds.) Applications of radiogenic isotope systems to problems in geology. Mineralogical Association of Canada, Toronto, 59-102.

Heidelbach, F., Post, A., Tullis, J. 2000. Crystallographic preferred orientation in albite samples deformed experimentally by dislocation and solution precipitation creep. J. Struct. Geol. 22, 1649-1661.

Heinrichs, H., Herrmann, A.G. 1990. Praktikum der Analytischen Geochemie. Springer, Berlin Heidelberg.

Hermann, J., Rubatto, D. 2003. Relating zircon and monazite domains to garnet growth zones: age and duration of granulite facies metamorphism in the Val Malenco lower crust. J. Metamorph. Geol. 21, 833-852.

Herwegh, M., Berger, A., Ebert, A., Brodhag, S. 2008. Discrimination of annealed and dynamic fabrics: Consequences for strain localization and deformation episodes of large-scale shear zones. Earth Planet. Sci. Lett. 276, 52-61.

Hirth, G., Tullis, J. 1992. Dislocation creep regimes in quartz aggregates. J. Struct. Geol. 14, 145-159.

Höckenreiner, M., Söllner, F., Miller, H. 2003. Dating the TIPA shear zone: an Early Devonian terrane boundary between the Famatinian and Pampean systems (NW Argentina). J. South Am. Earth Sci. 16, 45-66.

Hoffman, P.F. 1991. Did the breakout of Laurentia turn Gondwanaland inside-out?. Science 252, 1409-1412.

Hofmann, M., Linnemann, U., Hoffmann, K.-H., Gerdes, A., Eckelmann, K., Gärtner, A. 2014. The Namuskluft and Dreigratberg sections in southern Namibia (Kalahari Craton, Gariep Belt): a geological history of Neoproterozoic rifting and recycling of cratonic crust during the dispersal of Rodinia until the amalgamation of Gondwana. Int. J. Earth Sci. 103, 1187-1202.

Hongn, F.D., Hippertt, J.F. 2001. Quartz crystallographic and morphologic fabrics during folding/transposition in mylonites. J. Struct. Geol. 23, 81-92.

Horsman, E., Tikoff, B. 2007. Constraints on deformation path from finite strain gradients. J. Struct. Geol. 29, 256-272.

Hoskin, P.W.O., Schaltegger, U. 2003. The composition of zircon and igneous and metamorphic petrogenesis. In: Hanchar, J.M., Hoskin, P.W.O. (eds.) Zircon. Reviews in Mineralogy & Geochemistry, Mineralogical Society of America, Washington, 53, 27-62.

Howell, D.G., Jones, D.L., Schermer, E.R. 1985. Tectonostratigraphic terranes of the Circum-Pacific region. In: Howell, D.G. (ed.) Tectonostratigraphic terranes of the Circum-Pacific region. Circum-Pacific Council for Energy and Mineral Resources, Houston, 3-30.

Hull, J. 1988. Thickness-displacement relationships for deformation zones. J. Struct. Geol. 10, 431-435.

Jackson, S., Pearson, N.J., Griffin, W.L., Belousova, E.A. 2004. The application of laser ablation-inductively coupled plasma-mass spectrometry to in situ U-Pb zircon geochronology. Chem. Geol. 211, 47-69.

Jacobs, J., Thomas, R.J. 2004. Himalayan-type indenter-escape tectonics model for the southern part of the late Neoproterozoic-early Paleozoic Eart African-Antarctic orogen. Geology 32, 721-724.

Jacobs, J., Pisarevsky, S., Thomas, R.J., Becker, T. 2008. The Kalahari Craton during the assembly and dispersal of Rodinia. Precambrian Res. 160, 142-158.

Janasi, V.A., Andrade, S., Vasconcellos, A.C.B.C., Henrique-Pinto, R., Ulbrich, H.H.G.J. 2015. Timing and sources of granite magmatism in the Ribeira Belt, SE Brazil: Insights from zircon in situ U-Pb dating and Hf isotope geochemistry in granites from the São Roque Domain. J. South Am. Earth Sci., doi: 10.1016/j.jsames.2015.11.009.

Jäger, E. 1977. Introduction to geochronology. In: Jäger, E., Hunziker, J. (eds.) Lectures of isotope geology. Springer, Heidelberg, 1-12.

Jäger, E., Niggli, E., Wenk, E. 1967. Rb-Sr-Altersbestimmungen an Glimmern der Zentralalpen. Beiträge zur geologischen Karte der Schweiz, Kümmerly & Frey, Bern.

Jefferies, S.P., Holdsworth, R.E., Wibberley, C.A.J., Shimamoto, T., Spiers, C.J., Niemeijer, A.R., Lloyd, G.E. 2006. The nature and importance of phyllonite development in crustal-scale fault cores: an example form the Median Tectonic Line, Japan. J. Struct. Geol. 28, 220-235.

Jégouzo, P. 1980. The South Armorican Shear Zone. J. Struct. Geol. 2, 39-47.

Jenkin, G.R.T. 1997. Do cooling paths derived from mica Rb-Sr data reflect true cooling paths?. Geology 25, 907-910.

Jenkin, G.R.T., Ellam, R.M., Rogers, G., Stuart, F.M., 2001. An investigation of closure temperature of the biotite Rb-Sr system: The importance of cation exchange. Geochim. Cosmochim. Acta 65, 1141-1160.

Jessell, M.W., Lister, G.S. 1991. Strain localization behaviour in experimental shear zones. Pure Appl. Geophys. 137, 421-438.

Johansson, Å. 2014. From Rodinia to Gondwana with the "SAMBA" model - A distant view from Baltica towards Amazonia and beyond. Precambrian Res. 244, 226-235.

John, T., Schenk, V., Mezger, K., Tembo, F. 2004. Timing and PT evolution of whiteschist metamorphism in the Lufilian Arc-Zambezi Belt orogen (Zambia): Implications for the assembly of Gondwana. J. Geol. 112, 71-90.

Jones, G. 1956. Memoria explicativa y mapa geológico de la región oriental del Departamento de Canelones. Instituto Geológico del Uruguay, Montevideo, Boletín Nr. 34.

Jones, R.R., Holdsworth, R.E., Bailey, W. 1997. Lateral extrusion in transpression zones: the importance of boundary conditions. J. Struct. Geol. 19, 1201-1217.

Jones, R.R., Holdsworth, R.E., Clegg, P., McCaffrey, K., Tavarnelli, E. 2004. Inclined transpression. J. Struct. Geol. 26, 1531-1548.

Kemp, A.I.S., Hawkesworth, C.J., Paterson, B.A., Kinny, P.D. 2006. Episodic growth of the Gondwana supercontinent from hafnium and oxygen isotopes in zircon. Nature 439, 580-583.

Killian, R., Heilbronner, R., Stünitz, H. 2011. Quartz microstructures and crystallographic preferred orientation: Which shear sense do they indicate?. J. Struct. Geol. 33, 1446-1466.

Koester, E., Porcher, C.C., Pimentel, M.M., Fernandes, L.A.D., Vignol-Lelarge, M.L., Oliveira, L.D., Ramos, R.C. 2016. Further evidence of 777 Ma subduction-related continental arc magmatism in Eastern Dom Feliciano Belt, southern Brazil: The Chacará das Pedras Orthogneiss. J. South Am. Earth Sci., doi: 10.1016/j.jsames.2015.12.006.

Konopásek, J., Kröner, S., Kitt, S.L., Passchier, C.W., Kröner, A. 2005. Oblique collision and evolution of large-scale transcurrent shear zones in the Kaoko belt, NW Namibia. Precambrian Res. 139, 139-157.

Konopásek, J., Košler, J., Tajčmanová, L., Ulrich, S., Kitt, S.L. 2008. Neoproterozoic igneous complex emplaced along major tectonic boundary in the Kaoko Belt (NW Namibia): ion probe and LA-ICP-MS dating of magmatic and metamorphic zircons. J. Geol. Soc. London 165, 153-165.

Konopásek, J., Košler, J., Sláma, J., Janoušek, V. 2014. Timing and sources of pre-collisional Neoproterozoic sedimentation along the SW margin of the Congo Craton (Kaoko Belt, NW Namibia). Gondwana Res. 26, 386-401.

Kooijman, E., Mezger, K., Berndt, J. 2010. Constraints on the U-Pb systematics of metamorphic rutile from in situ LA-ICP-MS analysis. Earth Planet. Sci. Lett. 293, 321-330.

Kröner, A., Cordani, U. 2003. African, southern Indian and South American cratons were not part of the Rodinia supercontinent: evidence from field relationships and geochronology. Tectonophysics 375, 325-352.

Kröner, A., Stern, R.J. 2004. Pan-African Orogeny. In: Selley, R.C., Cocks, L.R.M., Plimer, I.R. (eds.) Encyclopedia of Geology, Elsevier, Amsterdam, 1-12.

Kröner, S., Konopásek, J., Kröner, A., Passchier, C.W., Poller, U., Wingate, M.W.D., Hofmann, K.H. 2004. U-Pb and Pb-Pb zircon ages for metamorphic rocks in the Kaoko Belt of Northwestern Namibia: a Palaeo- to Mesoproterozoic basement reworked during the Pan-African orogeny. South Afr. J. Geol. 107, 455-476.

Kröner, A., Wan, Y., Liu, X., Liu, D. 2014. Dating of zircon from high-grade rocks: Which is the most reliable method?. Geosci. Frontiers 5, 515-523.

Kröner, A., Rojas-Agramonte, Y., Wong, J., Wilde, S.A. 2015. Zircon reconnaisance dating of Proterozoic gneisses along the Kunene River of Northwestern Namibia. Tectonophysics 662, 125-139.

Kruhl, J.H. 1996. Prism- and basal-plane parallel subgrain boundaries in quartz: a microstructural geothermobarometer. J. Metamorph. Geol. 14, 581-589.

Kurz, G.A., Northrup, C.J. 2008. Structural analysis of mylonitic rocks in the Cougar Creek Complex, Oregon-Idaho using the porphyroclast hyperbolic distribution method, and potential use of SC´-extensional shear bands as quantitative vorticity indicators. J. Struct. Geol. 30, 1005-1012.

Lanphere, M.A., Dalrymple, G.B. 2000. First-principles calibration of ^{38}Ar tracers: implications for the ages of ^{40}Ar/^{39}Ar fluence monitors. U.S. Geological Survey, Professional Paper 1621.

Law, R.D. 2014. Deformation thermometry based on quartz c-axis fabrics and recrystallization microstructures: A review. J. Struct. Geol. 66, 129-161.

Layer, P.W. 2000. Argon-40/argon-39 age of the El'gygytgyn impact event, Chukotka, Russia. Meteorit. Planet. Sci. 35, 591-599.

Layer, P.W., Hall, C.M., York, D. 1987. The derivation of ^{40}Ar/^{39}Ar age spectra of single grains of hornblende and biotite by laser step heating. Geophys. Res. Lett. 14, 757-760.

Lease, R.O., Burbank, D.W., Gehrels, G.E., Wang, Z., Yuan, D. 2007. Signatures of mountain building: Detrital zircon U/Pb ages from northeastern Tibet. Geology 35, 239-242.

Leever, K.A., Gabrielsen, R.H., Sokoutis, D., Willingshofer, E. 2011. The effect of convergence angle on the kinematic evolution of strain partitioning in transpressional brittle wedges: Insight from analog modeling and high-resolution digital image analysis. Tectonics 30, TC2013.

Lehmann, J., Saalmann, K., Naydenov, K.V., Milani, L., Belyanin, G.A., Zwingmann, H., Charlesworth, G., Kinnaird, J.A. 2016. Structural and geochronological constraints on the Pan-African tectonic evolution of the northern Damara Belt, Namibia. Tectonics 35, 103-135.

Leite, J.A.D., Hartmann, L.A., Fernandes, L.A.D., McNaughton, N.J., Soliani Jr., Ê., Koester, E., Santos, J.O.S., Vasconcellos, M.A.Z. 2000. Zircon U-Pb SHRIMP dating of gneissic basement of the Dom Feliciano Belt, southernmost Brazil. J. South Am. Earth Sci. 13, 739-750.

Lenz, C., Fernandes, L.A.D., McNaughton, N.J., Porcher, C.C., Masquelin, H. 2011. U-Pb SHRIMP ages for the Cerro Bori Orthogneisses, Dom Feliciano Belt in Uruguay: Evidences of a ~800 Ma magmatic and a ~650 Ma metamorphic event. Precambrian Res. 185, 149-163.

Lenz, C., Porcher, C.C., Fernandes, L.A.D., Masquelin, H., Koester, E., Conceição, R.V. 2013. Geochemistry of the Neoproterozoic (800-767 Ma) Cerro Bori orthogneisses, Dom Feliciano Belt in Uruguay: tectonic evolution of an ancient continental arc. Miner. Petrol. 107, 785-806.

Li, Z.X., Bogdanova, S.V., Collins, A.S., Davidson, A., De Waele, B., Ernst, R.E., Fitzsimons, I.C.W., Fuck, R.A., Gladkochub, D.P., Jacobs, J., Karlstrom, K.E., Lu, S., Natapov, L.M., Pease, V., Pisarevsky, S.A., Thrane, K., Vernikovsky, V. 2008. Assembly, configuration, and break-up history of Rodinia: a synthesis. Precambrian Res. 160, 179-210.

Liégeois, J.P., Latouche, L., Boughrara, M., Navez, J., Guiraud, M. 2003. The LATEA metacraton (Central Hoggar, Tuareg shield, Algeria): behaviour of an old passive margin during the Pan-African orogeny. J. Afr. Earth Sci. 37, 161-190.

Liégeois, J.P., Abdesalam, M.G., Ennih, N., Ouabadi, A. 2013. Metacraton: nature, genesis and behavior. Gondwana Res. 23, 220-237.

Lisle, R.J. 2014. Strain analysis in dilatational shear zones, with examples from Marloes, SW Wales. In: Llana-Fúnez, S., Marcos, A., Bastida, F. (eds.) Deformation structures and processes within the continental crust. Geol. Soc. Spec. Pub., London, 394, 7-20.

Lister, G.S. 1977. Discussion: Crossed-girdle c-axis in quartzites plastically deformed by plane strain and progressive simple shear. Tectonophysics 39, 51-54.

Lister, G.S., Williams, P.F. 1983. The partitioning of deformation in flowing rock masses. Tectonophysics 92, 1-33.

Lloyd, G.E., Freeman, B. 1994. Dynamic recrystallization of quartz under greenschist conditions. J. Struct. Geol. 16, 867-881.

Lubnina, N.V., Pisarevsky, S.A., Puchkov, V.N., Kozlov, V.I., Sergeeva, N.D. 2014. New paleomagnetic data from Late Neoproterozoic sedimentary successions in Southern Urals, Russia: implications for the Late Neoproterozoic paleogeography of the Iapetan realm. Int. J. Earth Sci. 103, 1317-1334.

Ludwig, K. 2003. Isoplot/Ex version 3: A geochronological toolkit for Microsoft Excel. Berkeley Geochronology Center Special Publications, Berkeley.

Ludwig, K.R. 2008. Isoplot 3.70. A geochronological toolkit for Microsoft Excel. Berkeley Geochronology Center Special Publications, Berkeley.

Luft Jr, J.L., Chemale Jr, F., Armstrong, R. 2011. Evidence of 1.8- to 1.7-Ga collisional arc in the Kaoko Belt, NW Namibia. Int. J. Earth Sci. 100, 305-321.

Maki, K., Yui, T.-F., Miyazaki, K., Fukuyama, M., Wang, K.-L., Martens, U., Grove, M., Liou, J.G. 2014. Petrogenesis of metatexite and diatexite migmatites determined using zircon U-Pb age, trace element and Hf isotope data, Higo metamorphic terrane, central Kyushu, Japan. J. Metamorph. Geol. 32, 301-323.

Mainprice, D., Bouchez, J.L., Blumenfeld, P., Tubia, J.M. 1986. Dominant c slip in naturally deformed quartz: Implications for dramatic plastic softening at high temperature. Geology 14, 819-822.

Mallmann, G., Chemale Jr, F., Ávila, J.N., Kawashita, K., Armstrong, R.A. 2007. Isotope geochemistry and geochronology of the Nico Pérez Terrane, Rio de la Plata Craton, Uruguay. Gondwana Res. 12, 489-508.

Martínez, J.C., Dristas, J.A., van den Kerkhof, A., Wemmer, K., Massonne, H.J., Theye, T., Frisicale, M.C. 2013. Late-Neoproterozoic hydrothermal fluid activity in the Tandilia Belt, Argentina. Rev. Asoc. Geol. Argentina 70, 410-426.

Masquelin, H. 1990. Análisis estructural de las zonas de cizalla en las migmatitas de Punta del Este - Uruguay. Acta Geol. Leopoldensia 30, 139-158.

Masquelin, H., Sánchez Bettucci, L. 1993. Propuesta de Evolución tectono-sedimentaria para la fosa tardi-brasiliana en la región de Piriápolis, Uruguay. Rev. Bras. Geociências 23, 188-198.

Masquelin, H., Tabó, F. 1988. Memoria Explicativa de la Carta Geológica del Uruguay, Hoja Chafalote, Escala 1:100.000. DINAMIGE - Facultad de Agronomía - Facultad de Humanidades y Ciencias.

Massey, M.A., Moecher, D.P. 2013. Transpression, extrusion, partitioning, and lateral escape in the middle crust: Significance of structures, fabrics, and kinematics in the Bronson Hill zone, southern New England, U.S.A. J. Struct. Geol. 55, 62-78.

Matteini, M., Junges, S.L., Dantas, E.L., Pimentel, M.M., Bühn, B. 2010. *In situ* zircon U-Pb and Lu-Hf isotope systematic on magmatic rocks: Insights on the crustal evolution of the Neoproterozoic Goiás Magmatic Arc, Brasilia belt, Central Brazil. Gondwana Res. 17, 1-12.

Mattinson, J.M. 2010. Analysis of the relative decay constants of ^{235}U and ^{238}U by multi-step CA-TIMS measurements of closed-system natural zircon samples. Chem. Geol. 275, 186-198.

McCourt, S., Armstrong, R.A., Jelsma, H., Mapeo, R.B.M. 2013. New U-Pb SHRIMP ages from the Lubango region, SW Angola: insights into the Palaeoproterozoic evolution of the Angolan Shield, southern Congo Craton, Africa. J. Geol. Soc. London 170, 353-363.

McDougall, I., Harrison, T.M. 1999. Geochronology and thermochronology by the ^{40}Ar/^{39}Ar method. Oxford University Press, New York.

Means, W.D. 1984. Shear zones of types I and II and their significance for reconstruction of rock history. Geological Society America, Abstracts, 16, 50.

Means, W.D. 1995. Shear zones and rock history. Tectonophysics 247, 157-160.

Medlicott, H.B., Blanford, W.T. 1879. A manual of the geology of India and Burma. Records of the Geological Survey of India, Calcutta.

Meert, J.G. 2003. A synopsis of events related to the assembly of eastern Gondwana. Tectonophysics 362, 1-40.

Meert, J.G., Lieberman, B.S. 2004. A palaeomagnetic and palaeobiogeographical perspective on latest Neoproterozoic and Early Cambrian tectonic events. J. Geol. Soc. London 161, 1-11.

Mezger, K., Krogstad, E.J. 1997. Interpretation of discordant U-Pb zircon ages: An evaluation. J. Metamorph. Geol. 15, 127-140.

Mezger, K., Essene, E.J., Halliday, A.N. 1992. Closure temperatures of the Sm-Nd system in metamorphic garnets. Earth Planet. Sci. Lett. 193, 397-409.

Midot, D. 1984. Etude geologique et diagnostic metallogenique pour l'exploration du secteur de Minas (Uruguay). Ph.D. Thesis, Pierre et Marie Curie University.

Miller, R.McG. 1983. The Pan-African Damara Orogen of south west Africa/Namibia. Geol. Soc. South Afr. Spec. Pub. 11, 431-515.

Miller, C.F., McDowell, S.M., Mapes, R.W. 2003. Hot and cold granites? Implications of zircon saturation temperatures and preservation of inheritance. Geology 31, 529-532.

Mitchell, R.N., Kilian, T.M., Evans, D.A.D. 2012. Supercontinent cycles and the calculation of absolute palaeolongitue in deep time. Nature 482, 208-212.

Moloto-A-Kenguemba, G.R., Trindade, R.I.F., Monié, P., Nédélec, A., Siquiera, R. 2008. A late Neoproterozoic paleomagnetic pole for the Congo craton: Tectonic setting, paleomagnetism and geochronology of the Nola dike swarm (Central African Republic). Precambrian Res. 164, 214-226.

Montaña, J., Sprechmann, P. 1993. Calizas estromatolíticas y oolíticas y definición de la Formación Arroyo de la Pedrera (?Vendiano, Uruguay). Rev. Bras. Geociências 23, 306-312.

Montési, L.G.J. 2013. Fabric development as the key for forming ductile shear zones and enabling plate tectonics. J. Struct. Geol. 50, 254-266.

Morag, N., Avigad, D., Gerdes, A., Belousova, E., Harlavan, Y. 2011. Crustal evolution and recycling in the northern Arabian-Nubian Shield: New perspectives from zircon Lu-Hf and U-Pb systematics. Precambrian Res. 186, 101-116.

Morales Demarco, M., Oyhantçabal, P., Stein, K.J., Siegesmund, S. 2011. Black dimensional stones: geology, technical properties and deposit characterization of the dolerites from Uruguay. Environ. Earth Sci. 63, 1879-1909.

Mulch, A., Cosca, M.A. 2004. Recrystallization or cooling ages: in situ UV-laser $^{40}Ar/^{39}Ar$ geochronology of muscovite in mylonitic rocks. J. Geol. Soc. London 161, 573-582.

Murphy, J.B., Nance, R.D. 2003. Do supercontinents introvert or extrovert?: Sm-Nd isotope evidence. Geology 31, 873-876.

Murphy, J.B., Nance, R.D. 2005. Do supercontinents turn inside-in or inside-out?. Int. Geol. Rev. 47, 591-619.

Murphy, J.B., Nance, R.D. 2013. Speculations on the mechanisms for the formation and breakup of supercontinents. Geosci. Frontiers 4, 185-194.

Nance, R.D., Worsley, T.R., Moody, J.B. 1988. The supercontinent cycle. Sci. Am. 256, 72-79.

Nance, R.D., Murphy, J.B., Santosh, M. 2014. The supercontinent cycle: A retrospective essay. Gondwana Res. 25, 4-29.

Nasdala, L., Hofmeister, W., Norberg, N., Mattinson, J.M., Corfu, F., Dörr, W., Kamo, S.L., Kennedy, A.K., Kronz, A., Reiners, P.W., Frei, D., Košler, J., Wan, Y., Götze, J., Häger, T., Kröner, A., Valley, J.W. 2008. Zircon M257 - a homogeneous natural reference material for the ion microprobe U-Pb analysis of zircon. Geostand. Geoanal. Res. 32, 247-265.

Nebel-Yacobsen, Y., Münker, C., Nebel, O., Gerdes, A., Mezger, K., Nelson, D.R. 2010. Reworking of Earth´s first crust: Constraints from Hf isotopes in Archean zircons from Mt. Narryer, Australia. *Precambrian Res.* 182, 175-186.

Nedrebø, H. 2014. U-Pb zircon provenance of metamorphosed clastic sediments in a developing rift (Dom Feliciano Belt, Uruguay and Kaoko Belt, Namibia). M.Sc. Thesis, University of Bergen.

Neves, S.P. 2003. Proterozoic history of the Borborema province (NE Brazil): Correlations with neighboring cratons and Pan-African belts and implications for the evolution of western Gondwana. Tectonics 22, 1031.

O'Brien, T.M., van der Pluijm, B.A. 2012. Timing of Iapetus Ocean rifting from Ar geochronology of pseudo-tachylytes in the St. Lawrence rift system of southern Quebec. Geology 40, 443-446.

Okudaira, T., Takeshita, T., Hara, I., Ando, J. 1995. A new estimate of the conditions from transition from basal <a> to prism [c] slip in naturally deformed quartz. Tectonophysics 250, 31-46.

Oriolo, S., Oyhantçabal, P., Heidelbach, F., Wemmer, K., Siegesmund, S. 2015. Structural evolution of the Sarandí del Yí Shear Zone, Uruguay: kinematics, deformation conditions and tectonic significance. Int. J. Earth Sci. 104, 1759-1777.

Oriolo, S., Oyhantçabal, P., Basei, M.A.S., Wemmer, K., Siegesmund, S. 2016a. The Nico Pérez Terrane (Uruguay): from Archean crustal growth and connections with the Congo Craton to late Neoproterozoic accretion to the Río de la Plata Craton. Precambrian Research, doi: 10.1016/j.precamres.2016.04.014.

Oriolo, S., Oyhantçabal, P., Wemmer, K., Basei, M.A.S., Benowitz, J., Pfänder, J., Hannich, F., Siegesmund, S. 2016b. Timing of deformation in the Sarandí del Yí Shear Zone, Uruguay: implications for the amalgamation of Western Gondwana during the Neoproterozoic Brasiliano–Pan-African Orogeny. Tectonics 35, 754-771.

Oyhantçabal, P. 2005. The Sierra Ballena shear zone: kinematics, timing and its significance for the geotectonic evolution of southeast Uruguay. Ph.D. Thesis, Georg-August-Universität Göttingen.

Oyhantçabal, P., Vaz, N. 1990. Una asociación de cuarcitas y rocas máficas y ultramáficas en los alrededores de Isla Patrulla, Treinta y Tres, Uruguay. 1° Congreso Uruguayo de Geología, Montevideo.

Oyhantçabal, P., Muzio, R., de Souza, S. 1993. Geología y aspectos estructurales del borde orogénico en el extremo sur del cinturón Don Feliciano. Rev. Bras. Geociências 23, 296-300.

Oyhantçabal, P., Heimann, A., Miranda, S. 2001. Measurement and interpretation of strain in the syntectonic Solís de Mataojo Granitic Complex, Uruguay. J. Struct. Geol. 23, 807-817.

Oyhantçabal, P., Sánchez Bettucci, L., Pecoits, E., Aubet, N., Peel, E., Preciozzi, F., Basei, M.A.S. 2005. Nueva propuesta estratigráfica para las supracorticales del Cinturón Dom Feliciano (Proterozoico Uruguay). 12° Congreso Latinoamericano de Geología, Quito.

Oyhantçabal, P., Wemmer, K., Siegesmund, S., Spoturno, J. 2006. K-Ar geochronology of the Mosquitos shear zone (Piedra alta terrane-Río de la Plata craton-Uruguay). 5° South American Symposium on Isotope Geology, Punta del Este.

Oyhantçabal, P., Siegesmund, S., Wemmer, K., Frei, R., Layer, P. 2007. Post-collisional transition from calc-alkaline to alkaline magmatism during transcurrent deformation in the southernmost Dom Feliciano Belt (Braziliano–Pan-African, Uruguay). Lithos 98, 141-159.

Oyhantçabal, P., Siegesmund, S., Wemmer, K., Presnyakov, S., Layer, P. 2009a. Geochronological constraints on the evolution of the southern Dom Feliciano Belt (Uruguay). J. Geol. Soc. London 166, 1075-1084.

Oyhantçabal, P., Siegesmund, S., Wemmer, K., Layer, P. 2009b. The Sierra Ballena Shear Zone in the southernmost Dom Feliciano Belt (Uruguay): evolution, kinematics, and deformation conditions. Int. J. Earth Sci., doi: 10.1007/s00531-009-0453-1.

Oyhantçabal, P., Siegesmund, S., Wemmer, K. 2011a. The Río de la Plata Craton: a review of units, boundaries, ages and isotopic signature. Int. J. Earth Sci. 100, 201-220.

Oyhantçabal, P., Siegesmund, S., Wemmer, K., Passchier, C.W. 2011b. The transpressional connection between Dom Feliciano and Kaoko Belts at 580-550 Ma. Int. J. Earth Sci. 100, 379-390.

Oyhantçabal, P., Wegner-Eimer, M., Wemmer, K., Schulz, B., Frei, R., Siegesmund, S. 2012. Paleo- and Neoproterozoic magmatic and tectonometamorphic evolution of the Isla Cristalina de Rivera (Nico Pérez Terrane, Uruguay). Int. J. Earth Sci. 101, 1745-1762.

Oyhantçabal, P., Spoturno, J., Loureiro, L. 2013. Magmatismo félsico volcánico e hipabisal Ediacarano en la región sureste del Uruguay (Departamento de Maldonado). 7° Congreso Uruguayo de Geología, Montevideo.

Paixão, M.A.P., Nilson, A.A., Dantas, E.L. 2008. The Neoproterozoic Quatipuru ophiolite and the Araguaia fold belt, central-northern Brazil, compared with correlatives in NW Africa. In: Pankhurst, R.J., Trouw, R.A.J., Brito Neves, B.B., de Wit, M.J. (eds.) West Gondwana: Pre-Cenozoic correlations across the South Atlantic region. Geol. Soc. Spec. Publ., London,294, 297-318.

Pángaro, F., Ramos, V.A. 2012. Paleozoic crustal blocks of onshore and offshore central Argentina: New pieces of the southwestern Gondwana collage and their role in the accretion of Patagonia and the evolution of Mesozoic south Atlantic sedimentary basins. Mar. Petrol. Geol. 37, 162-183.

Passarelli, C.R., Basei, M.A.S., Siga Jr, O., Mc Reath, I., da Costa Campos Neto, M. 2010. Deformation and geochronology of syntectonic granitoids emplaced in the Major Gercino Shear Zone, southeastern South America. Gondwana Res. 17, 688-703.

Passarelli, C.R., Basei, M.A.S., Wemmer, K., Siga Jr, O., Oyhantçabal, P. 2011. Major shear zones of southern Brazil and Uruguay: escape tectonics in the eastern border of the Río de la Plata and Paranapanema cratons during the Western Gondwana amalgamation. Int. J. Earth Sci. 100, 391-414.

Passchier, C.W. 1985. Water-deficient mylonite zones - An example from the Pyrenees. Lithos 18, 115-127.

Passchier, C.W., Trouw, R.A.J. 2005. Microtectonics. Springer, Berlin Heidelberg.

Pazos, P., Rapalini, A., Sánchez Bettucci, L., Tófalo, R. 2011. The Playa Hermosa Formation, Playa Verde Basin, Uruguay. Geol. Soc. London Mem. 36, 547-553.

Pecoits, E., Aubet, N., Oyhantçabal, P., Sánchez Bettucci, L. 2005. Estratigrafía de sucesiones sedimentarias y volcanosedimentarias Neoproterozoicas del Uruguay. Rev. Soc. Uruguaya Geol. 11, 18-27.

Pecoits, E., Gingras, M., Aubet, N., Konhauser, K. 2008. Ediacaran in Uruguay: palaeoclimatic and palaeobiological implications. Sedimentology 55, 689-719.

Pecoits, E., Gingras, M.K., Konhauser, K. 2011. Las Ventanas and San Carlos formations, Maldonado Group, Uruguay. Geol. Soc. London Mem. 36, 555-564.

Pedrosa-Soares, A.C., Vidal, P., Leonardos, O.H., Brito Neves, B.B. 1998. Neoproterozoic oceanic remnants in eastern Brazil: Further evidence and refutation of an exclusively ensialic evolution for the Araçuaí-West Congo orogen. Geology 26, 519-522.

Peel, E., Preciozzi, F. 2006. Geochronological synthesis of the Piedra Alta Terrane, Uruguay. 5° South American Symposium on Isotope Geology, Punta del Este.

Peri, V.G., Barcelona, H., Pomposiello, M.C., Favetto, A. 2015. Magnetotelluric characterization through the Ambargasta-Sumampa Range: The connection between the northern and southern trace of the Río de la Plata Craton - Pampean Terrane tectonic boundary. J. South Am. Earth Sci. 59, 1-12.

Pertille, J., Hartmann, L.A., Philipp, R.P. 2015a. Zircon U-Pb age constraints on the Paleoproterozoic sedimentary basement of the Ediacaran Porongos Group, Sul-Riograndense Shield, southern Brazil. J. South Am. Earth Sci. 63, 334-345.

Pertille, J., Hartmann, L.A., Philipp, R.P., Petry, T.S., Lana, C.C. 2015b. Origin of the Ediacaran Porongos Group, Dom Feliciano Belt, southern Brazilian Shield, with emphasis on whole rock and detrital zircon geochemistry and U-Pb, Lu-Hf isotopes. J. South Am. Earth Sci. 64, 69-93.

Pimentel, M.M., Ferreira Filho, C.F., Armele, A. 2006. Neoproterozoic age of the Niquelândia Complex, central Brazil: Further ID-TIMS U-Pb and Sm-Nd isotopic evidence. J. South Am. Earth Sci. 21, 228-238.

Pettersson, Å., Cornell, D.H., Yuhara, M., Hirahara, Y. 2009. Sm-Nd data for granitoids across the Namaqua sector of the Namaqua-Natal Province, South Africa. In: Reddy, S.M., Mazumder, R., Evans, D.A.D., Collins, A.S. (eds.) Palaeoproterozoic supercontinents and global evolution. Geol. Soc. Spec. Publ., London, 323, 219-230.

Philipp, R.P., Massonne, H.-J., Sacks de Campos, R. 2013. Peraluminous leucogranites of the Cordilheira Suite: A record of Neoproterozoic collision and the generation of the Pelotas Batholith, Dom Feliciano Belt, Southern Brazil. J. South Am. Earth Sci. 43, 8-24.

Philipp, R.P., Molina Bom, F., Pimentel, M.M., Junges, S.L., Zvirtes, G. 2016. SHRIMP U-Pb age and high temperature conditions of the collisional metamorphism in the Várzea do Capivarita Complex: Implications for the origin of Pelotas Batholith, Dom Feliciano Belt, southern Brazil. J. South Am. Earth Sci. 66, 196-207.

Pisarevsky, S.A., Wingate, M.T.D., Powel, C.McA., Johnson, S., Evans, D.A.D. 2003. Models of Rodinia assembly and fragmentation. In: Yoshida, M., Windley, B.F., Dasgupta, S. (eds.) Proterozoic East Gondwana: Supercontinent assembly and breakup. Geol. Soc. Spec. Publ., London, 206, 35-55.

Pisarevsky, S.A., Murphy, J.B., Cawood, P.A., Collins, A.S. 2008. Late Neoproterozoic and Early Cambrian palaeogeography: models and problems. In: Pankhurst, R.J., Trouw, R.A.J., Brito Neves, B.B., de Wit, M.J. (eds.) West Gondwana: Pre-Cenozoic correlations across the South Atlantic region. Geol. Soc. Spec. Publ., London, 294, 9-31.

Platt, J.P., Behr, W.M. 2011a. Grainsize evolution in ductile shear zones: Implications for strain localization and the strength of the lithosphere. J. Struct. Geol. 33, 537-550.

Platt, J.P., Behr, W.M. 2011b. Lithospheric shear zones as constant stress experiments. Geology, 39, 127-130.

Poiré, D.G., González, P.D., Canalicchio, J.M., García Repetto, F. 2003. Litoestratigrafía y estromatolitos de la sucesión sedimentaria Precámbrica de la cantera Mina Verdún, Minas, Uruguay. Rev. Soc. Uruguaya Geol., Publicación Especial, 1, 108-123.

Pollack, H.N. 1986. Cratonization and thermal evolution of the mantle. Earth Planet. Sci. Lett. 80, 175-182.

Porada, H. 1985. Stratigraphy and facies in the Upper Proterozoic Damara Orogen, Namibia, based on a geodynamic model. Precambrian Res. 29, 235-264.

Porada, H. 1989. Pan-African rifting and orogenesis in southern to equatorial Africa and eastern Brazil. Precambrian Res. 44, 103-136.

Powell, C.McA., Young, G.M. 1995. Are Neoproterozoic glacial deposits preserved on the margins of Laurentia related to the fragmentation of two supercontinents?: Comment and Reply. Geology 23, 1053-1055.

Powell, C. McA., Li, Z.X., McElhinny, M.W., Meert, J.G., Park, J.K. 1993. Paleomagnetic constraints on timing of the Neoproterozoic breakup of Rodinia and the Cambrian formation of Gondwana. Geology 21, 889-892.

Pradhan, V.R., Meert, J.G., Pandit, M.K., Kamenov, G., Gregory, L.C., Malone, S.J. 2009. India´s changing place in global Proterozoic reconstructions: A review of geochronologic constraints and paleomagnetic poles form the Dharwar, Bundelkhand and Marwar cratons. J. Geodyn. 50, 224-242.

Prave, A.R. 1996. Tale of three cratons: Tectonostratigraphic anatomy of the Damara orogen in northwestern Namibia and the assembly of Gondwana. Geology 24, 1115-1118.

Preciozzi, F., Spoturno, J., Heinzen, W. 1979. Carta geo-estructural del Uruguay, escala 1:2.000.000. Instituto Geológico Ing. Terra Arocena, Montevideo.

Preciozzi, F., Spoturno, J., Heinzen, W., Rossi, P. 1985. Carta Geológica del Uruguay a escala 1:500.000. Dirección Nacional de Minería y Geología, Montevideo.

Preciozzi, F. 1989. Memoria explicativa del fotoplano Zapicán. Dirección Nacional de Minería y Geología - Facultad de Agronomía - Facultad de Humanidades y Ciencias, Montevideo.

Preciozzi, F., Pena, S., Masquelin, E., Pías, J., Tabo, F. 1989. Memoria explicativa del fotoplano Piriapolis. DINAMIGE - Universidad de la Rapública, Montevideo.

Preciozzi, F., Basei, M.A.S., Masquelin, H. 1999. New geochronological data from the Piedra Alta Terrane (Rio de La Plata Craton). 2° South American Symposium on Isotope Geology, Córdoba.

Pryer, L.L. 1993. Microstructures in feldspars from a major crustal thrust zone: the Grenville Front, Ontario, Canada. J. Struct. Geol. 15, 21-36.

Purdy, J.W., Jäger, E. 1976. K-Ar ages on rock-forming minerals from the Central Alps. Mem. Inst. Geol. Mineral. dell'università di Padova 30, 1-31.

Ramos, V.A. 1988. Late Proterozoic-Early Paleozoic of South America - a collisional history. Episodes 11, 168-174.

Ramsay, J.G. 1980. Shear zone geometry: a review. J. Struct. Geol. 2, 83-99.

Ramsay, J.G., Graham, R.H. 1970. Strain variation in shear belts. Can. J. Earth Sci. 7, 786-813.

Rapalini, A.E., Sánchez Bettucci, L. 2008. Widespread remagnetization of late Proterozoic sedimentary units of Uruguay and the apparent polar wonder path for the Río de La Plata craton. Geophys. J. Int. 174, 55-74.

Rapalini, A.E., Trindade, R.I., Poiré, D.G. 2013. The La Tinta pole revisited: Paleomagnetism of the Neoproterozoic Sierras Bayas Group (Argentina) and its implications for Gondwana and Rodinia. Precambrian Res. 224, 51-70.

Rapalini, A.E., Tohver, E., Sánchez Bettucci, L., Lossada, A.C., Barcelona, H., Pérez, C. 2015. The late Neoproterozoic Sierra de las Ánimas Magmatic Complex and Playa Hermosa Formation, southern

Uruguay, revisited: Paleogeographic implications of new paleomagnetic and precise geochronologic data. Precambrian Res. 259, 143-155.

Rapela, C.W., Pankhurst, R.J., Casquet, C., Baldo, E., Saavedra, J., Galindo, C., Fanning, C.M. 1998. The Pampean Orogeny of the southern proto-Andes: Cambrian continental collision in the Sierras de Córdoba. In: Pankhurst, R.J., Rapela, C.W. (eds.) The proto-Andean margin of Gondwana. Geol. Soc. Spec. Publ., London, 142, 181-217.

Rapela, C.W., Pankhurst, R.J., Casquet, C., Fanning, C.M., Baldo, E.G., González-Casado, J.M., Galindo, C., Dahlquist, J. 2007. The Río de la Plata craton and the assembly of SW Gondwana. Earth-Sci. Rev. 83, 49–82.

Rapela, C.W., Fanning, C.M., Casquet, C., Pankhurst, R.J., Spalletti, L., Poiré, D., Baldo, E.G. 2011. The Río de la Plata craton and the adjoining Pan-African/brasiliano terranes: Their origins and incorporation into south-west Gondwana. Gondwana Res. 20, 673-690.

Renne, P.R., Mundil, R., Balco, G., Min, K., Ludwig, K.R. 2010. Joint determination of ^{40}K decay constants and ^{40}Ar*/^{40}K for the Fish Canyon sanidine standard, and improved accuracy for ^{40}Ar/^{39}Ar geochronology. Geochim. Cosmochim. Acta 74, 5349-5367.

Rennie, S.F., Fagereng, Å., Diener, J.F.A. 2013. Strain distribution within a km-scale, mid-crustal shear zone: The Kuckaus Mylonite Zone, Namibia. J. Struct. Geol. 56, 57-69.

Roberts, N.M.W. 2012. Increased loss of continental crust during supercontinent amalgamation. Gondwana Res. 21, 994-1000.

Roberts, M.P., Finger, F. 1997. Do U-Pb zircon ages from granulites reflect peak metamorphic conditions?. Geology 25, 319-322.

Roberts, N.M.W., Spencer, C.J. 2015. The zircon archive of continent formation through time. In: Roberts, N.M.W., van Kranendonk, M., Parman, S., Shirey, S., Clift, P.D. (eds.) Continent formation through time. Geol. Soc. Spec. Pub., London, 389, 197-225.

Rolland, Y., Rossi, M., Cox, S.F., Corsini, M., Mancktelow, N., Pennacchioni, G., Fornari, M., Boullier, A.M. 2008. $^{40}Ar/^{39}Ar$ dating of synkinematic white data: insights from fluid-rock reaction in low-grade shear zones (Mont Blanc Massif) and constraints on timing of deformation in the NW external Alps. In: Wibberley, C.A.J., Kurz, W., Imber, J., Holdsworth, R.E., Collettini, C. (eds.) The internal structure of fault zones: implications for mechanical and fluid-flow properties. Geol. Soc. Spec. Publ., London, 299, 293-315.

Rosenberg, C.L. 2004. Shear zones and magma ascent: A model based on a review of the Tertiary magmatism in the Alps. Tectonics 23, TC3002.

Rosenberg, C.L., Stünitz, H. 2003. Deformation and recrystallization of plagioclase along a temperature gradient: an example from the Bergell tonalite. J. Struct. Geol. 25, 389-408.

Rossini, C.A., Legrand, J.M. 2003. Eventos tecto-metamórficos del Grupo Carapé: un modelo para su evolución neoproterozoica. Rev. Soc. Uruguaya Geol., Publicación Especial, 1, 49-67.

Rubatto, D., Williams, I.S., Buick, I.S. 2001. Zircon and monazite response to prograde metamorphism. Contrib. Mineral. Petrol. 140, 458-468.

Rutter, E.H. 1983. Pressure solution in nature, theory and experiment. J. Geol. Soc. London 140, 725-740.

Saalmann, K., Hartmann, L.A., Remus, M.V.D., Koester, E., Conceição, R.V. 2005. Sm-Nd isotope geochemistry of metamorphic volcano-sedimentary successions in the São Gabriel Block, southernmost Brazil: evidence for the existence of juvenile Neoproterozoic oceanic crust to the east of the Río de la Plata craton. Precambrian Res. 136, 159-175.

Saalmann, K., Gerdes, A., Lahaye, Y., Hartmann, L.A., Remus, M.V.D., Läufer, A. 2011. Multiple accretion at the eastern margin of the Río de la Plata craton: the prolonged Brasiliano orogeny in southernmost Brazil. Int. J. Earth Sci. 100, 355-378.

Sacks de Campos, R., Philipp, R.P., Massonne, H.-J., Chemale Jr., F. 2012. Early post-collisional Brasiliano magmatism in Botuverá region, Santa Catarina, southern Brazil: Evidence from petrology,

geochemistry, isotope geology and geochronology of the diabase and lamprophyre dikes. J. South Am. Earth Sci. 37, 266-278.

Samson, S.D., Alexander, E.C. 1987. Calibration of the interlaboratory ^{40}Ar/^{39}Ar dating standard, MMhbl. Chem. Geol. 66, 27-34.

Sánchez Bettucci, L. 1998. Evolución Tectónica del Cinturón Dom Feliciano en la región Minas-Piriápolis, República Oriental del Uruguay. Ph.D. Thesis, Universidad de Buenos Aires.

Sánchez Bettucci, L., Burgueño, A.M. 1993. Análisis sedimentológico y faciológico de la Formación Rocha (ex–Grupo Rocha). Rev. Bras. Geociências 23, 323-329.

Sánchez Bettucci, L., Preciozzi, F., Basei, M.A.S., Oyhantçabal, P., Peel, E., Loureiro, J. 2003. Campanero Unit: a probable Paleoproterozoic basement and its correlation to other units of southeastern Uruguay. 4° South American Symposium on Isotope Geology, Salvador.

Sánchez Bettucci, L., Oyhantçabal, P., Loureiro, J., Ramos, V.A., Preciozzi, F., Basei, M.A.S. 2004. Mineralizations of the Lavalleja group (Uruguay), a probable neoproterozoic volcano-sedimentary sequence. Gondwana Res. 6, 89-105.

Sánchez Bettucci, L., Masquelin, E., Peel, E., Oyhantçabal, P., Muzio, R., Ledesma, J.J., Preciozzi, F. 2010. Comment on "Provenance of the Arroyo del Soldado Group (Ediacaran to Cambrian, Uruguay): Implications for the palaeogeographic evolution of southwestern Gondwana" by Blanco et al. [Precambrian Res., 171 (2009), 57-73]. Precambrian Res. 180, 328-333.

Sanderson, D.J., Marchini, W.R.D. 1984. Transpression. J. Struct. Geol. 6, 449-458.

Santos, J.O.S., Hartmann, L.A., Bossi, J., Campal, N., Schipilov, A., Piñeyro, D., McNaughton, N.J. 2003. Duration of the Trans-Amazonian Cycle and its correlation within South America based on U-Pb SHRIMP geochronology of the La Plata Craton, Uruguay. Int. Geol. Rev. 45, 27-48.

Sato, K., Colombo Tassinari, C.G., Basei, M.A.S., Siga Junior, O., Takashi Onoe, A., Dias de Souza, M. 2014. Sensitive High Resolution Ion Microprobe (SHRIMP IIe/MC) of the Institute of Geosciences of the University of São Paulo, Brazil: analytical method and first results. Geol. USP Sér. Cient. 14, 3-18.

Schaltegger, U., Fanning, C.M., Günther, D., Maurin, J.C., Schulmann, K., Gebauer, D. 1999. Growth, annealing and recrystallization of zircon and preservation of monazite in high-grade metamorphism: conventional and in-situ U-Pb isotope, cathodoluminiscence and microchemical evidence. Contrib. Mineral. Petrol. 134, 186-201.

Schmid, S.M., Casey, M. 1986. Complete fabric analysis of some commonly observed quartz c-axis patterns. Geophys. Monogr. 36, 263-286.

Schmid, S.M., Aebli, H.R., Heller, F., Zingg, A. 1989. The role of the Periadriatic Line in the tectonic evolution of the Alps. In: Coward, M.P., Dietrich, D., Park, R.G. (eds.) Alpine tectonics. Geol. Soc. Spec. Publ., London, 45, 153-171.

Schmitt, R.S., Trouw, R.A.J., Passchier, C.W., Medeiros, S.R., Armstrong, R. 2012. 530 Ma syntectonic syenites and granites in NW Namibia - their relation with collision along the junction of the Damara and Kaoko belts. Gondwana Res. 21, 362-377.

Schulmann, K., Thompson, A.B., Lexa, O., Ježek, J. 2003. Strain distribution and fabric development modeled in active and ancient transpressive zones. J. Geophys. Res. 108(B1), 2023.

Schumacher, E. 1975. Herstellung von 99,9997% ^{38}Ar für die ^{40}K/^{40}Ar Geochronologie. Geochron. Chimia 24, 441-442.

Sengupta, S., Ghosh, S.K. 2004. Analysis of transpressional deformation from geometrical evolution of mesoscopic structures from Phulad shear zone, Rajasthan, India, J. Struct. Geol. 26, 1961-1976.

Seth, B., Kröner, A., Mezger, K., Nemchin, A.A., Pidgeon, R.T., Okrusch, M. 1998. Archean to Neoproterozoic magmatic events in the Kaoko Belt of NW Namibia and their geodynamic significance. Precambrian Res. 92, 341-363.

Shimizu, I. 1995. Kinetic of pressure solution creep in quartz: theoretical considerations. Tectonophysics 245, 121-134.

Sibson, R.H. 1977. Fault rocks and fault mechanisms. J. Geol. Soc. London 133, 191-213.

Sibson, R.H. 1983. Continental fault structure and the shallow earthquake source. J. Geol. Soc. London 140, 741-767.

Siegesmund, S., Layer, P., Dunkl, I., Vollbrecht, A., Steenken, A., Wemmer, K., Ahrendt, H. 2008. Exhumation and deformation history of the lower crustal section of the Valstrona di Omegna in the Ivrea Zone, southern Alps. In: Siegesmund, S., Fügenschuh, B., Froitzheim, N. (eds.) Tectonic aspects of the Alpine-Dinaride-Carpathian System. Geol. Soc. Spec. Publ., London, 298, 45-68.

Siegesmund, S., Steenken, A., Martino, R.D., Wemmer, K., López de Luchi, M.G., Frei, R., Presnyakov, S., Guereschi, A. 2010. Time constraints on the tectonic evolution of the Eastern Sierras Pampeanas (Central Argentina). Int. J. Earth Sci. 99, 1199-1226.

Sinha, S., Alsop, I.G., Biswal, T.K. 2010. The evolution and significance of microfracturing within feldspars in low-grade granitic mylonites: A case study from the Eastern Ghats Mobile Belt, India. J. Struct. Geol. 32, 1417-1429.

Sircombe, K.N. 2000. Quantitative comparison of large sets of geochronological data using multivariate analysis: A provenance study example from Australia. Geochim. Cosmochim. Acta 64, 1593-1616.

Sláma, J., Košler, J., Condon, D.J., Crowley, J.L., Gerdes, A., Hanchar, J.M., Horstwood, M.S.A., Morris, G.A., Nasdala, L., Norberg, N., Schaltegger, U., Schoene, B., Tubrett, M.N., Whitehouse, M.J. 2008. Plešovice zircon - a new natural reference material for U-Pb and Hf isotopic microanalysis. Chem. Geol. 249, 1-35.

Smith, S.A.F., Strachan, R.A., Holdsworth, R.E. 2007. Microstructural evolution within a partitioned midcrustal transpression zone, northeast Greenland Caledonides. Tectonics, 26, TC4003.

Söderlund, U., Patchett, P.J., Vervoort, J.D., Isachsen, C.E. 2004. The ^{176}Lu decay constant determined by Lu-Hf and U-Pb isotope systematics of Precambrian mafic intrusions. Earth Planet. Sci. Lett. 219, 311-324.

Spencer, C.J., Thomas, R.J., Roberts, N.M.W., Cawood, P.A., Millar, I., Tapster, S. 2015. Crustal growth during island arc accretion and transcurrent deformation, Natal Metamorphic Province, South Africa: New isotopic constraints. Precambrian Res. 265, 203-217.

Spoturno, J., Oyhantçabal, P., Goso, C., Aubet, N., Cazaux, S., Huelmo, S., Morales, E. 2004. Mapa geológico y de recursos minerales del Departamento de Canelones a escala 1:100.000. Facultad de Ciencias - Dirección Nacional de Minería y Geología, Montevideo.

Spoturno, J.J., Oyhantçabal, P., Loureiro, J. 2012. Mapa geológico del Departamento de Maldonado escala 1:100.000. Facultad de Ciencias (UdelaR) - Dirección Nacional de Minería y Geología (MIEM), Montevideo.

Stacey, J.S., Kramers, J.D. 1975. Approximation of terrestrial lead isotope evolution by a two-stage model. Earth Planet. Sci. Lett. 26, 207-221.

Steenken, A., Siegesmund, S., Heinrichs, T. 2000. The emplacement of the Rieserferner Pluton (Eastern Alps, Tyrol): constraints from field observations, magnetic fabrics and microstructures. J. Struct. Geol. 22, 1855-1873.

Steiger, R.H., Jaeger, E. 1977. Subcommission on geochronology: convention on the use of decay constants in geo- and cosmochronology. Earth Planet. Sci. Lett. 36, 359-362.

Stern, R.A. 1998. High resolution SIMS determination of radiogenic trace-isotopes ratios in minerals. In: Cabri, L.J., Vaughan, D.J. (eds.) Modern approaches to ore and environmental mineralogy. Mineralogical Association of Canada, Short Course Series, Ottawa, 241-268.

Stipp, M., Tullis, J. 2003. The recrystallized grain size piezometer for quartz. Geophys. Res. Lett. 30, 2088.

Stipp, M., Stünitz, H., Heilbronner, R., Schmid, S.M. 2002. The eastern Tonale fault: a `natural laboratory´ for crystal plastic deformation of quartz over a temperature range from 250 to 700°C. J. Struct. Geol. 24, 1861-1884.

Stipp, M., Fügenschuh, B., Gromet, L.P., Stünitz, H., Schmid, S.M. 2004. Contemporaneous plutoning and strike-slip faulting: A case study from the Tonale fault zone north of the Adamello Pluton (Italian Alps). Tectonics 23, TC3004.

Suess, E. 1885. Das Antlitz der Erde. Temsky, Vienna.

Sullivan, W.A, Law, R.D. 2007. Deformation path partitioning within the transpressional White Mountain shear zone, California and Nevada. J. Struct. Geol. 29, 583-598.

Sullivan, W.A., Boyd, A.S., Monz, M.E. 2013. Strain localization in homogeneous granite near the brittle-ductile transition: A case study of the Kellyland fault zone, Maine, USA. J. Struct. Geol. 56, 70-88.

Teixeira, W., Renne, P.R., Bossi, J., Campal, N., D'Agrella Filho, M.S. 1999. ^{40}Ar-^{39}Ar and Rb-Sr geochronology of the Uruguayan dike swarm, Rio de la Plata Craton and implications for Proterozoic intraplate activity in western Gondwana. Precambrian Res. 93, 153-180.

Teixeira, J.B.G., da Silva, M.G., Misi, A., Pereira Cruz, S.C., da Silva Sá, J.H. 2010. Geotectonic setting and metallogeny of the northern São Francisco craton, Bahia, Brazil. J. South Am. Earth Sci. 30, 71-83.

Teixeira, W., D'Agrella Filho, M.S., Hamilton, M., Ernst, R.E., Girardi, V.A.V., Mazzuchelli, M., Bethencourt, J.S. 2013. U-Pb (ID-TIMS) baddeleyite ages and paleomagnetism of 1.79 and 1.59 Ga tholeiitic dyke swarms, and position of the Rio de la Plata Craton within the Columbia supercontinent. Lithos 174, 157-174.

Teyssier, C., Tikoff, B., Markley, M. 1995. Oblique plate motion and continental tectonics. Geology 23, 447-450.

Thomas, R.J., Agenbacht, A.L.D., Cornell, D.H., Moore, J.M. 1994. The Kibaran of southern Africa: Tectonic evolution and metallogeny. Ore Geol. Rev. 9, 131-160.

Tibaldi, A.M., Otamendi, J.E., Cristofolini, E.A., Baliani, I., Walker Jr, B.A., Bergantz, G.W. 2013. Reconstruction of the Early Ordovician Famatinian arc through thermobarometry in lower and middle crustal exposures, Sierra de Valle Fértil, Argentina. Tectonophysics 589, 151-166.

Tohver, E., D'Agrella Filho, M.S., Trindade, R.I.F. 2006. Paleomagnetic record of Africa and South America for the 1200-500 Ma interval, and evaluation of Rodinia and Gondwana assemblies. Precambrian Res. 147, 193-222.

Toy, V.G., Prior, D.J., Norris, R.J. 2008. Quartz fabrics in the Alpine Fault mylonites: Influence of pre-existing preferred orientations on fabric development during progressive uplift. J. Struct. Geol. 30, 602-621.

Treagus, S.H., Treagus, J.E. 1992. Transected folds and transpression: how are they associated?. J. Struct. Geol. 14, 361-367.

Ulrich, S., Konopásek, J., Jeřábek, P., Tajčmanová, L. 2011. Transposition of structures in the Neoproterozoic Kaoko Belt (NW Namibia) and their absolute timing. Int. J. Earth Sci. 100, 415-429.

Umpierre, M., Halpern, M. 1971. Edades Sr-Rb del Sur de la República Oriental del Uruguay. Rev. Asoc. Geol. Argentina 26, 133-151.

van der Pluijm, B.A., Mezger, K., Cosca, M.A., Essene, E.J. 1994. Determining the significance of high-grade shear zones by using temperature-time paths, with examples from the Grenville orogen. Geology 22, 743-746.

van Schijndel, V., Cornell, D.H., Frei, D., Simonsen, S.L., Whitehouse, M.J. 2014. Crustal evolution of the Rehoboth Province from Archaean to Mesoproterozoic times: Insights from the Rehoboth Basement Inlier. Precambrian Res. 240, 22-36.

Vavra, G., Schmid, R., Gebauer, D. 1999. Internal morphology, habit and U-Th-Pb microanalysis of amphibolite-to-granulite facies zircons: geochronology of the Ivrea Zone (Southern Alps). Contrib. Mineral. Petrol. 134, 380-404.

Vermeesch, P. 2012. On the visualization of detrital age distributions. Chem. Geol. 312-313, 190-194.

Villa, I.M. 1998. Isotopic closure. Terra Nova 10, 42-47.

Viola, G., Henderson, I.H.C., Bingen, B., Thomas, R.J., Smethurst, M.A., de Azavedo, S. 2008. Growth and collapse of a deeply eroded orogen: Insights from structural, geophysical, and geochronological constraints on the Pan-African evolution of NE Mozambique. Tectonics 27, TC5009.

Vitale, S., Mazzoli, S. 2008. Strain analysis of heterogeneous ductile shear zones based on the attitudes of planar markers. J. Struct. Geol. 32, 321-329.

Voll, G. 1976. Recrystallization of quartz, biotite and feldspars from Erstfeld to the Leventina nappe, Swiss Alps, and its geological significance. Schweiz. Mineral. Petrographische Mitt. 56, 641-647.

von Blanckenburg, F., Davies, J.H. 1995. Slab breakoff: A model for syncollisional magmatism and tectonics in the Alps. Tectonics 14, 120-131.

Vry, J.K., Baker, J.A. 2006. LA-MC-ICPMS Pb-Pb dating of rutile from slowly cooled granulites: Confirmation of the high closure temperature for Pb diffusion in rutile. Geochim. Cosmochim. Acta 70, 1807-1820.

Wang, Y., Zwingmann, H., Zhou, L., Lo, C., Viola, G., Hao, J. 2016. Direct dating of folding events by 40Ar/39Ar analysis of synkinematic muscovite from flexural-slip planes. J. Struct. Geol. 83, 46-59.

Watson, E.B., Harrison, T.M. 1983. Zircon saturation revisited: temperature and composition effects in a variety of crustal magma types. Earth Planet. Sci. Lett. 64, 295-304.

Wegener, A. 1915. Die Entstehung der Kontinente und Ozeane. Friedrich Vieweg & Sohn, Braunschweig.

Wemmer, K. 1991. K/Ar-Altersdatierungsmöglichkeiten für retrograde Deformationsprozesse im spröden und duktilen Bereich - Beispiele aus der KTB-Vorbohrung (Oberpfalz) und dem Bereich der Insubrischen Linie (N-Italien). Göttinger Arb. Geol. Paläont. 51, 1-61.

West, T.E. 1998. Structural analysis of the Carolina-Inner Piedmont terrane boundary: Implications for the age and kinematics of the central Piedmont suture, a terrane boundary that records Paleozoic Laurentia-Gondwana interactions. Tectonics 17, 379-394.

White, S.H., Burrows, S.E., Carreras, J., Shaw, N.D., Humphreys, F.J. 1980. On mylonites in ductile shear zones. J. Struct. Geol. 2, 175-187.

Whitehouse, M.J., Platt, J.P. 2003. Dating high-grade metamorphism - constraints from rare-earth elements in zircon and garnet. Contrib. Mineral. Petrol. 145, 61-74.

Wiberley, C. 1999. Are feldspar-to-mica reactions necessarily reaction-softening processes in fault zones?. J. Struct. Geol. 21, 1219-1227.

Williams, I.S. 1998. U-Th-Pb geochronology by ion microprobe. In: McKibben, M.A., Shanks III, W.C., Ridley, W.I. (eds.) Applications of microanalytical techniques to understanding mineralizing processes. Society of Economic Geologists, Reviews in Economic Geology, Littleton, 1-35.

Wong, M.S., Peck, W.H., Selleck, B.W., Catalano, J.P., Hochman, S.D., Maurer, J.T. 2011. The Black Lake shear zone: a boundary between terranes in the Adirondack Lowlands, Grenville Province. Precambrian Res. 188, 57-72.

Ye, H.-M., Li, X.-H., Li, Z.-X., Zhang, C.-L. 2008. Age and origin of high Ba-Sr appinite-granites at the northwestern margin of the Tibet Plateau: Implications for early Paleozoic tectonic evolution of the Western Kunlun orogenic belt. Gondwana Res. 13, 126-138.

York, D., Hall, C.M., Yanase, Y., Hanes, J.A., Kenyon, W.J. 1981. ^{40}Ar/^{39}Ar dating of terrestrial minerals with a continuous laser. Geophys. Res. Lett. 8, 1136-1138.

Zhang, B., Zhang, J., Zhong, D. 2010. Structure, kinematics and ages of transpression during strain-partitioning in the Chongshan shear zone, western Yunnan, China. J. Struct. Geol. 32, 445-463.

Zhao, L., Li, T., Peng, P., Guo, J., Wang, W., Wang, H., Santosh, M., Zhai, M. 2015. Anatomy of zircon growth in high pressure granulites: SIMS U-Pb geochronology and Lu-Hf isotopes from the Jiaobei Terrane, eastern North China Craton. Gondwana Res. 28, 1373-1390.

Ziegler, U.R.F., Stoessel, G.F.U. 1991. New constraints on the age of the Weener Intrusive Suite, the Gamsberg Granite and the crustal evolution of the Rehoboth Basement Inlier, Namibia. Communs. Geol. Surv. Namibia 7, 81-85.

Ziegler, U.R.F., Stoessel, G.F.U. 1993. Age determinations in the Rehoboth Basement Inlier, Namibia. Geological Survey of Namibia, Windhoek.

Zimmermann, U. 2011. Comment on "Provenance of the Arroyo del Soldado Group (Ediacaran to Cambrian, Uruguay): Implications for the palaeogeographic evolution of southwestern Gondwana" by Blanco et al. [Precambrian Res., 171 (2009), 57-73] - A necessary remark on the use of provenance data. Precambrian Res. 186, 233-236.

-Appendix 1-

CPO Sample Locations

Unit	Sample	Location	
Sarandí del Yí Shear Zone	AA-12	33° 18.574´ S	55° 31.001´ W
	AA-15	33° 24.658´ S	55° 29.052´ W
	AA-75-2	34° 30.440´ S	55° 22.348´ W
	AA-76	34° 37.930´ S	55° 22.904´ W
	SY-45	33° 21.808´ S	55° 29.013´ W
Sierra de Sosa Shear Zone	UY-112-14	33° 32.303´ S	55° 01.366´ W
	UY-113-14	33° 32.707´ S	55° 01.630´ W
	UY-157-14	33° 47.333´ S	55° 11.798´ W
	UY-167-14	33° 38.036´ S	55° 07.904´ W
María Albina Shear Zone	UY-61-14	33° 27.323´ S	54° 44.707´ W
	UY–83–14	33° 23.940´ S	54° 45.332´ W
	UY-102-14	33° 22.643´ S	54° 45.125´ W
	UY-104-14	33° 22.339´ S	54° 44.814´ W
	UY-165-14	33° 28.567´ S	54° 46.370´ W
Arroyo Corrales Shear Zone	UY-89-14-1	33° 23.737´ S	54° 38.920´ W
	UY-89-14-2	33° 23.737´ S	54° 38.920´ W
María Albina Orthogneiss	UY-45-14	33° 22.615´ S	54° 40.963´ W
Cordillera Shear Zone	UY-9-14-2	34° 32.519´ S	54° 41.224´ W
Cerro Amaro Shear Zone	UY-48-14	32° 54.501´ S	54° 16.831´ W
Punta de las Palmas Shear Zone	UY-32-14	34° 16.983´ S	54° 41.080´ W

Table A.1: Summary of samples from mylonites collected for quartz CPO analyses. Sample locations are indicated in geographic coordinates (datum WGS84). Sample UY-61-14 corresponds to a minor outcrop of mylonites located near the María Albina Shear Zone and is thus analysed with the latter.

-Appendix 2-

Geochronology Samples

Sample	Unit	Method	Location	
AA-12	Mylonite SYSZ	U-Pb LA-ICP-MS Zrn (B) U-Pb LA-ICP-MS Ttn (B) Ar/Ar Hbl (A)	33° 18.574´ S	55° 31.001´ W
AA-13	Mylonite SYSZ	U-Pb LA-ICP-MS Zrn (B) U-Pb LA-ICP-MS Ttn (B) Hf isotopy (B)	33° 18.381´ S	55° 29.899´ W
BUY-81-11	Mylonite SYSZ	U-Pb SHRIMP Zrn (B) Ar/Ar Hbl (A)	33° 32.922´ S	55° 27.550´ W
BUY-84-11	Mylonite SYSZ	U-Pb SHRIMP Zrn (B)	33° 21.649´ S	55° 28.755´ W
BUY-93-11	Mylonite SYSZ	U-Pb LA-ICP-MS Zrn (B)	34° 26.938´ S	55° 22.159´ W
UY-22-14	Cerro Caperuza granite	U-Pb LA-ICP-MS Zrn (B)	34° 34.965´ S	55° 22.148´ W
BUY-92-11	Mylonite SYSZ	Ar/Ar Ms (F) Rb-Sr WR-Ms (G)	34° 26.938´ S	55° 22.159´ W
BUY-94-11	Mylonite SYSZ	Ar/Ar Ms (F) Rb-Sr WR-Ms (G)	34° 30.434´ S	55° 22.364´ W
BUY-54-11	Mafic granulite VRGC	U-Pb LA-ICP-MS Zrn (B) Hf isotopy (B)	31° 37.513´ S	55° 25.588´ W
BUY-57-11	Tonalitic-dioritic orthogneiss VRGC	U-Pb LA-ICP-MS Zrn (B) Hf isotopy (B)	31° 39.662´ S	55° 20.024´ W
BUY-61-11	Felsic orthogneiss VRGC	U-Pb LA-ICP-MS Zrn (B) Hf isotopy (B)	31° 42.218´ S	55° 09.152´ W
BUY-63-11	Amarillo granite	U-Pb LA-ICP-MS Zrn (B) Hf isotopy (B)	31° 37.388´ S	55° 07.247´ W
BUY-65-11	Felsic orthogneiss VRGC	U-Pb LA-ICP-MS Zrn (B) Hf isotopy (B)	32° 54.434´ S	54° 54.134´ W
BUY-77-11	Zapicán intrusion	U-Pb LA-ICP-MS Zrn (B) Hf isotopy (B)	33° 31.851´ S	54° 58.213´ W
BUY-88-11	Cerro Colorado granite	U-Pb LA-ICP-MS Zrn (B) Hf isotopy (B)	33° 51.927´ S	55° 32.764´ W
Nb-66	Augen gneiss Congo Craton	U-Pb LA-ICP-MS Zrn (B) Hf isotopy (B)	19° 03.205´ S	13° 24.565´ E
BUY-55-11	Minas de Corrales Formation	U-Pb LA-ICP-MS Zrn (B) Hf isotopy (B)	31° 33.423´ S	55° 29.574´ W
BUY-76-11	Las Tetas Complex	U-Pb LA-ICP-MS Zrn (B) Hf isotopy (B)	33° 34.914´ S	54° 50.634´ W
UY-4-13	Lavalleja Group	U-Pb LA-ICP-MS Zrn (S)	33° 23.673´ S	54° 39.678´ W
UY-6-13	Zanja del Tigre Complex	U-Pb LA-ICP-MS Zrn (S)	34° 10.790´ S	55° 17.242´ W
UY-8-13	Lavalleja Group	U-Pb LA-ICP-MS Zrn (S)	34° 29.745´ S	55° 12.973´ W
UY-9-13	Zanja del Tigre Complex	U-Pb LA-ICP-MS Zrn (S)	34° 33.303´ S	55° 05.355´ W
UY-16-13	Metasandstone NPT	U-Pb LA-ICP-MS Zrn (S)	33° 16.675´ S	55° 06.263´ W
UY-22-13	Las Tetas Complex	U-Pb LA-ICP-MS Zrn (S) Ar/Ar Ms (F)	33° 23.272´ S	54° 44.353´ W
UY-24-13	Mylonite MASZ	U-Pb LA-ICP-MS Zrn (S) Ar/Ar Ms (F)	33° 21.495´ S	54° 43.895´ W
BUY-64-11	Mylonite SSSZ	U-Pb LA-ICP-MS Zrn (B)	32° 57.341´ S	54° 52.355´ W
BUY-66-11	Mylonite TSZ	U-Pb LA-ICP-MS Zrn (B)	32° 48.706´ S	54° 39.985´ W
UY-13-14	Mylonite SBSZ	Ar/Ar Hbl (F)	34° 54.159´ S	55° 02.720´ W

UY-40-14	Amphibolite NPT	Ar/Ar Hbl (F)	33° 17.206′ S	54° 49.393′ W
UY-57-14	Amphibolite NPT	Ar/Ar Hbl (F)	32° 58.754′ S	54° 33.894′ W
U13MH04	Las Tetas Complex	Ar/Ar Ms (F) Rb-Sr WR-Ms (G)	33° 23.447′ S	54° 45.152′ W
UY-1-13	Las Tetas Complex	Ar/Ar Phl (F) Rb-Sr WR-Phl (G)	33° 22.518′ S	54° 41.870′ W
UY-3-13	Mylonite MASZ	Ar/Ar Ms (F)	33° 22.657′ S	54° 45.112′ W
UY-23-13	Las Tetas Complex	K-Ar Fc (G)	33° 23.270′ S	54° 44.205′ W
UY-26-14	Puntas del Arroyo Rocha granite	K-Ar Ms (G)	34° 20.155′ S	54° 36.402′ W
UY-27-14	Pegmatite	K-Ar Ms (G)	34° 20.155′ S	54° 36.402′ W
UY-41-14	Micaschist	K-Ar Ms (G)	33° 16.241′ S	55° 01.463′ W
UY-45-14	María Albina orthogneiss	K-Ar Ms (G)	33° 22.615′ S	54° 40.963′ W
UY-48-14	Mylonite CASZ	K-Ar Ms (G)	32° 54.501′ S	54° 16.831′ W
UY-54-14	Micaschist	K-Ar Ms (G)	33° 00.579′ S	54° 33.211′ W
UY-55-14	Micaschist	K-Ar Ms (G)	32° 58.754′ S	54° 33.894′ W
UY-64-14	Mylonitic orthogneiss	K-Ar Ms (G)	33° 31.565′ S	54° 49.750′ W
UY-6-14	Mylonite CSZ	K-Ar Ms (G)	34° 34.360′ S	54° 43.385′ W

Table A.2: Summary of geochronological data. Applied method, target (Zrn: zircon, Ttn: titanite, Hbl: hornblende, Ms: muscovite, WR: whole-rock, Phl: phlogopite, Fu: fuchsite), laboratory (A: Geochronology Laboratory of the University of Alaska Fairbanks, B: Geochronological Research Centre of the University of São Paulo, F: Argonlab Freiberg, G: Geoscience Centre of the Georg-August-Universität Göttingen, S: Central Analytical Facility of the Stellenbosch University) and unit are indicated. NPT: Nico Pérez Terrane, PAT: Piedra Alta Terrane, VRGC: Valentines-Rivera Granulitic Complex, SYSZ: Sarandí del Yí Shear Zone, MASZ: María Albina Shear Zone, SSSZ: Sierra de Sosa Shear Zone, TSZ: Tupambaé Shear Zone, SBSZ: Sierra Ballena Shear Zone, CASZ: Cerro Amaro Shear Zone, CSZ: Cordillera Shear Zone.

-Appendix 3-

U-Pb Geochronology

Sample	Spot	% Pb common	Pb rad (ppm)	Th (ppm)	U (ppm)	Th/U	$^{207}Pb/^{235}U$	±1σ	$^{206}Pb/^{238}U$	±1σ	Coef. Corr.	$^{238}U/^{206}Pb$	±1σ	$^{207}Pb/^{206}Pb$	±1σ	$^{206}Pb/^{238}U$	±1σ	$^{207}Pb/^{206}Pb$	±1σ	% Conc
																AGES (Ma)				
	1.1	0.22	105.2	125.3	240.4	0.521	6.7064	0.1273	0.3689	0.0045	0.29	2.7110	0.0329	0.1319	0.0025	2024	21	2123	33	95
	2.1	1.87	83.9	116.4	189.1	0.615	6.8040	0.1544	0.3804	0.0052	0.96	2.6285	0.0357	0.1297	0.0030	2078	24	2094	42	99
	3.1	0.17	142.8	199.5	314.4	0.635	6.7413	0.1226	0.3742	0.0044	0.94	2.6725	0.0315	0.1307	0.0023	2049	21	2107	31	97
	7.1	0.18	204.4	180.6	467.8	0.386	7.1240	0.1224	0.3919	0.0046	0.92	2.5519	0.0297	0.1319	0.0021	2131	21	2123	28	100
	8.1	0.13	142.7	190.4	327.3	0.582	6.5846	0.1368	0.3655	0.0048	0.90	2.7363	0.0358	0.1307	0.0026	2008	22	2107	35	95
	9.1	1.08	286.7	217.5	633.3	0.343	6.4513	0.1109	0.3617	0.0042	0.98	2.7645	0.0321	0.1293	0.0021	1990	20	2089	28	95
	10.1	0.14	758.2	563.8	1515.8	0.372	6.7559	0.0887	0.3767	0.0030	0.97	2.6544	0.0215	0.1301	0.0015	2061	14	2099	21	98
	10.2	1.33	86.6	123.6	186.6	0.662	6.0989	0.0979	0.3526	0.0038	0.95	2.8361	0.0308	0.1255	0.0021	1947	18	2035	29	95
	12.1	0.32	156.6	203.5	342.1	0.595	6.7121	0.0928	0.3742	0.0033	0.86	2.6722	0.0238	0.1301	0.0017	2049	16	2099	23	97
	13.1	0.06	144.3	262.1	297.7	0.880	6.6857	0.0969	0.3740	0.0036	0.53	2.6739	0.0255	0.1297	0.0018	2048	17	2093	25	97
	13.2	0.07	149.6	198.1	332.1	0.596	6.5823	0.0943	0.3711	0.0034	0.47	2.6945	0.0248	0.1286	0.0018	2035	16	2079	24	97
	14.1	3.16	332.8	179.4	847.2	0.212	6.0940	0.0675	0.3482	0.0024	1.00	2.8720	0.0198	0.1269	0.0016	1926	12	2056	22	93
BUY-54-11	14.2	0.39	99.2	124.7	222.6	0.560	6.5634	0.0994	0.3713	0.0038	0.32	2.6933	0.0272	0.1282	0.0019	2035	18	2074	26	98
	16.2	0.11	142.0	180.7	320.8	0.5630	6.5449	0.0908	0.3696	0.0033	0.63	2.7058	0.0243	0.1284	0.0018	2027	16	2077	24	97
	11.2	0.31	99.3	118.6	229.0	0.518	6.3731	0.1008	0.3665	0.0040	0.57	2.7284	0.0294	0.1261	0.0020	2013	19	2044	28	98
	16.1	0.00	92.3	2.0	149.7	0.013	6.2693	0.0789	0.3638	0.0028	0.35	2.7491	0.0215	0.1250	0.0015	2000	13	2029	21	98
	1.2	0.64	56.1	39.3	94.9	0.414	6.9253	0.1869	0.4197	0.0063	0.95	2.3827	0.0356	0.1197	0.0032	2259	29	1951	48	115
	4.1	2.08	323.5	297.5	718.9	0.414	5.7944	0.1137	0.3233	0.0040	0.99	3.0927	0.0383	0.1300	0.0026	1806	19	2098	35	86
	6.1	0.31	158.2	219.3	334.2	0.656	5.3562	0.1251	0.2988	0.0042	0.99	3.3470	0.0467	0.1300	0.0031	1685	21	2098	43	80
	11.1	0.00	331.8	553.2	714.7	0.774	5.3665	0.0766	0.3031	0.0027	0.99	3.2996	0.0295	0.1284	0.0016	1707	13	2077	22	82
	15.1	1.39	164.4	222.3	334.3	0.665	5.5247	0.0818	0.3114	0.0030	1.00	3.2113	0.0310	0.1287	0.0018	1748	15	2080	25	84
	15.2	2.72	55.2	84.5	165.0	0.512	4.9734	0.0869	0.2870	0.0035	0.97	3.4845	0.0430	0.1257	0.0023	1626	18	2038	31	79
	6.2	16.00	49.0	62.4	155.9	0.400	3.0405	0.0720	0.1795	0.0025	0.99	5.5701	0.0764	0.1228	0.0029	1064	13	1998	42	53
	4.2	9.85	28.1	9.3	58.4	0.160	7.6361	0.2597	0.4514	0.0081	0.92	2.2152	0.0398	0.1227	0.0040	2402	35	1996	57	120
	5.1	9.86	28.0	9.3	58.4	0.160	7.6289	0.2602	0.4511	0.0081	0.92	2.2167	0.0400	0.1226	0.0040	2400	35	1995	57	120
	5.2	7.61	30.4	12.4	47.2	0.263	8.7394	0.3426	0.5178	0.0103	0.95	1.9311	0.0385	0.1224	0.0053	2690	44	1992	76	135
	1.1	0.11	165.6	301.7	346.8	0.870	6.6848	0.1117	0.3757	0.0041	0.82	2.6614	0.0289	0.1290	0.0017	2056	19	2085	23	98
	2.1	0.21	93.3	43.9	223.4	0.197	6.9058	0.1179	0.3789	0.0044	0.99	2.6391	0.0309	0.1322	0.0020	2071	21	2127	27	97
	2.2	0.26	145.4	259.7	295.3	0.879	6.7728	0.1158	0.3775	0.0042	0.85	2.6490	0.0298	0.1301	0.0018	2065	20	2100	24	98
BUY-57-11	3.1	0.04	196.2	363.6	399.9	0.909	7.0911	0.1161	0.3936	0.0042	0.94	2.5408	0.0270	0.1307	0.0017	2139	19	2107	23	101
	5.1	0.66	44.8	39.5	107.0	0.369	6.1774	0.1278	0.3542	0.0050	0.97	2.8230	0.0401	0.1265	0.0024	1955	24	2050	35	95
	7.1	0.57	76.0	122.2	173.8	0.703	6.1681	0.1137	0.3558	0.0044	0.29	2.8104	0.0345	0.1257	0.0020	1962	21	2039	28	96
	8.1	0.08	118.3	149.7	255.3	0.586	6.7711	0.1234	0.3795	0.0046	0.18	2.6350	0.0318	0.1294	0.0020	2074	21	2090	27	99
	9.1	0.02	187.1	328.8	410.7	0.801	6.4875	0.1090	0.3663	0.0040	0.85	2.7301	0.0300	0.1285	0.0017	2012	19	2077	24	96
	10.1	0.23	67.7	48.1	168.1	0.286	6.2317	0.1238	0.3566	0.0048	0.84	2.8045	0.0374	0.1268	0.0022	1966	23	2053	31	95

	12.1	0.24	110.9	174.4	257.2	0.6780	6.0225	0.1159	0.3501	0.0046	0.69	2.8562	0.0378	0.1248	0.0020	1935	22	2025	28	95
	13.1	0.14	67.6	81.8	154.8	0.528	6.5265	0.1401	0.3650	0.0053	0.75	2.7397	0.0397	0.1297	0.0024	2006	25	2094	33	95
	16.1	0.23	121.7	202.2	258.7	0.781	6.4769	0.1210	0.3610	0.0047	0.13	2.7700	0.0362	0.1301	0.0020	1987	22	2100	27	94
	16.2	0.40	83.2	111.3	183.7	0.606	6.6220	0.1365	0.3666	0.0053	0.46	2.7281	0.0391	0.1310	0.0023	2013	25	2112	32	95
	18.1	0.18	145.9	258.6	323.0	0.801	6.0242	0.1172	0.3507	0.0047	0.63	2.8512	0.0382	0.1246	0.0020	1938	22	2023	29	95
	19.1	0.14	155.4	291.5	319.1	0.914	6.5949	0.1285	0.3684	0.0049	0.28	2.7147	0.0363	0.1298	0.0021	2022	23	2096	28	96
	20.1	0.30	65.3	64.3	158.3	0.4060	6.3318	0.1564	0.3599	0.0058	0.92	2.7784	0.0446	0.1276	0.0029	1982	27	2065	41	95
	4.1	0.45	56.8	11.0	176.4	0.062	5.1023	0.1011	0.3233	0.0043	0.91	3.0931	0.0407	0.1145	0.0020	1806	21	1871	33	96
	19.2	0.68	37.2	32.8	102.7	0.320	4.9172	0.1790	0.3172	0.0065	0.86	3.1528	0.0649	0.1124	0.0043	1776	32	1839	70	96
	11.1	0.35	56.5	40.0	138.8	0.288	4.9440	0.1359	0.3216	0.0059	0.96	3.1094	0.0573	0.1115	0.0032	1798	29	1824	49	98
	18.2	0.24	41.2	38.7	105.0	0.368	4.9725	0.1763	0.3148	0.0065	0.88	3.1770	0.0653	0.1146	0.0042	1764	32	1873	68	94
	14.2	0.73	43.7	36.5	116.3	0.314	4.6515	0.1904	0.2960	0.0067	0.82	3.3785	0.0769	0.1140	0.0051	1671	34	1864	81	89
	8.2	0.40	39.3	33.7	82.3	0.409	6.1365	0.1467	0.3661	0.0061	0.90	2.7317	0.0453	0.1216	0.0028	2011	28	1979	41	101
	14.1	0.21	68.8	100.7	164.6	0.612	5.6389	0.1331	0.3400	0.0052	0.73	2.9410	0.0450	0.1203	0.0026	1887	25	1960	39	96
	17.1	0.54	36.6	38.2	104.4	0.366	4.5066	0.1507	0.3039	0.0058	0.97	3.2903	0.0626	0.1075	0.0034	1711	28	1758	55	97
	6.1	0.02	161.7	282.2	329.3	0.857	7.1450	0.1182	0.3848	0.0042	0.87	2.5986	0.0285	0.1347	0.0018	2099	20	2160	23	97
	15.1	0.12	86.0	140.3	194.2	0.723	6.3345	0.1364	0.3726	0.0052	0.97	2.6842	0.0378	0.1233	0.0023	2041	25	2005	33	101
	5.1	0.17	377.0	326.1	605.8	0.538	11.6492	0.1479	0.4805	0.0040	0.88	2.0812	0.0175	0.1758	0.0018	2529	17	2614	17	96
	5.2	2.77	928.2	245.7	1967.4	0.125	8.6089	0.1027	0.4210	0.0033	0.90	2.3753	0.0186	0.1483	0.0014	2265	15	2327	17	97
	9.1	1.12	173.1	180.8	312.5	0.578	10.6769	0.1777	0.4643	0.0054	0.88	2.1537	0.0251	0.1668	0.0023	2459	24	2526	23	97
	12.1	0.47	685.3	397.6	1317.3	0.302	10.5855	0.1575	0.4662	0.0049	0.98	2.1448	0.0225	0.1647	0.0020	2467	22	2504	20	98
	13.1	0.35	211.0	118.7	423.8	0.280	8.8152	0.1355	0.4210	0.0045	0.99	2.3752	0.0253	0.1519	0.0019	2265	20	2367	22	95
	2.2	0.08	188.4	224.8	439.7	0.511	6.1924	0.0916	0.3559	0.0034	0.70	2.8097	0.0267	0.1262	0.0015	1963	16	2046	22	95
	3.1	1.98	98.4	331.8	184.8	1.795	5.8902	0.1052	0.3379	0.0038	0.87	2.9598	0.0329	0.1264	0.0020	1876	18	2049	28	91
	4.2	0.08	251.6	286.6	564.1	0.508	6.8720	0.0951	0.3821	0.0034	0.86	2.6169	0.0235	0.1304	0.0015	2086	16	2104	20	99
	6.2	0.14	151.3	242.7	335.2	0.724	6.3273	0.0981	0.3633	0.0035	0.80	2.7527	0.0267	0.1263	0.0017	1998	17	2047	23	97
	10.2	0.55	144.1	191.2	330.4	0.579	6.4577	0.1046	0.3659	0.0040	0.94	2.7329	0.0300	0.1280	0.0017	2010	19	2071	23	97
	7.1	0.06	227.3	233.3	531.9	0.439	6.3740	0.0869	0.3644	0.0032	0.86	2.7441	0.0243	0.1269	0.0014	2003	15	2055	20	97
BUY-61-11	11.1	0.44	1015.	239.5	2485.3	0.096	7.2274	0.1057	0.4050	0.0040	0.89	2.4689	0.0247	0.1294	0.0014	2192	19	2090	20	104
	14.1	2.78	282.7	183.1	700.0	0.262	6.5451	0.0883	0.3549	0.0033	1.00	2.8179	0.0263	0.1338	0.0017	1958	16	2148	22	91
	1.1	3.27	755.5	944.3	1196.8	0.7890	10.7135	0.1456	0.4450	0.0040	0.68	2.2470	0.0203	0.1746	0.0018	2373	18	2602	18	91
	2.1	0.00	220.7	152.5	420.2	0.363	8.5208	0.1136	0.4077	0.0037	0.97	2.4525	0.0220	0.1516	0.0017	2205	17	2364	19	93
	6.1	0.00	198.2	208.6	324.8	0.642	9.8619	0.1459	0.4290	0.0042	0.99	2.3311	0.0227	0.1667	0.0021	2301	19	2525	21	91
	7.2	0.24	171.2	706.4	277.1	2.549	6.6325	0.1034	0.3920	0.0038	0.99	2.5510	0.0250	0.1227	0.0018	2132	18	1996	26	106
	8.1	1.02	176.7	321.0	282.9	1.1350	10.6748	0.1834	0.4406	0.0054	0.95	2.2697	0.0280	0.1757	0.0024	2353	24	2613	23	90
	12.2	2.23	83.6	88.8	185.4	0.479	7.0102	0.1341	0.4020	0.0051	0.99	2.4875	0.0317	0.1265	0.0022	2178	24	2050	29	106
	15.2	1.06	36.2	145.2	66.2	2.192	6.1940	0.1878	0.3719	0.0070	0.85	2.6887	0.0505	0.1208	0.0040	2038	33	1968	60	103
	1.2	12.03	480.5	145.6	1240.3	0.117	4.6768	0.0694	0.2581	0.0025	0.99	3.8747	0.0370	0.1314	0.0014	1480	12	2117	19	69
	4.1	5.61	924.1	318.2	2116.1	0.150	6.2744	0.0833	0.3246	0.0029	0.91	3.0810	0.0272	0.1402	0.0014	1812	14	2230	17	81
	10.1	34.30	167.8	579.0	731.5	0.792	2.0667	0.0368	0.1188	0.0014	1.00	8.4147	0.1011	0.1261	0.0018	724	8	2045	25	35
	13.2	2.72	107.5	153.8	206.4	0.745	9.5919	0.1559	0.4163	0.0048	0.99	2.4020	0.0275	0.1671	0.0024	2244	22	2529	25	88
	15.1	7.44	410.3	747.8	832.6	0.898	9.8458	0.1402	0.4303	0.0044	0.97	2.3239	0.0237	0.1659	0.0019	2307	20	2517	20	91
BUY-63-11	3.1	1.86	18.0	88.1	172.2	0.512	0.8130	0.0556	0.0975	0.0015	0.62	10.2609	0.1601	0.0605	0.0043	599	9	622	159	96
	4.1	2.05	30.4	158.0	287.6	0.549	0.7819	0.0413	0.0957	0.0013	0.03	10.4502	0.1399	0.0593	0.0032	589	8	577	123	102
	7.1	1.58	8.7	102.6	67.2	1.525	0.8189	0.0825	0.0965	0.0020	0.46	10.3613	0.2128	0.0615	0.0068	594	12	658	228	90

8.1	0.21	53.5	209.8	528.9	0.397	0.7961	0.0240	0.0960	0.0010	0.97	10.4156	0.1044	0.0601	0.0018	591	6	609	62	97
9.1	9.90	37.4	392.3	274.5	1.429	0.7902	0.0463	0.0963	0.0014	0.64	10.3789	0.1474	0.0595	0.0035	593	8	585	124	101
12.1	1.58	23.3	221.6	192.8	1.1500	0.8111	0.0528	0.1001	0.0015	0.65	9.9928	0.1514	0.0588	0.0040	615	9	559	139	109
14.1	3.80	24.7	135.3	233.4	0.580	0.7976	0.0376	0.0948	0.0012	0.35	10.5479	0.1326	0.0610	0.0029	584	7	640	103	91
16.1	1.09	33.8	203.6	309.5	0.658	0.7759	0.0332	0.0963	0.0011	0.76	10.3819	0.1202	0.0584	0.0025	593	7	546	92	108
10.1	1.17	10.9	113.5	85.3	1.330	0.8085	0.1042	0.0927	0.0023	0.23	10.7824	0.2696	0.0632	0.0085	572	14	716	298	79
2.1	1.28	15.1	89.6	124.9	0.718	0.9219	0.0946	0.1036	0.0022	0.57	9.6562	0.2060	0.0646	0.0072	635	13	760	236	83
14.2	3.73	55.0	138.8	562.7	0.247	0.8284	0.0307	0.0968	0.0011	0.63	10.3292	0.1125	0.0621	0.0023	596	6	676	78	88
18.1	2.24	14.7	151.0	115.7	1.306	0.8006	0.0726	0.0998	0.0019	0.40	10.0161	0.1902	0.0582	0.0057	613	11	536	203	114
2.2	0.27	73.5	665.4	545.6	1.220	0.8946	0.0289	0.1075	0.0011	0.64	9.2986	0.0934	0.0603	0.0020	658	6	615	68	107
19.1	0.00	27.8	146.9	274.0	0.536	0.7554	0.0377	0.0915	0.0012	0.60	10.9270	0.1417	0.0599	0.0030	564	7	599	103	94
5.1	0.24	385.4	194.0	958.4	0.202	6.8711	0.1158	0.3660	0.0030	0.99	2.7323	0.0223	0.1362	0.0020	2010	14	2179	26	92
6.1	0.07	257.7	115.6	461.1	0.251	12.2006	0.2194	0.4995	0.0044	0.86	2.0021	0.0177	0.1772	0.0028	2612	19	2626	26	99
6.2	1.03	310.6	115.2	688.7	0.167	11.0578	0.1958	0.4795	0.0041	0.97	2.0855	0.0177	0.1673	0.0026	2525	18	2530	26	99
17.1	0.12	110.8	112.9	184.8	0.611	12.5689	0.2638	0.5017	0.0047	0.97	1.9933	0.0186	0.1817	0.0034	2621	20	2668	32	98
11.1	0.40	79.2	68.1	244.8	0.278	4.4671	0.1074	0.3002	0.0030	0.55	3.3308	0.0335	0.1079	0.0024	1692	15	1764	41	95
1.1	0.00	43.2	189.1	263.0	0.7190	0.3092	0.0106	0.0332	0.0004	0.99	30.1173	0.3418	0.0675	0.0019	211	2	0854	61	24
13.1	9.07	326.9	142.5	1642.3	0.087	2.4725	0.0527	0.1647	0.0014	0.99	6.0725	0.0519	0.1089	0.0019	983	8	1781	32	55
15.1	0.14	299.4	339.6	558.1	0.608	10.2287	0.2070	0.4064	0.0034	0.97	2.4604	0.0208	0.1825	0.0031	2199	16	2676	28	82
17.2	12.88	88.6	172.6	573.2	0.301	5.0234	0.1093	0.3074	0.0027	0.99	3.2530	0.0289	0.1185	0.0024	1728	14	1934	37	89
20.1	0.16	64.4	206.6	115.7	1.786	9.0068	0.2273	0.3889	0.0043	0.70	2.5713	0.0286	0.1680	0.0039	2118	20	2537	41	83
20.2	7.61	37.3	357.8	331.0	1.081	0.5379	0.0239	0.0638	0.0008	0.97	15.6618	0.1992	0.0611	0.0023	399	5	643	82	62
21.1	0.30	69.8	71.7	600.0	0.1200	1.1532	0.0330	0.1127	0.0011	1.00	8.8729	0.0862	0.0742	0.0018	688	6	1047	44	65
1.1	4.00	164.1	286.6	360.5	0.7950	6.9145	0.1122	0.3741	0.0044	0.45	2.6733	0.0318	0.1341	0.0021	2049	21	2152	27	95
10.1	0.35	581.8	553.8	1296.7	0.427	6.9107	0.1069	0.3837	0.0050	0.99	2.6064	0.0340	0.1306	0.0017	2093	24	2107	23	99
2.1	0.26	39.9	75.1	80.2	0.937	7.2977	0.2168	0.3935	0.0080	0.82	2.5416	0.0516	0.1345	0.0045	2139	37	2158	59	99
6.1	0.00	36.7	59.3	79.3	0.748	6.7401	0.1985	0.3661	0.0073	0.86	2.7319	0.0545	0.1335	0.0046	2011	34	2145	61	93
4.1	0.13	75.6	168.5	186.2	0.905	6.2093	0.1213	0.3603	0.0049	0.97	2.7756	0.0380	0.1250	0.0024	1984	23	2029	34	97
8.1	0.07	108.6	168.9	213.4	0.791	7.6731	0.1402	0.4078	0.0061	0.38	2.4520	0.0368	0.1365	0.0022	2205	28	2183	28	101
9.1	0.15	97.1	72.2	202.5	0.357	9.1774	0.1777	0.4195	0.0066	0.96	2.3836	0.0375	0.1587	0.0026	2258	30	2441	27	92
5.1	0.13	48.9	112.8	112.2	1.005	10.0645	0.3652	0.4335	0.0118	0.97	2.3066	0.0626	0.1684	0.0074	2322	52	2541	72	91
11.1	0.08	150.1	96.3	257.4	0.374	13.0114	0.2381	0.4999	0.0076	0.98	2.0003	0.0304	0.1888	0.0030	2613	32	2731	24	95
4.2	0.41	174.7	115.0	1778.7	0.065	0.8783	0.0126	0.1055	0.0010	1.00	9.4764	0.0938	0.0604	0.0008	647	6	617	30	104
BUY-65-11 7.1	0.08	146.9	186.3	415.0	0.449	4.8679	0.0890	0.3045	0.0039	0.99	3.2838	0.0417	0.1159	0.0021	1714	19	1894	32	90
1.2	287.10	130.4	617.9	3464.0	0.178	0.2944	0.0060	0.0298	0.0004	0.15	33.5604	0.4237	0.0717	0.0014	189	2	976	41	19
2.2	95.94	125.3	199.0	2897.5	0.069	0.3007	0.0063	0.0334	0.0004	0.94	29.9428	0.3826	0.0653	0.0013	212	3	784	42	27
3.2	123.49	114.4	257.7	1755.2	0.147	0.4857	0.0108	0.0513	0.0007	0.92	19.5119	0.2591	0.0687	0.0015	322	4	891	45	36
5.2	89.33	92.5	122.7	2448.6	0.050	0.2531	0.0061	0.0287	0.0004	0.95	34.8542	0.4800	0.0640	0.0014	182	2	741	45	24
6.2	181.25	130.7	390.7	3442.5	0.113	0.3026	0.0058	0.0304	0.0004	0.73	32.8481	0.3902	0.0721	0.0014	193	2	988	41	19
7.2	271.90	48.3	134.9	1319.3	0.1020	0.2525	0.0062	0.0233	0.0004	0.65	42.9475	0.7235	0.0786	0.0019	148	2	1163	46	12
8.2	17.16	159.5	302.5	1785.0	0.170	0.7070	0.0133	0.0852	0.0012	0.96	11.7320	0.1616	0.0602	0.0010	527	7	609	37	86
9.2	134.69	115.7	767.7	3258.7	0.236	0.3317	0.0078	0.0373	0.0006	0.84	26.7800	0.4296	0.0644	0.0014	236	4	755	42	31
10.2	37.62	107.8	288.2	1314.5	0.219	0.6607	0.0128	0.0750	0.0011	0.95	13.3289	0.1866	0.0639	0.0013	466	6	737	43	63
11.2	16.33	116.6	159.5	1207.2	0.132	0.7501	0.0147	0.0894	0.0013	0.97	11.1882	0.1579	0.0609	0.0012	552	7	634	42	86
12.2	324.63	116.1	635.1	3041.1	0.209	0.4319	0.0093	0.0443	0.0006	0.86	22.5642	0.3265	0.0707	0.0015	280	4	948	40	29

13.2	388.67	124.8	318.6	2678.4	0.1190	0.4220	0.0087	0.0380	0.0006	0.43	26.2829	0.4170	0.0804	0.0015	241	4	1208	41	19
3.1	22.23	6.3	25.3	42.3	0.599	2.2711	0.1575	0.1849	0.0060	0.93	5.4072	0.1746	0.0891	0.0083	1094	33	1406	184	77
12.1	8.57	22.6	143.3	45.5	3.151	4.7105	0.1707	0.2788	0.0071	0.50	3.5869	0.0919	0.1225	0.0054	1585	36	1994	74	79
13.1	15.90	82.4	226.4	222.3	1.018	4.1893	0.0928	0.2827	0.0047	0.94	3.5374	0.0590	0.1075	0.0024	1605	24	1757	40	91
1.2	0.88	14.9	126.3	116.2	1.087	0.7879	0.0402	0.0971	0.0023	0.44	10.2935	0.2484	0.0588	0.0033	598	14	560	119	106
3.2	0.38	41.3	418.8	302.0	1.387	0.7988	0.0281	0.0983	0.0017	0.51	10.1693	0.1742	0.0589	0.0021	605	10	564	76	107
5.1	0.88	27.5	241.7	237.1	1.019	0.8300	0.0322	0.1014	0.0019	0.71	9.8665	0.1856	0.0594	0.0024	622	11	581	88	107
6.1	0.91	18.0	157.7	151.5	1.041	0.8696	0.0395	0.1013	0.0023	0.61	9.8683	0.2240	0.0622	0.0031	622	13	682	108	91
7.1	0.45	27.1	253.3	225.0	1.126	0.8124	0.0330	0.0995	0.0019	0.52	10.0470	0.1963	0.0592	0.0025	612	11	574	92	106
10.1	0.53	31.8	370.9	228.0	1.626	0.7935	0.0322	0.0969	0.0019	0.35	10.3224	0.2003	0.0594	0.0025	596	11	582	89	102
12.1	0.50	17.6	118.7	154.7	0.768	0.8476	0.0315	0.1015	0.0017	0.56	9.8536	0.1686	0.0606	0.0025	623	10	624	91	99
13.1	0.17	44.0	468.6	344.5	1.360	0.8565	0.0258	0.1043	0.0015	0.78	9.5852	0.1400	0.0595	0.0020	640	9	587	72	108
14.1	2.58	15.6	144.5	120.7	1.197	0.7735	0.0716	0.0954	0.0034	0.01	10.4852	0.3761	0.0588	0.0065	587	20	561	201	104
17.1	6.09	4.2	67.6	37.2	1.816	0.8224	0.0368	0.0983	0.0020	0.44	10.1698	0.2115	0.0607	0.0030	605	12	627	114	96
19.1	0.18	38.0	361.0	292.6	1.234	0.8150	0.0342	0.0997	0.0019	0.66	10.0347	0.1920	0.0593	0.0027	612	11	579	104	105
21.1	0.90	24.2	243.7	195.5	1.247	0.8341	0.0293	0.1004	0.0016	0.82	9.9561	0.1631	0.0602	0.0024	617	10	612	85	100
BUY-77-11 1.1	0.19	28.3	267.0	226.8	1.1770	0.8020	0.0346	0.0996	0.0021	0.60	10.0431	0.2099	0.0584	0.0027	612	12	545	105	112
2.1	0.90	22.1	182.9	172.5	1.060	0.8490	0.0392	0.0982	0.0022	0.05	10.1790	0.2320	0.0627	0.0031	604	13	697	108	86
2.2	1.48	18.1	155.5	150.7	1.031	0.8447	0.0359	0.0971	0.0021	0.67	10.3027	0.2184	0.0631	0.0029	597	12	712	1	83
3.1	0.50	18.9	195.4	152.0	1.285	0.7973	0.0319	0.0928	0.0019	0.08	10.7801	0.2158	0.0623	0.0024	572	11	686	88	83
4.1	1.45	23.9	200.6	201.8	0.994	0.8903	0.0424	0.1012	0.0024	0.56	9.8856	0.2364	0.0638	0.0033	621	14	736	118	84
8.1	0.59	17.7	153.1	145.5	1.052	0.7996	0.0442	0.1018	0.0026	0.13	9.8278	0.2491	0.0570	0.0035	625	15	491	134	127
9.1	0.66	31.9	381.0	241.1	1.580	0.7767	0.0296	0.0985	0.0017	0.46	10.1547	0.1792	0.0572	0.0023	605	10	499	81	121
11.2	0.21	24.7	228.1	204.0	1.118	0.7823	0.0324	0.0978	0.0018	0.36	10.2227	0.1885	0.0580	0.0026	602	11	530	97	113
18.1	0.63	32.3	320.8	256.8	1.249	0.7868	0.0281	0.0979	0.0016	0.36	10.2189	0.1642	0.0583	0.0022	602	9	542	80	111
15.1	0.25	56.8	130.4	121.4	1.074	6.5681	0.1659	0.3680	0.0058	0.71	2.7172	0.0431	0.1294	0.0032	2020	27	2090	44	96
11.1	0.14	215.5	54.0	350.5	0.1540	17.7308	0.3358	0.5615	0.0063	0.95	1.7810	0.0199	0.2290	0.0037	2873	26	3045	26	94
22.1	0.19	72.2	112.6	212.9	0.5290	15.5721	0.2927	0.5350	0.0061	1.00	1.8693	0.0214	0.2111	0.0037	2762	26	2914	28	94
20.1	51.63	18.1	188.2	133.4	1.412	0.8730	0.0501	0.1022	0.0025	0.46	9.7867	0.2437	0.0620	0.0042	627	15	673	142	93
16.1	1.75	5.2	40.8	37.6	1.087	0.9705	0.1166	0.0994	0.0053	0.16	10.0597	0.5313	0.0708	0.0112	611	31	952	326	64
BUY-88-11 1.1	0.35	58.7	86.5	128.5	0.6730	6.7428	0.1434	0.3780	0.0049	0.27	2.6452	0.0343	0.1294	0.0024	2067	23	2089	32	98
5.1	0.12	58.2	101.3	122.5	0.827	6.5473	0.1423	0.3705	0.0050	0.80	2.6991	0.0361	0.1282	0.0025	2032	23	2073	35	98
6.1	0.23	39.0	58.2	84.5	0.689	6.5853	0.1744	0.3687	0.0058	0.61	2.7124	0.0430	0.1295	0.0033	2023	27	2092	44	96
9.1	0.47	332.9	282.9	777.9	0.364	6.6493	0.1104	0.3752	0.0040	0.95	2.6650	0.0281	0.1285	0.0018	2054	19	2078	24	98
17.1	0.53	13.2	21.5	28.5	0.755	6.7312	0.1992	0.3775	0.0076	0.29	2.6488	0.0536	0.1293	0.0047	2065	36	2089	64	98
30.1	0.70	16.0	20.2	36.9	0.547	6.7473	0.2939	0.3763	0.0096	0.05	2.6651	0.0676	0.1300	0.0073	2059	45	2098	97	98
29.1	0.43	24.7	33.1	53.5	0.619	6.6771	0.2363	0.3722	0.0076	0.39	2.6865	0.0545	0.1301	0.0055	2040	35	2099	74	97
28.1	0.61	27.0	45.0	63.0	0.715	6.6215	0.2180	0.3748	0.0069	0.84	2.6682	0.0493	0.1281	0.0051	2052	33	2073	69	99
27.1	4.41	24.8	39.9	56.5	0.706	6.6355	0.2064	0.3717	0.0065	0.03	2.6902	0.0470	0.1295	0.0046	2037	30	2091	64	97
23.1	0.07	347.3	426.9	767.8	0.556	6.8073	0.1035	0.3814	0.0029	0.94	2.6218	0.0196	0.1294	0.0018	2083	13	2090	24	99
16.1	0.29	32.8	54.0	69.3	0.779	6.7731	0.1567	0.3823	0.0055	0.69	2.6156	0.0379	0.1285	0.0034	2087	26	2077	46	100
20.1	0.11	37.8	47.2	84.2	0.561	6.8122	0.1383	0.3823	0.0046	0.50	2.6156	0.0318	0.1292	0.0029	2087	22	2088	40	99
22.1	0.06	111.5	194.8	233.6	0.8340	6.8357	0.1243	0.3861	0.0040	0.81	2.5900	0.0268	0.1284	0.0025	2105	19	2076	34	101
14.1	0.38	114.5	254.7	230.8	1.103	6.8750	0.1164	0.3890	0.0035	0.77	2.5705	0.0233	0.1282	0.0021	2118	16	2073	29	102
8.1	0.12	280.8	329.0	632.2	0.520	6.9594	0.1123	0.3919	0.0040	0.95	2.5515	0.0262	0.1288	0.0017	2132	19	2081	23	102

19.1	0.49	32.0	33.8	68.1	0.496	7.9309	0.1625	0.4173	0.0052	0.83	2.3962	0.0300	0.1378	0.0032	2248	24	2200	40	102
13.1	0.17	46.7	46.6	98.3	0.4740	7.7612	0.1562	0.4109	0.0050	0.43	2.4337	0.0293	0.1370	0.0029	2219	23	2190	37	101
3.1	1.50	498.3	66.7	1359.0	0.049	6.1952	0.0942	0.3504	0.0034	0.99	2.8540	0.0276	0.1282	0.0016	1936	16	2074	22	93
31.1	5.59	53.3	51.0	163.7	0.312	6.3890	0.1182	0.3618	0.0035	0.99	2.7639	0.0264	0.1281	0.0024	1991	16	2072	33	96
15.1	0.24	118.7	279.2	244.6	1.141	6.5615	0.1050	0.3702	0.0032	0.99	2.7009	0.0232	0.1285	0.0022	2031	15	2078	30	97
1.2	16.35	412.9	138.2	1616.7	0.085	2.4785	0.0451	0.1377	0.0016	0.97	7.2625	0.0825	0.1306	0.0017	832	9	2105	23	39
2.1	26.98	406.7	556.3	1910.8	0.291	2.7636	0.0451	0.1548	0.0016	0.94	6.4602	0.0665	0.1295	0.0017	928	9	2091	23	44
4.1	5.28	237.4	160.2	730.0	0.219	5.4401	0.0911	0.3058	0.0032	0.99	3.2702	0.0347	0.1290	0.0017	1720	16	2085	23	82
7.1	9.50	381.9	496.3	1565.9	0.317	3.1042	0.0493	0.1732	0.0017	0.98	5.7742	0.0579	0.1300	0.0017	1030	10	2098	23	49
10.1	7.55	401.5	535.4	1340.9	0.399	3.6835	0.0593	0.2094	0.0021	1.00	4.7766	0.0489	0.1276	0.0017	1225	11	2065	23	59
11.1	25.45	449.3	453.2	898.4	0.504	4.2635	0.0747	0.2416	0.0028	0.47	4.1388	0.0486	0.1280	0.0016	1395	14	2070	23	67
11.2	11.83	353.4	384.7	2085.3	0.184	2.3543	0.0371	0.1333	0.0013	0.98	7.5027	0.0751	0.1281	0.0017	807	8	2072	23	38
13.2	9.11	552.2	192.9	1858.7	0.104	3.9381	0.0594	0.2203	0.0017	1.00	4.5402	0.0344	0.1297	0.0019	1283	9	2094	25	61
18.1	11.03	395.6	276.4	1607.2	0.172	3.4056	0.0541	0.1935	0.0016	0.96	5.1689	0.0417	0.1277	0.0019	1140	8	2066	27	55
19.2	28.34	466.5	918.1	2429.7	0.378	2.1363	0.0323	0.1203	0.0009	0.83	8.3122	0.0634	0.1288	0.0019	732	5	2082	26	35
20.2	42.57	602.7	83.2	2747.3	0.030	3.5152	0.0562	0.1977	0.0016	0.98	5.0579	0.0407	0.1289	0.0019	1163	8	2084	25	55
21.1	9.73	578.2	374.7	1942.5	0.193	3.9657	0.0600	0.2211	0.0017	0.98	4.5219	0.0346	0.1301	0.0019	1288	9	2099	26	61
23.2	5.20	370.6	316.3	1107.9	0.285	4.9027	0.0792	0.2773	0.0022	1.00	3.6058	0.0289	0.1282	0.0018	1578	11	2074	25	76
24.1	5.65	373.2	483.6	938.6	0.515	5.9906	0.0934	0.3367	0.0026	0.98	2.9701	0.0227	0.1290	0.0018	1871	13	2085	25	89
25.1	4.79	18.6	24.4	75.9	0.322	3.6593	0.1502	0.2135	0.0048	0.98	4.6841	0.1048	0.1243	0.0060	1247	25	2019	84	61
26.1	50.79	546.5	425.2	1547.2	0.275	4.5549	0.0706	0.2536	0.0019	0.98	3.9435	0.0299	0.1303	0.0018	1457	10	2102	25	69
31.2	7.30	487.8	96.9	1559.2	0.062	4.8225	0.0717	0.2707	0.0020	1.00	3.6940	0.0271	0.1292	0.0018	1544	10	2087	24	73
32.1	5.89	47.7	63.7	127.9	0.4980	4.6731	0.0987	0.2736	0.0030	0.98	3.6547	0.0397	0.1239	0.0030	1559	15	2013	45	77
33.1	2.88	130.9	138.8	292.7	0.474	7.9887	0.1371	0.4517	0.0040	0.99	2.2136	0.0195	0.1283	0.0022	2403	18	2074	31	115
2.1	0.2	54.1	58.9	91.1	0.6	11.79350	0.24800	0.48710	0.00380	0.640	2.05300	0.01610	0.17560	0.00360	2558	16	2612	33	97
15.1	0.1	108.7	63.4	198.2	0.3	11.94300	0.20730	0.48810	0.00370	0.010	2.04860	0.01530	0.17740	0.00300	2563	16	2629	28	97
12.1	0.2	100.4	73.6	176.9	0.4	11.87440	0.25410	0.48890	0.00420	0.640	2.04540	0.01740	0.17620	0.00380	2566	18	2617	36	98
5.1	0.2	225.6	244.5	375.5	0.7	11.98150	0.23940	0.48980	0.00360	0.010	2.04180	0.01500	0.17740	0.00350	2570	16	2629	33	97
6.1	0.0	121.4	107.3	211.0	0.5	12.07470	0.24150	0.49650	0.00380	0.480	2.01410	0.01530	0.17640	0.00350	2599	16	2619	33	99
18.1	0.1	113.9	71.3	201.5	0.4	12.12650	0.20270	0.49380	0.00360	0.010	2.02530	0.01460	0.17810	0.00300	2587	15	2635	28	98
9.1	0.1	150.1	123.4	255.0	0.5	12.27480	0.24860	0.49940	0.00390	0.660	2.00250	0.01570	0.17830	0.00370	2611	17	2637	34	99
8.1	0.1	146.7	201.7	235.3	0.9	12.35420	0.27240	0.50010	0.00460	0.830	1.99940	0.01820	0.17920	0.00400	2614	20	2645	37	98
2.2	0.3	167.0	143.1	286.1	0.5	12.23870	0.25330	0.50260	0.00380	0.010	1.98980	0.01510	0.17660	0.00350	2625	16	2621	34	100
20.1	0.2	90.8	74.3	154.1	0.5	12.53670	0.21010	0.50840	0.00370	0.720	1.96700	0.01410	0.17880	0.00290	2650	16	2642	28	100
Nb-66 13.1	0.1	105.0	77.0	200.0	0.4	12.54420	0.21700	0.51030	0.00390	0.960	1.95970	0.01500	0.17830	0.00310	2658	17	2637	29	100
14.1	0.1	64.9	44.6	121.3	0.4	11.27680	0.22360	0.48970	0.00440	0.440	2.04210	0.01830	0.16700	0.00340	2569	19	2528	35	101
1.1	0.1	169.6	49.1	313.8	0.2	12.37410	0.25470	0.51220	0.00390	0.650	1.95230	0.01490	0.17520	0.00350	2666	17	2608	33	102
21.1	5.5	91.5	62.8	189.9	0.3	11.86670	0.19300	0.48550	0.00330	0.900	2.05980	0.01410	0.17730	0.00290	2551	14	2628	27	97
19.1	0.1	215.1	249.4	356.6	0.7	12.08010	0.20080	0.49310	0.00360	0.930	2.02810	0.01480	0.17770	0.00300	2584	16	2631	29	98
3.1	0.4	179.0	180.8	344.9	0.5	12.12050	0.24020	0.49420	0.00380	0.940	2.02330	0.01550	0.17790	0.00360	2589	16	2633	34	98
7.1	0.7	70.7	66.1	124.8	0.5	11.90820	0.27390	0.48450	0.00460	0.750	2.06400	0.01970	0.17830	0.00410	2547	20	2637	39	96
17.1	0.0	220.6	217.1	396.4	0.5	12.73360	0.22110	0.51780	0.00390	0.890	1.93110	0.01440	0.17830	0.00310	2690	16	2637	28	101
22.1	0.5	124.2	85.6	247.7	0.3	11.59170	0.19900	0.47710	0.00350	0.550	2.09600	0.01550	0.17620	0.00300	2515	15	2618	29	96
23.1	1.1	64.0	74.3	149.2	0.5	9.49400	0.17080	0.39780	0.00330	0.950	2.51370	0.02110	0.17310	0.00340	2159	16	2588	35	83
4.1	0.9	34.6	21.3	50.5	0.4	9.72980	0.19240	0.41740	0.00320	0.950	2.39560	0.01840	0.16910	0.00350	2249	14	2548	36	88

10.1	0.2	130.7	173.9	226.8	0.8	10.26700	0.20710	0.43950	0.00350	0.990	2.27510	0.01810	0.16940	0.00360	2349	16	2552	36	92
11.1	0.1	37.3	24.8	71.2	0.3	10.01870	0.24370	0.44550	0.00470	0.230	2.24470	0.02370	0.16310	0.00400	2375	21	2488	42	95
16.1	0.2	144.3	112.7	216.7	0.5	15.84230	0.28270	0.55300	0.00450	0.890	1.80840	0.01470	0.20780	0.00380	2838	19	2888	30	98
15.2	-2.0	-28.1	-6.1	-75.2	0.1	9.08500	0.15820	0.39900	0.00290	0.810	2.50640	0.01830	0.16510	0.00280	2164	13	2509	28	86
16.2	-0.2	-15.8	-15.0	-25.9	0.6	11.90820	0.20670	0.48850	0.00360	0.020	2.04720	0.01510	0.17680	0.00300	2564	16	2623	28	97
41.1	0.73	91.9	121.3	144.3	0.841	12.7563	0.2634	0.4775	0.0047	0.99	2.0944	0.0205	0.1938	0.0037	2516	20	2774	32	90
48.1	0.21	144.6	217.3	287.2	0.756	12.5119	0.2702	0.4793	0.0051	0.98	2.0866	0.0221	0.1893	0.0040	2524	22	2736	35	92
11.1	0.05	96.6	142.7	150.4	0.948	12.7205	0.2465	0.4809	0.0042	0.54	2.0794	0.0182	0.1918	0.0036	2531	18	2758	31	91
64.1	2.10	96.2	242.7	176.0	1.379	12.7704	0.1920	0.4827	0.0057	0.99	2.0717	0.0246	0.1919	0.0028	2539	26	2758	24	92
55.1	0.20	185.4	174.8	345.9	0.5050	13.0115	0.1859	0.4898	0.0042	0.97	2.0416	0.0173	0.1927	0.0025	2570	18	2765	21	92
65.1	0.11	161.8	152.2	283.8	0.536	12.9275	0.1836	0.4904	0.0055	0.99	2.0393	0.0230	0.1912	0.0025	2572	24	2753	21	93
36.1	0.02	125.7	80.5	205.6	0.392	13.0637	0.2892	0.4920	0.0061	0.95	2.0324	0.0252	0.1926	0.0036	2579	26	2764	31	93
7.1	0.23	107.3	211.7	161.8	1.308	12.9311	0.2408	0.4944	0.0046	0.95	2.0226	0.0187	0.1897	0.0034	2590	19	2739	29	94
26.1	0.17	120.2	148.3	183.4	0.809	13.1926	0.2690	0.4981	0.0046	0.99	2.0076	0.0184	0.1921	0.0039	2606	20	2760	33	94
39.1	0.28	50.9	92.7	76.9	1.206	13.3407	0.3736	0.4987	0.0079	0.71	2.0051	0.0317	0.1940	0.0047	2608	34	2776	40	93
9.1	0.09	84.6	144.0	115.2	1.251	13.2597	0.2185	0.5020	0.0040	0.99	1.9921	0.0160	0.1916	0.0031	2622	17	2756	27	95
69.1	0.05	104.5	173.5	154.0	1.127	13.4292	0.2204	0.5020	0.0065	0.95	1.9919	0.0258	0.1940	0.0029	2623	28	2776	25	94
20.1	1.54	184.6	204.2	281.1	0.727	13.5601	0.2709	0.5041	0.0046	0.74	1.9836	0.0179	0.1951	0.0037	2631	19	2786	31	94
70.2	0.21	113.4	133.5	191.2	0.698	13.5872	0.2058	0.5101	0.0061	0.97	1.9604	0.0235	0.1932	0.0026	2657	26	2769	22	95
51.2	0.21	131.3	75.6	227.2	0.333	13.6300	0.2049	0.5125	0.0046	0.98	1.9512	0.0174	0.1929	0.0027	2667	20	2767	23	96
58.1	0.14	135.6	98.4	236.7	0.416	13.5289	0.2039	0.5131	0.0046	0.95	1.9489	0.0173	0.1912	0.0027	2670	20	2753	23	96
29.1	0.32	124.0	156.1	254.9	0.612	13.7160	0.2930	0.5207	0.0050	0.99	1.9205	0.0184	0.1911	0.0038	2702	21	2751	33	98
27.1	0.08	175.6	307.2	238.5	1.288	13.9356	0.2910	0.5239	0.0050	0.86	1.9088	0.0181	0.1929	0.0038	2716	21	2767	33	98
3.1	0.14	201.2	33.0	354.8	0.093	14.1671	0.2155	0.5283	0.0038	0.98	1.8928	0.0138	0.1945	0.0028	2734	16	2780	24	98
32.1	0.23	81.8	144.1	108.0	1.335	14.1015	0.3462	0.5295	0.0073	0.73	1.8886	0.0260	0.1932	0.0039	2739	31	2769	34	98
32.2	0.10	144.4	285.0	186.3	1.530	14.1475	0.3128	0.5310	0.0065	0.86	1.8834	0.0232	0.1933	0.0035	2745	28	2770	30	99
56.1	0.20	69.3	98.8	97.0	1.019	14.3879	0.2696	0.5387	0.0061	0.77	1.8563	0.0211	0.1937	0.0034	2778	26	2774	29	100
33.1	0.82	74.0	112.2	104.3	1.075	14.3511	0.3776	0.5389	0.0079	0.95	1.8556	0.0271	0.1931	0.0043	2779	33	2769	37	100
54.1	0.09	75.6	136.4	100.4	1.359	14.4643	0.2569	0.5415	0.0057	0.42	1.8467	0.0194	0.1937	0.0032	2790	24	2774	27	100
70.1	0.28	51.5	63.3	75.5	0.838	14.6543	0.2683	0.5466	0.0078	0.74	1.8294	0.0262	0.1944	0.0032	2811	32	2780	27	101
24.1	0.08	173.1	6.3	277.4	0.023	16.4430	0.3131	0.5381	0.0047	0.99	1.8582	0.0161	0.2216	0.0041	2776	20	2992	30	92
71.1	0.62	80.8	11.7	122.5	0.095	18.1436	0.2854	0.5898	0.0074	0.76	1.6955	0.0214	0.2231	0.0030	2989	30	3003	22	99
67.1	0.22	73.2	57.6	88.0	0.655	24.0868	0.3748	0.6737	0.0086	0.95	1.4842	0.0190	0.2593	0.0035	3320	33	3242	21	102
62.1	0.56	77.4	25.6	96.7	0.265	40.0205	0.6726	0.7799	0.0114	0.99	1.2823	0.0187	0.3722	0.0053	3717	41	3800	21	97
57.1	0.15	65.9	50.9	93.9	0.542	18.4713	0.2923	0.5979	0.0058	0.71	1.6725	0.0163	0.2241	0.0033	3021	23	3010	24	100
53.1	0.42	61.2	26.8	91.6	0.293	18.9188	0.3166	0.6055	0.0062	0.97	1.6514	0.0170	0.2266	0.0034	3052	25	3028	24	100
50.1	0.79	33.1	17.1	43.2	0.397	23.8801	0.5353	0.6787	0.0104	0.85	1.4735	0.0225	0.2552	0.0054	3339	40	3217	34	103
44.1	0.20	39.3	25.9	49.3	0.525	20.6420	0.6096	0.6091	0.0101	0.58	1.6418	0.0273	0.2458	0.0067	3066	41	3158	43	97
42.1	0.17	68.3	6.0	98.3	0.061	18.7732	0.4443	0.5979	0.0072	0.96	1.6724	0.0201	0.2277	0.0049	3022	29	3036	34	99
43.1	0.76	16.8	10.6	19.3	0.552	22.3670	1.0232	0.6410	0.0185	0.37	1.5600	0.0449	0.2531	0.0107	3193	72	3204	65	99
40.1	0.20	53.4	20.9	76.9	0.271	17.2283	0.4158	0.5759	0.0070	0.89	1.7364	0.0212	0.2170	0.0047	2932	29	2958	35	99
35.1	0.26	43.1	10.6	60.1	0.176	22.6219	0.7815	0.6485	0.0138	0.73	1.5419	0.0328	0.2530	0.0075	3222	54	3204	47	100
2.2	0.19	105.0	82.8	153.2	0.540	21.8189	0.3553	0.6193	0.0052	0.99	1.6149	0.0135	0.2555	0.0040	3107	21	3219	25	96
5.1	0.13	100.3	38.2	151.4	0.252	18.7699	0.2999	0.5627	0.0045	0.97	1.7771	0.0142	0.2419	0.0038	2878	19	3133	25	91
2.1	0.00	49.0	29.9	59.8	0.501	23.3665	0.4316	0.6614	0.0067	0.77	1.5119	0.0153	0.2562	0.0047	3273	26	3224	29	101

BUY-76-11

1.1	21.72	99.6	119.4	140.0	0.852	13.1696	0.2331	0.4994	0.0043	0.79	2.0024	0.0174	0.1913	0.0035	2611	19	2753	30	94
14.1	6.99	75.2	93.2	150.9	0.618	9.8926	0.2154	0.3843	0.0037	0.98	2.6021	0.0248	0.1867	0.0036	2096	17	2713	31	77
15.1	9.22	2.4	0.1	3.4	0.031	19.0522	1.8680	0.4970	0.0422	0.12	2.0119	0.1708	0.2780	0.0272	2601	177	3352	183	77
28.1	20.66	14.5	28.4	220.9	0.129	0.5183	0.0375	0.0354	0.0008	0.97	28.2272	0.6225	0.1061	0.0069	224	5	1734	118	12
62.2	14.42	56.6	86.7	608.4	0.143	0.7791	0.0160	0.0760	0.0010	0.92	13.1636	0.1668	0.0744	0.0014	472	6	1052	39	44
68.1	1.43	162.6	225.4	416.4	0.541	2.6020	0.0907	0.1128	0.0029	0.99	8.8682	0.2280	0.1674	0.0023	689	15	2531	22	27
66.1	0.00	190.5	196.8	-119.1	-1.652	0.8543	0.0150	0.0464	0.0006	0.99	21.5350	0.2789	0.1334	0.0021	293	4	2144	27	13
35.2	4.30	109.4	150.1	440.7	0.341	2.5986	0.0606	0.0985	0.0012	0.99	10.1528	0.1287	0.1913	0.0037	606	7	2754	32	21
13.1	0.91	210.2	163.2	1796.1	0.091	0.9178	0.0183	0.0984	0.0008	0.57	10.1636	0.0795	0.0677	0.0012	605	4	858	39	70
30.1	0.57	225.0	441.4	271.3	1.627	6.0456	0.1521	0.1988	0.0028	0.99	5.0311	0.0699	0.2206	0.0039	1169	14	2985	28	39
19.1	0.47	129.1	128.9	237.9	0.542	14.3439	0.2662	0.4311	0.0036	0.99	2.3196	0.0195	0.2413	0.0045	2311	16	3129	30	73
8.1	0.21	173.4	251.1	341.6	0.735	16.1966	0.2357	0.4994	0.0035	0.99	2.0026	0.0142	0.2352	0.0034	2611	15	3088	23	84
34.1	5.64	3.5	7.5	10.8	0.692	4.7094	0.6458	0.2835	0.0140	0.57	3.5273	0.1748	0.1205	0.0177	1609	72	1963	292	81
63.2	1.37	134.2	461.5	515.0	0.896	2.9243	0.0493	0.1484	0.0019	0.98	6.7389	0.0862	0.1429	0.0019	892	10	2263	23	39
16.1	1.67	154.6	318.2	389.3	0.817	3.7594	0.0762	0.1724	0.0015	0.99	5.8010	0.0500	0.1582	0.0031	1025	8	2436	31	42
61.1	2.06	62.6	59.6	240.9	0.247	5.3061	0.0898	0.2141	0.0020	0.99	4.6700	0.0445	0.1797	0.0035	1251	11	2650	32	47
31.2	1.41	151.6	218.0	460.5	0.473	4.9811	0.1159	0.2216	0.0027	0.99	4.5124	0.0557	0.1630	0.0030	1290	14	2487	30	51
49.1	1.09	195.9	724.8	442.7	1.637	5.6427	0.1333	0.2385	0.0026	0.99	4.1935	0.0456	0.1716	0.0038	1379	13	2574	36	53
13.2	0.90	143.8	253.6	1130.5	0.224	6.0498	0.1183	0.2547	0.0022	0.99	3.9256	0.0332	0.1722	0.0032	1463	11	2580	31	56
21.1	5.94	54.1	204.7	184.0	1.113	6.7757	0.1642	0.2595	0.0028	0.99	3.8537	0.0423	0.1894	0.0045	1487	15	2737	39	54
47.2	0.62	118.0	237.7	270.8	0.878	6.5518	0.1398	0.2668	0.0026	0.99	3.7484	0.0365	0.1781	0.0035	1524	13	2635	33	57
45.2	0.63	134.3	235.4	372.7	0.632	6.7720	0.1495	0.2737	0.0028	0.99	3.6532	0.0371	0.1794	0.0036	1560	14	2648	34	58
11.2	1.49	165.6	133.1	502.0	0.265	6.6600	0.1187	0.2788	0.0021	0.99	3.5869	0.0272	0.1733	0.0031	1585	11	2589	30	61
47.1	4.95	130.8	194.7	294.7	0.6610	7.3392	0.1550	0.2906	0.0028	0.99	3.4417	0.0333	0.1832	0.0036	1644	14	2682	32	61
46.1	1.86	113.2	257.1	270.1	0.952	7.5945	0.1919	0.3048	0.0036	0.98	3.2811	0.0390	0.1807	0.0042	1715	18	2660	38	64
26.2	1.00	176.7	347.2	336.5	1.032	7.4861	0.1539	0.3071	0.0028	0.98	3.2557	0.0292	0.1768	0.0038	1727	14	2623	35	65
52.1	1.29	139.4	29.8	223.9	0.133	8.1625	0.1232	0.3131	0.0027	0.99	3.1941	0.0279	0.1891	0.0026	1756	13	2734	22	64
23.1	0.54	168.3	189.7	418.3	0.454	8.0408	0.1571	0.3272	0.0028	0.98	3.0562	0.0261	0.1782	0.0034	1825	14	2636	32	69
10.2	0.51	136.2	126.3	286.9	0.4400	8.0143	0.1561	0.3290	0.0027	0.99	3.0399	0.0253	0.1767	0.0032	1833	13	2622	30	69
60.1	0.74	76.8	158.4	153.3	1.033	8.8598	0.1488	0.3426	0.0033	0.99	2.9190	0.0285	0.1876	0.0028	1899	16	2721	24	69
59.1	0.90	136.1	232.6	342.1	0.680	8.6842	0.1214	0.3452	0.0028	0.99	2.8972	0.0236	0.1825	0.0025	1911	13	2676	23	71
17.2	0.79	99.3	96.6	246.7	0.392	9.3327	0.1805	0.3615	0.0031	0.98	2.7665	0.0239	0.1873	0.0034	1989	15	2718	30	73
48.2	1.54	161.1	200.7	373.6	0.537	9.1853	0.1548	0.3623	0.0028	0.99	2.7600	0.0214	0.1839	0.0034	1993	14	2688	30	74
14.2	1.44	138.6	123.4	255.7	0.483	9.4005	0.1727	0.3717	0.0029	0.99	2.6904	0.0213	0.1834	0.0032	2037	14	2684	29	75
12.1	1.49	51.2	81.0	108.1	0.749	9.6893	0.2094	0.3721	0.0037	0.98	2.6877	0.0265	0.1889	0.0039	2039	17	2732	34	74
6.1	0.46	170.5	232.2	356.1	0.652	9.5181	0.1503	0.3817	0.0029	0.99	2.6197	0.0196	0.1808	0.0027	2084	13	2661	25	78
13.3	0.52	92.9	147.3	382.7	0.3850	9.8224	0.2174	0.3875	0.0038	0.99	2.5807	0.0255	0.1838	0.0040	2111	18	2688	36	78
25.1	0.16	129.6	196.8	413.8	0.476	10.2811	0.2184	0.3976	0.0038	0.99	2.5149	0.0242	0.1875	0.0038	2158	18	2721	35	79
1.2	0.12	124.0	70.4	196.7	0.358	10.3915	0.1630	0.3988	0.0030	0.99	2.5074	0.0191	0.1890	0.0028	2164	14	2733	25	79
45.1	0.26	99.7	128.5	166.1	0.774	10.4998	0.2588	0.4019	0.0048	0.99	2.4881	0.0297	0.1895	0.0044	2178	22	2738	38	79
7.2	0.46	178.8	92.4	382.4	0.242	10.3841	0.1544	0.4045	0.0029	0.99	2.4725	0.0174	0.1862	0.0027	2190	13	2709	24	80
37.1	0.57	150.4	357.5	290.0	1.233	10.5627	0.2150	0.4089	0.0047	0.99	2.4458	0.0279	0.1874	0.0033	2210	22	2719	29	81
22.1	0.44	97.4	97.8	172.2	0.568	10.5856	0.2213	0.4109	0.0038	0.99	2.4337	0.0228	0.1868	0.0038	2219	18	2715	33	81
10.1	0.59	171.7	206.2	366.1	0.563	10.5454	0.1643	0.4140	0.0031	0.99	2.4156	0.0180	0.1848	0.0028	2233	14	2696	25	82
38.1	0.09	79.0	153.5	170.6	0.900	10.5981	0.2408	0.4178	0.0053	0.99	2.3937	0.0301	0.1840	0.0035	2250	24	2689	32	83

Sample																				
	63.1	0.35	102.4	218.4	160.8	1.358	10.9879	0.1900	0.4227	0.0057	0.99	2.3658	0.0318	0.1885	0.0027	2273	26	2729	23	83
	51.1	0.27	128.1	102.8	274.8	0.374	10.8002	0.1541	0.4229	0.0035	0.99	2.3647	0.0198	0.1852	0.0026	2274	16	2700	23	84
	4.1	0.30	155.4	116.5	304.6	0.383	11.0631	0.1514	0.4307	0.0029	0.99	2.3218	0.0155	0.1863	0.0027	2309	13	2710	25	85
	17.1	0.08	118.6	162.2	199.6	0.813	11.5454	0.2251	0.4374	0.0039	0.97	2.2863	0.0201	0.1914	0.0036	2339	17	2755	31	84
	18.1	0.90	63.1	100.2	105.4	0.9500	11.5616	0.2476	0.4341	0.0043	0.98	2.3039	0.0227	0.1932	0.0039	2324	19	2769	33	83
	31.1	0.83	135.7	472.0	500.7	0.943	11.4661	0.2513	0.4413	0.0054	0.99	2.2661	0.0277	0.1884	0.0034	2356	24	2729	30	86
	1.1	0.65	41.3	68.3	154.2	0.4430	2.9691	0.0706	0.2421	0.0031	0.83	4.1312	0.0528	0.0890	0.0021	1397	16	1403	45	99
	2.1	0.20	86.6	122.7	195.2	0.628	6.6224	0.1188	0.3853	0.0043	0.98	2.5956	0.0289	0.1247	0.0021	2101	20	2024	30	103
	3.1	0.58	63.1	114.1	173.1	0.659	4.6714	0.0966	0.3166	0.0038	0.81	3.1584	0.0384	0.1070	0.0021	1773	19	1749	36	101
	4.1	0.16	92.3	99.8	98.2	1.017	28.0033	0.4553	0.6923	0.0077	0.95	1.4445	0.0162	0.2934	0.0042	3391	30	3436	22	98
	6.1	0.57	39.7	34.6	57.7	0.599	16.5580	0.3157	0.5652	0.0075	0.93	1.7693	0.0234	0.2125	0.0037	2888	31	2924	29	98
	6.2	1.07	78.5	90.9	124.6	0.730	15.3085	0.2749	0.5500	0.0067	0.85	1.8181	0.0222	0.2019	0.0033	2825	28	2841	26	99
	7.1	0.25	62.9	226.9	141.9	1.599	4.8358	0.1027	0.3240	0.0040	0.74	3.0861	0.0382	0.1082	0.0022	1809	20	1770	37	102
	8.1	0.87	24.9	263.2	92.7	2.840	1.3584	0.0701	0.1458	0.0028	0.43	6.8585	0.1327	0.0676	0.0039	877	16	855	118	102
	9.1	1.34	75.5	183.2	275.3	0.665	2.9491	0.0589	0.2429	0.0027	0.65	4.1164	0.0466	0.0880	0.0017	1402	14	1383	37	101
	10.1	5.25	100.5	267.6	402.1	0.666	2.6591	0.0519	0.2205	0.0024	0.79	4.5351	0.0499	0.0875	0.0016	1285	13	1371	34	93
	11.1	0.34	140.2	296.2	311.9	0.950	6.4653	0.1009	0.3730	0.0029	0.86	2.6807	0.0208	0.1257	0.0020	2044	14	2039	28	100
	12.1	0.00	59.8	83.0	217.1	0.382	3.7080	0.0802	0.2809	0.0026	0.96	3.5601	0.0332	0.0957	0.0022	1596	13	1543	43	103
	13.1	0.97	25.9	292.8	96.8	3.025	1.5335	0.0968	0.1590	0.0028	0.47	6.2900	0.1103	0.0700	0.0049	951	16	927	145	102
	14.1	0.22	33.7	115.0	139.3	0.826	2.3299	0.0603	0.2090	0.0020	0.72	4.7848	0.0462	0.0809	0.0023	1223	11	1218	56	100
	18.1	2.15	16.0	98.5	122.2	0.806	0.9538	0.0602	0.1099	0.0018	0.19	9.1008	0.1488	0.0630	0.0043	672	10	707	154	95
	20.1	0.30	82.5	120.0	175.2	0.685	7.6186	0.1204	0.4083	0.0032	0.99	2.4492	0.0193	0.1353	0.0022	2207	15	2168	29	101
	22.1	0.36	32.2	99.8	109.4	0.913	2.9505	0.0957	0.2448	0.0039	0.59	4.0849	0.0656	0.0874	0.0031	1412	20	1370	70	103
	23.1	0.92	31.1	174.1	249.1	0.699	0.9286	0.0301	0.1085	0.0014	0.55	9.2165	0.1206	0.0621	0.0023	664	8	677	79	98
BUY-55-11	24.1	0.43	79.1	170.1	259.0	0.657	3.4797	0.0680	0.2680	0.0028	0.59	3.7315	0.0384	0.0942	0.0019	1531	14	1512	38	101
	25.1	1.22	22.1	60.4	91.3	0.662	2.3173	0.0743	0.2098	0.0031	0.59	4.7662	0.0711	0.0801	0.0029	1228	17	1200	70	102
	26.1	0.10	56.3	79.1	131.6	0.601	5.9795	0.1269	0.3582	0.0043	0.57	2.7914	0.0334	0.1211	0.0027	1974	20	1972	40	100
	28.1	1.96	26.0	105.7	148.6	0.711	1.5539	0.0623	0.1597	0.0026	0.21	6.2624	0.1032	0.0706	0.0032	955	15	945	89	101
	30.1	0.44	87.0	266.9	212.0	1.259	4.5858	0.0831	0.3118	0.0030	0.87	3.2075	0.0314	0.1067	0.0019	1749	15	1743	33	100
	32.1	0.24	62.7	78.0	209.0	0.373	3.6382	0.0776	0.2775	0.0031	0.48	3.6034	0.0406	0.0951	0.0021	1579	16	1530	42	103
	32.2	2.53	91.6	275.5	314.2	0.8770	3.4735	0.0617	0.2653	0.0025	0.84	3.7689	0.0353	0.0949	0.0017	1517	13	1527	34	99
	33.1	1.31	103.3	106.6	505.6	0.211	2.0679	0.0379	0.1917	0.0018	0.94	5.2171	0.0481	0.0782	0.0015	1130	10	1153	38	98
	34.2	2.23	108.8	95.1	532.3	0.179	2.2984	0.0457	0.2057	0.0020	0.90	4.8607	0.0477	0.0810	0.0017	1206	11	1222	41	98
	36.1	2.95	89.9	163.2	346.3	0.471	3.0230	0.0670	0.2424	0.0027	0.95	4.1249	0.0459	0.0904	0.0021	1399	14	1435	44	97
	37.1	0.00	31.7	90.6	129.0	0.702	2.6240	0.0652	0.2197	0.0026	0.99	4.5507	0.0541	0.0866	0.0021	1281	14	1352	46	94
	39.1	1.18	121.5	444.2	264.3	1.681	4.7797	0.0988	0.3195	0.0036	0.89	3.1303	0.0349	0.1085	0.0023	1787	17	1775	39	100
	5.1	16.87	223.6	871.9	760.9	1.146	4.2685	0.0693	0.2489	0.0025	0.99	4.0185	0.0406	0.1244	0.0018	1433	13	2020	26	70
	5.2	57.96	37.4	236.0	263.8	0.895	2.3267	0.0561	0.1476	0.0020	0.95	6.7753	0.0932	0.1143	0.0029	887	11	1869	45	47
	7.2	8.31	15.8	32.7	62.4	0.524	3.2904	0.1310	0.2607	0.0050	0.82	3.8356	0.0730	0.0915	0.0041	1494	26	1458	82	102
	10.2	14.48	15.2	47.5	79.8	0.5950	1.8333	0.1041	0.1665	0.0029	0.92	6.0064	0.1052	0.0799	0.0049	993	16	1194	119	83
	13.2	9.51	14.1	201.1	68.8	2.922	1.4892	0.1144	0.1490	0.0031	0.51	6.7094	0.1401	0.0725	0.0064	896	17	999	189	89
	15.1	0.86	28.7	233.5	174.7	1.337	1.0700	0.0365	0.1247	0.0013	0.50	8.0176	0.0828	0.0622	0.0023	758	7	682	78	111
	16.1	45.48	138.4	662.4	773.0	0.857	1.6747	0.0275	0.1208	0.0009	0.99	8.2796	0.0611	0.1006	0.0018	735	5	1635	33	44
	17.1	3.93	122.8	208.1	318.5	0.654	4.7915	0.0755	0.2982	0.0023	0.99	3.3539	0.0256	0.1166	0.0018	1682	11	1904	28	88
	19.1	16.05	116.1	325.2	465.1	0.699	2.6638	0.0419	0.1961	0.0014	0.99	5.0992	0.0362	0.0985	0.0018	1154	8	1596	36	72

Group	Spot																			
	21.1	10.00	97.9	151.6	270.6	0.5600	5.7855	0.1087	0.3281	0.0030	0.97	3.0477	0.0277	0.1279	0.0024	1829	14	2069	33	88
	27.1	17.50	85.4	247.2	493.1	0.501	1.9852	0.0398	0.1784	0.0018	0.95	5.6043	0.0567	0.0807	0.0016	1058	10	1214	39	87
	29.1	6.92	249.9	269.7	748.3	0.360	5.0586	0.0811	0.3040	0.0026	0.99	3.2891	0.0286	0.1207	0.0019	1711	13	1966	28	87
	31.1	11.73	131.9	415.3	464.5	0.894	4.6262	0.0727	0.2649	0.0023	0.99	3.7751	0.0331	0.1267	0.0022	1515	12	2052	30	73
	34.1	0.00	57.8	99.0	190.9	0.518	1.8689	0.0438	0.1606	0.0018	0.99	6.2275	0.0706	0.0844	0.0021	960	10	1302	49	73
	35.1	46.64	35.9	311.5	301.8	1.032	1.0677	0.0392	0.1024	0.0015	0.81	9.7683	0.1417	0.0756	0.0036	628	9	1086	89	57
	35.2	39.83	70.7	663.1	685.2	0.968	1.0417	0.0278	0.0966	0.0011	0.87	10.3497	0.1224	0.0782	0.0024	595	7	1152	61	51
	38.1	10.53	237.6	414.7	518.3	0.800	12.1716	0.2010	0.4337	0.0043	1.00	2.3057	0.0228	0.2035	0.0034	2322	19	2855	27	81
	1.1	0.65	41.3	68.3	154.2	0.4430	2.9691	0.0706	0.2421	0.0031	0.83	4.1312	0.0528	0.0890	0.0021	1397	16	1403	45	99
	2.1	0.20	86.6	122.7	195.2	0.628	6.6224	0.1188	0.3853	0.0043	0.98	2.5956	0.0289	0.1247	0.0021	2101	20	2024	30	103
	3.1	0.58	63.1	114.1	173.1	0.659	4.6714	0.0966	0.3166	0.0038	0.81	3.1584	0.0384	0.1070	0.0021	1773	19	1749	36	101
	A_01	-	74	-	123	0.07	18.72	0.36	0.600	0.009	0.83	-	-	0.226	0.002	3028	38	3027	17	100
	A_01	-	69	-	109	0.66	22.13	0.42	0.640	0.010	0.82	-	-	0.251	0.003	3190	40	3189	17	100
	A_01	-	70	-	156	0.94	11.48	0.22	0.446	0.007	0.83	-	-	0.187	0.002	2380	31	2712	18	88
	A_01	-	87	-	298	0.46	5.21	0.10	0.294	0.005	0.81	-	-	0.129	0.001	1659	23	2081	20	80
	A_02	-	33	-	73	0.48	9.47	0.18	0.448	0.007	0.82	-	-	0.153	0.002	2387	32	2383	19	100
	A_02	-	36	-	433	1.42	1.52	0.03	0.083	0.001	0.72	-	-	0.133	0.002	513	8	2137	27	24
	A_02	-	65	-	681	0.68	1.52	0.03	0.096	0.002	0.82	-	-	0.115	0.001	589	9	1882	20	31
	A_02	-	98	-	379	0.32	4.39	0.08	0.260	0.004	0.82	-	-	0.123	0.001	1490	21	1993	20	75
	A_02	-	71	-	170	0.95	9.04	0.18	0.418	0.007	0.81	-	-	0.157	0.002	2253	30	2421	19	93
UY-6-13	A_02	-	43	-	113	0.55	6.63	0.13	0.377	0.006	0.81	-	-	0.128	0.001	2061	28	2065	20	100
	A_02	-	44	-	116	0.61	6.74	0.13	0.380	0.006	0.81	-	-	0.129	0.001	2077	28	2079	20	100
	A_02	-	103	-	948	1.51	1.72	0.03	0.109	0.002	0.79	-	-	0.115	0.001	668	10	1873	22	36
	A_03	-	26	-	64	0.72	7.64	0.15	0.403	0.006	0.80	-	-	0.138	0.002	2182	29	2197	21	99
	A_03	-	50	-	182	2.16	4.72	0.09	0.272	0.004	0.80	-	-	0.126	0.001	1553	22	2040	21	76
	A_03	-	44	-	67	1.06	24.32	0.47	0.663	0.010	0.81	-	-	0.266	0.003	3280	41	3283	18	100
	A_03	-	84	-	286	0.24	5.11	0.10	0.293	0.005	0.80	-	-	0.127	0.002	1654	23	2053	21	81
	A_03	-	10	-	42	0.66	2.79	0.07	0.231	0.004	0.69	-	-	0.087	0.002	1341	20	1369	33	98
	A_03	-	90	-	393	0.13	3.70	0.07	0.228	0.004	0.80	-	-	0.118	0.001	1323	19	1924	21	69
	A_03	-	117	-	714	0.32	2.91	0.06	0.164	0.003	0.78	-	-	0.129	0.002	976	14	2086	22	47
	A_21	-	116	-	491	1.15	7.05	0.11	0.237	0.003	0.72	-	-	0.216	0.002	1370	13	2949	17	46
	A_21	-	43	-	66	0.24	24.35	0.37	0.655	0.007	0.72	-	-	0.270	0.003	3247	28	3304	17	98
	A_21	-	161	-	264	0.51	23.16	0.35	0.609	0.007	0.72	-	-	0.276	0.003	3064	26	3341	16	92
	A_21	-	96	-	2667	1.04	1.43	0.02	0.036	0.000	0.72	-	-	0.290	0.003	228	2	3415	16	7
	A_21	-	39	-	58	0.41	25.77	0.39	0.678	0.007	0.72	-	-	0.276	0.003	3337	28	3338	16	100
	A_22	-	97	-	146	0.23	24.24	0.37	0.661	0.007	0.72	-	-	0.266	0.003	3271	28	3282	16	100
	A_22	-	39	-	58	0.40	25.90	0.39	0.679	0.007	0.72	-	-	0.277	0.003	3339	28	3345	16	100
UY-22-13	A_22	-	167	-	891	0.96	6.67	0.10	0.187	0.002	0.72	-	-	0.258	0.003	1107	11	3236	16	34
	A_22	-	102	-	1253	0.56	2.55	0.04	0.082	0.001	0.72	-	-	0.226	0.002	506	5	3026	17	17
	A_22	-	131	-	314	0.64	12.96	0.19	0.416	0.005	0.72	-	-	0.226	0.002	2243	21	3022	17	74
	A_22	-	107	-	269	0.51	13.32	0.20	0.400	0.004	0.72	-	-	0.242	0.003	2167	20	3132	17	69
	A_22	-	51	-	73	0.33	27.67	0.42	0.694	0.008	0.72	-	-	0.289	0.003	3396	29	3414	16	99
	A_22	-	113	-	274	0.51	12.81	0.19	0.411	0.004	0.72	-	-	0.226	0.002	2221	20	3024	16	73
	A_23	-	49	-	79	0.55	20.39	0.31	0.618	0.007	0.72	-	-	0.239	0.003	3103	27	3115	17	100
	A_23	-	128	-	235	0.53	17.27	0.26	0.545	0.006	0.72	-	-	0.230	0.002	2805	25	3051	17	92

A_23	-	94	-	730	0.64	3.88	0.06	0.129	0.001	0.72	-	-	0.218	0.002	784	8	2965	17	26
A_23	-	66	-	96	0.50	25.77	0.39	0.682	0.007	0.72	-	-	0.274	0.003	3353	28	3329	16	101
A_23	-	98	-	216	0.61	14.08	0.21	0.453	0.005	0.72	-	-	0.226	0.002	2407	22	3022	17	80
A_23	-	130	-	315	0.61	13.30	0.20	0.412	0.004	0.72	-	-	0.234	0.002	2223	20	3082	16	72
A_23	-	77	-	158	0.22	17.19	0.26	0.485	0.005	0.72	-	-	0.257	0.003	2550	23	3229	17	79
A_23	-	172	-	563	0.26	8.67	0.13	0.305	0.003	0.72	-	-	0.206	0.002	1717	16	2875	17	60
A_23	-	140	-	272	0.57	18.56	0.28	0.515	0.006	0.72	-	-	0.262	0.003	2676	24	3256	16	82
A_23	-	34	-	52	0.31	24.41	0.38	0.665	0.007	0.71	-	-	0.266	0.003	3285	28	3285	17	100
A_24	-	108	-	225	0.92	15.79	0.24	0.478	0.005	0.72	-	-	0.240	0.002	2520	23	3117	16	81
A_24	-	71	-	196	0.58	11.86	0.18	0.361	0.004	0.72	-	-	0.238	0.002	1989	19	3107	17	64
A_24	-	74	-	131	0.81	18.74	0.28	0.568	0.006	0.72	-	-	0.239	0.003	2900	25	3115	17	93
A_24	-	22	-	40	0.87	17.13	0.26	0.555	0.006	0.71	-	-	0.224	0.002	2844	25	3010	17	94
A_24	-	130	-	690	0.70	5.73	0.09	0.188	0.002	0.72	-	-	0.221	0.002	1110	11	2990	17	37
A_24	-	112	-	530	1.03	6.01	0.09	0.212	0.002	0.72	-	-	0.206	0.002	1237	12	2874	17	43
A_24	-	97	-	624	0.38	3.79	0.06	0.156	0.002	0.72	-	-	0.176	0.002	934	9	2616	18	36
A_24	-	132	-	308	0.58	13.02	0.20	0.430	0.005	0.72	-	-	0.220	0.002	2306	21	2978	17	77
A_25	-	108	-	173	0.56	20.64	0.31	0.624	0.007	0.72	-	-	0.240	0.003	3124	27	3120	17	100
A_25	-	146	-	390	0.54	11.84	0.18	0.373	0.004	0.72	-	-	0.230	0.002	2045	19	3052	17	67
A_25	-	57	-	92	0.81	21.06	0.32	0.626	0.007	0.72	-	-	0.244	0.003	3135	27	3145	17	100
A_25	-	115	-	1188	0.67	3.46	0.05	0.096	0.001	0.72	-	-	0.260	0.003	594	6	3248	16	18
A_25	-	95	-	152	0.55	20.75	0.31	0.623	0.007	0.72	-	-	0.242	0.003	3121	27	3131	17	100
A_25	-	108	-	208	0.33	20.36	0.31	0.519	0.006	0.71	-	-	0.285	0.003	2695	24	3388	17	80
A_25	-	49	-	74	0.42	24.67	0.38	0.663	0.007	0.72	-	-	0.270	0.003	3279	28	3305	17	99
A_25	-	106	-	302	1.01	12.69	0.20	0.351	0.004	0.70	-	-	0.262	0.003	1941	19	3258	18	60
A_26	-	42	-	126	0.59	11.07	0.17	0.332	0.004	0.71	-	-	0.241	0.003	1850	18	3130	17	59
A_26	-	24	-	34	0.52	29.31	0.45	0.708	0.008	0.71	-	-	0.300	0.003	3450	29	3472	16	99
A_26	-	121	-	543	0.85	6.63	0.10	0.223	0.002	0.72	-	-	0.215	0.002	1298	13	2947	17	44
A_26	-	52	-	77	0.49	25.78	0.39	0.681	0.007	0.72	-	-	0.275	0.003	3347	28	3333	17	100
A_26	-	112	-	471	0.88	7.07	0.11	0.237	0.003	0.72	-	-	0.216	0.002	1371	13	2954	17	46
A_26	-	117	-	663	0.64	5.25	0.08	0.176	0.002	0.72	-	-	0.216	0.002	1045	10	2952	17	35
A_26	-	78	-	1130	0.61	1.95	0.03	0.069	0.001	0.71	-	-	0.204	0.002	432	5	2862	17	15
A_26	-	35	-	62	1.21	21.01	0.34	0.557	0.006	0.70	-	-	0.274	0.003	2854	26	3327	18	86
A_26	-	100	-	476	0.81	5.93	0.09	0.210	0.002	0.71	-	-	0.204	0.002	1231	12	2861	17	43
A_27	-	97	-	343	0.68	8.31	0.13	0.282	0.003	0.71	-	-	0.214	0.002	1600	15	2937	17	54
A_27	-	133	-	191	0.57	27.86	0.42	0.697	0.008	0.71	-	-	0.290	0.003	3410	29	3417	16	100
A_27	-	102	-	230	0.55	13.66	0.21	0.444	0.005	0.71	-	-	0.223	0.002	2368	22	3005	17	79
A_27	-	123	-	768	0.69	5.55	0.08	0.160	0.002	0.71	-	-	0.251	0.003	958	10	3193	17	30
A_27	-	109	-	628	0.59	4.47	0.07	0.173	0.002	0.71	-	-	0.187	0.002	1031	10	2714	18	38
A_27	-	23	-	44	0.47	17.31	0.28	0.518	0.006	0.69	-	-	0.243	0.003	2689	25	3137	18	86
A_04	-	34	-	73	1.27	10.80	0.21	0.475	0.008	0.82	-	-	0.1648	0.0019	2506	33	2506	19	100
A_04	-	33	-	73	1.12	9.86	0.19	0.455	0.007	0.83	-	-	0.1570	0.0017	2420	32	2423	18	100
A_04	-	65	-	172	1.83	6.56	0.13	0.376	0.006	0.83	-	-	0.1265	0.0013	2057	28	2050	19	100
A_04	-	73	-	145	0.47	12.24	0.23	0.503	0.008	0.84	-	-	0.1765	0.0019	2625	34	2621	17	100
A_04	-	53	-	103	0.55	12.72	0.24	0.510	0.008	0.83	-	-	0.1808	0.0019	2658	35	2661	17	100
A_04	-	37	-	71	0.50	13.47	0.26	0.523	0.008	0.83	-	-	0.1868	0.0020	2712	35	2714	18	100

UY-8-13

201

A_04	-	25	-	55	1.26	10.15	0.20	0.460	0.007	0.80	-	-	0.1599	0.0019	2441	33	2454	20	99
A_04	-	45	-	94	0.95	10.64	0.20	0.473	0.008	0.83	-	-	0.1632	0.0017	2497	33	2489	18	100
A_05	-	106	-	210	0.55	12.44	0.24	0.506	0.008	0.84	-	-	0.1781	0.0018	2641	34	2635	17	100
A_05	-	59	-	94	0.00	21.13	0.40	0.629	0.010	0.84	-	-	0.2437	0.0026	3145	40	3144	17	100
A_05	-	100	-	218	0.45	10.06	0.19	0.457	0.007	0.84	-	-	0.1595	0.0017	2427	32	2451	18	99
A_05	-	42	-	111	0.72	6.56	0.13	0.375	0.006	0.83	-	-	0.1269	0.0014	2053	28	2056	19	100
A_05	-	215	-	354	0.01	19.43	0.37	0.608	0.010	0.84	-	-	0.2318	0.0024	3062	39	3065	16	100
A_05	-	46	-	86	0.13	13.75	0.26	0.540	0.009	0.83	-	-	0.1848	0.0020	2781	36	2697	17	103
A_05	-	178	-	346	0.37	12.87	0.24	0.513	0.008	0.84	-	-	0.1819	0.0019	2671	35	2670	17	100
A_05	-	70	-	152	0.60	9.92	0.19	0.457	0.007	0.84	-	-	0.1575	0.0017	2425	32	2429	18	100
A_06	-	65	-	140	0.56	10.16	0.19	0.461	0.007	0.83	-	-	0.1597	0.0017	2445	32	2453	18	100
A_06	-	62	-	120	0.40	12.83	0.24	0.513	0.008	0.83	-	-	0.1815	0.0019	2669	35	2666	17	100
A_06	-	50	-	125	0.17	7.52	0.14	0.398	0.006	0.83	-	-	0.1370	0.0015	2161	29	2190	18	99
A_06	-	171	-	1337	3.56	2.78	0.05	0.128	0.002	0.82	-	-	0.1572	0.0017	777	12	2426	18	32
A_06	-	216	-	420	0.84	13.01	0.25	0.516	0.008	0.84	-	-	0.1829	0.0019	2681	35	2679	17	100
A_06	-	185	-	413	0.39	9.56	0.18	0.447	0.007	0.84	-	-	0.1550	0.0016	2383	32	2402	17	99
A_06	-	205	-	415	0.19	11.60	0.22	0.494	0.008	0.84	-	-	0.1703	0.0018	2587	34	2561	17	101
A_06	-	200	-	379	0.10	13.58	0.26	0.527	0.008	0.84	-	-	0.1870	0.0019	2728	35	2716	17	100
A_06	-	98	-	220	0.35	13.32	0.26	0.447	0.007	0.83	-	-	0.2163	0.0023	2380	32	2953	17	81
A_06	-	128	-	208	0.60	20.11	0.38	0.616	0.010	0.84	-	-	0.2369	0.0024	3093	39	3099	16	100
A_07	-	108	-	345	2.93	5.54	0.11	0.313	0.005	0.84	-	-	0.1283	0.0013	1757	24	2075	18	85
A_07	-	106	-	213	0.56	11.98	0.23	0.497	0.008	0.84	-	-	0.1747	0.0018	2602	34	2604	17	100
A_07	-	99	-	268	0.35	7.35	0.14	0.368	0.006	0.84	-	-	0.1449	0.0015	2019	28	2286	18	88
A_07	-	78	-	155	0.29	12.30	0.23	0.505	0.008	0.84	-	-	0.1766	0.0018	2637	34	2621	17	101
A_07	-	155	-	342	0.41	9.62	0.18	0.452	0.007	0.84	-	-	0.1544	0.0016	2405	32	2395	17	100
A_07	-	68	-	110	0.58	20.06	0.38	0.615	0.010	0.84	-	-	0.2367	0.0025	3088	39	3098	17	100
A_07	-	82	-	180	0.48	9.98	0.19	0.458	0.007	0.84	-	-	0.1580	0.0017	2432	32	2435	18	100
A_07	-	30	-	63	0.49	10.77	0.21	0.473	0.008	0.82	-	-	0.1651	0.0018	2498	33	2509	19	100
A_08	-	22	-	58	0.94	6.38	0.13	0.370	0.006	0.80	-	-	0.1251	0.0015	2030	28	2030	21	100
A_08	-	46	-	121	2.06	6.61	0.13	0.376	0.006	0.82	-	-	0.1275	0.0014	2057	28	2064	19	100
A_08	-	12	-	30	1.03	7.11	0.17	0.392	0.007	0.71	-	-	0.1315	0.0022	2133	30	2118	29	101
A_08	-	32	-	86	1.59	6.63	0.13	0.377	0.006	0.82	-	-	0.1277	0.0014	2062	28	2066	20	100
A_08	-	65	-	140	0.28	10.38	0.20	0.466	0.007	0.82	-	-	0.1617	0.0018	2464	33	2474	19	100
A_08	-	46	-	114	0.75	7.66	0.15	0.405	0.006	0.83	-	-	0.1372	0.0015	2191	30	2192	19	100
A_08	-	65	-	162	0.67	8.19	0.16	0.399	0.006	0.83	-	-	0.1489	0.0016	2164	29	2334	18	93
A_08	-	136	-	380	0.48	8.02	0.15	0.359	0.006	0.83	-	-	0.1620	0.0017	1978	27	2476	18	80
A_08	-	80	-	156	0.34	12.94	0.25	0.513	0.008	0.84	-	-	0.1829	0.0019	2670	35	2679	17	100
A_09	-	54	-	143	0.72	6.50	0.12	0.374	0.006	0.83	-	-	0.1260	0.0014	2049	28	2043	19	100
A_09	-	64	-	133	0.47	11.01	0.21	0.481	0.008	0.83	-	-	0.1662	0.0018	2530	33	2520	18	100
A_09	-	84	-	165	0.52	12.69	0.24	0.510	0.008	0.84	-	-	0.1805	0.0019	2657	35	2657	17	100
A_09	-	26	-	70	2.27	6.47	0.13	0.374	0.006	0.81	-	-	0.1255	0.0014	2047	28	2037	20	101
A_09	-	100	-	214	0.79	10.36	0.20	0.466	0.007	0.84	-	-	0.1612	0.0017	2467	33	2469	17	100
A_09	-	106	-	269	0.39	7.25	0.14	0.394	0.006	0.84	-	-	0.1334	0.0014	2142	29	2144	18	100
A_09	-	203	-	777	0.34	4.66	0.09	0.261	0.004	0.84	-	-	0.1294	0.0013	1497	21	2089	18	72
A_10	-	59	-	110	0.68	14.22	0.27	0.536	0.009	0.84	-	-	0.1925	0.0020	2766	36	2763	17	100

	A_10	-	18	-	47	2.95	6.59	0.14	0.376	0.006	0.79	-	-	0.1269	0.0016	2060	28	2056	22	100
	A_10	-	126	-	338	0.40	6.49	0.12	0.373	0.006	0.84	-	-	0.1260	0.0013	2045	28	2043	18	100
	A_10	-	143	-	213	0.76	25.05	0.47	0.672	0.011	0.84	-	-	0.2705	0.0028	3312	41	3309	16	100
	A_10	-	101	-	194	0.59	13.23	0.25	0.520	0.008	0.84	-	-	0.1844	0.0019	2700	35	2693	17	100
	A_10	-	337	-	471	0.12	29.81	0.56	0.715	0.011	0.84	-	-	0.3024	0.0031	3477	43	3483	16	100
	A_10	-	76	-	166	0.54	10.16	0.19	0.462	0.007	0.84	-	-	0.1596	0.0017	2447	32	2452	18	100
	A_10	-	80	-	206	0.57	7.07	0.13	0.390	0.006	0.84	-	-	0.1315	0.0014	2122	29	2118	18	100
	A_11	-	178	-	1247	2.79	2.91	0.06	0.142	0.002	0.83	-	-	0.1482	0.0016	858	13	2325	19	37
	A_11	-	34	-	86	0.77	7.21	0.14	0.393	0.006	0.82	-	-	0.1329	0.0015	2139	29	2137	20	100
	A_11	-	75	-	200	0.59	6.62	0.13	0.378	0.006	0.83	-	-	0.1272	0.0014	2065	28	2059	19	100
	A_11	-	69	-	134	0.64	12.90	0.25	0.514	0.008	0.84	-	-	0.1820	0.0019	2674	35	2671	17	100
	A_11	-	99	-	203	1.07	11.57	0.22	0.488	0.008	0.84	-	-	0.1719	0.0018	2562	34	2576	17	99
	A_11	-	97	-	178	0.56	17.46	0.34	0.545	0.009	0.82	-	-	0.2324	0.0026	2804	36	3069	17	91
	A_11	-	43	-	96	0.44	9.64	0.19	0.451	0.007	0.83	-	-	0.1550	0.0017	2400	32	2402	18	100
	A_11	-	66	-	159	0.84	9.18	0.17	0.415	0.007	0.84	-	-	0.1604	0.0017	2237	30	2460	18	91
	A_11	-	27	-	69	1.10	7.31	0.14	0.394	0.006	0.82	-	-	0.1345	0.0015	2143	29	2157	19	99
	A_12	-	167	-	2703	4.29	1.32	0.02	0.062	0.001	0.84	-	-	0.1542	0.0016	387	6	2393	17	16
	A_12	-	10	-	20	1.14	11.93	0.24	0.498	0.008	0.80	-	-	0.1737	0.0022	2606	35	2594	21	100
	A_12	-	115	-	222	0.45	13.19	0.25	0.518	0.008	0.84	-	-	0.1847	0.0019	2691	35	2695	17	100
	A_12	-	95	-	189	0.62	13.68	0.26	0.501	0.008	0.84	-	-	0.1979	0.0021	2620	34	2809	17	93
	A_12	-	51	-	110	0.16	10.37	0.20	0.466	0.007	0.83	-	-	0.1614	0.0017	2466	33	2470	18	100
	A_12	-	144	-	421	0.39	7.58	0.14	0.342	0.005	0.84	-	-	0.1610	0.0017	1895	26	2466	17	77
	A_13	-	12	-	32	1.49	6.77	0.14	0.381	0.006	0.78	-	-	0.1287	0.0017	2083	29	2080	22	100
	A_13	-	14	-	28	0.63	12.12	0.25	0.500	0.008	0.80	-	-	0.1757	0.0022	2615	35	2613	20	100
	A_13	-	83	-	180	0.57	10.10	0.19	0.462	0.007	0.84	-	-	0.1586	0.0017	2447	32	2441	18	100
	A_13	-	152	-	391	0.61	7.07	0.13	0.389	0.006	0.84	-	-	0.1317	0.0014	2120	29	2121	18	100
	A_13	-	15	-	32	2.29	9.75	0.20	0.454	0.007	0.80	-	-	0.1557	0.0019	2414	32	2409	20	100
	A_13	-	22	-	60	0.94	6.03	0.12	0.360	0.006	0.81	-	-	0.1217	0.0014	1981	27	1981	21	100
	A_13	-	31	-	58	1.13	14.33	0.28	0.537	0.009	0.83	-	-	0.1935	0.0021	2771	36	2772	17	100
	A_13	-	81	-	174	0.40	10.17	0.19	0.462	0.007	0.84	-	-	0.1595	0.0017	2450	32	2450	17	100
	A_13	-	27	-	55	0.37	11.56	0.22	0.491	0.008	0.82	-	-	0.1708	0.0019	2574	34	2566	18	100
	A_13	-	102	-	220	1.45	10.36	0.20	0.465	0.007	0.83	-	-	0.1615	0.0017	2463	33	2472	18	100
	A_00	-	176	-	524	0.19	6.10	0.12	0.335	0.005	0.82	-	-	0.132	0.001	1865	25	2123	19	88
	A_00	-	63	-	545	0.32	2.08	0.04	0.116	0.002	0.79	-	-	0.130	0.002	707	11	2101	22	34
	A_00	-	56	-	144	0.66	7.00	0.14	0.388	0.006	0.79	-	-	0.131	0.002	2114	28	2110	22	100
	A_01	-	96	-	279	0.46	6.11	0.12	0.342	0.005	0.81	-	-	0.130	0.001	1897	26	2092	20	91
	A_01	-	73	-	307	0.22	4.34	0.08	0.239	0.004	0.81	-	-	0.132	0.002	1383	20	2120	20	65
	A_01	-	48	-	136	0.26	6.51	0.17	0.355	0.006	0.61	-	-	0.133	0.003	1957	27	2140	35	91
UY-4-13	A_01	-	33	-	180	0.69	1.90	0.04	0.183	0.003	0.80	-	-	0.075	0.001	1083	16	1080	23	100
	A_01	-	61	-	337	0.42	1.90	0.04	0.182	0.003	0.81	-	-	0.076	0.001	1078	16	1091	22	99
	A_01	-	77	-	328	0.18	4.28	0.09	0.235	0.004	0.72	-	-	0.132	0.002	1359	19	2127	26	64
	A_02	-	29	-	118	0.32	4.46	0.09	0.243	0.004	0.74	-	-	0.133	0.002	1400	20	2141	25	65
	A_02	-	98	-	701	0.29	2.51	0.05	0.140	0.002	0.80	-	-	0.131	0.002	842	12	2107	20	40
	A_02	-	80	-	365	0.30	3.95	0.08	0.218	0.003	0.81	-	-	0.132	0.001	1270	18	2119	20	60
	A_02	-	88	-	241	0.24	6.64	0.13	0.364	0.006	0.82	-	-	0.132	0.001	1999	27	2131	19	94

Sample																				
	A_02	-	121	-	1345	0.35	1.63	0.03	0.090	0.001	0.80	-	-	0.131	0.002	556	8	2109	21	26
	A_03	-	107	-	517	0.31	3.71	0.07	0.206	0.003	0.82	-	-	0.130	0.001	1210	17	2102	19	58
	A_03	-	93	-	355	0.25	4.76	0.09	0.263	0.004	0.81	-	-	0.131	0.002	1504	21	2116	20	71
	A_03	-	89	-	195	0.99	9.96	0.19	0.458	0.007	0.81	-	-	0.158	0.002	2431	32	2432	19	100
	A_03	-	98	-	285	0.21	6.39	0.13	0.344	0.005	0.75	-	-	0.135	0.002	1907	26	2158	24	88
	A_03	-	67	-	174	0.35	6.98	0.13	0.387	0.006	0.81	-	-	0.131	0.001	2111	28	2106	20	100
	A_03	-	108	-	279	0.27	6.90	0.13	0.387	0.006	0.81	-	-	0.130	0.001	2107	28	2092	20	101
	A_03	-	111	-	351	0.54	5.68	0.11	0.315	0.005	0.81	-	-	0.131	0.002	1766	24	2108	20	84
	A_07	-	111	-	380	0.31	6.65	0.13	0.292	0.005	0.84	-	-	0.165	0.002	1650	23	2511	17	66
	A_07	-	74	-	182	0.44	11.01	0.21	0.408	0.007	0.84	-	-	0.196	0.002	2204	30	2793	17	79
	A_07	-	105	-	181	0.55	18.91	0.36	0.578	0.009	0.84	-	-	0.237	0.002	2941	38	3101	16	95
	A_07	-	15	-	74	0.66	5.41	0.12	0.199	0.003	0.77	-	-	0.197	0.003	1170	18	2803	23	42
	A_08	-	36	-	67	0.75	14.59	0.28	0.543	0.009	0.84	-	-	0.195	0.002	2795	37	2784	17	100
	A_08	-	94	-	152	0.83	20.17	0.39	0.615	0.010	0.84	-	-	0.238	0.002	3090	40	3106	17	99
	A_08	-	34	-	69	0.79	13.37	0.26	0.490	0.008	0.84	-	-	0.198	0.002	2570	34	2810	17	91
	A_08	-	89	-	142	0.32	23.97	0.46	0.623	0.010	0.84	-	-	0.279	0.003	3123	40	3357	16	93
	A_09	-	39	-	72	0.89	14.40	0.28	0.538	0.009	0.84	-	-	0.194	0.002	2773	36	2779	17	100
	A_10	-	107	-	192	0.30	22.52	0.44	0.555	0.009	0.84	-	-	0.294	0.003	2847	37	3440	16	83
	A_10	-	119	-	355	0.56	9.98	0.19	0.335	0.005	0.84	-	-	0.216	0.002	1862	26	2952	17	63
	A_10	-	28	-	77	0.66	9.97	0.19	0.364	0.006	0.84	-	-	0.199	0.002	2001	28	2816	17	71
UY-24-13	A_10	-	21	-	40	0.57	15.54	0.30	0.528	0.009	0.83	-	-	0.213	0.002	2732	36	2932	17	93
	A_10	-	113	-	196	0.41	22.55	0.44	0.578	0.009	0.84	-	-	0.283	0.003	2939	38	3380	16	87
	A_11	-	11	-	42	0.46	7.09	0.19	0.257	0.005	0.67	-	-	0.200	0.004	1476	23	2826	32	52
	A_11	-	72	-	151	0.22	15.84	0.30	0.480	0.008	0.84	-	-	0.240	0.002	2525	34	3117	16	81
	A_11	-	71	-	131	0.59	14.53	0.28	0.542	0.009	0.84	-	-	0.195	0.002	2790	37	2781	17	100
	A_12	-	59	-	123	0.54	16.21	0.31	0.483	0.008	0.84	-	-	0.243	0.003	2541	34	3142	17	81
	A_12	-	28	-	46	0.30	20.07	0.39	0.614	0.010	0.83	-	-	0.237	0.003	3087	40	3100	17	100
	A_12	-	56	-	97	0.22	16.85	0.33	0.574	0.009	0.84	-	-	0.213	0.002	2925	38	2928	17	100
	A_12	-	29	-	54	0.85	14.60	0.32	0.540	0.009	0.77	-	-	0.196	0.003	2784	38	2794	23	100
	A_13	-	74	-	348	0.06	6.12	0.13	0.213	0.004	0.80	-	-	0.209	0.003	1243	19	2896	20	43
	A_13	-	124	-	331	0.28	11.34	0.22	0.374	0.006	0.84	-	-	0.220	0.002	2049	28	2979	17	69
	A_13	-	131	-	263	1.51	14.68	0.29	0.499	0.008	0.82	-	-	0.213	0.002	2611	35	2930	18	89
	A_13	-	114	-	200	1.21	16.54	0.33	0.569	0.009	0.82	-	-	0.211	0.002	2903	38	2912	18	100
	A_00	-	36	-	133	0.67	5.05	0.08	0.268	0.003	0.69	-	-	0.136	0.002	1532	15	2183	19	70
	A_00	-	72	-	131	0.68	15.37	0.22	0.552	0.006	0.72	-	-	0.202	0.002	2832	24	2844	16	100
	A_00	-	213	-	1047	0.77	3.67	0.05	0.204	0.002	0.71	-	-	0.131	0.001	1195	11	2108	18	57
	A_00	-	156	-	623	0.30	4.75	0.07	0.251	0.003	0.72	-	-	0.137	0.001	1445	14	2192	18	66
	A_00	-	179	-	326	0.81	16.00	0.24	0.548	0.006	0.71	-	-	0.212	0.002	2818	24	2918	17	97
UY-9-13	A_00	-	134	-	339	0.18	10.38	0.15	0.396	0.004	0.72	-	-	0.190	0.002	2149	19	2745	17	78
	A_01	-	251	-	831	0.14	7.00	0.10	0.302	0.003	0.72	-	-	0.168	0.002	1702	16	2539	17	67
	A_01	-	153	-	703	0.58	6.28	0.09	0.218	0.002	0.72	-	-	0.209	0.002	1272	12	2897	17	44
	A_01	-	146	-	245	0.23	18.57	0.27	0.596	0.006	0.72	-	-	0.226	0.002	3014	25	3024	16	100
	A_01	-	57	-	95	0.71	18.28	0.27	0.597	0.006	0.72	-	-	0.222	0.002	3016	25	2997	16	101
	A_01	-	90	-	374	0.95	4.40	0.06	0.242	0.003	0.72	-	-	0.132	0.001	1396	13	2125	18	66
	A_01	-	128	-	459	0.45	7.32	0.11	0.279	0.003	0.71	-	-	0.190	0.002	1586	15	2746	17	58

A_01	-	47	-	88	0.39	13.89	0.20	0.530	0.006	0.71	-	-	0.190	0.002	2740	23	2744	17	100
A_01	-	106	-	191	0.56	15.53	0.23	0.555	0.006	0.72	-	-	0.203	0.002	2846	24	2851	16	100
A_02	-	87	-	143	0.71	19.56	0.29	0.613	0.006	0.72	-	-	0.231	0.002	3082	26	3062	16	101
A_02	-	66	-	266	0.45	4.48	0.07	0.249	0.003	0.71	-	-	0.130	0.001	1435	13	2101	18	68
A_02	-	131	-	222	0.55	22.48	0.33	0.591	0.006	0.71	-	-	0.276	0.003	2994	25	3339	16	90
A_02	-	127	-	303	0.67	9.38	0.14	0.420	0.004	0.72	-	-	0.162	0.002	2258	20	2478	17	91
A_02	-	39	-	130	0.70	9.29	0.14	0.300	0.003	0.71	-	-	0.225	0.002	1689	16	3016	17	56
A_02	-	96	-	161	0.54	18.65	0.28	0.597	0.006	0.71	-	-	0.227	0.002	3019	25	3028	17	100
A_02	-	83	-	597	0.66	3.25	0.05	0.138	0.001	0.71	-	-	0.171	0.002	834	8	2566	17	33
A_02	-	85	-	216	0.57	7.43	0.11	0.395	0.004	0.71	-	-	0.136	0.001	2147	19	2182	18	98
A_03	-	92	-	327	0.12	8.63	0.13	0.281	0.003	0.71	-	-	0.222	0.002	1598	15	2998	17	53
A_03	-	186	-	392	0.86	13.94	0.20	0.475	0.005	0.71	-	-	0.213	0.002	2503	22	2929	16	85
A_03	-	109	-	682	1.21	3.90	0.06	0.160	0.002	0.71	-	-	0.177	0.002	957	9	2623	17	36
A_03	-	50	-	94	1.11	13.64	0.20	0.529	0.006	0.71	-	-	0.187	0.002	2736	23	2717	17	101
A_03	-	46	-	114	1.41	7.52	0.11	0.399	0.004	0.71	-	-	0.137	0.001	2164	19	2186	18	99
A_03	-	66	-	169	0.10	7.32	0.11	0.392	0.004	0.70	-	-	0.135	0.001	2132	19	2170	18	98
A_03	-	68	-	122	0.32	16.29	0.24	0.555	0.006	0.70	-	-	0.213	0.002	2845	24	2929	17	97
A_03	-	105	-	224	0.30	14.10	0.21	0.470	0.005	0.71	-	-	0.218	0.002	2483	22	2964	16	84
A_04	-	30	-	114	0.87	4.96	0.08	0.259	0.003	0.67	-	-	0.139	0.002	1487	14	2212	20	67
A_04	-	214	-	821	0.71	7.70	0.11	0.261	0.003	0.71	-	-	0.214	0.002	1495	14	2937	16	51
A_04	-	157	-	414	0.20	10.16	0.15	0.380	0.004	0.71	-	-	0.194	0.002	2075	18	2777	17	75
A_04	-	123	-	259	0.40	13.28	0.19	0.476	0.005	0.71	-	-	0.202	0.002	2509	22	2846	17	88
A_04	-	85	-	143	0.50	18.34	0.27	0.594	0.006	0.71	-	-	0.224	0.002	3005	25	3010	16	100
A_04	-	93	-	237	0.41	7.37	0.11	0.394	0.004	0.71	-	-	0.136	0.001	2141	19	2172	18	99
A_04	-	109	-	292	0.47	11.48	0.17	0.373	0.004	0.71	-	-	0.223	0.002	2045	18	3004	16	68
A_04	-	210	-	2039	0.18	0.86	0.01	0.103	0.001	0.70	-	-	0.060	0.001	633	6	614	23	103
A_04	-	27	-	65	0.76	7.83	0.12	0.411	0.004	0.70	-	-	0.138	0.001	2218	20	2207	18	100
A_04	-	179	-	273	0.70	23.27	0.34	0.654	0.007	0.71	-	-	0.258	0.003	3244	27	3234	16	100
A_05	-	124	-	206	0.46	19.15	0.28	0.602	0.006	0.71	-	-	0.230	0.002	3040	25	3055	16	99
A_05	-	199	-	833	1.11	5.83	0.09	0.238	0.002	0.71	-	-	0.177	0.002	1379	13	2629	17	52
A_05	-	55	-	559	0.17	0.83	0.01	0.099	0.001	0.63	-	-	0.061	0.001	606	6	652	28	93
A_05	-	189	-	884	0.18	5.35	0.08	0.213	0.002	0.71	-	-	0.182	0.002	1247	12	2671	17	47
A_05	-	120	-	311	0.16	6.85	0.10	0.385	0.004	0.71	-	-	0.129	0.001	2098	19	2087	18	101
A_05	-	82	-	225	0.15	6.27	0.09	0.364	0.004	0.70	-	-	0.125	0.001	2001	18	2026	19	99
A_05	-	167	-	253	0.20	23.66	0.35	0.657	0.007	0.71	-	-	0.261	0.003	3257	27	3253	16	100
A_05	-	130	-	554	0.57	5.87	0.09	0.234	0.002	0.71	-	-	0.182	0.002	1357	13	2667	17	51
A_06	-	70	-	179	0.37	8.44	0.12	0.392	0.004	0.71	-	-	0.156	0.002	2133	19	2415	18	88
A_06	-	145	-	359	0.31	7.55	0.11	0.403	0.004	0.71	-	-	0.136	0.001	2181	19	2176	18	100
A_06	-	112	-	268	0.37	12.58	0.19	0.419	0.004	0.71	-	-	0.218	0.002	2257	20	2963	17	76
A_06	-	71	-	425	0.85	4.70	0.07	0.167	0.002	0.70	-	-	0.204	0.002	995	10	2862	17	35
A_06	-	48	-	76	0.33	21.59	0.32	0.632	0.007	0.70	-	-	0.248	0.003	3159	26	3170	17	100
A_07	-	270	-	461	0.34	17.68	0.26	0.586	0.006	0.71	-	-	0.219	0.002	2971	25	2973	17	100
A_07	-	10	-	27	1.14	6.99	0.13	0.386	0.004	0.61	-	-	0.131	0.002	2106	20	2116	26	100
A_07	-	46	-	132	0.73	6.16	0.09	0.350	0.004	0.71	-	-	0.128	0.001	1934	17	2066	18	94
A_07	-	106	-	348	1.33	5.31	0.08	0.304	0.003	0.71	-	-	0.127	0.001	1710	16	2053	18	83

UY-16-13

Sample	Spot																			
	A_07	-	12	-	32	0.85	6.45	0.10	0.370	0.004	0.68	-	-	0.126	0.001	2029	18	2049	20	99
	A_07	-	36	-	96	3.09	6.51	0.10	0.375	0.004	0.70	-	-	0.126	0.001	2052	18	2042	19	100
	A_08	-	107	-	285	0.37	8.09	0.12	0.376	0.004	0.71	-	-	0.156	0.002	2059	18	2412	17	85
	A_08	-	93	-	229	0.06	9.24	0.14	0.406	0.004	0.71	-	-	0.165	0.002	2197	19	2507	17	88
	A_08	-	41	-	132	0.73	6.53	0.10	0.310	0.003	0.70	-	-	0.153	0.002	1743	16	2376	18	73
	A_08	-	260	-	493	0.38	13.69	0.20	0.526	0.006	0.70	-	-	0.189	0.002	2725	23	2731	17	100
	A_08	-	23	-	58	0.78	7.14	0.11	0.390	0.004	0.70	-	-	0.133	0.001	2123	19	2136	19	99
	A_08	-	109	-	980	3.88	2.58	0.04	0.111	0.001	0.71	-	-	0.168	0.002	680	7	2541	17	27
	A_08	-	117	-	537	2.48	4.74	0.07	0.219	0.002	0.71	-	-	0.157	0.002	1276	12	2426	17	53
	A_09	-	65	-	174	0.30	8.65	0.13	0.375	0.004	0.70	-	-	0.167	0.002	2055	19	2529	18	81
	A_09	-	18	-	63	0.79	4.55	0.07	0.289	0.003	0.70	-	-	0.114	0.001	1636	15	1870	19	87
	A_09	-	204	-	392	0.65	13.53	0.20	0.521	0.005	0.71	-	-	0.188	0.002	2703	23	2728	17	99
	A_09	-	125	-	569	1.30	3.45	0.05	0.220	0.002	0.71	-	-	0.114	0.001	1282	12	1860	19	69
	A_09	-	60	-	143	0.35	8.42	0.12	0.422	0.004	0.71	-	-	0.145	0.002	2269	20	2284	18	99
	A_10	-	63	-	193	2.10	5.61	0.09	0.324	0.003	0.69	-	-	0.125	0.001	1811	17	2035	19	89
	A_10	-	19	-	50	1.79	6.43	0.10	0.371	0.004	0.70	-	-	0.126	0.001	2034	18	2039	19	100
	A_10	-	13	-	109	0.80	1.49	0.03	0.120	0.001	0.54	-	-	0.090	0.002	730	8	1426	33	51
	A_10	-	7	-	67	0.79	0.81	0.02	0.098	0.001	0.51	-	-	0.060	0.001	603	6	605	40	100
	A_10	-	153	-	321	0.64	11.89	0.18	0.476	0.005	0.71	-	-	0.181	0.002	2509	22	2663	17	94
	A_10	-	20	-	52	1.26	7.04	0.11	0.387	0.004	0.70	-	-	0.132	0.001	2111	19	2121	19	100
	A_10	-	58	-	99	0.99	17.79	0.27	0.584	0.006	0.71	-	-	0.221	0.002	2965	25	2988	17	99
	A_11	-	203	-	433	0.18	11.16	0.16	0.469	0.005	0.71	-	-	0.173	0.002	2479	22	2583	17	96
	A_11	-	218	-	440	0.02	12.30	0.18	0.495	0.005	0.71	-	-	0.180	0.002	2594	22	2653	17	98
	A_11	-	51	-	164	0.45	7.93	0.12	0.312	0.003	0.71	-	-	0.184	0.002	1749	16	2693	17	65
	A_11	-	85	-	226	1.36	6.55	0.10	0.376	0.004	0.71	-	-	0.126	0.001	2057	19	2048	18	100
	A_11	-	131	-	259	0.31	12.32	0.18	0.505	0.005	0.71	-	-	0.177	0.002	2636	23	2623	17	101
	A_11	-	86	-	225	0.57	6.93	0.10	0.383	0.004	0.71	-	-	0.131	0.001	2092	19	2112	18	99
	A_11	-	225	-	546	0.25	9.43	0.14	0.412	0.004	0.71	-	-	0.166	0.002	2223	20	2519	17	88
	A_11	-	58	-	226	1.63	4.69	0.08	0.257	0.003	0.65	-	-	0.133	0.002	1472	14	2133	22	69
	A_12	-	42	-	112	0.85	6.68	0.10	0.374	0.004	0.70	-	-	0.129	0.001	2050	19	2090	19	98
	A_12	-	55	-	146	0.70	6.46	0.10	0.373	0.004	0.71	-	-	0.126	0.001	2043	18	2037	19	100
	A_12	-	100	-	357	0.16	5.15	0.08	0.280	0.003	0.69	-	-	0.134	0.001	1590	15	2146	19	74
	A_12	-	57	-	152	0.79	6.50	0.10	0.375	0.004	0.71	-	-	0.126	0.001	2052	19	2041	19	101
	A_13	-	23	-	231	1.05	0.82	0.01	0.099	0.001	0.68	-	-	0.060	0.001	608	6	609	24	100
	A_13	-	38	-	101	1.98	6.70	0.10	0.379	0.004	0.70	-	-	0.128	0.001	2072	19	2073	19	100
	A_13	-	118	-	321	0.54	6.35	0.10	0.367	0.004	0.69	-	-	0.126	0.001	2015	18	2037	20	99
	2.1	0.88	33.9	116.6	282.9	0.412	0.7792	0.0511	0.0950	0.0019	0.29	10.5227	0.2127	0.0595	0.0042	585	11	584	157	100
	3.1	1.51	9.5	44.2	78.6	0.562	0.8343	0.1077	0.0950	0.0033	0.37	10.5272	0.3639	0.0637	0.0093	585	19	732	301	79
	3.2	0.66	25.2	67.9	222.2	0.305	0.8346	0.0534	0.0977	0.0020	0.39	10.2320	0.2125	0.0619	0.0042	601	12	672	158	89
	4.1	0.69	19.0	63.5	163.9	0.387	0.7684	0.0541	0.0944	0.0020	0.56	10.5987	0.2240	0.0591	0.0046	581	12	569	169	102
AA-12	6.1	1.63	18.6	57.5	168.7	0.341	0.8208	0.0628	0.0961	0.0022	0.55	10.4049	0.2409	0.0619	0.0053	592	13	672	189	88
	7.1	2.33	15.8	68.9	131.1	0.525	0.7194	0.1129	0.0954	0.0035	0.01	10.4823	0.3798	0.0547	0.0099	587	20	400	349	146
	9.1	1.06	19.1	85.4	162.5	0.526	0.7720	0.0935	0.0942	0.0030	0.07	10.6156	0.3342	0.0594	0.0079	580	17	583	263	99
	10.1	1.74	13.3	40.7	116.8	0.349	0.7991	0.1115	0.0936	0.0034	0.55	10.6832	0.3838	0.0619	0.0096	577	20	671	288	85
	11.1	0.66	18.3	85.8	150.7	0.569	0.7347	0.0998	0.0940	0.0032	0.39	10.6327	0.3585	0.0567	0.0088	579	19	478	292	121

	12.1	0.40	20.2	91.5	162.0	0.565	0.7980	0.1088	0.0956	0.0033	0.37	10.4656	0.3641	0.0606	0.0094	588	20	624	329	94
	13.1	2.28	18.3	49.3	157.7	0.313	0.8058	0.0481	0.0973	0.0022	0.01	10.2745	0.2285	0.0600	0.0041	599	13	605	141	98
	14.1	3.20	5.5	20.9	45.7	0.458	0.7911	0.0934	0.0987	0.0038	0.25	10.1351	0.3890	0.0581	0.0084	607	22	535	280	113
	15.1	0.14	41.5	198.9	317.9	0.626	0.7657	0.0314	0.0931	0.0016	0.63	10.7420	0.1884	0.0597	0.0026	574	10	591	95	97
	15.2	0.92	10.6	35.7	84.3	0.424	0.8682	0.0766	0.0989	0.0032	0.35	10.1102	0.3258	0.0637	0.0065	608	19	730	228	83
	16.1	0.93	22.3	101.1	179.2	0.564	0.8453	0.0425	0.0979	0.0020	0.57	10.2137	0.2124	0.0626	0.0034	602	12	695	121	86
	17.1	2.16	11.6	37.5	96.7	0.388	0.7614	0.0671	0.0968	0.0028	0.12	10.3276	0.3028	0.0570	0.0058	596	17	493	213	120
	18.1	2.54	12.7	59.1	100.8	0.586	0.7245	0.0844	0.0962	0.0035	0.58	10.3982	0.3738	0.0546	0.0069	592	20	398	245	148
	19.1	2.18	20.8	83.3	170.1	0.490	0.8559	0.0336	0.1027	0.0018	0.83	9.7339	0.1662	0.0604	0.0025	630	10	619	89	101
	20.1	2.15	9.5	45.0	72.3	0.623	0.8176	0.0768	0.0963	0.0033	0.38	10.3810	0.3524	0.0616	0.0067	593	19	659	246	90
	21.1	3.02	21.6	59.1	183.6	0.322	0.7705	0.0444	0.0963	0.0021	0.01	10.3858	0.2255	0.0580	0.0037	593	12	531	132	111
	21.2	1.32	8.5	36.0	63.1	0.571	0.8337	0.0871	0.0930	0.0035	0.30	10.7510	0.4081	0.0650	0.0083	573	21	775	266	74
	5.1	2.49	6.0	19.8	48.1	0.411	0.7712	0.1475	0.0997	0.0043	0.47	10.0341	0.4343	0.0561	0.0124	612	25	457	365	133
	8.1	0.68	9.7	43.4	76.8	0.565	0.6745	0.1189	0.0939	0.0036	0.43	10.6505	0.4104	0.0521	0.0104	579	21	290	340	199
	1.1	5.39	3.7	13.0	33.5	0.388	0.9177	0.2978	0.0953	0.0080	0.38	10.4950	0.8833	0.0699	0.0258	587	47	924	652	63
AA-13	17.2	0.4	85.7	24.6	226.5	0.1	6.27580	0.16540	0.36270	0.00440	0.820	2.75680	0.03380	0.12550	0.00320	1995	21	2036	45	98
	11.2	0.5	61.0	56.4	155.7	0.4	6.28330	0.16950	0.36230	0.00520	0.450	2.75980	0.03940	0.12580	0.00340	1993	24	2040	47	97
	11.1	0.9	53.6	38.0	135.0	0.3	6.33980	0.21090	0.36190	0.00620	0.480	2.76290	0.04730	0.12700	0.00430	1991	29	2057	60	96
	13.1	0.1	159.7	133.1	395.6	0.3	6.57710	0.14710	0.37780	0.00410	0.920	2.64710	0.02860	0.12630	0.00260	2066	19	2047	36	100
	10.1	0.0	53.9	36.5	137.7	0.3	6.41280	0.19140	0.36660	0.00580	0.690	2.72810	0.04280	0.12690	0.00390	2013	27	2055	55	97
	3.1	0.4	50.5	35.7	122.1	0.3	6.48400	0.20090	0.36840	0.00590	0.550	2.71410	0.04370	0.12760	0.00390	2022	28	2066	53	97
	20.1	0.2	65.5	54.0	159.6	0.3	6.52650	0.16240	0.36940	0.00440	0.520	2.70720	0.03210	0.12810	0.00310	2027	21	2073	42	97
	7.2	0.2	34.9	45.6	83.6	0.5	6.67220	0.24910	0.37720	0.00720	0.690	2.65100	0.05030	0.12830	0.00510	2063	34	2075	70	99
	19.1	0.6	35.4	28.1	83.1	0.3	6.64980	0.24520	0.37510	0.00610	0.150	2.66620	0.04320	0.12860	0.00480	2053	28	2079	64	98
	21.1	0.2	55.7	28.8	148.4	0.2	6.68880	0.18360	0.37720	0.00480	0.960	2.65130	0.03380	0.12860	0.00340	2063	23	2079	47	99
	8.1	0.2	137.4	124.9	319.4	0.4	6.76870	0.15130	0.38070	0.00470	0.650	2.62690	0.03240	0.12900	0.00270	2079	22	2084	37	99
	12.1	0.1	84.7	57.3	209.5	0.3	6.57630	0.16100	0.36960	0.00440	0.010	2.70570	0.03190	0.12910	0.00290	2027	21	2085	40	97
	1.1	0.2	72.8	58.5	170.5	0.3	6.63200	0.17810	0.37210	0.00540	0.800	2.68780	0.03910	0.12930	0.00330	2039	25	2088	45	97
	18.1	0.1	81.3	45.3	204.0	0.2	6.54350	0.20050	0.36700	0.00520	0.860	2.72480	0.03830	0.12930	0.00390	2015	24	2089	53	96
	9.1	0.7	60.5	50.2	144.3	0.3	6.69340	0.26590	0.37500	0.00760	0.850	2.66660	0.05370	0.12940	0.00570	2053	36	2091	76	98
	22.1	0.1	62.9	54.3	150.0	0.4	6.69990	0.18920	0.37370	0.00490	0.570	2.67610	0.03500	0.13000	0.00350	2047	23	2098	47	97
	16.1	0.1	109.4	126.0	246.0	0.5	6.65310	0.15440	0.37030	0.00420	0.150	2.70060	0.03050	0.13030	0.00280	2031	20	2102	37	96
	17.1	0.6	34.2	28.2	79.9	0.4	6.70640	0.23900	0.37310	0.00590	0.670	2.68030	0.04250	0.13040	0.00460	2044	28	2103	63	97
	2.1	0.1	94.6	54.8	219.9	0.2	6.58390	0.17100	0.36580	0.00520	0.610	2.73370	0.03870	0.13050	0.00330	2010	24	2105	44	95
	7.1	0.4	43.8	32.5	101.8	0.3	6.69760	0.18190	0.37190	0.00550	0.220	2.68910	0.03950	0.13060	0.00340	2038	26	2106	47	96
	5.1	0.4	18.4	10.8	44.6	0.2	6.71230	0.35410	0.37070	0.00970	0.390	2.69780	0.07040	0.13130	0.00770	2033	45	2116	102	96
	16.2	0.6	54.9	36.4	142.8	0.3	6.75870	0.19200	0.37230	0.00530	0.030	2.68620	0.03800	0.13170	0.00360	2040	25	2120	51	96
	15.1	0.4	146.7	49.3	376.1	0.1	6.90710	0.15850	0.39060	0.00430	0.590	2.56010	0.02820	0.12820	0.00270	2126	20	2074	37	102
	14.1	0.1	90.6	65.0	235.9	0.3	6.02230	0.14820	0.35050	0.00410	0.540	2.85310	0.03360	0.12460	0.00290	1937	20	2023	41	95
	4.1	0.1	113.4	83.5	287.7	0.3	6.23850	0.14430	0.35220	0.00450	0.800	2.83960	0.03660	0.12850	0.00270	1945	22	2077	38	93
	6.1	0.1	60.3	54.0	133.6	0.4	7.20260	0.15450	0.40630	0.00490	0.810	2.46100	0.02990	0.12860	0.00260	2198	23	2078	35	105
BUY-81-11	1.1	2.4	44.5	51.8	487.6	0.1	0.8709	6.8087	0.1037	2.1560	0.316	9.4099	2.1310	0.0795	2.1250	636	13	635	139	100
	2.1	12.5	87.5	50.2	1029.1	0.0	0.6868	27.8881	0.0865	2.2791	0.081	10.1098	2.1067	0.1551	1.2842	535	12	514	611	96
	3.1	0.4	12.9	24.9	45.5	0.5	5.5849	3.4664	0.3277	3.1336	0.904	3.0379	3.1300	0.1268	1.1147	1827	50	2009	26	110
	4.1	1.1	48.1	41.5	547.3	0.1	0.8683	3.7704	0.1011	2.1322	0.565	9.7827	2.1259	0.0707	1.3609	621	13	684	66	110

	5.1	0.2	67.5	90.6	213.4	0.4	6.3403	2.2533	0.3674	2.1671	0.961	2.7160	2.1664	0.1267	0.4939	2017	38	2031	11	101
	6.1	0.2	20.9	21.0	235.0	0.1	0.8419	2.8481	0.1035	2.2943	0.805	9.6421	2.2929	0.0605	1.2393	635	14	567	37	89
	7.1	0.1	66.3	65.2	808.2	0.1	0.7742	2.6010	0.0954	2.1235	0.816	10.4706	2.1232	0.0597	1.3934	587	12	562	33	96
	9.1	0.3	116.7	58.4	385.2	0.2	5.9619	2.3053	0.3514	2.1976	0.953	2.8368	2.1967	0.1253	0.5240	1941	37	2001	12	103
	10.1	0.5	23.9	46.3	78.6	0.6	5.8241	2.6534	0.3522	2.3186	0.873	2.8254	2.3143	0.1233	0.8618	1945	39	1955	23	101
	11.1	0.7	333.6	181.0	1088.9	0.2	6.1152	2.2271	0.3542	2.1109	0.947	2.8040	2.1098	0.1300	0.2206	1955	36	2032	13	104
	12.1	0.4	17.7	17.2	205.9	0.1	0.8314	3.7193	0.0998	2.1978	0.590	9.9849	2.1913	0.0633	1.8837	613	13	619	65	101
	13.1	1.5	52.6	44.7	639.1	0.1	0.7698	5.5895	0.0944	2.1313	0.381	10.4390	2.1226	0.0708	3.0540	581	12	573	112	99
	13.2	0.1	21.6	29.1	64.0	0.5	7.0120	2.5608	0.3919	2.3435	0.915	2.5501	2.3431	0.1302	0.9970	2132	43	2095	18	98
	14.1	0.1	27.8	36.6	325.9	0.1	0.8251	2.7271	0.0990	2.1545	0.790	10.0825	2.1538	0.0615	1.4664	609	13	619	36	98
	15.1	0.3	23.0	19.4	258.4	0.1	0.8530	3.1930	0.1032	2.1717	0.680	9.6665	2.1690	0.0621	1.7495	633	13	602	51	95
BUY-84-11	1.1	0.1	171.9	74.3	536.7	0.1	6.5665	2.2391	0.3724	2.2029	0.983	2.6824	2.2027	0.1286	0.3591	2041	39	2069	7	101
	2.1	0.1	136.0	138.7	413.3	0.3	6.7439	2.1700	0.3826	2.1270	0.980	2.6119	2.1269	0.1283	0.3953	2088	38	2068	8	99
	3.1	0.1	116.3	46.7	363.5	0.1	6.4971	2.1848	0.3717	2.1360	0.977	2.6865	2.1356	0.1277	0.3765	2038	37	2054	8	101
	3.2	0.1	118.0	89.1	367.4	0.2	6.7905	2.1702	0.3735	2.1333	0.983	2.6760	2.1331	0.1323	0.3620	2046	37	2123	7	104
	4.1	0.2	47.1	22.4	146.0	0.2	6.5496	2.3615	0.3745	2.2327	0.945	2.6638	2.2312	0.1285	0.5918	2051	39	2054	14	100
	5.1	0.1	57.9	154.4	173.2	0.9	6.9598	2.2633	0.3890	2.1837	0.964	2.5688	2.1833	0.1302	0.5358	2118	39	2095	10	99
	6.1	0.0	157.0	181.6	493.8	0.4	6.5482	2.1993	0.3701	2.1755	0.989	2.7022	2.1755	0.1283	0.3227	2030	38	2075	6	102
	7.1	0.1	16.5	160.3	287.4	0.6	0.5347	2.6971	0.0668	2.1704	0.804	14.9505	2.1697	0.0590	1.3918	417	9	532	35	128
BUY-93-11	3.1	0.1	67.3	80.8	139.3	0.6	7.1111	0.1675	0.4026	0.0046	0.810	2.4841	0.0281	0.1281	0.0030	2181	21	2072	42	105
	17.1	0.1	79.4	145.0	175.8	0.8	6.1110	0.1393	0.3678	0.0040	0.730	2.7189	0.0293	0.1205	0.0027	2019	19	1964	39	102
	5.1	0.4	102.6	118.3	261.3	0.5	6.2486	0.1164	0.3577	0.0033	0.980	2.7960	0.0255	0.1267	0.0022	1971	16	2053	30	96
	8.1	0.2	52.4	114.1	119.0	1.0	5.1727	0.1458	0.3316	0.0040	0.810	3.0156	0.0368	0.1131	0.0032	1846	20	1850	51	99
	2.1	0.2	63.7	61.3	135.1	0.5	6.8749	0.1480	0.3746	0.0039	0.720	2.6698	0.0275	0.1331	0.0028	2051	18	2140	36	95
	6.1	0.3	58.6	49.6	120.8	0.4	7.0472	0.1486	0.3836	0.0039	0.700	2.6069	0.0267	0.1332	0.0026	2093	18	2141	34	97
	12.1	0.3	80.6	94.5	172.9	0.5	7.0020	0.1498	0.3794	0.0039	0.850	2.6356	0.0273	0.1338	0.0027	2074	18	2149	36	96
	13.1	0.1	122.5	111.3	268.7	0.4	7.5703	0.1590	0.4098	0.0042	0.940	2.4403	0.0248	0.1340	0.0026	2214	19	2151	34	102
	14.1	0.3	109.7	137.3	262.3	0.5	6.2292	0.1376	0.3456	0.0037	0.840	2.8933	0.0306	0.1307	0.0027	1914	17	2108	36	90
	15.2	4.6	256.4	83.3	2592.8	0.0	0.7650	0.0156	0.0922	0.0008	0.960	10.8467	0.0965	0.0602	0.0011	568	5	610	40	93
	4.1	0.3	38.5	379.9	274.6	1.4	0.8051	0.0612	0.0974	0.0017	0.660	10.2659	0.1820	0.0599	0.0050	599	10	602	168	99
	15.1	1.9	52.1	288.2	494.2	0.6	0.8055	0.0276	0.0955	0.0011	0.710	10.4712	0.1178	0.0612	0.0022	588	6	645	76	91
	11.2	2.0	69.9	226.0	650.6	0.3	0.8228	0.0260	0.0967	0.0011	0.580	10.3429	0.1133	0.0617	0.0020	595	6	664	74	89
	2.2	3.9	190.0	62.1	1757.8	0.0	0.9267	0.0230	0.1007	0.0010	0.970	9.9353	0.0952	0.0668	0.0015	618	6	831	47	74
	7.1	0.3	232.8	210.2	990.9	0.2	3.2274	0.0505	0.2065	0.0016	0.990	4.8423	0.0375	0.1133	0.0016	1210	9	1854	27	65
	9.1	4.9	16.7	117.2	149.5	0.8	0.7431	0.0804	0.0841	0.0020	0.960	11.8903	0.2880	0.0641	0.0071	521	12	744	237	69
	10.1	0.1	189.7	293.3	556.2	0.5	2.8658	0.0716	0.1972	0.0022	1.000	5.0721	0.0560	0.1054	0.0021	1160	11	1722	34	67
	12.2	2.3	174.9	172.3	873.2	0.2	2.9830	0.0558	0.1969	0.0017	0.970	5.0796	0.0451	0.1099	0.0021	1158	9	1798	35	64
	16.1	0.6	135.3	233.0	411.2	0.6	4.6891	0.0887	0.2726	0.0025	0.950	3.6683	0.0330	0.1248	0.0022	1554	12	2025	31	76
	1.1	3.2	13.1	50.4	93.6	0.5	1.0842	0.1113	0.1173	0.0028	0.010	8.5258	0.2063	0.0670	0.0075	715	16	839	231	85
	4.2	20.8	104.4	127.7	1675.5	0.1	0.3942	0.0108	0.0470	0.0005	0.950	21.2808	0.2082	0.0608	0.0015	296	3	634	53	46
	11.1	9.7	244.1	604.0	2387.1	0.3	0.8293	0.0180	0.0988	0.0009	0.880	10.1210	0.0929	0.0609	0.0013	607	5	635	45	95
	13.2	5.8	187.8	251.2	733.1	0.3	3.6341	0.0566	0.2292	0.0018	1.000	4.3632	0.0334	0.1150	0.0020	1330	10	1880	34	70
	18.1	6.4	35.2	138.5	490.8	0.3	0.8090	0.0296	0.0965	0.0011	0.990	10.3637	0.1132	0.0608	0.0025	594	6	632	89	93
	5.2	0.3	188.1	36.8	1780.7	0.0	0.7187	0.0158	0.0858	0.0008	0.970	11.6538	0.1039	0.0607	0.0014	531	4	630	49	84
	9.2	6.2	122.0	610.4	1190.5	0.5	0.7111	0.0215	0.0865	0.0009	0.850	11.5546	0.1155	0.0596	0.0017	535	5	589	62	90

	26.1	0.0	78.1	107.6	581.7	0.2	0.7086	0.0204	0.0887	0.0012	0.950	11.2748	0.1480	0.0579	0.0014	548	7	528	57	103
	16.1	0.0	18.2	28.3	165.3	0.2	0.7496	0.0248	0.0909	0.0012	0.940	11.0003	0.1478	0.0598	0.0020	561	7	597	73	94
	13.1	0.3	19.5	40.0	154.2	0.3	0.7609	0.0317	0.0927	0.0014	0.650	10.7922	0.1617	0.0596	0.0027	571	8	588	101	97
	17.1	1.2	64.5	217.3	490.8	0.4	0.7608	0.0157	0.0945	0.0010	0.950	10.5785	0.1167	0.0584	0.0010	582	6	544	38	107
	2.1	1.1	23.9	38.8	211.0	0.2	0.7644	0.0259	0.0951	0.0012	0.430	10.5182	0.1311	0.0583	0.0021	585	7	542	81	108
	1.1	2.1	48.3	80.0	400.9	0.2	0.7826	0.0176	0.0972	0.0009	0.950	10.2911	0.0935	0.0584	0.0015	598	5	545	55	109
	24.1	1.4	41.8	69.5	348.3	0.2	0.8057	0.0202	0.0994	0.0012	0.970	10.0554	0.1189	0.0588	0.0013	611	7	558	48	109
	12.1	0.0	48.3	341.1	274.7	1.2	0.8267	0.0391	0.1008	0.0016	0.850	9.9250	0.1593	0.0595	0.0033	619	10	586	116	105
	5.1	1.2	8.9	15.6	81.0	0.2	0.7409	0.0406	0.0879	0.0016	0.520	11.3804	0.2128	0.0612	0.0039	543	10	645	141	84
	9.1	0.9	10.3	38.5	79.4	0.5	0.7811	0.0554	0.0921	0.0022	0.320	10.8627	0.2617	0.0615	0.0051	568	13	658	165	86
	19.1	1.2	61.7	152.1	446.6	0.3	0.7603	0.0198	0.0957	0.0011	0.970	10.4501	0.1224	0.0576	0.0015	589	7	515	56	114
	20.1	2.6	40.4	59.6	299.1	0.2	0.7953	0.0259	0.0994	0.0013	0.870	10.0592	0.1316	0.0580	0.0019	611	8	531	71	115
UY-22-14	23.1	0.0	72.9	98.1	615.4	0.2	0.8176	0.0165	0.1013	0.0011	0.690	9.8716	0.1073	0.0585	0.0010	622	6	550	36	113
	3.1	4.2	36.7	173.3	268.6	0.6	0.7892	0.0258	0.0990	0.0012	0.720	10.1033	0.1211	0.0578	0.0021	608	7	523	78	116
	8.1	4.9	74.2	157.7	627.7	0.3	0.7707	0.0150	0.0949	0.0008	0.960	10.5382	0.0870	0.0589	0.0013	584	5	564	48	103
	22.1	8.8	11.2	55.5	128.6	0.4	0.5809	0.0268	0.0701	0.0012	0.530	14.2692	0.2365	0.0601	0.0028	437	7	608	105	71
	6.1	18.1	60.4	140.8	443.7	0.3	0.7071	0.0173	0.0867	0.0009	0.880	11.5388	0.1133	0.0592	0.0015	536	5	574	57	93
	11.1	16.5	18.4	63.5	141.0	0.5	0.7503	0.0333	0.0957	0.0014	0.590	10.4455	0.1577	0.0568	0.0028	589	8	485	112	121
	15.1	2.4	10.3	25.5	86.1	0.3	0.7647	0.0447	0.0973	0.0019	0.050	10.2801	0.1989	0.0570	0.0034	598	11	492	129	121
	10.1	0.2	11.1	39.9	85.1	0.5	0.7801	0.0673	0.1008	0.0026	0.720	9.9220	0.2543	0.0561	0.0056	619	15	458	206	135
	7.1	0.4	131.3	242.4	1095.4	0.2	0.6196	0.0124	0.0768	0.0007	0.950	13.0182	0.1147	0.0585	0.0011	477	4	549	41	86
	21.1	0.2	136.2	306.8	1038.1	0.3	0.8098	0.0162	0.1006	0.0011	0.850	9.9365	0.1047	0.0584	0.0010	618	6	543	36	113
	14.1	0.0	162.1	236.5	1372.7	0.2	0.8192	0.0166	0.1020	0.0011	0.010	9.8075	0.1044	0.0583	0.0010	626	6	540	37	115
	18.1	0.1	150.0	270.3	1193.6	0.2	0.7439	0.0159	0.0916	0.0010	0.690	10.9148	0.1210	0.0589	0.0011	565	6	563	40	100
	25.1	0.6	113.3	78.7	972.1	0.1	0.8196	0.0161	0.1025	0.0011	0.980	9.7524	0.1003	0.0580	0.0010	629	6	529	39	119
	4.1	0.0	-1.8	-17.6	-23.1	0.8	0.7584	0.0126	0.0930	0.0007	0.960	10.7558	0.0802	0.0592	0.0011	573	4	573	40	99
	2.1	0.33	73.4	370.3	628.7	0.589	0.7870	0.0312	0.0963	0.0014	0.82	10.3887	0.1497	0.0593	0.0024	592	8	578	90	102
	9.1	0.00	131.5	377.2	1316.0	0.287	0.7900	0.0195	0.0965	0.0011	0.49	10.3602	0.1174	0.0594	0.0014	594	6	580	52	102
	18.1	0.30	83.2	121.0	820.2	0.148	0.7983	0.0233	0.0970	0.0011	0.61	10.3106	0.1185	0.0597	0.0018	597	7	593	64	100
	14.1	0.31	57.3	258.2	493.0	0.524	0.8055	0.0289	0.0971	0.0013	0.50	10.3001	0.1329	0.0602	0.0022	597	7	610	80	97
	3.2	2.07	132.9	460.2	1215.7	0.379	0.8034	0.0207	0.0971	0.0011	0.85	10.3030	0.1181	0.0600	0.0015	597	7	605	55	98
	12.1	0.17	117.0	378.1	1084.9	0.348	0.8031	0.0204	0.0971	0.0011	0.62	10.2953	0.1114	0.0600	0.0015	598	6	602	55	99
	19.1	0.23	80.8	232.3	754.5	0.3080	0.8101	0.0241	0.0975	0.0011	0.68	10.2573	0.1179	0.0603	0.0018	600	7	613	64	97
	15.2	0.85	101.2	237.4	989.1	0.240	0.8055	0.0202	0.0977	0.0010	0.88	10.2319	0.1075	0.0598	0.0015	601	6	595	56	100
BUY-64-11	1.1	0.45	280.7	863.1	2802.4	0.3080	0.8151	0.0143	0.0979	0.0010	0.99	10.2180	0.1013	0.0604	0.0009	602	6	618	34	97
	7.1	1.96	128.2	401.1	1240.5	0.323	0.7726	0.0190	0.0935	0.0011	0.74	10.6958	0.1224	0.0599	0.0014	576	6	601	51	95
	5.1	0.78	21.3	203.0	153.0	1.327	0.7525	0.0808	0.0956	0.0026	0.63	10.4551	0.2856	0.0571	0.0070	589	15	494	243	119
	14.2	1.88	69.7	213.4	638.3	0.334	0.8395	0.0239	0.1009	0.0011	0.77	9.9075	0.1125	0.0603	0.0017	620	7	615	63	100
	13.1	0.69	65.8	332.8	559.1	0.595	0.8496	0.0301	0.1014	0.0013	0.54	9.8577	0.1247	0.0607	0.0022	623	8	630	77	98
	16.2	3.80	84.9	363.8	769.7	0.473	0.6458	0.0200	0.0782	0.0010	0.97	12.7827	0.1566	0.0599	0.0016	486	6	599	60	81
	17.1	0.78	248.8	869.6	2280.1	0.381	0.8425	0.0181	0.1022	0.0010	0.91	9.7807	0.0985	0.0598	0.0012	628	6	595	45	105
	6.1	2.05	123.1	467.6	1049.4	0.446	0.8684	0.0216	0.1060	0.0012	0.61	9.4360	0.1074	0.0594	0.0015	649	7	583	53	111
	4.1	3.94	91.6	469.2	912.6	0.514	0.8701	0.0744	0.1043	0.0025	0.91	9.5835	0.2325	0.0605	0.0057	640	15	621	212	103
	10.2	3.19	237.5	715.8	1991.0	0.3590	0.7356	0.0171	0.0892	0.0010	0.98	11.2144	0.1199	0.0598	0.0013	551	6	597	47	92
	11.1	0.80	941.6	4725.5	11325.2	0.417	0.4671	0.0092	0.0599	0.0006	0.99	16.6954	0.1664	0.0566	0.0010	375	4	474	39	79

	3.1	0.16	147.1	166.0	206.5	0.804	14.1171	0.2761	0.5264	0.0063	0.88	1.8996	0.0229	0.1945	0.0035	2726	27	2781	29	98
	1.2	13.52	74.2	78.6	736.4	0.107	0.7609	0.0253	0.0922	0.0012	0.92	10.8471	0.1406	0.0599	0.0020	568	7	599	71	94
	8.1	6.04	46.6	386.8	418.0	0.925	0.8666	0.0461	0.1063	0.0018	0.91	9.4103	0.1595	0.0591	0.0036	651	11	572	131	113
	8.2	11.56	116.1	394.7	1158.1	0.341	0.7224	0.0187	0.0862	0.0010	0.96	11.5981	0.1320	0.0608	0.0016	533	6	631	59	84
	10.1	8.10	34.4	252.2	279.7	0.901	0.9953	0.0744	0.1150	0.0025	0.68	8.6919	0.1886	0.0627	0.0052	702	14	699	175	100
	15.1	8.51	33.9	272.5	302.6	0.901	0.8185	0.0397	0.0987	0.0014	0.88	10.1356	0.1481	0.0602	0.0032	607	9	610	120	99
	16.1	8.60	128.6	427.8	1165.0	0.367	0.7797	0.0189	0.0946	0.0010	0.99	10.5671	0.1104	0.0598	0.0015	583	6	595	53	98
BUY-66-11	14.1	6.62	37.1	166.0	375.9	0.442	0.7235	0.0239	0.0849	0.0011	0.49	11.7808	0.1557	0.0618	0.0022	525	7	668	75	78
	3.1	2.17	51.8	306.5	503.4	0.609	0.7160	0.0242	0.0880	0.0011	0.07	11.3641	0.1479	0.0590	0.0021	544	7	568	75	95
	19.1	0.86	34.5	249.9	314.0	0.796	0.7311	0.0271	0.0884	0.0012	0.41	11.3062	0.1596	0.0600	0.0024	546	7	602	91	90
	17.1	0.57	11.2	66.4	107.4	0.618	0.7089	0.0710	0.0899	0.0024	0.13	11.1251	0.2923	0.0572	0.0066	555	14	499	241	111
	15.1	8.79	43.4	348.5	385.7	0.904	0.7344	0.0275	0.0904	0.0012	0.98	11.0630	0.1514	0.0589	0.0026	558	7	564	98	98
	16.1	4.53	45.0	214.8	466.3	0.461	0.7620	0.0180	0.0908	0.0010	0.80	11.0161	0.1248	0.0609	0.0015	560	6	635	55	88
	18.1	1.64	6.8	106.2	47.2	2.252	0.8110	0.1725	0.0908	0.0048	0.31	11.0073	0.5794	0.0647	0.0160	561	28	766	403	73
	9.1	7.31	29.1	129.8	281.9	0.460	0.7874	0.1245	0.0924	0.0047	0.01	10.8255	0.5451	0.0618	0.0122	570	28	668	274	85
	11.1	2.28	7.2	20.0	18.9	1.059	3.7355	0.3946	0.2605	0.0115	0.59	3.8383	0.1692	0.1040	0.0119	1493	58	1697	194	87
	4.1	1.89	21.8	63.6	62.1	1.025	4.4056	0.1346	0.2935	0.0048	0.63	3.4074	0.0559	0.1089	0.0034	1659	24	1781	56	93
	1.1	0.41	8.9	24.4	24.3	1.007	3.9573	0.2207	0.2865	0.0086	0.50	3.4903	0.1045	0.1002	0.0061	1624	43	1627	106	99
	21.1	2.33	6.6	18.8	24.1	0.782	3.0773	0.2406	0.2085	0.0071	0.20	4.7967	0.1632	0.1071	0.0098	1221	38	1750	172	69
	22.1	1.32	8.8	26.5	30.0	0.881	2.9977	0.2806	0.2219	0.0083	0.76	4.5069	0.1695	0.0980	0.0099	1292	44	1586	194	81
	9.2	254.26	21.0	382.5	677.1	0.565	0.1914	0.0050	0.0180	0.0002	0.21	55.6666	0.6678	0.0773	0.0024	115	1	1128	64	10
	7.2	64.55	6.0	85.9	235.6	0.364	0.1752	0.0172	0.0229	0.0007	0.90	43.6793	1.3197	0.0555	0.0057	146	4	433	178	33
	7.1	114.62	50.5	415.1	965.7	0.430	0.3660	0.0097	0.0424	0.0005	0.23	23.5989	0.2636	0.0626	0.0018	268	3	696	61	38
	8.2	68.46	61.5	464.0	1012.3	0.458	0.4099	0.0102	0.0489	0.0005	0.30	20.4489	0.2053	0.0608	0.0016	308	3	632	55	48
	20.1	5.82	28.2	233.4	319.0	0.732	0.5998	0.0269	0.0685	0.0011	0.61	14.5940	0.2237	0.0635	0.0032	427	6	724	105	58
	5.1	8.17	86.5	530.1	789.0	0.672	0.6385	0.0136	0.0763	0.0007	0.93	13.0998	0.1214	0.0607	0.0014	474	4	627	50	75
	21.2	35.80	61.2	357.6	752.8	0.475	0.7402	0.0283	0.0802	0.0012	0.94	12.4663	0.1845	0.0669	0.0028	497	7	835	86	59
	10.1	58.43	74.2	427.9	882.5	0.485	0.6590	0.0175	0.0814	0.0009	0.72	12.2800	0.1331	0.0587	0.0016	505	5	556	63	90
	8.1	9.24	16.2	75.0	147.5	0.509	4.9843	0.0983	0.2449	0.0028	1.00	4.0826	0.0462	0.1476	0.0033	1412	15	2318	39	60
	2.1	25.42	160.6	62.0	681.5	0.091	4.8863	0.0856	0.1900	0.0017	1.00	5.2645	0.0470	0.1866	0.0030	1121	9	2712	26	41
	13.1	222.17	12.7	131.4	61.5	2.135	0.8907	0.1096	0.0941	0.0034	0.49	10.6275	0.3858	0.0686	0.0099	580	20	888	286	65
	12.1	13.84	27.5	319.5	236.0	1.354	0.7426	0.0316	0.0895	0.0014	0.71	11.1699	0.1700	0.0602	0.0029	553	8	609	105	90
AA-12 (Ttn)	10.1	13.00	9	100	67	1.50	0.9134	0.1582	0.0929	0.0032	0.01	10.7688	0.3726	0.0713	0.0126	572	19	967	363	86
	1.1	6.76	11	165	72	2.29	0.8013	0.1175	0.0931	0.0026	0.24	10.7413	0.2966	0.0624	0.0100	574	15	689	316	96
	17.1	14.21	12	78	102	0.76	0.8427	0.1260	0.0937	0.0041	0.30	10.6749	0.4654	0.0652	0.0116	577	24	782	347	93
	13.1	21.35	8	122	42	2.93	0.6949	0.2278	0.0965	0.0042	0.01	10.3604	0.4477	0.0522	0.0181	594	24	295	496	110
	2.1	17.84	12	162	80	2.04	0.7473	0.1337	0.0967	0.0028	0.01	10.3442	0.3046	0.0561	0.0104	595	17	455	340	104
	3.1	20.53	16	167	129	1.30	0.7806	0.0783	0.0969	0.0019	0.01	10.3197	0.2076	0.0584	0.0064	596	11	546	232	101
	4.1	12.20	20	201	154	1.30	0.6781	0.0920	0.0986	0.0022	0.27	10.1457	0.2225	0.0499	0.0073	606	13	190	228	115
	6.1	29.56	10	127	77	1.66	0.6591	0.1355	0.0993	0.0028	0.01	10.0688	0.2798	0.0481	0.0110	610	16	106	326	118
	5.1	50.27	8	97	49	2.01	0.8625	0.1830	0.1002	0.0035	0.37	9.9814	0.3507	0.0624	0.0144	616	21	689	450	97
	8.1	18.02	12	177	74	2.39	0.6826	0.1310	0.1002	0.0028	0.22	9.9808	0.2829	0.0494	0.0101	616	17	168	351	116
	9.1	17.13	8	116	47	2.50	0.8719	0.1990	0.1005	0.0038	0.37	9.9506	0.3785	0.0629	0.0159	617	22	706	445	96
	11.1	14.99	15	159	99	1.61	0.8621	0.1129	0.1007	0.0025	0.09	9.9291	0.2486	0.0621	0.0090	619	15	677	281	97
	7.1	16.45	14	228	93	2.45	0.8056	0.1388	0.1017	0.0028	0.30	9.8293	0.2708	0.0574	0.0108	625	16	508	300	104

	12.1	38.72	11	170	63	2.71	0.7755	0.1617	0.1022	0.0033	0.48	9.7850	0.3126	0.0550	0.0127	627	19	414	416	107
	14.1	20.84	8	92	57	1.62	0.6674	0.1839	0.0930	0.0063	0.01	10.7572	0.7280	0.0521	0.0156	573	37	289	359	110
	13.2	34.87	6	110	38	2.86	0.9528	0.2178	0.0910	0.0070	0.43	10.9903	0.8413	0.0759	0.0220	561	41	1094	613	82
	15.1	25.93	8	113	61	1.86	0.7122	0.1831	0.0915	0.0059	0.53	10.9299	0.7058	0.0565	0.0161	564	35	470	433	103
	18.1	32.19	6	95	48	1.98	0.8901	0.1782	0.0922	0.0056	0.31	10.8460	0.6620	0.0700	0.0166	569	33	929	415	87
	16.1	80.12	2	6	32	0.17	0.6250	0.2354	0.0872	0.0076	0.86	11.4743	0.9971	0.0520	0.0228	539	45	286	521	109
	1.1	23.93	6	9	61	0.14	0.8016	0.0931	0.0948	0.0022	0.34	10.5488	0.2481	0.0613	0.0079	584	13	651	250	97
	9.1	32.38	3	14	30	0.47	0.6967	0.1456	0.0928	0.0031	0.21	10.7711	0.3550	0.0544	0.0125	572	18	389	317	106
	16.1	33.43	3	23	25	0.90	0.8340	0.1749	0.0983	0.0036	0.17	10.1710	0.3706	0.0615	0.0142	605	21	657	450	98
	1.2	60.97	3	5	26	0.19	0.8826	0.1138	0.0980	0.0025	0.33	10.1993	0.2608	0.0653	0.0092	603	15	784	313	93
	5.1	61.72	2	1	24	0.05	0.7513	0.1937	0.0905	0.0040	0.18	11.0542	0.4941	0.0602	0.0171	558	24	612	457	98
	2.1	76.99	2	7	19	0.38	0.9626	0.1956	0.0984	0.0044	0.01	10.1623	0.4517	0.0710	0.0168	605	26	956	438	88
	15.1	81.42	2	1	25	0.02	0.8250	0.2588	0.0891	0.0051	0.27	11.2266	0.6366	0.0672	0.0215	550	30	843	537	90
	17.1	87.40	1	0	12	0.02	1.1560	0.3327	0.1061	0.0063	0.59	9.4218	0.5563	0.0790	0.0268	650	37	1172	597	83
AA-13 (Ttn)	13.1	0.08	79	79	200	0.39	6.9499	0.0914	0.3962	0.0031	0.89	2.5241	0.0197	0.1272	0.0018	2151	14	2060	25	102
	14.1	0.42	123	51	325	0.16	7.3467	0.1041	0.4170	0.0034	0.95	2.3981	0.0196	0.1278	0.0018	2247	16	2068	24	104
	6.1	98.31	1	0	7	0.03	0.3191	0.9056	0.1924	0.0183	0.09	5.1975	0.4940	0.0120	0.0614	1134	104	0	993	403
	3.1	174.85	1	0	9	0.03	0.1385	0.5718	0.0751	0.0108	0.54	13.3170	1.9235	0.0134	0.0458	467	64	0	513	354
	4.1	276.76	1	1	6	0.13	0.0805	0.7680	0.0853	0.0147	0.20	11.7244	2.0220	0.0068	0.0592	528	86	0	527	671
	12.1	240.92	1	1	6	0.17	0.5080	0.6771	0.0940	0.0119	0.52	10.6361	1.3407	0.0392	0.0567	579	70	0	951	138
	18.1	130.36	1	1	10	0.09	0.6730	0.6341	0.0970	0.0115	0.42	10.3056	1.2189	0.0503	0.0510	597	67	209	930	114
	7.1	72.57	2	4	24	0.19	0.3021	0.2527	0.0929	0.0050	0.50	10.7598	0.5767	0.0236	0.0201	573	29	0	120	213
	8.1	118.82	1	2	14	0.13	0.6039	0.3475	0.0966	0.0066	0.48	10.3484	0.7061	0.0453	0.0288	595	39	0	444	123
	10.1	133.71	2	1	16	0.06	0.6111	0.3332	0.0953	0.0063	0.41	10.4975	0.6890	0.0465	0.0271	587	37	25	579	121
	11.1	146.15	1	1	13	0.09	0.5706	0.2562	0.0954	0.0050	0.53	10.4870	0.5549	0.0434	0.0213	587	30	0	438	128

Hf Isotopy Results

Sample	Spot	$^{176}Hf/^{177}Hf$	±2σ	$^{176}Lu/^{177}Hf$	±2σ	U-Pb Age (Ma)	ε_{Hf} (T$_0$)	$^{176}Hf/^{177}Hf$ (T$_1$)	ε_{Hf} (T$_1$)	$^{176}Hf/^{177}Hf$ (T)	T$_{DM}$ (Ma)	$^{176}Hf/^{177}Hf$ (T)	ε_{Hf} (T$_{DM}$)
	10.2	0.281298	0.000071	0.001679	0.000057	1947	-52.14	0.281236	-10.92	0.281799	3222	0.280838	4.43
	9.1	0.281309	0.000054	0.000476	0.000004	1990	-51.72	0.281291	-7.95	0.281767	3068	0.280955	5.00
	8.1	0.281319	0.000038	0.000331	0.000001	2008	-51.40	0.281306	-7.03	0.281754	3024	0.280989	5.17
	1.1	0.281350	0.000036	0.000344	0.000000	2024	-50.29	0.281337	-5.57	0.281742	2944	0.281050	5.47
BUY-	13.2	0.281340	0.000045	0.000338	0.000001	2035	-50.63	0.281327	-5.65	0.281734	2957	0.281039	5.42
54-11	13.1	0.281340	0.000041	0.000446	0.000008	2048	-50.63	0.281323	-5.51	0.281724	2958	0.281039	5.41
	3.1	0.281343	0.000037	0.000300	0.000001	2049	-50.55	0.281331	-5.20	0.281723	2940	0.281053	5.48
	12.1	0.281356	0.000054	0.000390	0.000001	2049	-50.07	0.281341	-4.85	0.281723	2917	0.281070	5.57
	10.1	0.281312	0.000042	0.001013	0.000007	2061	-51.65	0.281272	-7.03	0.281714	3064	0.280958	5.02
	2.1	0.281500	0.000053	0.000888	0.000044	2078	-44.98	0.281465	0.23	0.281702	2617	0.281298	6.68
	7.1	0.281417	0.000053	0.000536	0.000002	2131	-47.90	0.281396	-1.02	0.281662	2737	0.281207	6.23
	19.2	0.281273	0.000035	0.000249	0.000002	1839	-53.01	0.281264	-12.36	0.281880	3229	0.280832	4.40
	14.2	0.281267	0.000043	0.000276	0.000005	1864	-53.23	0.281257	-12.04	0.281861	3229	0.280833	4.41
	4.1	0.281357	0.000051	0.000416	0.000003	1871	-50.04	0.281342	-8.86	0.281856	3034	0.280981	5.13
	18.2	0.281255	0.000034	0.000286	0.000002	1873	-53.65	0.281245	-12.28	0.281854	3251	0.280816	4.32
BUY-	18.1	0.281342	0.000038	0.000519	0.000006	2023	-50.56	0.281322	-6.10	0.281743	2977	0.281025	5.34
57-11	12.1	0.281326	0.000055	0.000846	0.000010	2025	-51.15	0.281293	-7.09	0.281741	3041	0.280976	5.11
	20.1	0.281254	0.000044	0.000238	0.000001	2065	-53.68	0.281245	-7.90	0.281711	3123	0.280914	4.80
	13.1	0.281350	0.000040	0.000374	0.000005	2094	-50.29	0.281335	-4.02	0.281690	2899	0.281084	5.63
	19.1	0.281444	0.000056	0.000708	0.000007	2096	-46.96	0.281416	-1.11	0.281688	2715	0.281223	6.31
	16.1	0.281333	0.000027	0.000266	0.000004	2100	-50.90	0.281322	-4.35	0.281685	2925	0.281064	5.54
	16.2	0.281320	0.000031	0.000278	0.000002	2112	-51.34	0.281309	-4.53	0.281676	2945	0.281049	5.46
	2.2	0.281143	0.000036	0.000469	0.000013	2046	-57.6	0.281125	-12.6	0.281725	3403	0.280699	3.8
	6.2	0.281120	0.000029	0.000374	0.000005	2047	-58.4	0.281105	-13.3	0.28172468	3446	0.280666	3.6
	3.1	0.281149	0.000039	0.000403	0.000005	2049	-57.4	0.281133	-12.2	0.281723	3382	0.280716	3.8
	7.1	0.281148	0.000030	0.000515	0.000014	2055	-57.4	0.281128	-12.3	0.281719	3390	0.280709	3.8
BUY-	10.2	0.281151	0.000030	0.000404	0.000002	2071	-57.3	0.281135	-11.7	0.281707	3364	0.280729	3.9
61-11	11.1	0.281136	0.000028	0.000859	0.000008	2090	-57.9	0.281102	-12.4	0.281693	3425	0.280682	3.7
	4.2	0.281105	0.000022	0.000408	0.000002	2104	-58.9	0.281089	-12.5	0.28168208	3445	0.280668	3.6
	5.2	0.281080	0.000029	0.000601	0.000018	2327	-59.8	0.281053	-8.7	0.281515	3374	0.280722	3.9
	12.1	0.281040	0.000042	0.001122	0.000029	2504	-61.3	0.280986	-7.0	0.281382	3402	0.280701	3.8
	9.1	0.281064	0.000025	0.000289	0.000001	2526	-60.4	0.281051	-4.2	0.281365	3242	0.280823	4.4
	5.1	0.281010	0.000029	0.001203	0.000012	2614	-62.3	0.280950	-5.7	0.281299	3407	0.280697	3.7
	3.1	0.281564	0.000025	0.000630	0.000001	622	-42.7	0.281556	-29.3	0.282775	3342.0	0.280746	4.0
	4.1	0.281470	0.000022	0.000292	0.000003	577	-46.1	0.281467	-33.5	0.282808	3562.3	0.280577	3.2
	8.1	0.281626	0.000034	0.000687	0.000025	609	-40.5	0.281618	-27.4	0.28278462	3214.8	0.280843	4.5
	7.1	0.281513	0.000047	0.001025	0.000003	658	-44.5	0.281500	-30.5	0.282749	3442.4	0.280669	3.6
BUY-	9.1	0.281929	0.000034	0.000679	0.000017	585	-29.8	0.281922	-17.2	0.28280207	2563.4	0.281338	6.9
63-11	12.1	0.281868	0.000032	0.001187	0.000025	559	-32.0	0.281856	-20.1	0.282821	2723.5	0.281217	6.3
	14.2	0.281918	0.000033	0.000488	0.000005	676	-30.2	0.281912	-15.5	0.282736	2530.1	0.281363	7.0
	14.1	0.281795	0.000031	0.000336	0.000008	640	-34.5	0.281791	-20.6	0.282762	2817.4	0.281146	5.9
	10.1	0.281716	0.000032	0.000325	0.000002	716	-37.4	0.281711	-21.7	0.282707	2947.4	0.281047	5.5
	16.1	0.281913	0.000028	0.000299	0.000000	546	-30.4	0.281910	-18.5	0.282830	2611.5	0.281301	6.7
	2.1	0.281548	0.000023	0.000355	0.000002	760	-43.3	0.281543	-26.7	0.282675	3290.6	0.280786	4.2
	1.1	0.281837	0.000061	0.001974	0.000089	2152	-33.08	0.281756	12.25	0.281646	1901	0.281834	9.29
	4.2	0.281671	0.000021	0.001133	0.000024	617	-38.95	0.281657	-25.85	0.282779	3124	0.280913	4.80
	7.1	0.281359	0.000031	0.000063	0.000002	1894	-49.95	0.281357	-7.81	0.281839	2985	0.281018	5.31
	4.1	0.280963	0.000042	0.000376	0.000008	2029	-63.96	0.280949	-19.23	0.281738	3806	0.280390	2.24
BUY-	10.1	0.281280	0.000046	0.001657	0.000135	2107	-52.76	0.281213	-8.05	0.281680	3164	0.280882	4.65
65-11	6.1	0.281287	0.000042	0.000326	0.000001	2145	-52.52	0.281274	-5.04	0.281651	3003	0.281005	5.25
	2.1	0.281320	0.000031	0.000382	0.000005	2158	-51.35	0.281304	-3.65	0.281642	2925	0.281064	5.54
	8.1	0.281257	0.000042	0.000906	0.000004	2183	-53.57	0.281219	-6.09	0.281623	3099	0.280932	4.89
	9.1	0.281297	0.000039	0.001850	0.000058	2441	-52.15	0.281211	-0.46	0.281429	2938	0.281054	5.49
	5.1	0.280873	0.000037	0.000387	0.000003	2541	-67.16	0.280854	-10.84	0.281354	3673	0.280492	2.74

	11.1	0.281079	0.000034	0.001013	0.000018	2731	-59.86	0.281026	-0.32	0.281210	3151	0.280892	4.70
BUY-77-11	1.2	0.281620	0.000035	0.000299	0.000014	560	-40.7	0.281617	-28.5	0.282820	3246.2	0.280819	4.3
	3.2	0.281626	0.000045	0.000717	0.000004	564	-40.5	0.281618	-28.4	0.282817	3240.1	0.280824	4.4
	5.1	0.281638	0.000030	0.000877	0.000015	581	-40.1	0.281628	-27.7	0.28280498	3209.4	0.280848	4.5
	6.1	0.281646	0.000021	0.000689	0.000004	682	-39.8	0.281637	-25.1	0.282731	3130.4	0.280908	4.8
	7.1	0.281572	0.000027	0.001212	0.000013	574	-42.4	0.281559	-30.3	0.28281006	3364.6	0.280729	3.9
	10.1	0.281578	0.000044	0.001263	0.000043	582	-42.2	0.281564	-29.9	0.282804	3347.5	0.280742	4.0
	12.1	0.281555	0.000045	0.001189	0.000016	624	-43.0	0.281541	-29.8	0.282774	3373.5	0.280722	3.9
	13.1	0.281544	0.000051	0.001028	0.000011	587	-43.4	0.281533	-30.9	0.282801	3413.6	0.280691	3.7
	14.1	0.281688	0.000046	0.000876	0.000036	561	-38.3	0.281679	-26.3	0.282820	3109.6	0.280924	4.9
	17.1	0.281702	0.000037	0.000996	0.000005	627	-37.8	0.281690	-24.5	0.282772	3046.9	0.280971	5.1
	21.1	0.281635	0.000053	0.001771	0.000051	612	-40.2	0.281615	-27.5	0.282782	3220.8	0.280839	4.4
BUY-88-11	1.1	0.281689	0.000022	0.000401	0.000001	2089	-38.3	0.281673	7.9	0.281693	2135.6	0.281659	8.4
	5.1	0.281665	0.000031	0.000834	0.000008	2073	-39.2	0.281632	6.0	0.281705	2240.3	0.281581	8.1
	6.1	0.281624	0.000025	0.000805	0.000007	2092	-40.6	0.281591	5.0	0.28169105	2319.5	0.281521	7.8
	9.1	0.281683	0.000032	0.003378	0.000018	2078	-38.5	0.281549	3.2	0.281702	2425.2	0.281442	7.4
	17.1	0.281624	0.000027	0.001123	0.000046	2089	-40.6	0.281579	4.5	0.28169329	2349.0	0.281499	7.7
	30.1	0.281616	0.000032	0.000762	0.000011	2098	-40.9	0.281585	5.0	0.281687	2329.7	0.281513	7.7
	29.1	0.281616	0.000026	0.000551	0.000004	2099	-40.9	0.281594	5.3	0.281686	2308.5	0.281529	7.8
	28.1	0.281713	0.000037	0.002023	0.000021	2073	-37.5	0.281633	6.1	0.281705	2238.5	0.281582	8.1
	27.1	0.281637	0.000034	0.000779	0.000011	2091	-40.1	0.281606	5.5	0.281692	2287.6	0.281545	7.9
	23.1	0.281811	0.000051	0.003862	0.000045	2090	-34.0	0.281658	7.3	0.281693	2170.0	0.281633	8.3
	16.1	0.281698	0.000032	0.001441	0.000010	2077	-38.0	0.281641	6.4	0.281702	2217.7	0.281597	8.1
	20.1	0.281687	0.000028	0.000656	0.000008	2088	-38.4	0.281661	7.4	0.281694	2164.1	0.281638	8.3
	22.1	0.281660	0.000031	0.001147	0.000014	2076	-39.3	0.281614	5.5	0.281703	2278.3	0.281552	7.9
	14.1	0.281821	0.000037	0.003169	0.000075	2073	-33.6	0.281696	8.3	0.281705	2095.3	0.281689	8.6
Nb-66	1.1	0.281118	0.000030	0.001198	0.000031	2608	-58.5	0.281058	-2.0	0.281303	3165.7	0.280881	4.6
	2.1	0.281194	0.000028	0.001166	0.000006	2612	-55.8	0.281136	0.8	0.281300	2987.8	0.281016	5.3
	2.2	0.281166	0.000015	0.000777	0.000002	2621	-56.8	0.281127	0.7	0.28129358	3000.6	0.281007	5.3
	3.1	0.281151	0.000027	0.000590	0.000010	2633	-57.3	0.281122	0.8	0.281285	3004.7	0.281004	5.2
	5.1	0.281122	0.000028	0.000706	0.000005	2629	-58.4	0.281086	-0.6	0.28128754	3088.1	0.280940	4.9
	6.1	0.281170	0.000023	0.000629	0.000011	2619	-56.6	0.281139	1.1	0.281295	2975.4	0.281026	5.3
	8.1	0.281273	0.000037	0.000489	0.000003	2645	-53.0	0.281248	5.6	0.281275	2707.0	0.281229	6.3
	9.1	0.281163	0.000028	0.000793	0.000005	2637	-56.9	0.281123	0.9	0.281281	2998.6	0.281008	5.3
	12.1	0.281172	0.000022	0.000362	0.000006	2617	-56.6	0.281154	1.6	0.281297	2941.7	0.281051	5.5
	13.1	0.281150	0.000025	0.000490	0.000014	2637	-57.4	0.281125	1.0	0.281281	2993.5	0.281012	5.3
	14.1	0.281126	0.000023	0.000487	0.000008	2528	-58.2	0.281103	-2.3	0.281364	3122.4	0.280914	4.8
	15.1	0.281193	0.000038	0.000305	0.000011	2629	-55.8	0.281178	2.7	0.281288	2879.4	0.281099	5.7
	18.1	0.281116	0.000025	0.000502	0.000001	2635	-58.6	0.281090	-0.3	0.281283	3074.3	0.280951	5.0
	19.1	0.281102	0.000034	0.000497	0.000002	2631	-59.1	0.281077	-0.8	0.281286	3107.8	0.280925	4.9
	20.1	0.281165	0.000029	0.000477	0.000004	2642	-56.8	0.281140	1.7	0.281278	2955.4	0.281041	5.4
	21.1	0.281068	0.000044	0.000774	0.000006	2628	-60.3	0.281029	-2.6	0.281288	3218.7	0.280840	4.4
BUY-76-11	29.1	0.280934	0.000027	0.000502	0.000010	2751.0	-65.00	0.280908	-4.08	0.281195	3406	0.280698	3.74
	58.1	0.280964	0.000037	0.001174	0.000071	2753.0	-63.94	0.280902	-4.23	0.281194	3417	0.280689	3.70
	27.1	0.281043	0.000044	0.002018	0.000071	2767.0	-61.15	0.280936	-2.70	0.281183	3330	0.280756	4.03
	32.1	0.281053	0.000043	0.003413	0.000001	2769.0	-60.77	0.280872	-4.92	0.281182	3472	0.280646	3.49
	32.2	0.280960	0.000029	0.001265	0.000001	2770.0	-64.08	0.280893	-4.16	0.281181	3425	0.280682	3.67
	3.1	0.280912	0.000027	0.000409	0.000003	2780.0	-65.78	0.280890	-4.03	0.281173	3424	0.280683	3.67
	57.1	0.280987	0.000030	0.001351	0.000015	3010.0	-63.11	0.280909	2.01	0.280999	3214	0.280844	4.46
	35.1	0.280864	0.000025	0.001035	0.000022	3204.0	-67.47	0.280800	2.67	0.280851	3320	0.280763	4.07
	43.1	0.280871	0.000036	0.001111	0.000006	3204.0	-67.22	0.280803	2.75	0.280851	3314	0.280767	4.09
	50.1	0.280952	0.000028	0.001286	0.000018	3217.0	-64.36	0.280872	5.54	0.280841	3145	0.280897	4.72
	2.1	0.280799	0.000022	0.000815	0.000003	3224.0	-69.78	0.280748	1.28	0.280836	3424	0.280684	3.68
BUY-55-11	23.1	0.282717	0.000030	0.001540	0.000052	664	-1.94	0.282698	12.04	0.282745	771	0.282667	13.33
	18.1	0.282703	0.000029	0.001205	0.000029	672	-2.43	0.282688	11.88	0.282739	788	0.282655	13.27
	25.1	0.282155	0.000025	0.001535	0.000007	1200	-21.83	0.282120	3.55	0.282352	1730	0.281961	9.91
	14.1	0.281955	0.000031	0.001033	0.000022	1218	-28.89	0.281931	-2.73	0.282339	2144	0.281653	8.41
	34.2	0.282094	0.000020	0.000949	0.000011	1222	-23.98	0.282072	2.35	0.282336	1823	0.281892	9.57
	24.1	0.281806	0.000031	0.001347	0.000004	1512	-34.16	0.281767	-1.91	0.282122	2318	0.281522	7.77
	32.2	0.281891	0.000032	0.000943	0.000018	1527	-31.15	0.281864	1.84	0.282111	2091	0.281693	8.60
	32.1	0.281940	0.000024	0.000466	0.000004	1530	-29.41	0.281927	4.14	0.282109	1946	0.281801	9.13
	12.1	0.282042	0.000043	0.001366	0.000013	1543	-25.82	0.282002	7.10	0.282099	1766	0.281935	9.78

	6.1	0.281078	0.000035	0.000503	0.000017	2924	-59.90	0.281050	5.01	0.281064	2956	0.281040	5.42
	4.1	0.280765	0.000035	0.001324	0.000013	3436	-70.99	0.280677	3.72	0.280673	3428	0.280680	3.66
	1.1	0.281663	0.000028	0.000692	0.000005	2088	-39.2	0.281636	6.5	0.281694	2221.4	0.281595	8.1
	2.1	0.281670	0.000028	0.000706	0.000002	2105	-39.0	0.281641	7.1	0.281681	2196.3	0.281614	8.2
	3.1	0.281717	0.000032	0.001603	0.000054	2066	-37.3	0.281654	6.7	0.2817105	2196.0	0.281614	8.2
	5.1	0.281662	0.000034	0.001182	0.000016	2116	-39.3	0.281614	6.4	0.281673	2251.2	0.281572	8.0
	7.1	0.281534	0.000039	0.001076	0.000021	2106	-43.8	0.281491	1.8	0.2816806	2538.0	0.281357	7.0
	7.2	0.281596	0.000033	0.000730	0.000003	2075	-41.6	0.281567	3.8	0.281704	2386.1	0.281471	7.5
	8.1	0.281642	0.000026	0.000677	0.000008	2084	-40.0	0.281615	5.7	0.281697	2270.7	0.281558	7.9
	9.1	0.281604	0.000031	0.000716	0.000020	2091	-41.3	0.281575	4.4	0.281692	2357.6	0.281493	7.6
	10.1	0.281592	0.000027	0.000468	0.000002	2055	-41.7	0.281573	3.5	0.281719	2386.8	0.281471	7.5
	11.1	0.281573	0.000039	0.000960	0.000002	2057	-42.4	0.281536	2.3	0.281717	2470.6	0.281408	7.2
AA-13	11.2	0.281585	0.000033	0.000479	0.000002	2040	-42.0	0.281567	3.0	0.281730	2411.9	0.281452	7.4
	13.1	0.281676	0.000027	0.000834	0.000003	2047	-38.8	0.281643	5.9	0.281725	2232.9	0.281586	8.1
	12.1	0.281606	0.000028	0.000774	0.000008	2085	-41.2	0.281576	4.3	0.281696	2360.3	0.281491	7.6
	15.1	0.281569	0.000032	0.000652	0.000005	2074	-42.6	0.281543	2.9	0.281705	2442.4	0.281429	7.3
	16.1	0.281702	0.000039	0.002208	0.000041	2102	-37.9	0.281613	6.0	0.281684	2262.9	0.281564	8.0
	16.2	0.281578	0.000028	0.000586	0.000006	2120	-42.2	0.281555	4.4	0.281670	2383.7	0.281473	7.5
	17.1	0.281603	0.000035	0.000943	0.000022	2103	-41.3	0.281565	4.4	0.281683	2371.1	0.281482	7.6
	18.1	0.281584	0.000029	0.000702	0.000001	2089	-42.0	0.281556	3.7	0.281693	2401.4	0.281460	7.5
	19.1	0.281587	0.000034	0.000758	0.000003	2079	-41.9	0.281557	3.5	0.281701	2406.4	0.281456	7.4
	20.1	0.281615	0.000029	0.000702	0.000021	2073	-40.9	0.281587	4.4	0.281705	2343.0	0.281503	7.7
	21.1	0.281610	0.000028	0.000411	0.000002	2079	-41.1	0.281593	4.8	0.281701	2324.0	0.281518	7.7
	22.1	0.281680	0.000036	0.000761	0.000001	2098	-38.6	0.281649	7.2	0.281687	2183.3	0.281623	8.3

-Appendix 5-

Rb-Sr Geochronology

Sample	Rb (μg/g)	Sr (μg/g)	$^{87}Rb/^{86}Sr$	±2σ (%)	$^{87}Sr/^{86}Sr$	±2σ (%)	±2σ	T_{DM} (Ga)
BUY-92-11 Ms	298.0	26	33.303882	0.5	1.016576	0.00281	0.000029	0.66
BUY-92-11 WR	91.8	164	1.614827	0.5	0.760806	0.00259	0.000020	2.53
BUY-94-11 Ms	364.2	40	26.452916	0.5	0.941649	0.00652	0.000061	0.63
BUY-94-11 WR	93.0	260	1.028606	0.5	0.736273	0.00420	0.000031	2.32
UY-1-13 Phl	335.6	18.9	51.161133	0.5	1.130063	0.00123	0.000014	0.59
UY-1-13 WR	8.4	87.9	0.273940	0.5	0.730735	0.00276	0.000020	7.48
U13MH04 Ms	175.3	32.0	15.788259	0.5	0.977857	0.00142	0.000014	1.22
U13MH04 WR	37.5	10.1	10.708015	0.5	0.935135	0.00112	0.000010	1.52

-Appendix 6-

K-Ar Geochronology

Sample	Spike (N°)	K_2O (%wt)	$^{40}Ar^*$ (nl/g)	$^{40}Ar^*$ (%)	Age (Ma)	2σ (Ma)
UY-23-13	5059	10.24	246.05	99.42	623.9	7.4
UY-23-13	5059	10.24	245.88	99.49	625.9	7.4
U13MH04	5083	10.02	232.18	99.00	605.0	10.8
UY-6-14	5408	9.54	233.07	98.58	632.7	6.1
UY-26-14	5259	10.14	228.13	99.53	589.7	6.2
UY-27-14	5205	10.32	239.22	96.77	605.0	7.2
UY-41-14	5255	9.85	228.30	99.48	604.9	6.3
UY-45-14	5238	10.47	249.47	99.16	619.4	8.5
UY-48-14	5404	10.38	245.36	92.76	615.2	6.6
UY-54-14	5254	9.98	239.84	99.36	623.8	6.6
UY-55-14	5263	10.10	236.61	99.69	610.4	6.5
UY-64-14	5264	10.04	238.68	99.35	618.1	7.6

-CURRICULUM VITAE-

1. PERSONAL INFORMATION

Name: Sebastián Oriolo
Date of birth: 30.07.1987
Place of birth: Buenos Aires, Argentina

2. EDUCATION

Since October 2013. PhD Student Geosciences. Georg-August-Universität Göttingen, Germany.

2007-2012. Licenciatura Ciencias Geológicas. Universidad de Buenos Aires, Argentina.

3. SCHOLARSHIPS AND DISTINCTIONS

2013-2016. Deutscher Akademischer Austauschdienst (DAAD) scholarship for PhD students.

2016. Göttingen International travel grant. Georg-August-Universität Göttingen, Germany.

2015. PROMOS DAAD travel grant. Georg-August-Universität Göttingen, Germany.

2012. Licenciatura Ciencias Geológicas, average grade: 9.96 (maximum 10.00). Universidad de Buenos Aires, Argentina.

2011-2012. Research scholarship for undergraduate scientists. Centro Interuniversitario Nacional (CIN), Argentina. Project: *Analogue modelling of shear zones controlled by previous anisotropies*.

2006-2011. Scholarship for undergraduate students of Engineering and Geosciences. Roberto Rocca Education Program, Techint Group.

2011. Grant to attend the course *Principles of structural and tectonic analysis: their application to vein-type ore deposits*. XVIII Argentinian Geological Congress, Argentina.

4. PUBLICATIONS

Oriolo, S., Oyhantçabal, P., Wemmer, K., Basei, M.A.S., Benowitz, J., Pfänder, J., Hannich, F., Siegesmund, S. 2016. Timing of deformation in the Sarandí del Yí Shear Zone, Uruguay: Implications for the amalgamation of western Gondwana during the Neoproterozoic Brasiliano-Pan-African Orogeny. Tectonics 35, 754-771.

Oriolo, S., Oyhantçabal, P., Basei, M.A.S., Wemmer, K., Siegesmund, S. 2016. The Nico Pérez Terrane (Uruguay): from Archean crustal growth and connections with the Congo Craton to late Neoproterozoic accretion to the Río de la Plata Craton. Precambrian Research 280, 147-160.

Japas, M.S., Ré, G.H., **Oriolo, S.**, Vilas, J.F. 2016. Basement-involved deformation overprinting thin-skinned deformation in the Pampean flat-slab segment of the southern Central Andes, Argentina. Geological Magazine, doi: 10.1017/S001675681600056X.

Oriolo, S., Oyhantçabal, P., Heidelbach, F., Wemmer, K., Siegesmund, S. 2015. Structural evolution of the Sarandí del Yí Shear Zone, Uruguay: kinematics, deformation conditions and tectonic significance. International Journal of Earth Sciences 104, 1759-1777.

Japas, M.S., Ré, G.H., **Oriolo, S.**, Vilas, J.F. 2015. Palaeomagnetic data from the Precordillera fold and thrust belt constraining foreland evolution of the Pampean flat slab segment (Central Andes, Argentina). In: Pueyo, E.L., Cifelli, F., Sussman, A.J., Oliva-Urcia, B. (Eds.) Palaeomagnetism in fold and thrust belts: new perspectives. Geological Society of London, Special Publication 425, doi: 10.1144/SP425.9.

Oriolo, S., Cristallini, E.O., Japas, M.S., Yagupsky, D.L. 2015. Neogene structure of the Andean Precordillera, Argentina: insights from analogue models. Andean Geology 42, 20-35.

Oriolo, S.*, Japas, M.S., Cristallini, E.O., Giménez, M. 2014. Cross-strike structures controlling magmatism emplacement in a flat-slab setting (Precordillera, Central Andes of Argentina). In: Llana Fúnez, S., Marcos, A., Bastida, F. (Eds.) Deformation structures and processes within the continental crust. Geological Society of London, Special Publication 394, 113-127.

Oriolo, S., Ré, G.H., Japas, M.S., Cristallini, E.O. 2014. Controles de la fábrica magnética en areniscas de la Formación Cuculí (Mioceno, Precordillera de San Juan). Geoacta 39, 30-43.